Renu Kumari
J. Dutta Majumdar
Ajit Behera   *Editors*

Recent Advances in Manufacturing Processes

Select Proceedings of RDMPMC 2020

Springer

Lecture Notes in Mechanical Engineering

Lecture Notes in Mechanical Engineering (LNME) publishes the latest developments in Mechanical Engineering—quickly, informally and with high quality. Original research reported in proceedings and post-proceedings represents the core of LNME. Volumes published in LNME embrace all aspects, subfields and new challenges of mechanical engineering. Topics in the series include:

- Engineering Design
- Machinery and Machine Elements
- Mechanical Structures and Stress Analysis
- Automotive Engineering
- Engine Technology
- Aerospace Technology and Astronautics
- Nanotechnology and Microengineering
- Control, Robotics, Mechatronics
- MEMS
- Theoretical and Applied Mechanics
- Dynamical Systems, Control
- Fluid Mechanics
- Engineering Thermodynamics, Heat and Mass Transfer
- Manufacturing
- Precision Engineering, Instrumentation, Measurement
- Materials Engineering
- Tribology and Surface Technology

To submit a proposal or request further information, please contact the Springer Editor of your location:

China: Ms. Ella Zhang at ella.zhang@springer.com
India: Priya Vyas at priya.vyas@springer.com
Rest of Asia, Australia, New Zealand: Swati Meherishi
at swati.meherishi@springer.com
All other countries: Dr. Leontina Di Cecco at Leontina.dicecco@springer.com

To submit a proposal for a monograph, please check our Springer Tracts in Mechanical Engineering at http://www.springer.com/series/11693 or contact Leontina.dicecco@springer.com

Indexed by SCOPUS. All books published in the series are submitted for consideration in Web of Science.

More information about this series at http://www.springer.com/series/11236

Renu Kumari · J. Dutta Majumdar · Ajit Behera
Editors

Recent Advances in Manufacturing Processes

Select Proceedings of RDMPMC 2020

Editors
Renu Kumari
Department of Metallurgical and Materials
Engineering
National Institute of Technology
Jamshedpur
Jamshedpur, Jharkhand, India

J. Dutta Majumdar
Department of Metallurgical and Materials
Engineering
Indian Institute of Technology Kharagpur
Kharagpur, West Bengal, India

Ajit Behera
Department of Metallurgical and Materials
Engineering
National Institute of Technology Rourkela
Rourkela, Odisha, India

Contents

About the Editors

Dr. Renu Kumari is currently working as Assistant Professor in Metallurgical and Materials Department at National Institute of Technology, Jamshedpur. She has completed her B.E. (metallurgy) from Vinoba Bhave University, Hazaribagh; M.Tech. (metallurgical and materials engineering) from IIT Kharagpur; and Ph.D. (metallurgical and materials engineering) from IIT Kharagpur. Her areas of research interests include corrosion, wear, biomaterials, laser materials processing, thermal spraying, electrophoretic deposition, and dip coating. She has published 13 papers in reputed international journals and presented 13 papers in national and international conferences.

Prof. J. Dutta Majumdar is working as Professor in the Department of Metallurgical and Materials Engineering, Indian Institute of Technology Kharagpur. She has completed her B.E. (metallurgy) from Calcutta University; M.Tech. (metallurgical and materials engineering) from IIT Kharagpur; Ph.D. (metallurgical and materials engineering) from IIT Kharagpur; and Dr.-Ing (materials science and technology) from T. U. Clausthal, Germany. Her areas of research interests include corrosion and surface protection, laser materials processing, biomaterials, advanced materials developed by non-equilibrium processing routes, and advanced welding of similar and dissimilar materials. She made fundamental contributions on development of coatings by laser and plasma processing routes for improved wear, corrosion, and high-temperature oxidation resistance applications, and established understanding of the metallurgy of rapid solidification of metals under the specific heat input of a laser source. She also made extensive efforts for the development of compositionally graded surface and nano-dispersed surface for thermal barrier, hot corrosion, and bio-implant applications by using hybrid coating technology. Her recent research interest concerns ultra-fast laser processing of materials, development of coatings for bio-implant applications, electron beam welding, and laser-aided 3-D manufacturing of objects. She has published more than 150 papers in the international journals of repute and is recipient of several national and international awards.

Dr. Ajit Behera is currently working as Assistant Professor in Metallurgical and Materials Department at National Institute of Technology Rourkela. He has completed his Ph.D. from IIT Kharagpur in 2016. He got National "Yuva Rattan Award" in 2020 for his contribution towards society along with his academic carrier. He also received "Young Faculty Award" in 2017 and "C. V. Raman Award" in 2019. He has published more than 75 publications including books, chapters, and journals. Currently, he is involved with many reputed scientific organizations throughout the world. More than 10 Ph.D. students are from his institute/outside the institute, and 4 foreign exchange students are working on different projects with him.

Tribological Behaviour of Carbon Fiber Reinforced Polyester Composites
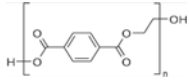
M. V. Sai Kumar and **Y. N. V. Sai Ram**

1 Introduction

Composite materials, polymers, and ceramics have dominated as new materials over few years. Due to their unique qualities like high stiffness and strength-to-weight ratio, the number of applications for composites (especially polymeric composites reinforced with synthetic fibres such as glass, carbon, and aramid) has constantly increased. In recent decades, there has been a surge in demand for such composite materials used in various applications like chassis frames and wheels in automotive industry. A major field of polyester area has developed and advanced to specific composites for aerospace and other applications. The life span of commercial polymers are increased by boosting their mechanical properties [1]. In addition to their desirable mechanical properties, the corrosion resistance is also an enticing consideration for the use of such composites in different areas. Since polyester is sensitive to ultra violet rays, humidity, and moisture conditions, a good maintenance of the nature leads to increase in their life span [2, 3]. The chemical composition and mechanical properties of carbon fiber and polyester resin are shown in Table 1 [2]. The polyesters are extensively used for matrix purposes, predominantly with glass fiber as reinforcement because it is an economically resilient and cost-effective material, with high dimensional stability and low absorption of moisture content. The polyester composites are reinforced with graphite fibers coupled with certain vegetable oils which can be used as self-lubricated materials because they have a low friction coefficient and low wear levels [4–6]. In a composite natural fibers possess remarkable characteristics such as low weight, low cost and high potential applications. Reinforcement of polyester resin with coconut fiber has a great tensile strength, low weight and extremely flexible also, it can be deformed easily to high values of strain. The percentage increase of bagasse fiber with polyester matrix had increased the characteristics of flexural as well as tensile properties [7–12]. With an increased

M. V. Sai Kumar (✉) · Y. N. V. Sai Ram
R.V.R. & J.C. College of Engineering, Guntur, India

Table 1 Chemical composition and mechanical properties of carbon fiber and polyester resin

Property	Carbon fiber	Polyester resin
Chemical composition	Carbon–95%, Nitrogen–4%, Oxygen–0.9%, Hydrogen–0.1%	Polyethylene terephthalate glycol (PETG)
Tensile strength (N/mm^2)	600	40–85
Compressive strength (N/mm^2)	570	140–410
Density (g/cm^3)	1.298	1.1–1.4
Young's modulus (N/mm^2)	113	2–4.5

reinforcement percentage, the mechanical properties of polyester gets strengthened [13].

The carbon content in carbon fibers are more than 90% with an irregular graphite crystal structure along the axis of the fiber. Most commonly used natural fibres are jute, cotton, sisal and matrix materials such as polyester, polyamide, PVC, polythene, etc. are studied as potential precursors for the development of carbon fiber. Finally, rayon (Regenerated cellulose), pitch and polyacrylonitrile (PAN) are the three precursors used for the production of carbon fibers with better mechanical properties [14–16]. Some researchers studied on Polyphenylene sulphide to check the wear and friction with addition of carbon fiber. From the study it is reported that at higher loads,wear levels were decreased when fiber proportion exceeds 50%. The wear rate was minimum at 15–20%, which was apparently dependent on the product pressure and velocity. Carbon fibers have been more effective than glass fibers in enhancing wear properties. Carbon fibers have improved the effectiveness due to change in smoother film into the counterphase, increased thermal conductivity and heat distortion in the polymer [17–20]. Carbon based composites are being used most commonly in structural design of air crafts, transportation vehicles, architectural designs, communication equipment's and so on. These applications and its new technologies are driven by high-performance characteristics and economical production of carbon fibers [21, 22]. Long-carbon fibers reinforced with epoxy resins have outstanding mechanical properties that are used to manufacture aircraft structural components. Once the carbon fiber is burned better organic adhesion is achieved due to its physical and chemical sizing. One of the reasons for pores presence may be due to the poor physical and chemical treatment. Fiber breakage is another reason for high porosity. The same was reported by Schwarz et al. and Selmi et al. for fibre breakage along with soft microcavities [23–25]. The comparison of mechanical properties with carbon-epoxy composite was shown in Table 2.

Various kinds of wear mechanisms can take place during relative movement. Typical wear mechanisms include adhesive wear, abrasive wear, wear of fatigue and

Table 2 Comparison of mechanical properties with carbon-epoxy composite [26]

Composite	Tensile strength (N/mm^2)	% Elongation	Tensile modulus (N/mm^2)
Carbon-epoxy	172	16.5	1042.42

corrosive/oxidative wear. If a rough surface slides over a smoother surface, there is abrasive wear. Abrasive wear may be caused by metallic and non-metallic particles but non-metallic particles in may cause more abrasion. If two flat metal surfaces are allowed to slide under an applied load against each other, adhesive wear takes place. When the contacting surfaces exposed with the environment, corrosion wear takes place along with surface asperties formed by the reaction products. Fatigue wear exists on the surface of products that are loaded cyclically [27]. Few researchers conducted the dry sliding tests at ambient conditions of temperature (22–25 °C), humidity, at different applied loads (30, 50, 70 and 100 N), sliding velocities (2.8, and 3.9 m/s), and sliding distances (0–14 km) [28, 29].

In this paper, work is focussed on the examination of the microstructure and wear behaviour of polymer matrix composite (PMC) of polyester resin of thermoset category. Using die casting technique PMCs were prepared with varying 4% composition of carbon fibers of 85 μm. The novelty of the present work is to investigate the effect of carbon fiber when reinforced with polyester resin and it is discussed in the following sections.

2　Experimentation Work

2.1　Selection of Materials

In our work, a thermosetting polyester from the Bindu agencies, Vijayawada is used as a base material and in that carbon fibers from SMS pharmaceuticals Ltd, Hyderabad. With the reinforcement additions of carbon fiber increased from 4 to 12% in weight at 4%wt intervals. The catalyst, MEKP (Methyl Ethyl Ketone Peroxide) ($C_8H_{18}O_6$, Colourless liquid) and Cobalt octoate ($[CH_3(CH_2)_3CH(C_2H_5)COO]_2Co$, Purple Blue Clear Liquid) is added to cure and also to harden the resin. The weight fractions of various carbon fibers (CF) ranging from 4 to 12% in weight are calculated as CF 4% with 208.33gr, CF 8% with 217.391gr and CF 12% with 227.27gr respectively. In further sections pure polyester, polyester + CF 4%, polyester + CF 8%, polyester + CF 12% are designated with terms as letters P_I, P_{II}, P_{III} and P_{IV}.

Figure 1 indicates the systematic procedure for the fabrication of polyester composites. First weighting the required amount of carbon fibers, polyester resin and suitable quantity of MEKP, Cobalt octoate. The weighted quantity is mixed in a beaker by mechanical stirring at a suitable speed of 110 rpm thoroughly, until it comes to the semi solid state. For fabricating these composites/specimens, a mild steel
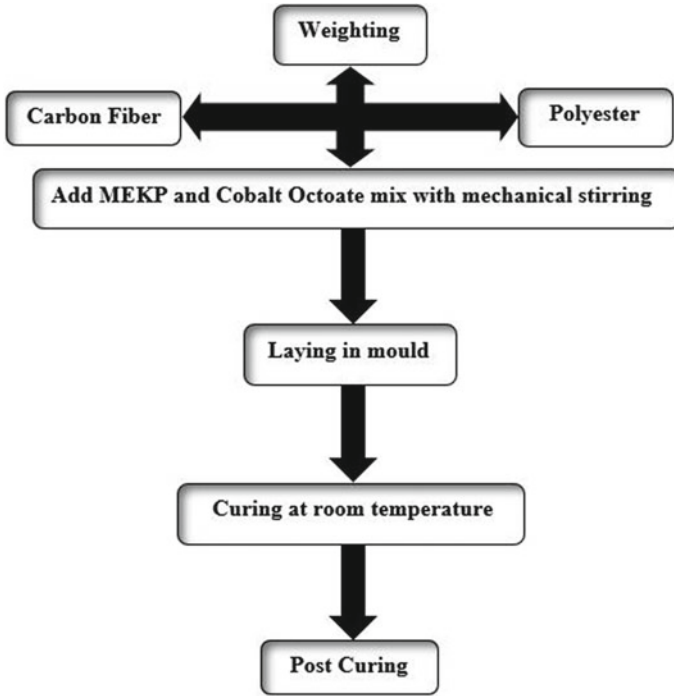
Fig. 1 Systematic procedure for the fabrication of polyester composites

mould/die of Φ15 mm $\times$ 150 mm in length was prepared shown in Fig. 2(Before). For the easy removal of composites from the die a release agent(wax) coat was applied to the mould before pouring the polyester resin. The semi solid state mixture is now poured into the die setup and left it for 24 h. After 24 h die setup is removed shown

Fig. 2 Polyester fabrication setup
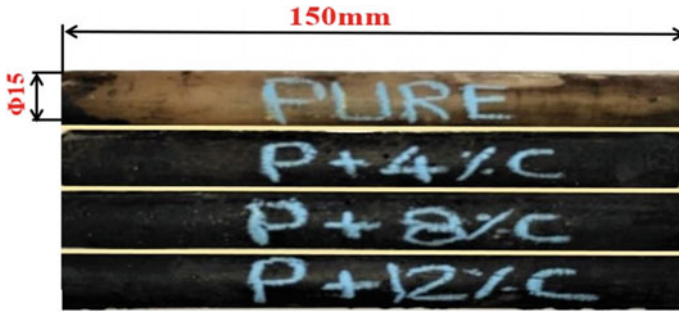
Fig. 3 Fabricated Polyester-Carbon fiber reinforced composite

in Fig. 2(After) and the specimens were taken out and then it is left for post cured (Fig. 3).

2.2 Methods Used

Sliding wear tests. Figure 4 depicts the experimental setup for the measurement of wear. The disc used during the experimentation is made of the material EN 31
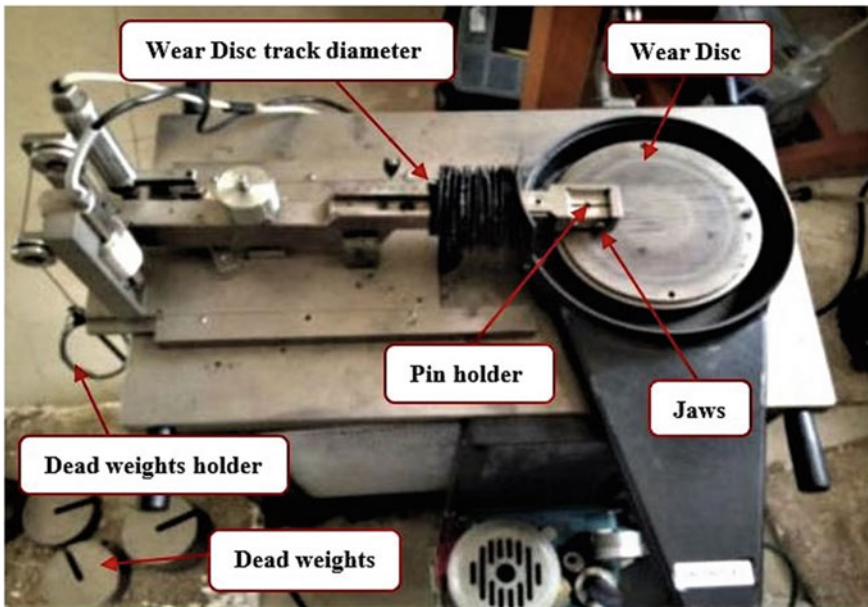
Fig. 4 Pin-on-disc test setup [30]
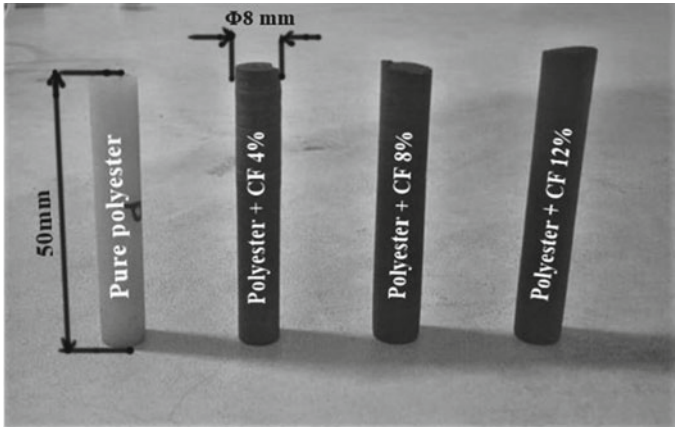
Fig. 5 Wear test Specimens pins

steel. EN stands European norms. EN31 is a high-quality carbon alloy steel with composition (C–1%, Mn–0.5%, Cr–1.4%, Si–0.2%) that provides a high degree of hardness with compressive strength and abrasion resistance. The experimentation is carried out under dry conditions at room temperature for various polyester reinforced carbon fiber samples. Testing has been performed on an EN 31 steel disc with wear track diameter of 0.1 m loaded with a dead weight of 10 N and 20 N with a sliding velocity of 1, 2 and 3 m/s. As per the specifications, wear pin samples of $\Phi 8$ mm $\times$ 50 mm length were machined by using lathe (Fig. 5). Pre and after each test the samples and wear track were cleansed by acetone and weighed using a digital balance (up to $\pm$ 0.1gm). The wear rate is set using height loss technique and expressed by unit sliding distance in terms of wear volume loss. Throughout this experiment, parameters namely load, speed, distance, and time for all experimental tests are kept constant. The specifications of machine and parameters considered during test are given below in Table 3.

2.3 Hardness Measurement

A Digital Micro-Vickers Hardness Tester (Model: HVS 1000B) was used to measure the hardness of the composite samples. The Vickers hardness measurements were carried out to investigate the effect of the reinforcement weight fraction on the matrix content. The load applied was 300gf, 500gf, 1000gf with diamond indenter on the cross-section surface area for a duration of 15 s. The machine specifications and parameters considered during the hardness test are given below in Table 4.

Table 3 Specifications of the machine and parameters taken constant during wear test

Model	Wear & friction monitor TR-20
Pin material	P_I, P_{II}, P_{III} and P_{IV}
Pin dimensions	Φ8 mm $\times$ 50 mm length
Sliding speed (m/s)	1(191 rpm), 2(382 rpm), 3(573 rpm)
Wear test time (minutes)	For 1 m/s = 8.33, 2 m/s = 4.16, 3 m/s = 2.77
Wear track diameter (m)	0.1
Normal load applied (N)	10, 20
Sliding range(m)	500
Disc material	EN31 steel
Normal load range of the machine (N)	4.9 to 200
Wear measurement range of the machine	0 to 2000 micro meters
Sliding speed of the machine (m/s)	0.26 to 1.3

Table 4 Specifications of the machine and parameters considered during hardness test

Model	HVS 1000B
Applied force	300gf, 500gf, 1000gf
Hardness measuring range	5–3000HV
Test force	10 to 2000gf
Magnification of the measuring system	400X, 100X
Minimum reading	0.01 mm
Hardness value	5 Digits
Operating temperature	10 to 45°C
Maximum specimen height	210 mm
Dimensions	470 $\times$ 320 $\times$ 500 mm
Weight	40 kg
Measurement	Vickers and Knoop

2.4 Characterization of CFRP Specimens Using SEM & EDX Analysis

For SEM analysis, specimen surfaces were gold (Au) coated to make them conductive with the aid of a sputter coating equipment (Model: SC7620) before starting the scanning process. Gold coated CFRP samples are shown in Fig. 6.

The use of aluminium stubs is recommended for loading a sample into a scanning electron microscope. When a non-conductive material is imaged, the electrons accelerated to the sample do not have a path to ground potential and accumulate on the surface. This will result in a gradual increase in the brightness of the image until all details are no longer visible. To make a solution for non-conductive specimens,
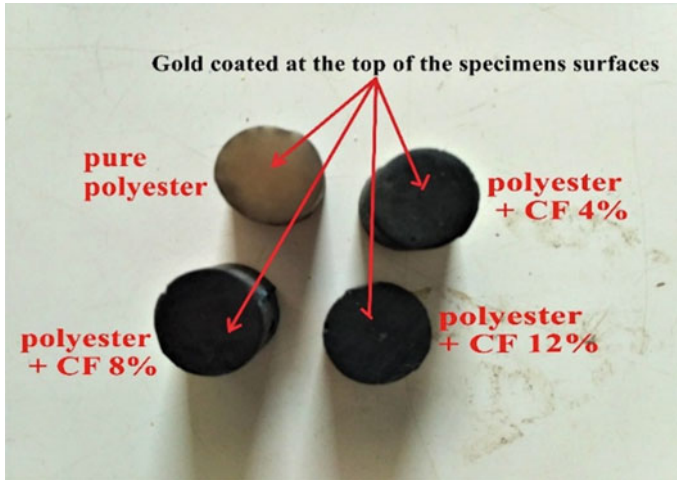
Fig. 6 Sputter coated CFRP samples

Table 5 Parameters considered during sputtering technique

Material	Gold (Au)
Target distance	45 mm
Plasma current	18 mA for 120 s
Gas medium	Argon
Coating thickness	367 Angstroms
Sample size	1 cm^3

we coated the surface of the specimens using the sputter coating technique. The parametric values at which sputtering has adopted were included in the Table 5.

For microstructural analysis, Scanning Electron Microscope (Model: VEGA3, TESCAN) coupled with Energy dispersive X-ray (Model: BRUKER nano, GmbH, D-12489) is used.

3 Results and Discussions

3.1 Wear Analysis

Wear test measurements were carried out on the base sample and composite samples by using wear testing machine to assess the rate of wear. Normal load applied on the samples was 10 N and 20 N in the normal direction. The wear tests results obtained are shown below:

Time versus Wear. Experiments were carried out for reinforcement of carbon fiber at a 4%wt interval ranging from 4%wt to 12%wt, wear-resistance and hardness increase proportionally with percentages of carbon fiber enhancement, as shown in Figs. 7, 8, 9, 10, 11 and 12. The abrupt changes in the wear shown in the Figs. 8
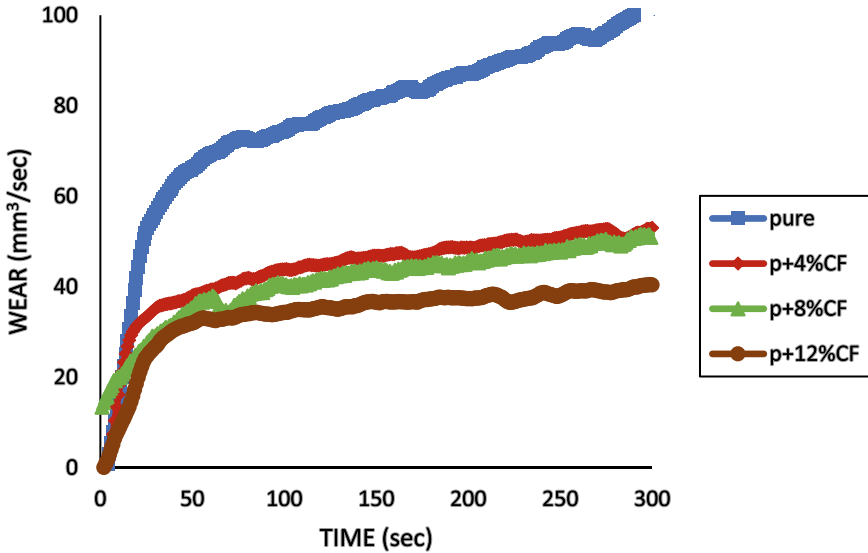
Fig. 7 Time versus Wear for 10 N at 1 m/s
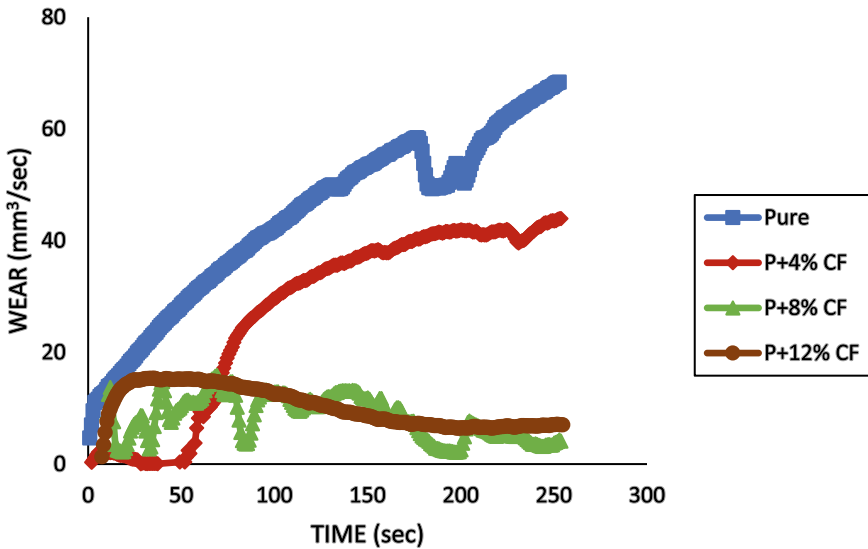
Fig. 8 Time versus Wear for 10 N at 2 m/s
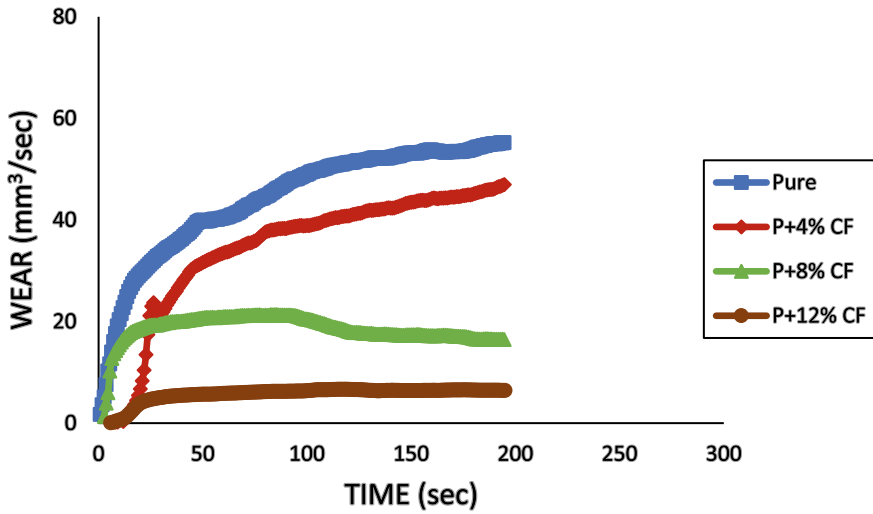
Fig. 9 Time versus Wear for 10 N at 3 m/s
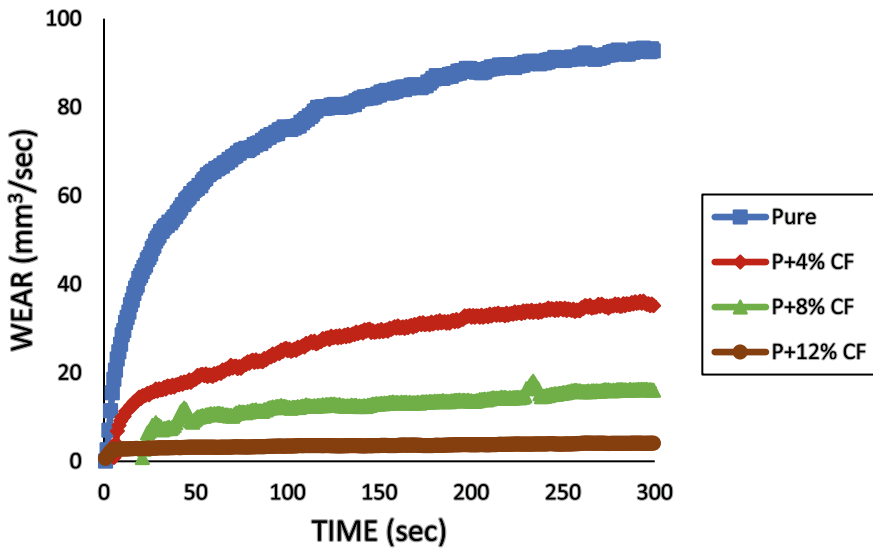
Fig. 10 Time versus Wear for 20 N at 1 m/s

and 9 are due to presence of agglomerated carbon particles or may be due presence of minimal blow holes in the composite samples.

Wear Rate. It is well known that carbon fibers are typically embedded on the frictional surfaces of composites in the polyester matrix are also easily transferred to the matrix's counterpart surface and deposited during sliding through the transfer film.
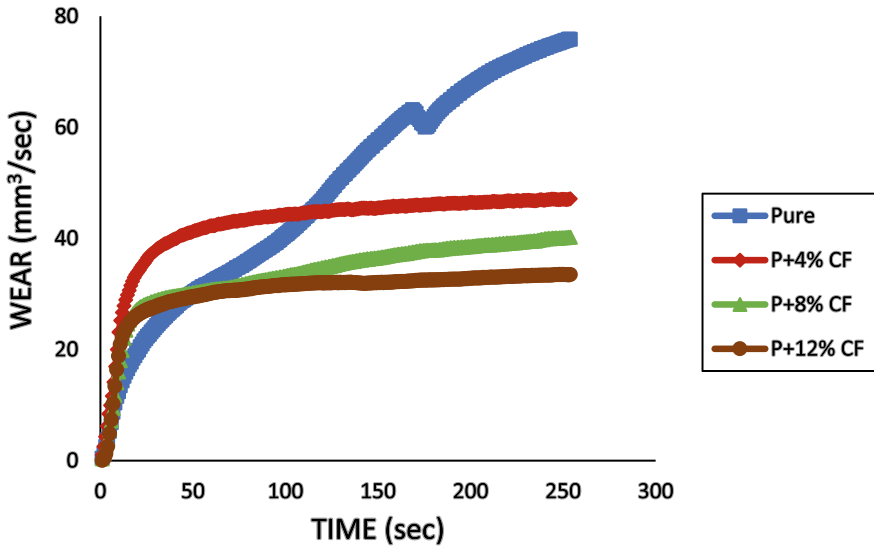
Fig. 11 Time versus Wear for 20 N at 2 m/s
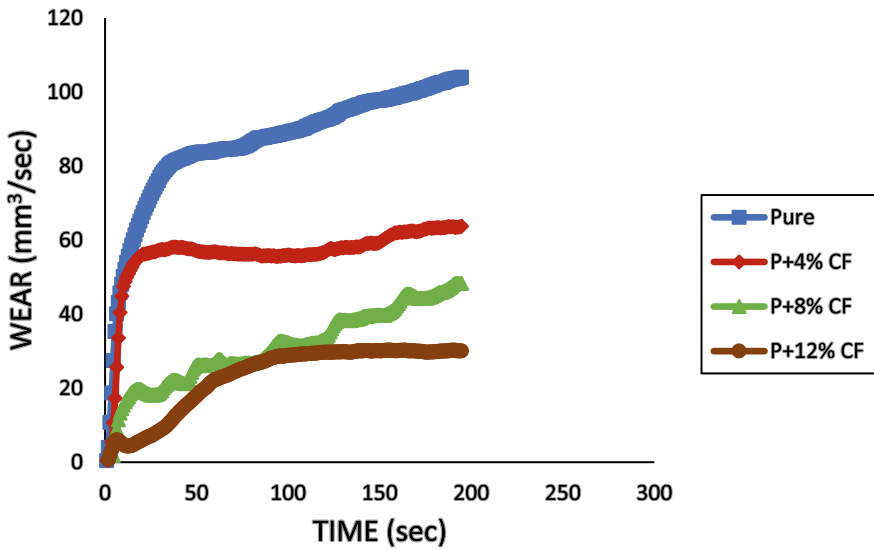
Fig. 12 Time versus Wear for 20 N at 3 m/s

The polyester composites packed with varying quantities of carbon fibers demonstrate excellent wear properties by increasing the speed after the transient wear stage. With P_I, P_{II}, P_{III} and P_{IV} carbon filled polyester composites, the wear properties are tested. The wear rate of base material reinforced with carbon fiber composites at 1 m/s decreases but when increasing the speed (i.e. at 2, 3 m/s) the wear rate is lowered when compared to 1 m/s by keeping the load constant (i.e. 10 N and 20 N) and it can be perceived in Figs. 13 and 14.
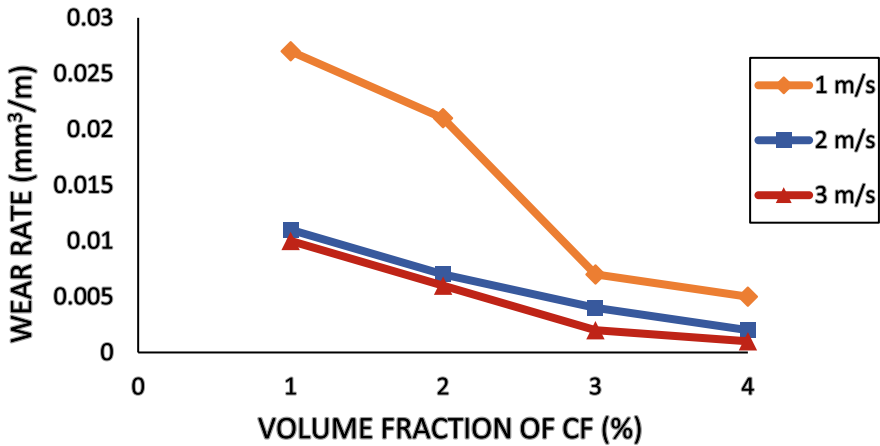
Fig. 13 Percentage of CF versus wear rate for 10 N at 1, 2 and 3 m/s
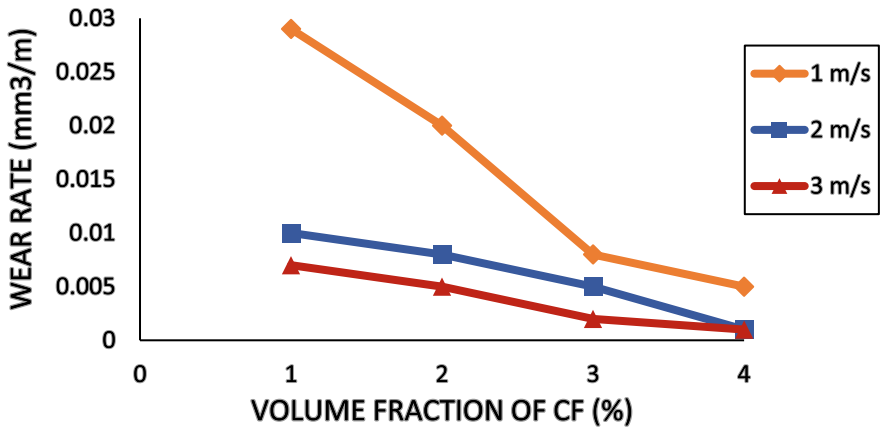
Fig. 14 Percentage of CF versus wear rate for 20 N at 1, 2 and 3 m/s

3.2 SEM & EDX Analysis of P_I, P_{II}, P_{III} and P_{IV} Carbon Fiber Reinforced Polyester (CFRP) Composites

To examine proper dispersion of carbon fibers in pure polyester, micro structures are taken by using scanning electron microscopy (SEM) equipment. Figure 15a shows the SEM image of a pure polyester (P_I). SEM test results of carbon fiber-reinforced polyester composites showed clearly that carbon fibers are extensively blended into the base matrix without any aggregation of carbon particles seen in the composite of P_{II} (Fig. 16a) and also noted that there is a smooth surface for P_{II} composite. In the SEM images, it is observed that the carbon particles in composites P_{III} and P_{IV} are aggregated (Figs. 17a and 18a). On the basis of this study, we found the Low-percent carbon evenly spread on the base surface of the polyester composite, minimizing wear degradation of the polyester. It was also found that, in the polymer matrix, greater proportions of the reinforcing parts result in aggregation.

Figures 15b, 16b, 17b and 18b indicates that the elemental distribution of CFRP specimens is based on an EDX analysis. The EDX study shows that there is a homogenous distribution of carbon fibre and polyester in the specimen.

3.3 Hardness

Vickers micro hardness tester has been used to assess the hardness of the raw material with carbon fiber enhancement. Figure 19 indicates the hardness value resulting in different volume fractions of the reinforcement. Hardness of pure polyester is 11.28 $\times 10^6$ N/mm^2 whereas for 12%wt CF is 101.18 $\times 10^6$ N/mm^2.

Hardness is increased almost nine times as compared to base material. Due to abrasive wear mechanism, mostly load carrying capacity was carried out by the reinforcement thereby hardness increases. The tests showed that the hardness increases as the percentage of the carbon fiber increases. Hard carbon fiber, which serves as a dis-localization barrier in the base matrix, is the main cause of this difficulty [31].

4 Conclusions

Carbon fiber reinforced Polyester composites of various concentrations were successfully fabricated by using die casting. The following conclusions were drawn on the basis of the experimental observations:

- Using the die casting methodology, the specimens are fabricated successfully with homogenous distribution.
- Carbon fibers were found to spread evenly in the base matrix. EDX reports confirms the distribution and elemental composition of the prepared composites.
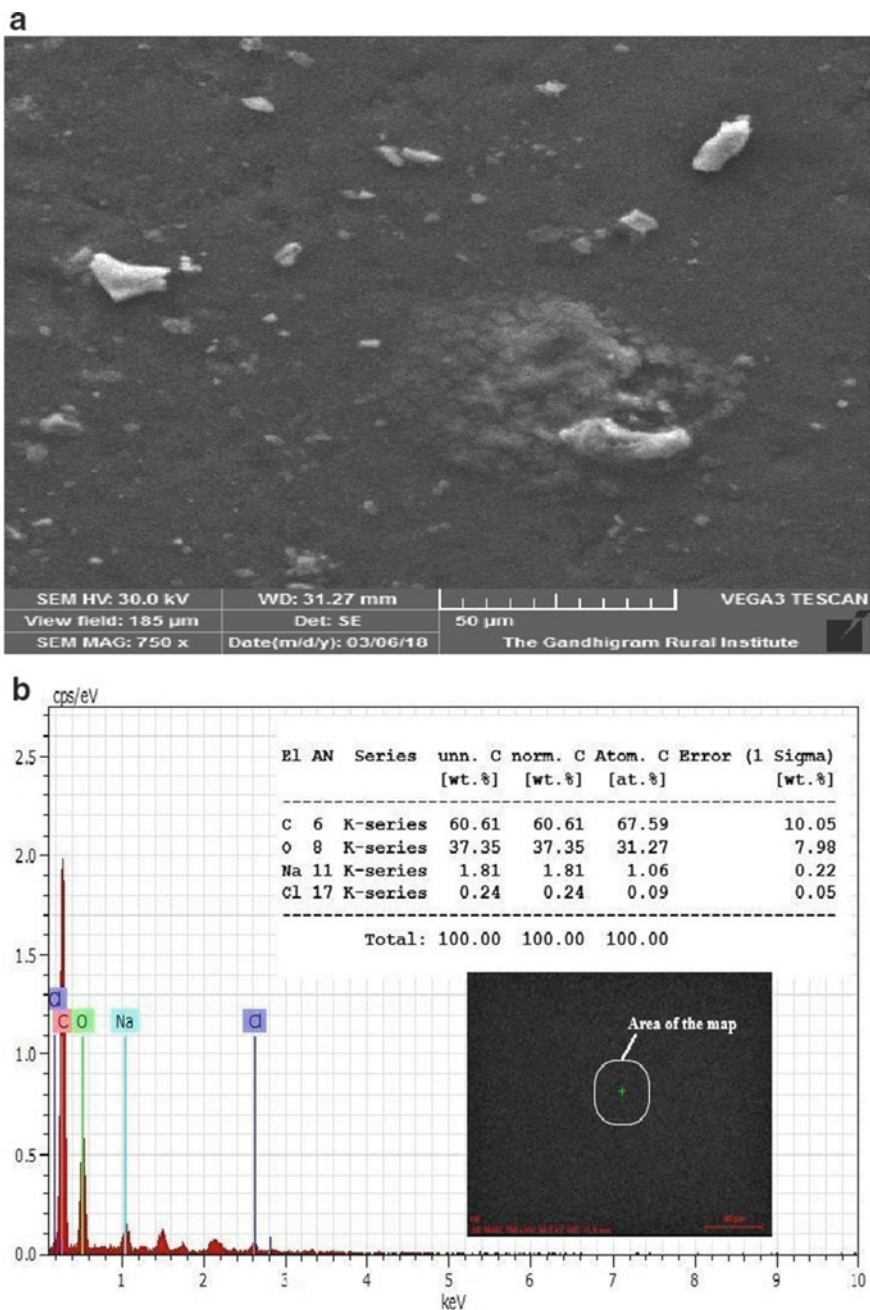
Fig. 15 **a** SEM image of P_I **b** EDX Report of P_I
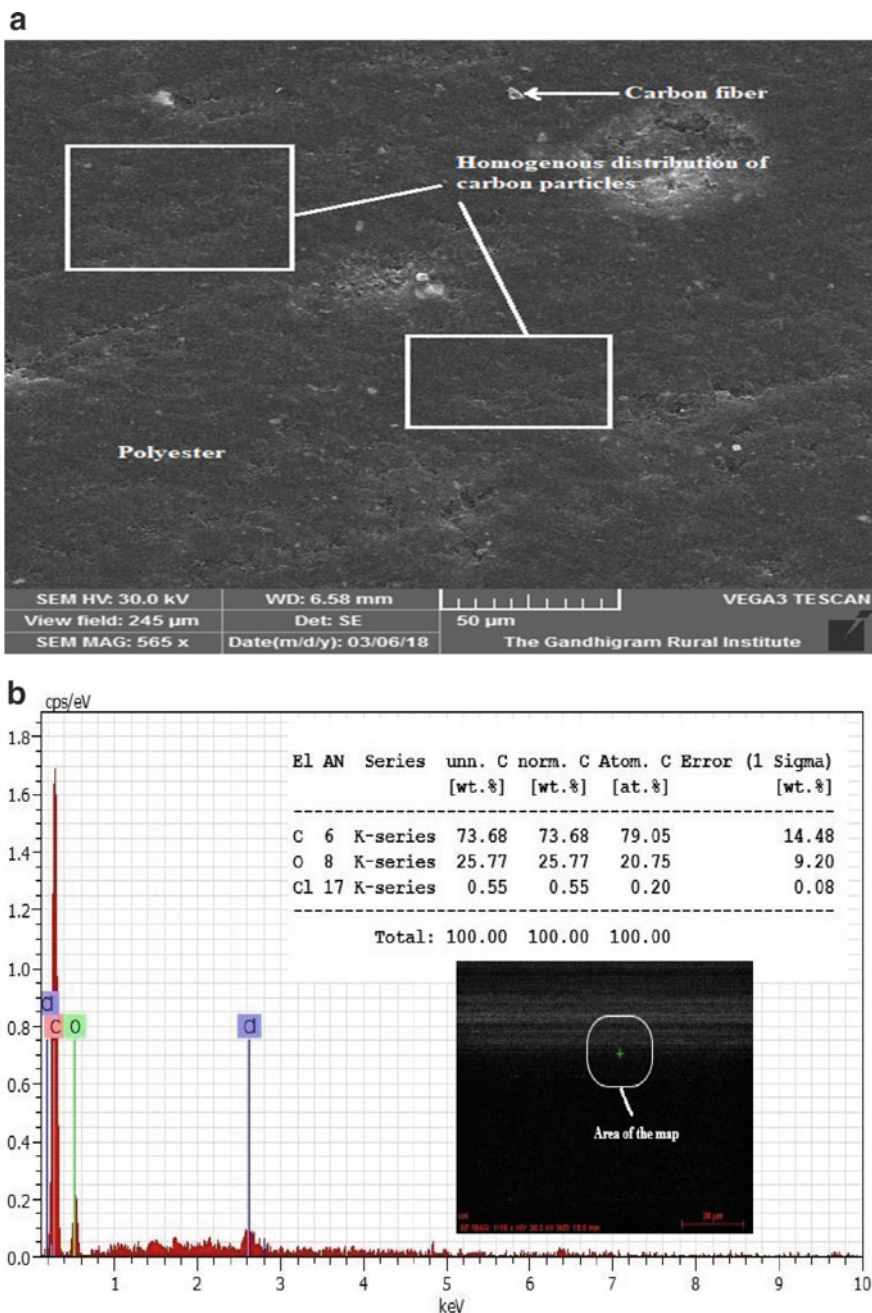
Fig. 16 **a** SEM image of P_{II} **b** EDX Report of P_{II}
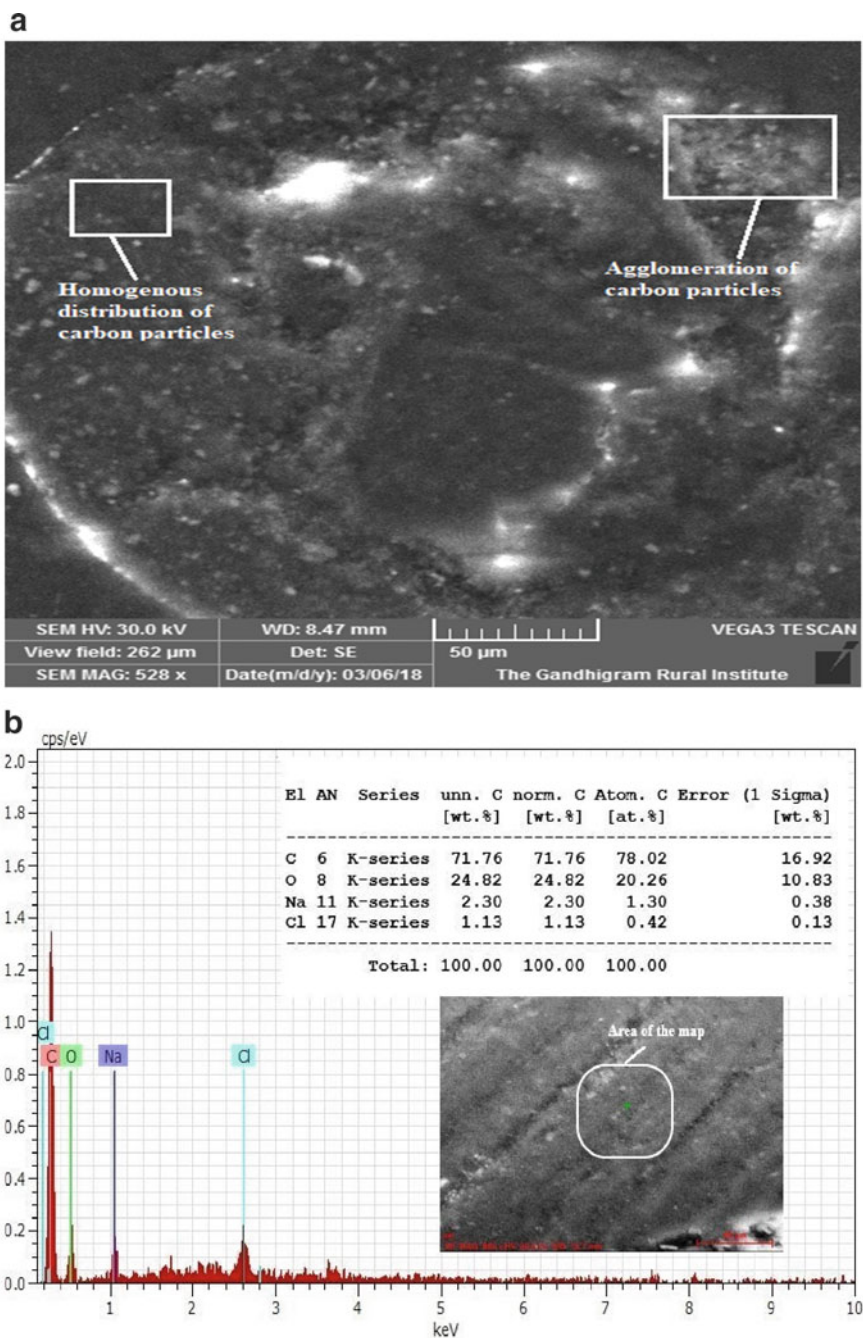
Fig. 17 **a** SEM image of P_{III} **b** EDX Report of P_{III}
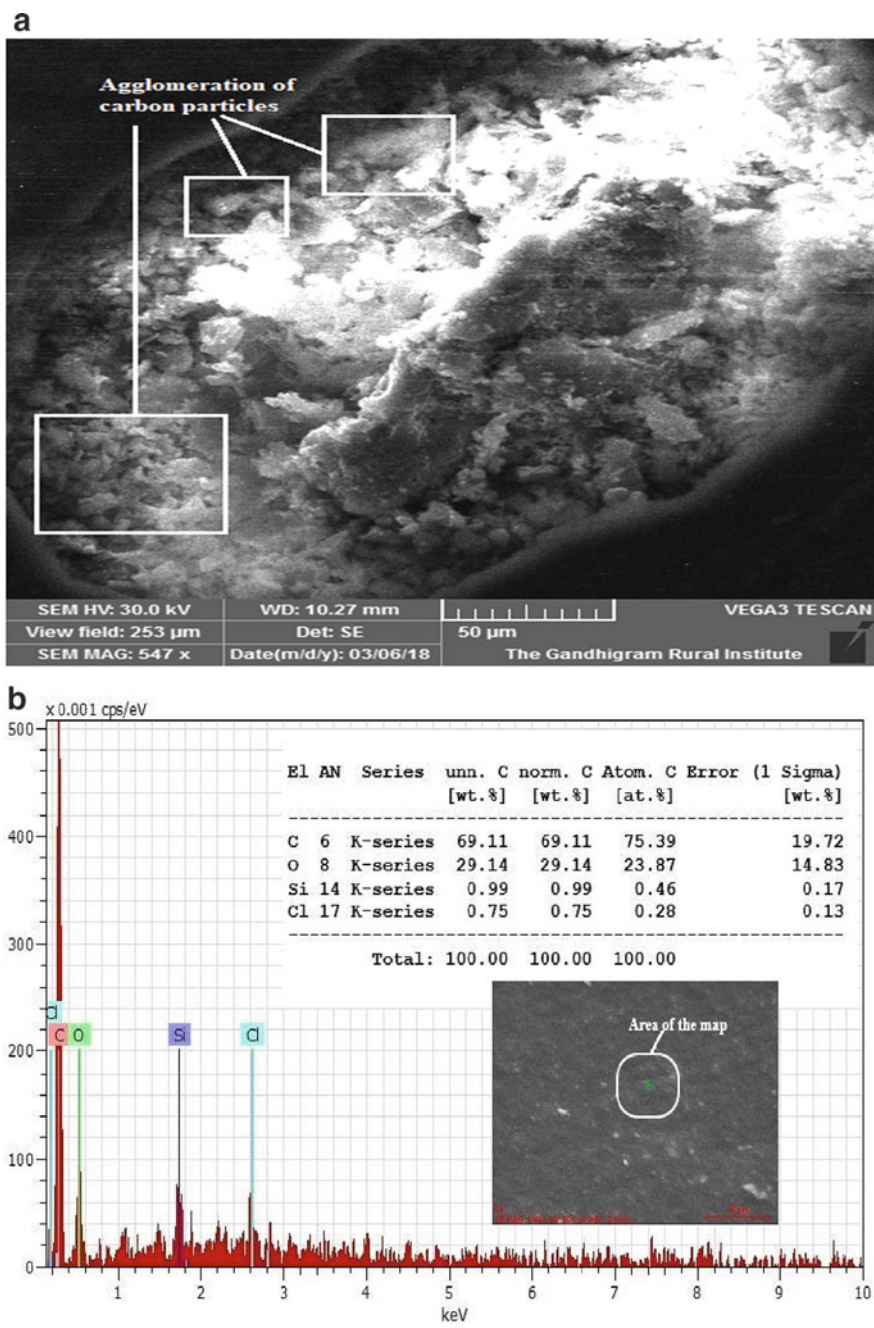
Fig. 18 a SEM image of P_{IV} **b** EDX Report of P_{IV}
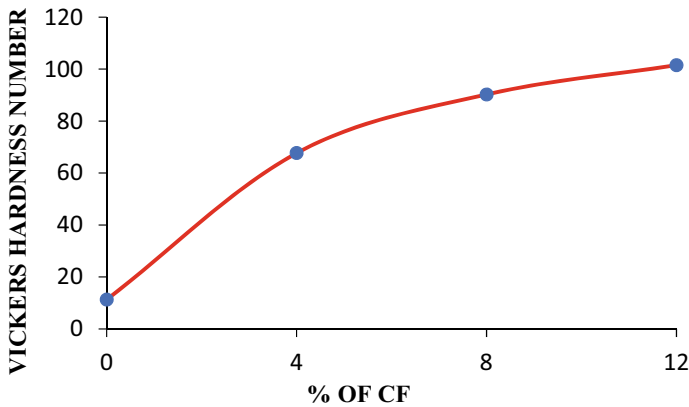
Fig. 19 Hardness variation of Carbon fibre and polyester composites with weight fractions

- Under constant load and by increasing speed it is monitored that rate of wear for polyester reinforced with 12%wt CF ($\mathbf{P_{IV}}$) decreased by three times as compared to the remaining composites.
- On increasing the reinforcement from 4 to 12% wt of carbon fiber at 4%wt intervals the hardness also increased by three times correspondingly to it.
- In the automobile industry and related applications, CFRP composites can be used in the manufacture of chassis frames, wheels, etc. in order to gain less weight and thereby improve fuel efficiency.
- In addition, by using optimization methods, the research can be continued.

References

1. Velmurugan K, Gopinath R (2015) Characterization of polyester based composites, international journal of science. Eng Technol Res 4(7). ISSN: 2278-7798. http://ijsetr.org/wp-content/uploads/2015/07/IJSETR-VOL-4-ISSUE-7-2466-2469.pdf
2. Bagherpour S (2012) Fibre reinforced polyester composites. London: InTech. pp 135–166. https://doi.org/10.5772/48697
3. Black T, Kosher R (2008) Non metallic materials: plastic, elastomers, ceramics and composites. Mater Proc Manuf 10:162–194. ISBN: 978-0470-05512-0
4. Pıhtılı H, Tosun N (2002) Investigation of the wear behaviour of a glass-fibre-reinforced composite and plain polyester resin. Compos Sci Technol 62(3):367–370. https://doi.org/10.1016/s0266-3538(01)00196-8
5. Hutchings IM "Wear-resistant materials: into the next century". J Mat Sci Eng pp 185–195. https://doi.org/10.1016/0921-5093(94)91031-6
6. Ahmed IR, Yousry AW (2012) Tribological properties of polyester composites: effects of vegetable oils and polymer fibers. Rijeka: InTech. pp 203–226. https://doi.org/10.5772/39230
7. Al-Mosawi AI, Al-Maamori MH, Wetwet ZA (2012) Mechanical properties of composite material reinforcing by natural-synthetic fibers. Acad Res Int 3(3):108. ISSN: 2223-9944

8. Brahim SB, Cheikh RB (2007) Influence of fibre orientation and volume fraction on the tensile properties of unidirectional Alfa-polyester composite. Compos Sci Technol 67(1):140–147. https://doi.org/10.1016/j.compscitech.2005.10.006

9. Prasad BD, Reddy GK, Yadav AA (2014) Mechanical properties of composite material reinforced by Jute and E-Glass fibers. Int J Emerg Eng Res Technol 2(5):35–138. ISSN(Online): 2349–4409 (Online) http://www.ijeert.org/pdf/v2-i5/16.pdf

10. Ewins DJ, Saunders H (1986) Modal testing: theory and practice. J Vib Acoust Stress Reliab Des 108(1):109. https://doi.org/10.1115/1.3269294

11. Harris B (1999) Engineering composite materials

12. Durairaj RB, Mageshwaran G, Sriram V (2016) Investigation on mechanical properties of glass and carbon fiber reinforced with polyester resin composite. Int J ChemTech Res 9(06):424–431. ISSN(Online):2455–9555. http://sphinxsai.com/2016/ch_vol9_no6/2/(417423)V9N6CT.pdf

13. Abdul-Hamead AA, Kasim T, Mohammed AA (2014) Mechanical properties for polyester resin reinforce with Fe weave wire. Int J Appl Innov Eng Manage (IJAIEM) 3(7). ISSN 2319-4847. https://www.ijaiem.org/Volume3Issue7/IJAIEM-2014-07-04-10.pdf

14. Towne MK, Dowell MB (1976) Papers of the American association for textile technology. Inc., Mod. Tex, p 51

15. Starr T (1994) Carbon and high performance fibres directory and databook. Springer Sci Bus Media. https://doi.org/10.1007/978-94-011-0695-5

16. Donnet JB, Bansal RC (1998) Carbon fibers. CRC Press. ISBN 0-8247-0172-0. https://doi.org/10.1002/pat.1992.220030109

17. Zeng H, He G, Yang G (1987) Friction and wear of poly (phenylene sulphide) and its carbon fibre composites: I unlubricated. Wear 116(1):59–68. https://doi.org/10.1016/0043-1648(87)90267-5

18. Voss H, Friedrich K (1985) The wear behavior of short fiber reinforced thermoplastics sliding against smooth steel surfaces. Wear Mater 742

19. Theberge J, Arkles B (1974) Wear characteristics of carbon fiber reinforced thermoplastics. Lubr Eng 30(12):585–589. https://www.researchgate.net/publication/273714286

20. Bahadur S, Zheng Y (1990) Mechanical and tribological behavior of polyester reinforced with short glass fibers. Wear 137(2):251–266. https://doi.org/10.1016/0043-1648(90)90138-z

21. Azhari F, Banthia N (2012) Cement-based sensors with carbon fibers and carbon nanotubes for piezoresistive sensing. Cement Concr Compos 34(7):866–873. https://doi.org/10.1016/j.cemconcomp.2012.04.007

22. Salvado R, Lopes C, Szojda L, Araújo P, Gorski M, Velez FJ, Krzywon R (2015) Carbon fiber epoxy composites for both strengthening and health monitoring of structures. Sensors 15(5):10753–10770. https://doi.org/10.3390/s150510753

23. Boeing 787 features composite window frames (2007) Reinforced plastics, 51(3):4. https://doi.org/10.1016/S0034-3617(07)70095-4

24. Schwartz MM (1997) Composite materials: properties, non-destructive testing, and repair, vol 1. Prentice Hall. ISBN: 0-13-300047-8

25. Selmi A (May 2014) Void effect on carbon fiber epoxy composites. In: 2nd International conference on emerging trends in engineering and technology, ICETET2014. pp 179–183. https://doi.org/10.15242/IIE.E0514613

26. Anigol N, Nakadi MO, Hukkeri MN. International journal of engineering sciences & research technology study of effects of various filler materials on mechanical properties of carbon-epoxy composite. ISSN: 2277-9655

27. Rohatgi PK, Tabandeh-Khorshid M, Omrani E, Lovell MR, Menezes PL (2013) Tribology of metal matrix composites. In: Tribology for scientists and engineers. Springer, New York, NY, pp 233–268. https://doi.org/10.1007/978-1-4614-1945-7_8

28. Yousif BF, El-Tayeb NSM (2007) Tribological evaluations of polyester composites considering three orientations of CSM glass fibres using BOR machine. Appl Compos Mater 14(2):105–116. https://doi.org/10.1007/s10443-007-9034-2

29. El-Tayeb NSM, Yousif BF, Yap TC (2006) Tribological studies of polyester reinforced with CSM 450-R-glass fiber sliding against smooth stainless steel counterface. Wear 261(3–4):443–452. https://doi.org/10.1016/j.wear.2005.12.014

30. Ram YS, Kammaluddin S, Raj CD, MastanRao P (2016) Sliding wear behavior of high velocity oxy-fuel sprayed WC-CO coatings. Int J Adv Sci Technol 93:45–54. https://doi.org/10.14257/ijast.201

31. Wu H, Fan G (2020) An overview of tailoring strain delocalization for strength-ductility synergy. Prog Mater Sci. https://doi.org/10.1016/j.pmatsci.2020.100675

Tribological Behaviour of Silicon Carbide Reinforced AA2024 Composites

A. A. Krishna Vamsi, S. Dheeraj Kumar, and Y. N. V. Sai Ram

1   Introduction

Metal-Matrix Composites (MMC's) find wide applications in aviation and automotive production because of their enlarge properties like stiffness, tensile strength, wear resistance elastic modulus and substantial weight reduction over alloys which are unreinforced [1]. Metal matrices are broadly utilized include copper, titanium, magnesium and their alloys. These alloys are desired matrix materials to render MMC's. Ceramics are used in the form of whiskers, particulates and fibers [2]. Particle-reinforced composites have the benefit of formability with a cost advantage over others [3].

Aluminium Metal-matrix Composites (AMMC's) are rapidly increasing popularity in industrial field now-a-days because they possess very awesome properties like resilience, durability, high strength to weight ratio, etc. Because of its enhanced mechanical properties, MMC's are generally utilized in aviation, industrial, military, marine and industrial applications [4–8]. However, aluminum alloys have low melting point which limits their applications. Reinforcement is frequently done to strengthen the base metal's properties. In the properties of MMC's, the particle distribution plays a significant job. For Metal-matrix composites, copper, aluminum and magnesium have attracted the most interest as the base metal. Because of the communication of nano particles with the separation development, the utilization of nano particles has been found to be significant over the recent years [9–11]. By mixing nano particles in ceramic mode in the AMMC's, this problem can be diminished to some extent.

Usually, AMMC's are formed by scattering with different reinforced materials like B_4C, SiO_2, ZrO_2, TiB_2, and Al_2O_3. Various metal matrix composites are prepared using various operations like powder metallurgy, stir casting, ball milling

A. A. Krishna Vamsi · S. Dheeraj Kumar · Y. N. V. Sai Ram (✉)
RVR&JC College of Engineering, Guntur, India

and centrifugal casting [12–15]. Cast iron cylinder liners currently provide magnificent protection to wear at elevated temperatures. Life time of cylinder liners is reduced due to the formation of air pockets. Metal-matrix composite (MMC) was utilized like a coating for the cylinder to overcome this constraint, providing superior tribological characteristics and adequate strength. Copper is graded like a main item for aluminium by 2xxx number. AA2024 has high wear and fracture rates among the Al-Cu alloys. The application of coating (firm material) to MMC is well identified to increase tribological and mechanical properties. MMC's keeps the property of durability, matrix-derived flexibility, strength, and reinforcement stiffness.

Particles from silicon carbide (SiC), aluminum oxide (Al_2O_3), and graphite (Gr) often extended as replacements for particular applications [16]. Extensions of reinforcement (hard element) to MMC's ultimately improve its mechanical properties and wear [17]. SiC was selected as reinforcing element to improve hardness and resistance to wear [18]. Aluminium alloy-SiC blends recorded increased resistance to wear, toughness along with hike in moreover magnificent thermal conductivity [19]. A356 aluminum alloy strengthened with 2 wt% SiC 30 nm grain size working with ultrasonic stir casting exhibit non-uniform circulation of particles in matrix [20].

Diminishing resistance to wear with increased sliding distance, load and abrasive grit size [21]. Many researchers performed their experimentation on AA6061 reinforced with SiC for dissimilar weight fractions and reported that adding SiC particles improved wear resistance and hardness [22–25].

During the relative motion, different types of wear mechanisms can take place. Adhesive, abrasive, fatigue, and corrosive/oxidative wears are the typical mechanisms of wear. Abrasive wear may be due to both metallic and non-metallic particles, but abrasion is caused mainly by non-metallic particles. When two metallic surfaces allowed to slide across each other under the load, adhesive wear occurs. When contacting surfaces exposed to the environment, corrosive wear takes place along with reaction products formed as asperities on the surfaces. When the surface of materials undergo cyclic loading, fatigue wear occurs [26].

Aluminium is a universal element. But, the drawback of this material is it has low tribological properties. So, the main concern among the researchers is to promote advanced material with good tribological properties. It also should have better wear resistance, without much compromise on strength to weight ratio get to improvement of MMC. Novelty of the present study was to fabricate the composites such as AA2024 pure, AA2024 + 4% SiC, AA2024 + 8% SiC and AA2024 + 12% SiC by using Stir casting method. The tribological behavior of the composites was assessed by means of wear test (pin-on-disk equipment), corrosion test (Salt spray method) and hardness test (Vickers hardness test). The outcomce of this research will helpful to aerospace and automotive system applications.

Table 1 Chemical composition of AA2024

Elements	SiC	Mg	Cu	Mn	Fe	Ni	Ti	Zn	Pb	Sn	Al
Contents (wt.%)	0.5	0.065	4.51	0.13	0.663	0.075	0.013	0.11	0.029	0.021	Balance

2   Materials and Methods

2.1   Material Selection

AA2024 material is utilized extensively because it has leading engineering properties like high wear resistance, low density, stiffness and specific strength. This material also has strong machining features including higher strength and fatigue resistance. AA2024 is machined very easily and having decent workability. Tables 1 and 2 recorded the chemical composition and properties of AA2024.

Reinforcement supplied in this job is Silicon Carbide(SiC). SiC is a stable and chemically inert substance with a good corrosion resistance. It is having characteristics e.g. hardness, high thermal conductivity, resistance to abrasion,etc. It also maintains its strength up to a temperature 1400 °C. SiC powder used with particle size of 75 nm. SiC particulates are harder and present to the top of specimen and protected the alloy among sliding & abrasion wears, erosion, corrosion, etc. SiC particulates stops the plastic flow of material even at high temperatures. Extension of SiC lowers the tendency of sticking and adhesion with the counter surface. Table 3 listed the properties of SiC.

2.2   Methods

In further sections, AA2024 pure, AA2024 + SiC 4%, AA2024 + SiC 8% and AA2024 + SiC 12% are designated as AI, AII, AIII and AIV respectively.

2.2.1   Preparation of AMMC (Aluminium Metal Matrix Composite)

Fabrication is done by modifying the portion of sintered SiC (0%, 4%, 8%, and 12%) into the AA2024 (AI) matrix by using stir casting method. Initially, the AI was heated in graphite crucible at 750 °C up to whole metal in container is soften. Reinforced particles (SiC) were preheated to 300 °C prior to fusion in the melt to eliminate moisture. Later Molten metal was entirely melted, Degassing tablet (coverall powder) was applied to lower the porosity. Simultaneously, magnesium of 1% aside weight was applied to melted portion for bringing the wetness among reinforcements and matrix. A stainless-steel stirrer introduced within the melted portion to gently mix molten metal by a speed of 700 rpm. Figure 1 shows stirrer inside the crucible in

Table 2 Properties of AA2024

Materials/Properties	Melting point (°C)	Density (g/cc)	Tensile strength (mpa)	Shear Strength (mpa)	Yield Strength (mpa)	Fatigue Strength (mpa)	Thermal Conductivity (W/mk)	Young's modulus (Gpa)
AA2024	500	2.78	185	283	324	138	193	73

Table 3 Properties of SiC

Material/properties	Melting point(°C)	Mohr's hardness	Density (g/cc)	Tensile strength (mpa)	Young's modulus (Gpa)	Flexural strength (mpa)	Thermal conductivity (W/mk)
Silicon carbide	2730	9	3.21	310	476	324	41
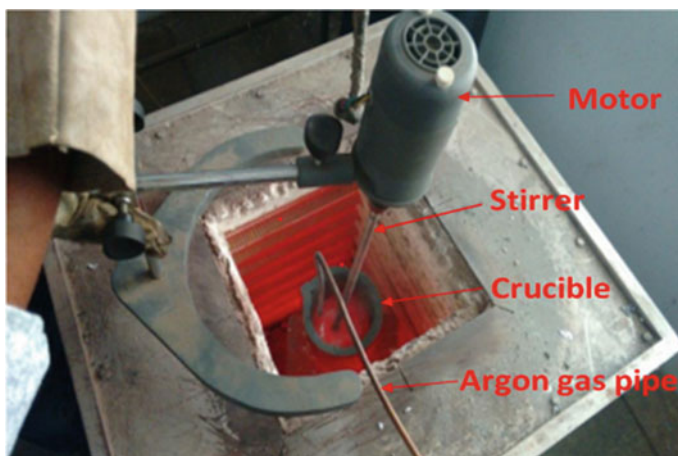
Fig. 1 Stirrer inside the crucible in argon gas atmosphere

argon gas atmosphere to avoid oxidation of molten metal. Preheated SiC particulates were dispersed within the AI base matrix. For stirring about 5–10 min, constant distribution is obtained. Figure 2a depicts the die for fabrication of composites, By stir casting process, 0, 4, 8 and 12 by weight proportions of SiC particle-reinforced composites were produced. Figure 2b depicts the composites after knock out.
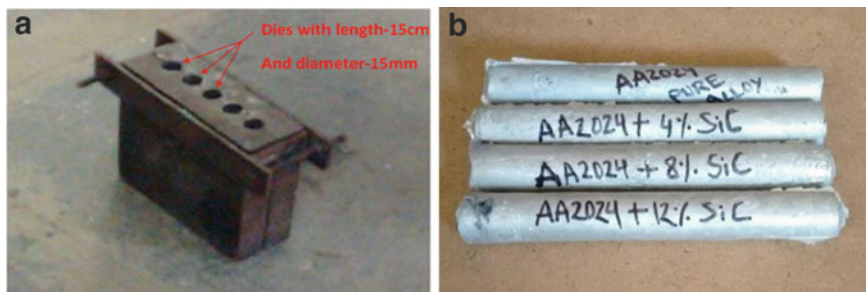
Fig. 2 a Die for fabrication of composites. **b** Composites after knock out
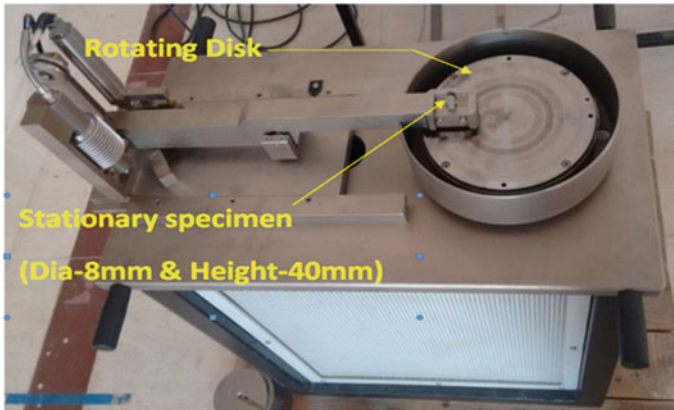
Fig. 3 Wear and friction monitor (TR-20LE-PHM-400)

Table 4 Parameters taken in sliding wear test

Disc speed	100 to 2000 rpm
Sliding speed	2 to 8 m/s
Wear disc diameter	165 mm (EN 32 disc 58–60 HRC)
Specimen pin diameter	8 mm
Wear track disc diameter	10 to 140 mm
Pin length	40 mm
Normal load	2 kgf
Sliding distance	3000 m

2.2.2 Wear Test

Experiment was done using the pin-on-disk tribometer (Fig. 3), which model named Wear and Friction Monitor (TR-20LE-PHM-400). Disk used in the experimentation is made of material EN 32 steel. The pins worked for conducting the experiment are made of AI, AII, AIII and AIV. Experimentation was done in dry condition at a room temperature of 30 °C by applying a load of 20 N. A sliding distance of 3000 m was utilized with changing the sliding speed of 2, 4, 6& 8 m/s. Parameters taken in sliding wear test is represented in Table 4. Before Experimentation, disc and pins were cleaned with acetone. Wear rate was determined from weight reduction method.

2.2.3 Corrosion Test

Corrosion is concerned because material changes over the time as they unprotected to environment. Consideration of Corrosion is important because it determines the age of a material lasts without losing its primary characteristics. Salt Spray Method (SSM)

was performed to check the resistance to corrosion of materials. Before conducting test, all samples i.e.AI, AII, AIII & AIV were cleaned with acetone and weighed before the immersion in salt solution. The salt solution is maintained at a concentration level of 3.5 wt% Nacl and group of samples were placed for 1 week. Later the samples were eliminated from solution and calculated the parameters like weight loss, density, etc.

2.2.4 Hardness Test

Hardness analysis was done on composite specimens by using Digital Micro-Vickers Hardness Tester (Model: HVS 10000B). The loads applied are 100 kgf and 200 kgf. A diamond indenter of pyramid shaped was utilized for impression. Over a wider material surface, deep and wide indentations were marked by indenter to obtain the outcome of the hardness. Time taken during indentation was 15 s. Analysis was done at four various positions on the surface of specimens, So that an average was made of all value. The Table 5 represents the specifications of hardness measuring device.

Best method from amid all to attain micro Hardness of materials moreover it is valuable for arrangement which is not in similar. Vickers's number (VHN) is computed by the following Eq. (1), F is applied load, D^2 is the area of indentation [27].

$$\textbf{VHN} = \textbf{1.854}\big(\textbf{F/D}^2\big) \tag{1}$$

Table 5 Specifications of hardness measuring device (Model: HVS 10000B)

Hardness measuring range	5–3000 HV
Test force	10, 25, 50, 100, 200, 300, 500, 1000 kgf
Magnifications of the measuring system	400X, 100X
Minimum reading	0.01 mm
Operating temperature	10 to 45^0c
Maximum specimen height	210 mm
Power supply	LED Light (3 W)

3   Results and Discussion

3.1   Micro Structural Analysis

Cross sections of prepared samples i.e., AI, AII, AIII, & AIV were observed to confirm the homogenous circulation of reinforced particles in base cast. Figures 4, 5, 6 and 7 depicts the SEM images of AI, AII, AIII & AIV samples with respective EDX analysis. Adherence among the base matrix as well as reinforcement seems to be
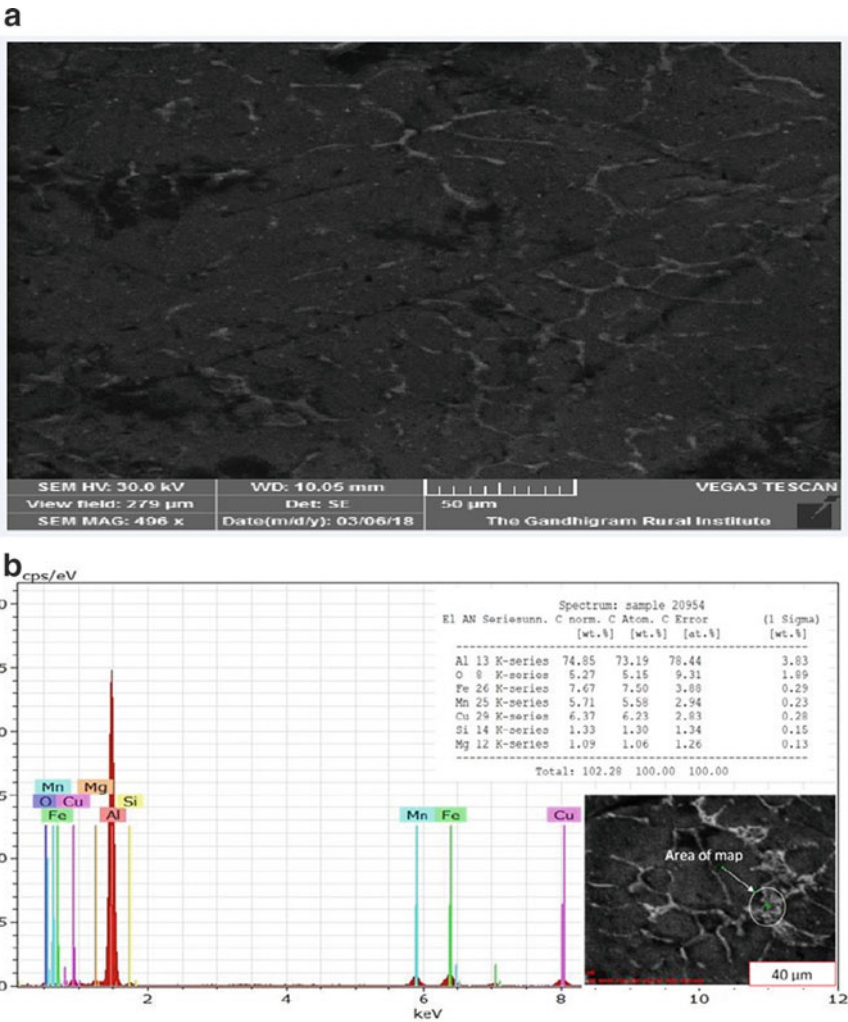
Fig. 4   **a** SEM image of AI. **b** EDX report of AI
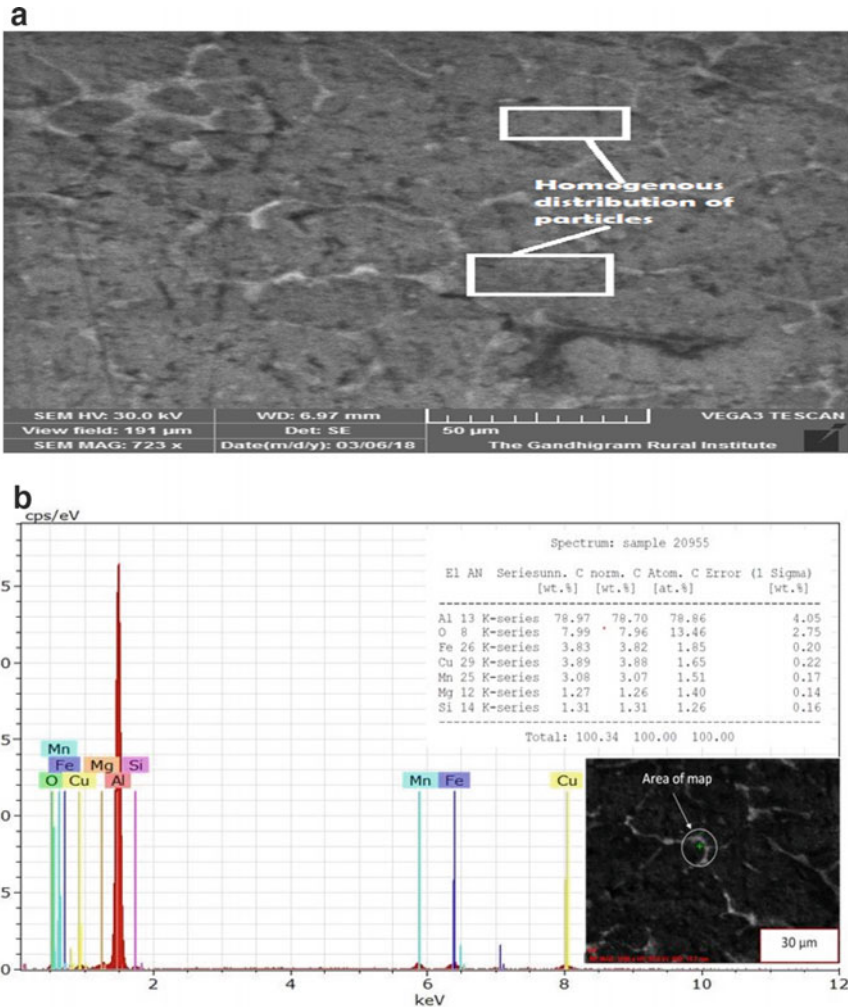
Fig. 5 **a** SEM image of AII. **b** EDX report of AII

good at interface as we observe the low existence of void and porosity. In some places agglomeration of particles is observed as the reinforcement percentage is increased this may be due to less stirring time apart from that homogenous distribution is observed. In conjunction with SEM, EDX was used to characterize the chemical content. It is evident that from figures shown below Mg, Al & Mn peaks were detected in AI and Mg, Mn, Si peaks were observed in AII. But, For AIII & AIV, Mg & Si peaks were observed. Less oxygen peaks were watched in alloy area confirmed that prepared alloy does not contain any extra defilement against climate due to the reason of Argon gas atmosphere.
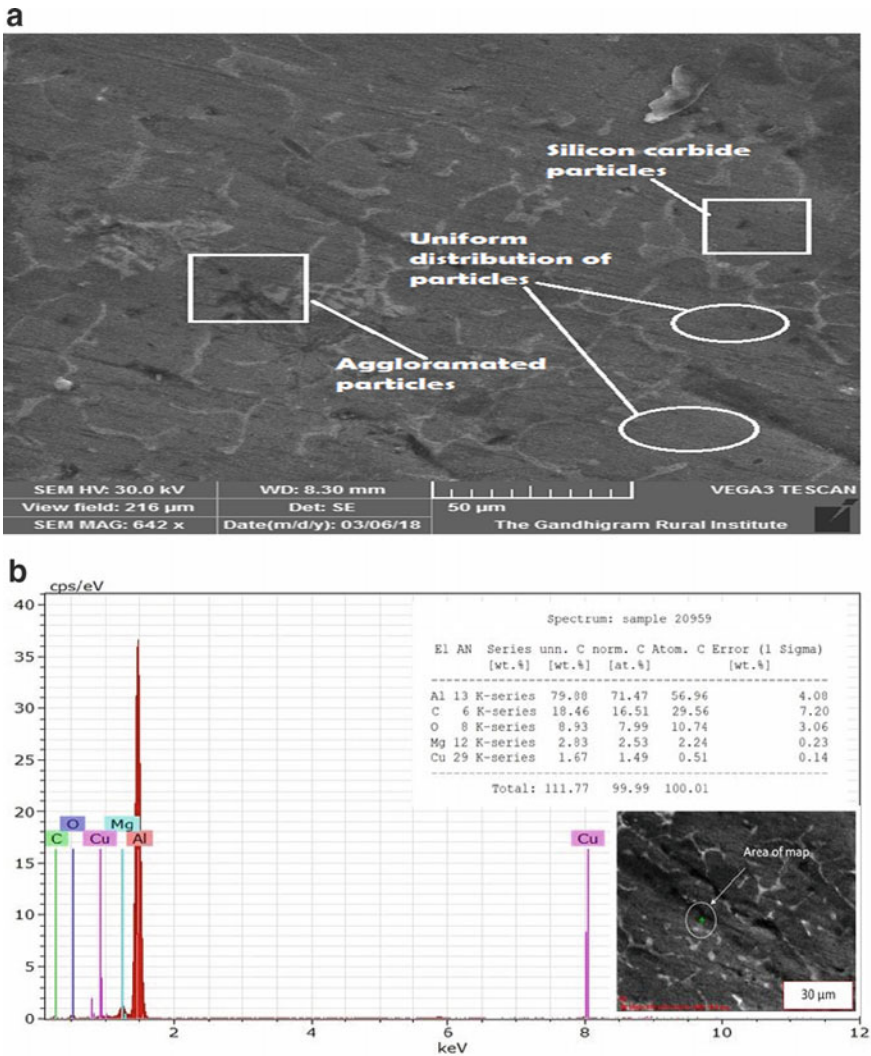
Fig. 6 a SEM image of AIII. b EDX report of AIII

3.2   Wear Analysis

From the specifications of pin-on-disk tribometer, wear pins were fabricated with a diameter of 8 mm as well as elevation of 40 mm. Pins (AI, AII, AIII & AIV) are as shown in Fig. 8. Wear analysis was performed to all pins at different sliding speeds (2, 4, 6 & 8 m/s) at a traditional load of 20 N; time gap for experiment is considered. When a hard-harsh surface slips across a smooth surface, abrasive wear take place. Abrasive wear may be due to both metallic and non-metallic particles, but
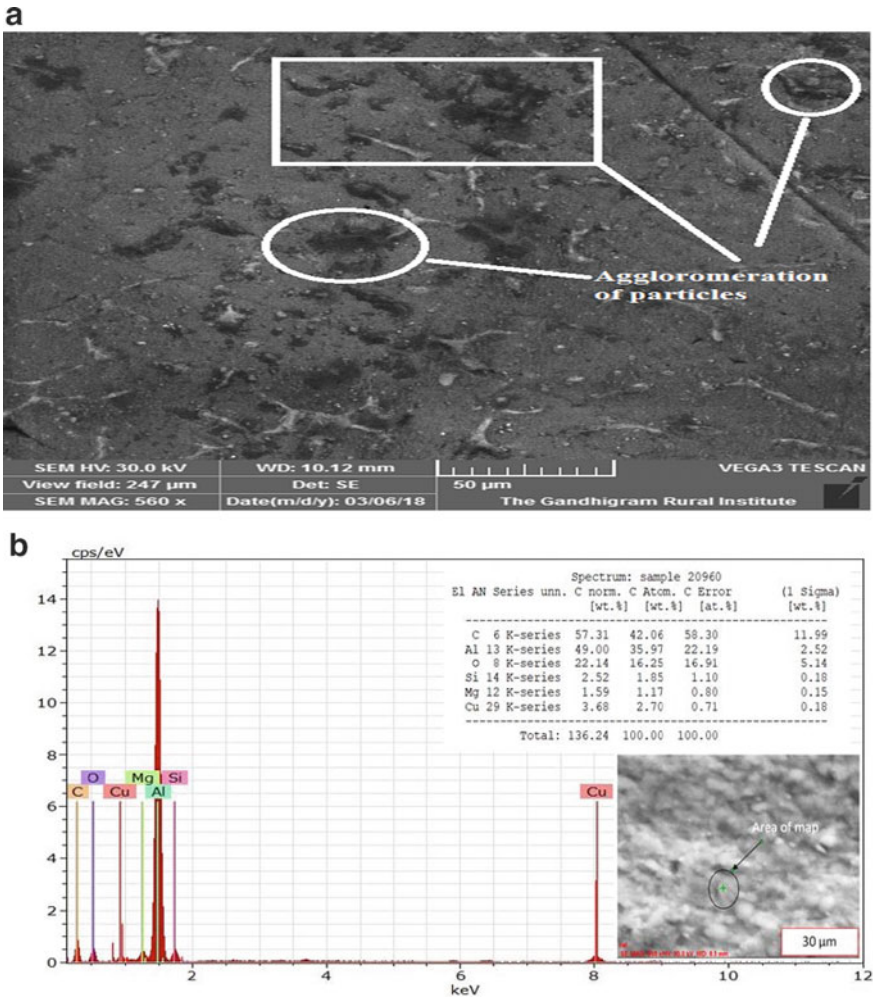
Fig. 7 **a** SEM image of AIV. **b** EDX report of AIV

abrasion is caused by more non-metallic particles. Loss of weight was observed on pins before and after the experimentation due to abrasive wear mechanism. Volume loss is calculated. From this analysis, we detected that as the supply of reinforcement (SiC) in AI increased proportionately and wear rate is decreased. At the same time, wear rate of AIV is decreased by 3 times as compared to wear rate of AI. The abrupt changes in the wear rate shown in the Figs. 9, 10, 11 and 12 are due to presence of agglomerated Silicon carbide particles or may be due to presence of minimal blow holes.

Fig. 8 Fabricated wear pins
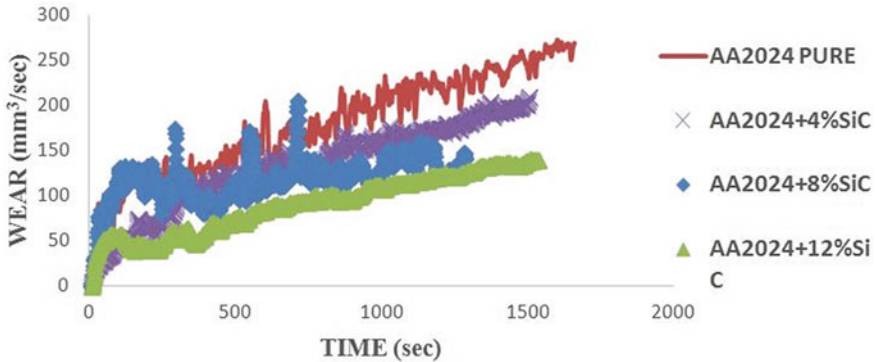
Fig. 9 Time versus wear at sliding velocity of 2 m/s

3.3 Corrosion Test

During the test, the salt solution was maintained at a concentration level of 3.5 wt% Nacl and group of samples were placed for 1 week. Later the samples were eliminated from solution and calculated the parameters like weight loss, density, etc.. Corrosion rate is generally measured in terms of Corrosion Penetration Rate (CPR). The CPR of composites was calculated by weight loss method using the Eq. (2),where K is Corrosion Constant, ρ is the density of metal, W is Weight loss, A is Surface area of metal piece. Following table represents the values of loss of weight of specimen for different Corrosion period. Table 6 shows the values of weight loss for different corrosion where as Table 7 shows the Comparison of CPR values of AI, AII, AIII and AIV [28].
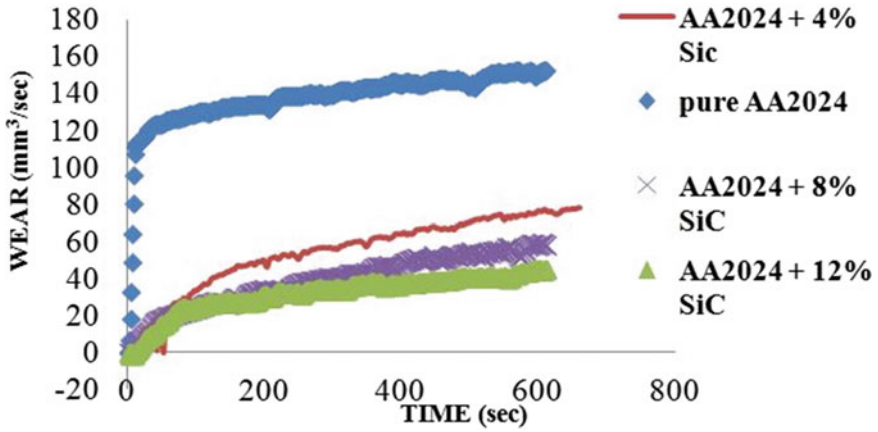
Fig. 10 Time versus wear at sliding velocity of 4 m/s
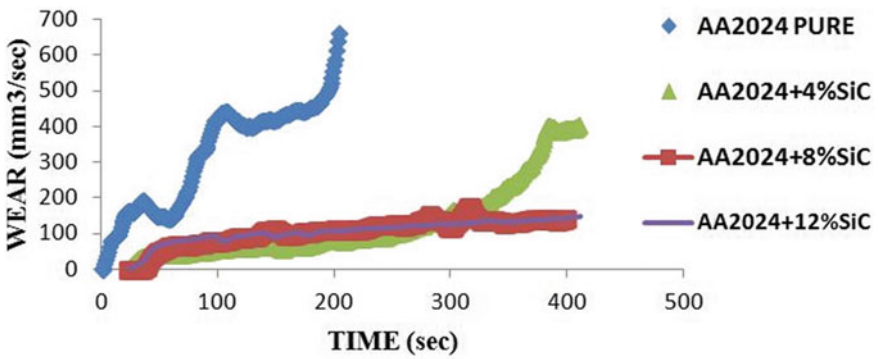
Fig. 11 Time versus wear at sliding velocity of 6 m/s
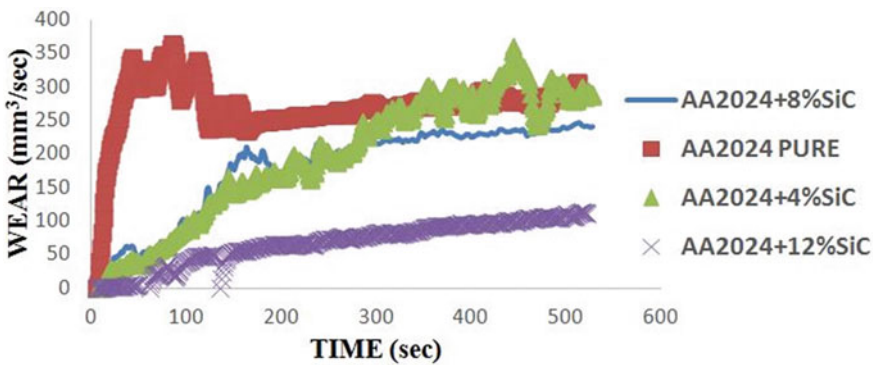
Fig. 12 Time versus wear at sliding velocity 8 m/s

Table 6 Values of weight loss for different corrosion period

Time (Hrs)	AI			AII			AIII			AIV		
	Initial.wt (gms)	Final.wt (gms)	Wt loss	Initial.wt (gms)	Final.wt (gms)	Wt loss	Initial. wt (gms)	Final.wt (gms)	Wt loss	Initial.wt (gms)	Final.wt (gms)	Wt loss
24	4.44	4.43	0.01	4.06	4.05	0.01	4.11	4.10	0.007	5.44	5.435	0.005
48	4.23	4.2	0.03	4.5	4.42	0.08	4.11	4.02	0.09	4.1	4.096	0.004
72	4.96	4.84	0.12	4.43	4.34	0.09	3.91	3.89	0.01	5.12	5.109	0.011
96	4.09	3.97	0.12	4.40	4.29	0.11	4.09	3.98	0.10	4.45	4.38	0.07

Table 7 Comparison of CPR values of AI, AII, AIII and AIV

Time (Hrs)	CPR (mm/yr)			
	AI	AII	AII	AIV
24	0.909	0.871	0.589	0.475
48	1.427	3.64	3.928	0.167
72	3.805	2.736	0.290	0.306
96	2.854	2.508	2.182	1.464

$$\mathbf{CPR} = \frac{KW}{\rho AT} \qquad (2)$$

From Table 7, it was observed that the rate of corrosion of AIV is lesser than the rate of corrosion of AI. So, corrosion resistance of AIV is improved compared to AI. Figures 13, 14, 15 and 16 depicts the SEM images of AI, AII, AIII and AIV specimens after Corrosion. Micro structural studies affirm the agglomeration of SiC particles in composites. This results an escalation of corrosion resistance with the rise of SiC particles in composites. Pitting Mechanism was observed on surface moreover in some places de-lamination of surface layer was noticed. Our work focused on study the effect of SiC addition in their various proportions to AA2024 alloy on corrosion and pitting defenselessness in marine environment.
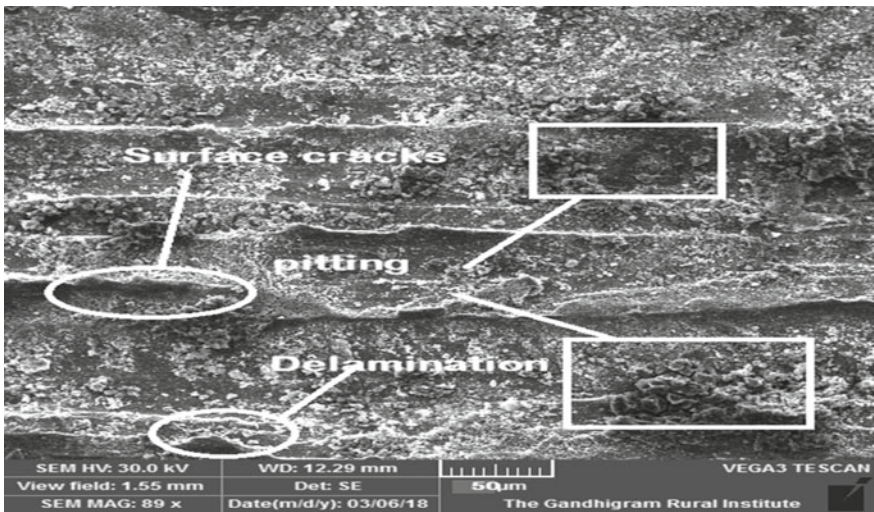
Fig. 13 Corroded SEM image of AI
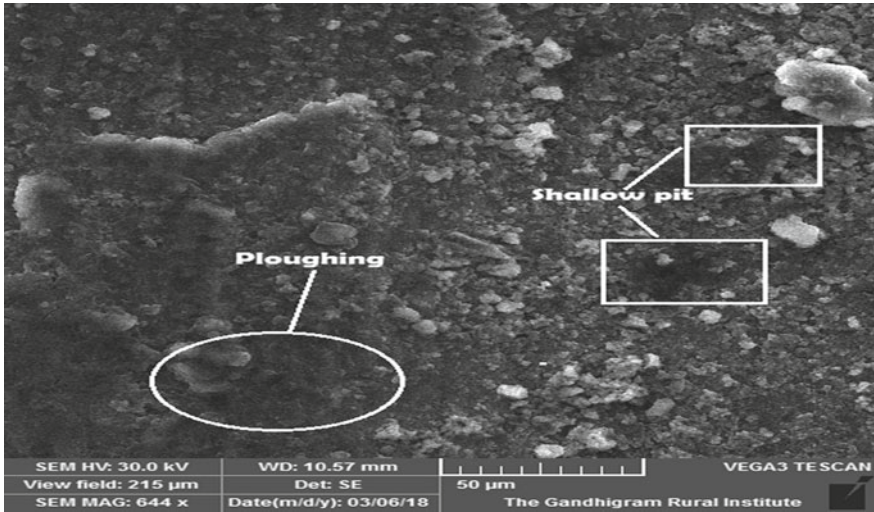
Fig. 14 Corroded SEM image of AII
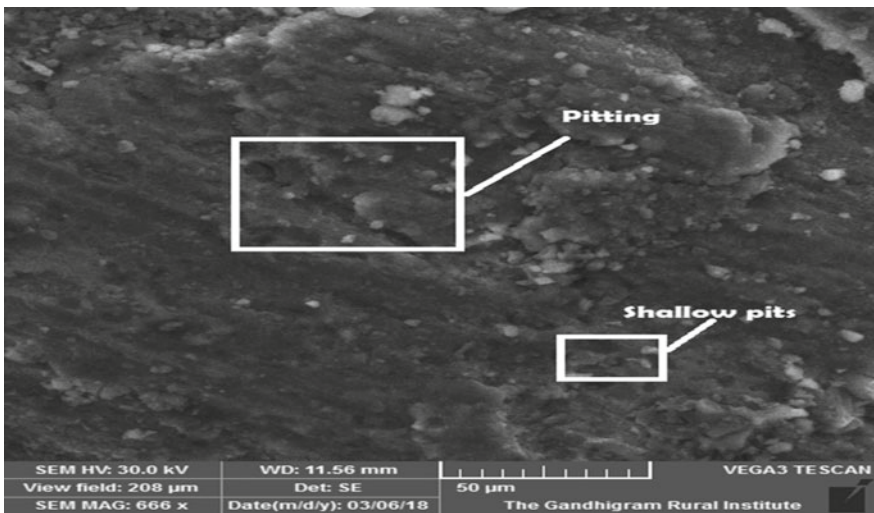
Fig. 15 Corroded SEM images of AIII

3.4 Hardness Test

Micro Hardness was determined by Vickers's Hardness test. The test was conducted at loads of 100 kgf and 200 kgf. Hardness mainly influenced by distribution, size of grain, volume fraction and issue of heat treatment. Hardness was executed on the sample before as well as after age hardening. Figure 17 depicts the samples for age
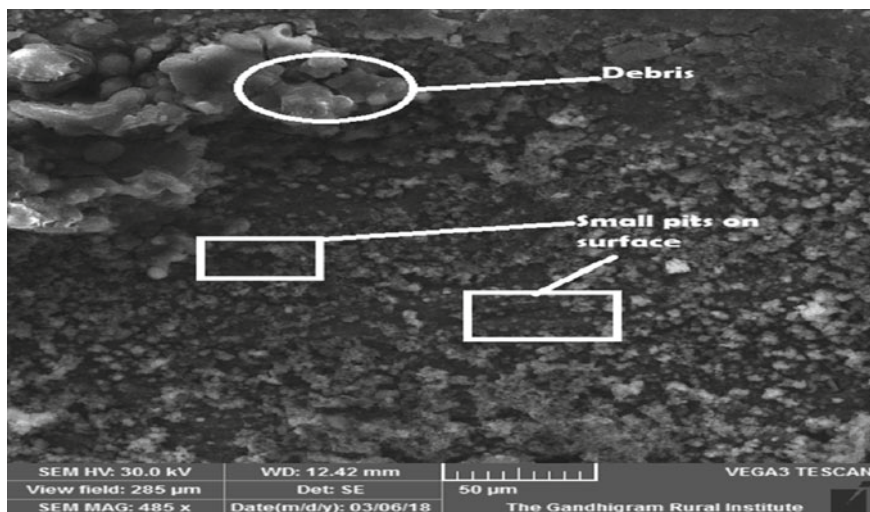
Fig. 16 Corroded SEM image of AIV
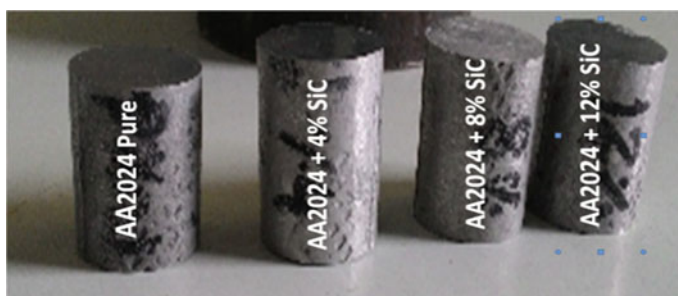
Fig. 17 Samples for age cast and heat treatment

cast and heat treatment. Table 8 shows the comparison of hardness value at Before Heat Treatment (BHT) and After Heat Treatment (AHT) (Fig. 18).

Vickers hardness values of AI and AIV at before heat treatment are 41HV and 125.9HV. Hardness values of AI and AIV at after heat treatment are 53HV and

S.No	Material	BHT Hardness value(HV)	AHT Hardness value(HV)
1	AI	41	49
2	AII	63	75
3	AIII	101	111
4	AIV	125.9	141.9

Table 8 Comparison of Hardness value at Before Heat Treatment and After Heat Treatment

Fig. 18 Hardness variation
AA2024/Sic composites with
respect to heat treatment
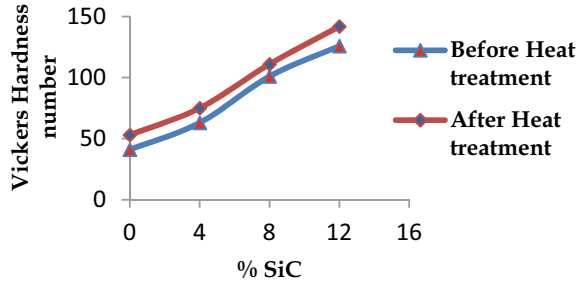
141.9HV. It was recognized that hardness of sample AIV was increased by 3 times
to that of sample AI. As seen from above graph, It was observed that as the SiC
in base matrix increases in the samples AI, AII, AIII & AIV, there is increment
in Hardness also. It was detected that maximum hardness was noticed at 12% SiC
weight fraction.

4   Conclusion

For manufacturing Aluminium Metal Matrix Composites (AMMC), Stir Casting
method was used. Base matrix was strengthened with SiC in disparate proportions of
0, 4, 8 & 12%. The following conclusions were drawn on the basis of the experimental
observations:

- Using the methodology specimens are fabricated successfully with homogenous
  distribution.
- Silicon carbide particles were found to spread evenly in the base matrix. EDX
  reports confirm the distribution and elemental composition of the prepared
  composites.
- Under constant load and by increasing speed it is monitored that rate of wear for
  AA2024 reinforced with 12% SiC (AIV) decreased by 3 times as compared to
  the remaining composites.
- On increasing the reinforcement from 4 to 12%, At 4% interval the hardness also
  increased by 3 times correspondingly to it.
- Corrosion resistance for AIV (AA2024 + SiC 12%) was improved compared to
  AI (AA2024 pure).
- In Hardness test measurement is carried out before heat treatment and after heat
  treatment for both the cases hardness of AIV was almost increased by 3 times to
  that of AI and noticed that as the SiC in base matrix increases there is increment
  in Hardness also.
- These assessed outcomes of investigation very likely helpful in automotive and
  aerospace system applications.

Nomenclature

AI	AA2024 pure
AII	AA2024 + 4% SiC
AIII	AA2024 + 8% SiC
AIV	AA2024 + 12% SiC
AMMC	Aluminium Metal Matrix Composite
EDX	Energy-Dispersive X-Ray Spectroscopy
SEM	Scanning electron Microscopy
SSM	Salt Solution Method
SiC	Silicon Carbide

References

1. Dwivedi R (1994) Performance of MMC rotors in dynamometer testing (No. 940848). SAE technical paper. https://doi.org/10.4271/940848
2. Miyajima T, Iwai Y (2003) Effects of reinforcements on sliding wear behavior of aluminium matrix composites. Wear 255(1–6):606–616. https://doi.org/10.1016/S0043-1648(03)00066-8
3. Mortensen A, Wong T (1990) Infiltration of fibrous performs by pure metal: part III capillary phenomena. Metallurgicaltransactions A 21(8):2257–2263. https://doi.org/10.1007/BF02647888
4. Fridlyander IN, Sister VG, Grushko OE, Berstenev VV, Sheveleva LM, Ivanova LA (2002) Aluminum alloys: promising materials in the automotive industry. Met Sci Heat Treat 44(9–10):365–370. https://doi.org/10.1023/A:1021901715578
5. Prasad SV, Asthana R (2004) Aluminum metal-matrix composites for automotive applications: tribological considerations. Tribol Lett 17(3):445–453. https://doi.org/10.1023/B:TRIL.0000044492.91991.f3
6. Singh J, Chauhan A (2016) Characterization of hybrid aluminum matrix composites for advanced applications—a review. J Market Res 5(2):159–169. https://doi.org/10.1016/j.jmrt.2015.05.004
7. Casati R, Vedani M (2014) Metal matrix composites reinforced by nano-particles—a review. Metals 4(1):65–83. https://doi.org/10.3390/met4010065
8. Nturanabo F, Masu L, Kirabira JB (2019) Novel applications of aluminium metal matrix composites. In: Aluminium alloys and composites. IntechOpen. https://doi.org/10.5772/intechopen.86225
9. Zhang Z, Chen DL (2008) Contribution of Orowan strengthening effect in particulate-reinforced metal matrix nanocomposites. Mater Sci Eng, A 483:148–152. https://doi.org/10.1016/j.msea.2006.10.184
10. Yang Y, Lan J, Li X (2004) Study on bulk aluminum matrix nano-composite fabricated by ultrasonic dispersion of nano-sized SiC particles in molten aluminum alloy. Mater Sci Eng, A 380(1–2):378–383. https://doi.org/10.1016/j.msea.200.03.073
11. Esawi A, Morsi K (2007) Dispersion of carbon nanotubes (CNTs) in aluminum powder. Compos A Appl Sci Manuf 38(2):646–650. https://doi.org/10.1016/j.compositesa.2006.04.006
12. Ali SM (2019) The effect of reinforced SiC on the mechanical properties of the fabricated hypoeutectic Al-Si alloy by centrifugal casting. Eng Sci Technol, Int J 22(4):1125–1135. https://doi.org/10.1016/j.jestch.2019.02.009

13. Tosun G, Kurt M (2019) The porosity, microstructure, and hardness of Al-Mg composites reinforced with micro particle SiC/Al2O3 produced using powder metallurgy. Compos B Eng 174:106965. https://doi.org/10.1016/j.compositesb.2019.106965

14. Hashim J, Looney L, Hashmi MSJ (1999) Metal matrix composites: production by the stir casting method. J Mater Process Technol 92:1–7. https://doi.org/10.1016/S0924-0136(99)001 18-1

15. Ružbarský J (2019) Al–Si alloy casts by die casting. In: Al-Si alloys casts by die casting. Springer, Cham, pp 1–71. https://doi.org/10.1007/978-3-030-25150-5

16. Singh J (2016) Fabrication characteristics and tribological behavior of Al/SiC/Gr hybrid aluminum matrix composites: a review. Friction 4(3):191–207. https://doi.org/10.1007/s40544-016-0116-8

17. Basavarajappa S, Chandramohan G, Davim JP (2007) Application of Taguchi techniques to study dry sliding wear behaviour of metal matrix composites. Mater Des 28(4):1393–1398. https://doi.org/10.1016/j.matdes.2006.01.006

18. Kök M, Özdin K (2007) Wear resistance of aluminium alloy and its composites reinforced by Al2O3 particles. J Mater Process Technol 183(2–3):301–309. https://doi.org/10.1016/j.jmatpr otec.2006.10.021

19. Baradeswaran A, Elaya Perumal A (2015) Effect of graphite on tribological and mechanical properties of AA7075 composites. Tribol Trans 58(1):1–6. https://doi.org/10.1080/10402004. 2014.947663

20. Shorowordi KM, Laoui T, Haseeb AA, Celis JP, Froyen L (2003) Microstructure and interface characteristics of B4C, SiC and Al2O3 reinforced Al matrix composites: a comparative study. J Mater Process Technol 142(3):738–743. https://doi.org/10.1016/S0924-0136(03)00815-X

21. Pradhan S, Ghosh S, Barman TK, Sahoo P (2017) Tribological behavior of Al-SiC metal matrix composite under dry, aqueous and alkaline medium. SILICON 9(6):923–931. https://doi.org/ 10.1007/s12633-016-9504-y

22. Alpas AT, Zhang J (1992) Effect of SiC particulate reinforcement on the dry sliding wear of aluminium-silicon alloys (A356). Wear 155(1):83–104. https://doi.org/10.1016/0043-164 8(92)90111-K

23. How HC, Baker TN (1997) Dry sliding wear behaviour of Saffil-reinforced AA6061 composites. Wear 210(1–2):263–272. https://doi.org/10.1016/S0043-1648(97)00060-4

24. Liang YN, Ma ZY, Li SZ, Li S, Bi J (1995) Effect of particle size on wear behaviour of SiC particulate-reinforced aluminum alloy composites. J Mater Sci Lett 14(2):114–116. https://doi. org/10.1007/BF00456563

25. Kumar GV, Rao CSP, Selvaraj N (2012) Studies on mechanical and dry sliding wear of Al6061–SiC composites. Compos B Eng 43(3):1185–1191. https://doi.org/10.1016/j.compositesb.2011. 08.046

26. Rohatgi PK, Tabandeh-Khorshid M, Omrani E, Lovell MR, Menezes PL (2013) Tribology of metal matrix composites. In: Tribology for scientists and engineers. Springer, New York, NY, pp 233–268. https://doi.org/10.1007/978-1-4614-1945-7_8

27. Broitman E, Indentation Hardness Measurements at Macro-, micro-, and Nanoscale: a critical overview. https://doi.org/10.1007/s11249-016-0805-5

28. Jaiswal S, Rajamurugan G, Krishnasamy P, Shaswat Y, Kaushik M (2019) Mechanical and corrosion behaviour of Al 7075 composite reinforced with TiC and Al_2O_3 particles (No. 2019-28-0094). SAE Technical Paper. https://doi.org/10.4271/2019-28-0094

Study on the Effect of Heat-Treatment on Microstructure and Corrosion Resistance of 0.6% Carbon Steel

Renu Kumari, Priyanka Bharti, and Promod Kumar

1 Introduction

Medium carbon steel (varies between 0.3 and 0.7% C) is widely used in automotive, aerospace, agriculture and structural application. This is also used in railways such as coupling, driving rings and flanges, hand tools; sockets, machinery parts (such as nuts and bolts), shafts and connecting rods [1–5]. However, the limitation of the medium carbon steel is loose its mechanical strength due to corrosion. Corrosion is a natural destructive attack of a material through interaction with its environment [6]. Heat treatment is a cost effective method to improve the corrosion resistance, mechanical properties, electrical properties and magnetic properties of the structural steel. Heat treatment is a heating and cooling process of the material to get desired properties [7]. In the past, several work had been done on the heat treatment on steel to improve its properties. Guma et al. [8] studies the effect of different type of heat treatment (normalizing, annealing and water-quenching) of low and medium carbon steel on corrosion in 0.5M H_2SO_4 containing 3.5%-wt sodium chloride solution. They found that low carbon steel had low resistance to corrosion as compared to medium carbon steel, furthermore, in medium carbon steel, quenched samples had better corrosion resistance than annealed and normalized samples [8]. Oluyemi et al. [9] applied quenching, lamellae formation and tempering heat treatment process on rolled steel. They reported that excellent tensile strength, hardness and impact strength and corrosion resistance, which was beneficial for structural application. Yang et al. [10] investigated the corrosion behavior of quenched and partitioned medium carbon steel in 3.5 wt.% NaCl solution as compared to quenched and tempered steel with the

R. Kumari (✉)
Department of Metallurgical and Materials Engineering, NIT Jamshedpur, Jharkhand, India

P. Bharti
Department of Mechanical Engineering, BCE Bhagalpur, Bihar, India

P. Kumar
Department of Metallurgical and Materials Engineering, NIFFT Ranchi, Jharkhand, India

same composition. They showed that both steel showed similar trend of corrosion behavior, however, quenched and partitioned steel had better corrosion properties. Fauzi et al. [11] studied effect of annealing, normalizing, quenching heat treatments on microstructure, mechanical properties and corrosion behavior of low, medium and high carbon steel. They found that corrosion behavior was dependent on carbon content and type of heat treatment which affect the microstructure [11]. Ismail et al. [12] studied the effect of heat treatment on the hardness and impact properties of medium carbon steel and reported that hardness and impact property dependent on type heat treatment.The effect of cyclic quenching and tempering on mechanical and corrosion properties of medium carbon low alloy steel was investigated by Chukka et al. [13]. They reported that improvement in corrosion resistance after cyclic heat–treatments which was attributed to refinement in grain size. Gebril et al. [14] studied the effect of tempering on mechanical properties and corrosion rate of medium and high carbon steel. And found that hardness and ultimate tensile strength were gradually decreased and ductility was improved, however, multiphase structure had higher corrosion rate as compared to martensitic structure [14].

From the aforementioned literature review it is concluded that a detailed study of effect of different heat treatment on microstructural characterization and corrosion has not been investigated in detail. In the present study the effect of different heat treatment such as, annealing, normalizing and quenching on microstructural characterization and corrosion behavior of 0.6 % C steel have been studied.

2   Methodology

In the present study, 0.6% carbon steel was used as substrate material.The samples were cut by using abrasive cutter by 10 mm × 10 mm × 5 mm dimension. Heating of the samples were done at 910 °C for 2 h than furnace cooling (annealing), air cooling (normalizing) and water quenching (quenching) were done. Followed by heat treatment, samples were polished up to 0.5 μm. Optical microscope was used to investigate the microstructure of the samples. Phase analysis of the as received and heat treated samples were done by XRD techniques ((D8Advance, Bruker) using Cu Kα radiation. The corrosion properties in terms of corrosion rate was analyzed by weight loss method 3.5 wt.% NaCl solution. In this test, samples were dip in 3.5 wt.% NaCl solution up to maximum 72 h after that weight changed was observered. Than corrosion rate was calculated by using Eq. (1) [6].

$$\text{Corrosion rate,} \ \ CR = \frac{87.6 \times W}{DAT} mm/Y \tag{1}$$

where,

W   Weight loss in the sample in milligram.
D   Density of the material in g/cm^3.

A   Area of cross-section in cm^2.
T   Time in hours.

3   Results and Discussions

Figure 1 shows the optical micrographs of the (a) as received 0.6% C steel and (b) high magnification view of the same. From Fig. 1, it is observed that ferrite and pearlitestructure, which is further confirmed by XRD analysis.

Figure 2 shows the optical microstructures (a) the annealed 0.6% C steel and (b)high magnification view of the samples. The microstructures reveals that formation of coarse pearlite and coarse ferrite grains (cf. Fig. 2).

Figure 3 shows the optical microstructures of (a) the normalized 0.6% C steel and (b) high magnification view of the same. From Fig. 3 it is observed that fine pearlite grains and fine ferrite grains are formed in the microstructure. A close comparison of Figs. 3 and 2 shows that refinement of grain in normalized sample as compared to
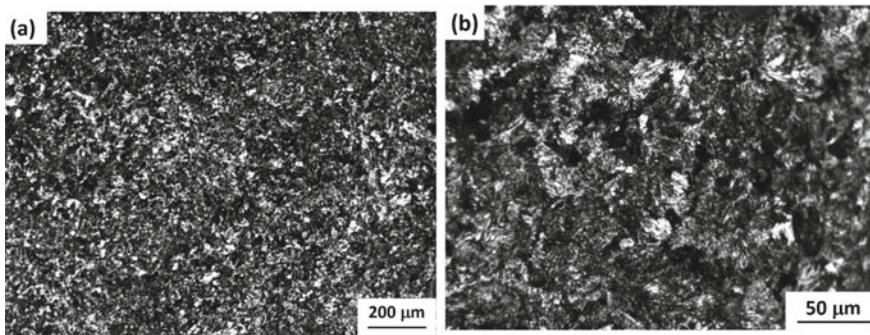
Fig. 1   A shows the optical micrographs of **(a)** 0.6% C steel, and **(b)** same at high magnification
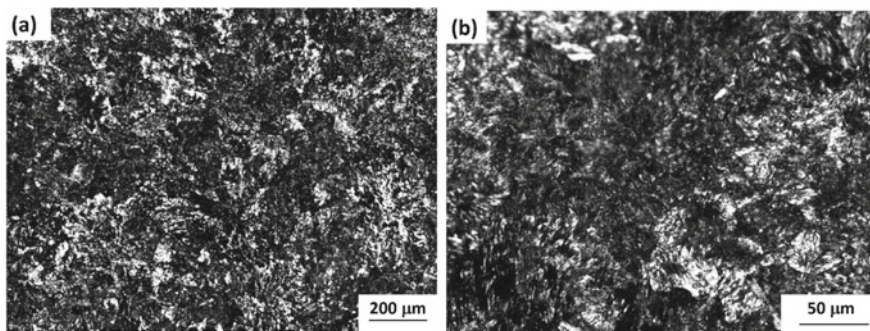
Fig. 2   Optical microstructures **(a)** the annealed 0.6% C steel and **(b)** high magnification view of the samples
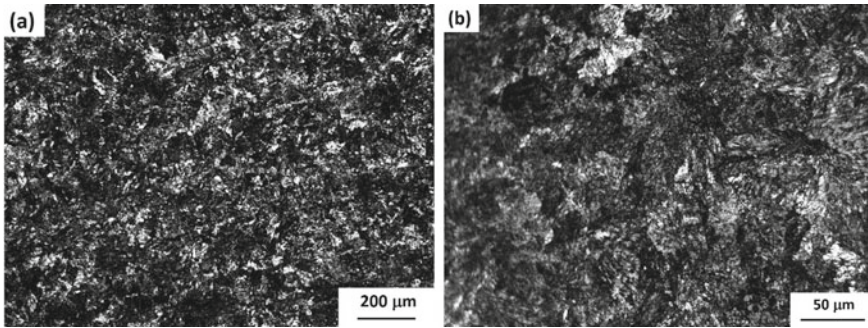
Fig. 3 Optical microstructures of **(a)** the normalized 0.6% C steel and **(b)** high magnification view of the same

annealed samples. In contrary to this, Guma et al. [8] reported annealing produced finer grains as compared to the normalized and the quenched hardened finest grains on average basis.

Figure 4 shows the optical microstructure of (a) the quenched 0.6% C steel and (b) high magnification view of the same. From Fig. 4 it is observed that presence of needle like structure, which is martensite. High magnification view shows the uniform distribution of needle like martensite structure. Hafeez et al. [13] reported that refinement of grains along with presence of lath martensite and retained austenite in cyclic quenched medium carbon low alloy steel. Guma et al. [8] reported that re-orientation of the grain size of the carbides, ferrites in the heat treated medium carbon steel.

Figure 5(a–d) shows the X-ray diffraction pattern of (a) as received, (b) annealed, (c) normalized and (d) quenched 0.6% C steel. From Fig. 5(a) it is observed that presence of ferrite and carbide phase in as received 0.6% C steel. Presence of ferrite and carbide phase are also observed in annealed and normalized 0.6% C steel, however, the peak intensity of carbide phase has increased in normalized sample (cf. Fig. 5(b,
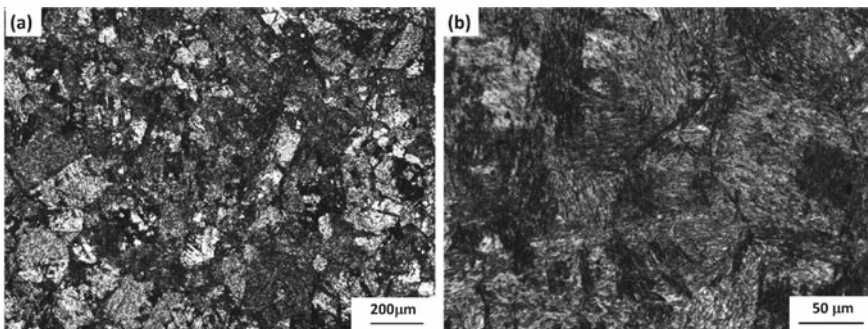
Fig. 4 Optical microstructures of **(a)** the quenched 0.6% C steel and **(b)** high magnification view of the same
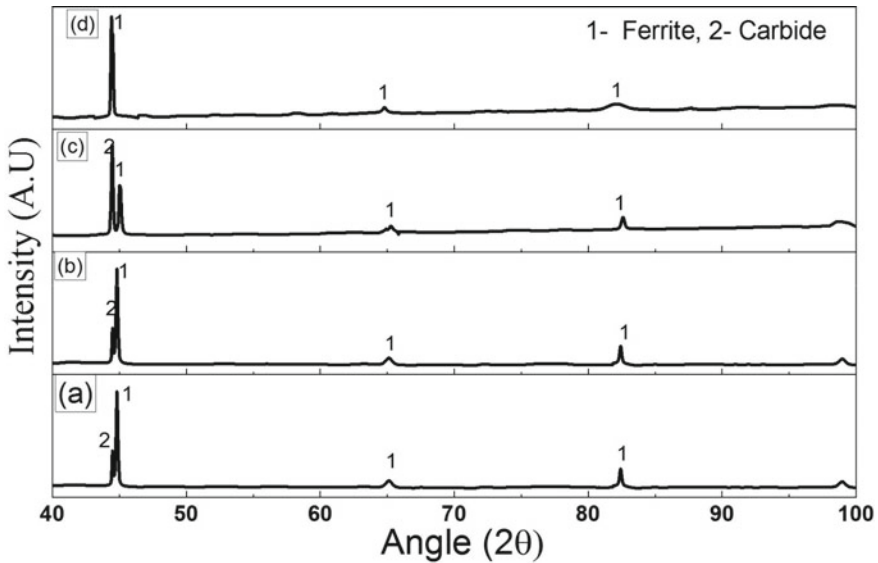
Fig. 5 (a–d) X-ray diffraction pattern of **(a)** as received, **(b)** annealed, **(c)** normalized and **(d)** quenched 0.6% C steel

c)). Quenched samples show the presence of ferrite phase only (cf. Fig. 5(d)). Similarly, presence of ferrite and cementite phases was reported by Saha et al. [15] in cyclic heat treated 0.6% C Steel. Peak intensity at 44° for carbide phase is increased in normalized sample as compared to as received and annealed sample, which indicate the increased mass fraction of carbide phase in normalized sample. On the other hand, this peak disappears in quenched sample, which may be due to carbide dissolve and form solid solution. A close investigation shows that ferrite peak is significantly broaden at peak position 82°, which may be due to lattice strain generated due to carbon entrapment in ferrite phase.

Corrosion analysis of as received and heat treated 0.6% C steel was done by weight loss method and data are summarized in Table 1. From Table 1 it is noted that a significant reduction in corrosion rate from 4.91×10^{-5} mm/year for as received 0.6% C steel to $2.23 \times 10^{-5} - 3.12 \times 10^{-5}$ mm/year for heat treated 0.6% C steel. The

Table 1 Summarized phases, hardness and corrosion rate of as received and heat treated samples

Sample	Phases	Corrosion rate (mm/year)
1. As received 0.6% C steel	Ferrite, carbide	4.91×10^{-5}
2. Annealed 0.6% C steel	Ferrite, carbide	3.12×10^{-5}
3. Normalized 0.6% carbon steel	Ferrite, carbide	3.12×10^{-5}
4. Quenched 0.6% C steel	Ferrite	2.23×10^{-5}

improvement in corrosion resistance of heat treated samples may be due to homogenization of structure. Furthermore, improvement is more in quenched samples as compared to annealed and normalized samples. The better corrosion resistance of quenched steel is attributed to the presence of single phase ferrite only. On the other hand, presence of ferrite and carbide phase in annealed and normalized samples, so which may be form galvanic cell and increased the corrosion rate. Similarly, Gebril et al. [14] reported that increased corrosion rate in multiple phase structure as compared to martensite structure even its stressed structure. Guma et al. [8] reported that improvement in corrosion resistance of the heat treated the of medium carbon steel.

4   Conclusions

A detailed study of the effect of heat-treatment on microstructure and corrosion resistance of 0.6% carbon steel have been carried out. And the following conclusions may be drawn:

- Microstructure analysis shows the presence of ferrite and pearlite grain in as received, annealed and normalized samples, whereas coarse ferrite and pearlite grains is observed in annealed sample as compared to normalized and as received 0.6% C steel. On the other hand, martensite grains are observed in quenched 0.6% C steel.
- Phase analysis shows the ferrite and carbide phase in as received, annealed and normalized 0.6% C steel, whereas ferrite phase is present in quenched 0.6% C steel.
- There is a significant improvement in corrosion resistance from 4.91×10^{-5} mm/year for as received samples to $3.12 \times 10^{-5} - 2.23 \times 10^{-5}$ mm/year for heat treated 0.6% C steel, whereas improvement is more in quenched 0.6% C steel (2.23×10^{-5} mm/year) as compared to annealed (3.12×10^{-5} mm/year) and normalized 0.6% C steel (3.12×10^{-5} mm/year).

References

1. Liu X, Xiao L, Wei C, Xu X, Luo M, Yan W (2018) Effect of multi-directional forging and annealing on abrasive wear behavior in a medium carbon low alloy steel. TribolInt 119:608–613
2. Sanij MHK, Banadkouki SSG, Mashreghi AR, Moshrefifar M (2012) The effect of single and double quenching and tempering heat treatments on the microstructure and mechanical properties of AISI 4140 steel. Mater Des 42:339–346
3. Bardelcik A, Worswick MJ, Wells MA (2014) The influence of martensite, bainite and ferrite on the as-quenched constitutive response of simultaneously quenched and deformed boron steel, experiments and model. Mater Des 55:509–525
4. Guma TN, Abu J (2018) A field survey of outdoor atmospheric corrosion rates of mild steel around kaduna metropolis. SSRG Int J Mech Eng 5(11):7–21
5. Ayodele CO, Nenuwa OB (2013) Investigation of the effects of heat treatment on the corrosion behaviour of welded low carbon steel in different environments. Int J Sci Technol 3(8):333–340
6. Fontana MG (2005) Corrosion engineering, 3rd edn. Tata McGraw-Hill Publishing Company, New Delhi
7. Rajan TV, Sharma CP, Sharma A (1989) Heat treatment principles and techniques. New Delhi, Prentice Hall of India Private Limited
8. Guma TN, Olayiwola O, Garba DK, Effects of some heat treatments on corrosion of low and medium carbon steel in acidic chloride medium. World Sci News 132:169–186
9. Oluyemi DO, Oluwole OI, Adewuyi BO (2011) Studies of the properties of heat treated rolled medium carbon steel. Mat Res 14(2):135–141
10. Yanga J, Lua Y, Guoa Z, Gub J, Gu C (2018) Corrosion behaviour of a quenched and partitioned medium carbon steel in 3.5 wt.% NaCl solution. Corros Sci 130:64–75
11. Fauzi MAM, Saud SN, Hamzah E, Mamat MF, Ming LJ (2019) In vitro microstructure, mechanical properties and corrosion behaviour of low, medium and high carbon steel under different heat treatments. J Bio- Tribo-Corrosion 5:37
12. Noor MI, Khatif NM, Kecik NAA, Shaharudin MAH (2016) The effect of heat treatment on the hardness and impact properties of medium carbon steel. IOP conference series: materials science and engineering 114:012108
13. Hafeez MA, Inam A, Farooq A (2020) Mechanical and corrosion properties of medium carbon low alloy steel after cyclic quenching and tempering heat–treatments. Mater Res Express 7:016553
14. Mohamed A, Gebril MA, Aldlemey MS, Abdessalam FK (2013) Effect of tempering on mechanical properties and corrosion rate of medium and high carbon steel. Adv Mater Res 685:81–85
15. Sahaa A, Mondal DK, Maity J (2010) Effect of cyclic heat treatment on microstructure and mechanical properties of 0.6 wt% carbon steel. Mater Sci Eng, A 527:4001–4007

Investigation of the Degreasing Process to Improve Adhesion Between Oxidized Galvannealed Coating and Electroplated Nickel

Arup Kumar Halder and Anindita Chakraborty

1 Introduction

Corrosion protection of steel by coating of sacrificial material like zinc is an age-old process. The process steps of applying zinc coating on steel is widely researched in the last century for various application sector. Presently the process of industrial hot dip galvanising is widely accepted and followed across the world. Among different application sectors, the galvanised coated steel sheets are used in large quantity in the automotive sector. However, the requirement of proper forming, welding and post painting has led to different modifications of the conventional galvanised coatings. Galvannealing coating is one such modification or improvement over conventional galvanised coatings. The galvannealing coating is nothing but an iron-zinc alloy coating. This type of coating offers better welding and painting properties [1–5]. So, this has become the choice for automakers over last few decades. Galvannealing coating, if not passivated properly has tendency to corrode as there is about 10–12 wt.% iron on the top surface of the coating. Moreover, in the process of galvannealing, occurrence of surface defect is a major issue that result in downgrading and rejection of materials. There are several ways to further improve the properties of galvannealing coating like improve phosphatability [6–8] as well as lubricity [9]. Electroplating of nickel is reported to be one of them. There are several researches available that discuss the effect of electroplated nickel on the top surface of galvannealing coating to improve the corrosion properties, welding behaviour, hardness etc. of the primary galvannealing coating. However, it must be mentioned that plating of nickel on galvannealing sheet in batch mode is very difficult due to the surface condition in galvannealing coatings. Often industrially there is no online nickel plating facility rather it is done in batch mode. So the nickel coating adhesion is an issue needs to be addressed. The present paper discuss the surface preparation methods of industrially produced galvanneal coatings and the effect on the surface preparation

A. Kumar Halder (✉) · A. Chakraborty
Surface Engineering Research Group, R&D, Tata Steel Limited, Jamshedpur, India

technique on the adhesion of the galvanneal and nickel coating. The performance of the nickel coated galvanneal coating is also evaluated and presented in the present work.

2 Experimental

2.1 As-Received Coated Substrate

The substrate steel sheet was cold rolled from Tata Steel with thickness of 1.5 mm. The composition of the steel is (Wt%) given in Table 1.

The starting steel microstructure was a ferrite-perlite structure (Fig. 1) and average hardness value was 120–130 HV_1 and tensile strength was 360–379 MPa. The GA coating thickness was about 8–9 μm (Fig. 2a). The industrial application of this steel grade is high temperature body panel like, furnace body, car body panel.

2.2 Experimental Procedure:

As-received GA coated steel samples were cut as per requirement. Composition of steel substrate was detected by Optical Emission Spectroscopy method. The cut-to-size samples were then degreased by concentrated ammonium chloride solution as described in Sect. 2.3. Finally, samples were dipped into the Ni plating solution. The nickel plating process details are given in Sect. 2.4. Characterization of Ni coated samples were done thereafter.

2.3 Surface Preparation of GA Sheets

GA sample was degreased by commercial alkaline solution (Ammonium chloride-NH_4Cl) and solution pH was above 12 pH (12.5–13 pH). Selection of pH was the crucial finding for this old GA sample which will be discussed later (Sect. 3.2). Degreasing solution temperature was about 45–50 °C. GA sample was dipped inside the solution for two times. 1st dipping time was 15–20 s after that sample was rubbed mechanically followed by cleaning with DM water and then again dipped in solution for 2nd time until bubble formation and the dipping time was 30–90 s. After degreasing, sample was clean thoroughly by DM water. Finally, the sample was pickled by 2% dilute HCl solution for 3–5 s and then rinsed with deionized water.

Table 1 Chemical composition of steel sample, wt%

C	Mn	S	P	Si	Al	Cu	Cr	Ni	Mo	V	Nb	Ti
0.11	2.02	0.007	0.015	0.56	0.4	0.026	0.5	0.001	0.001	0.001	0.001	0.0002
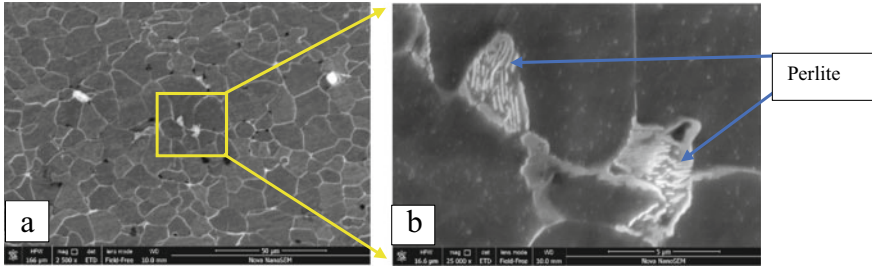
Fig. 1 Cross-section of steel sample: **a** Magnification 2.5 K and **b** Perlite, Area magnified image of (**a**)
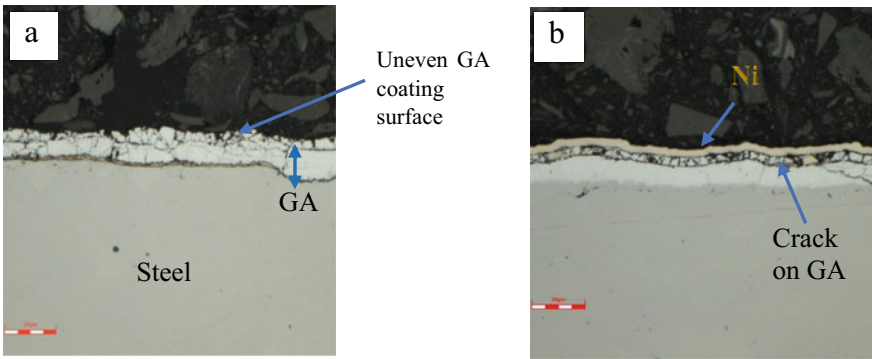
Fig. 2 **a** GA coating cross-section, optical image, **b** Cross-section of Ni coated GA; Mag-1000X

2.4 Ni Plating on GA Steel Sheet

Ni electroplating was done on small lab samples (5×3 cm^2) by using silicon rectifier unit (maximum current 25Amp) and bigger size sample (20×11 cm^2–50×35 cm^2) were done on pilot line by using high power rectifier (maximum current 600Amp). Two pure Ni bar (size 10×5 cm^2) (for lab sample) and 8 no. pure Ni bar (size 72×9 cm^2) for bigger size samples were used as anode and GA steel sample used as working cathode. anode was clean by degreasing and DM water. Electrolyte was stirred continuously and solution temperature was maintained 50–55 °C. Live current was given before immersing the cathode or GA sample to electrolyte. 400 A/m^2 current density was applied for 5 and 8 min plating time. Current density and dipping time was optimised after investigating the surface appearance and cross-section of the coating. Ni plating was performed by using conventional Watt bath solution.

2.5 Procedure to Check the Ni Coating Adhesion

Adhesion check was done by heating and bending process. Sample size was 5×35 cm^2. Heating was done by using high temp muffle furnace (maximum temperature 1200 °C) at normal atmosphere up to 700–850 °C for 3–5 min followed by bending at 90° and quenching on normal atmosphere. The adhesion test was performed following B571-97 standard.

2.6 Coating Cross-Section

Coating cross-section was one of the critical process to observe the coating thickness, of GA and Ni layer. Sample was cut on small pieces (2×1 cm^2) by using diamond cutter and cutting speed was 300 to 400 rpm. Sample was hot mounted by conductive phenolic resin (with carbon powder). Grinding was done using grit P600, M-type SiC abrasive paper followed by P800, P1200, P4000 and diamond polishing was done by using 3μ and ¼ μ diamond suspension. Coating thickness, composition was taken on scanning electron microscopy (SEM, NOVA NNS 450) and EDS scan. Image was also taken by using optical microscopy (Leica).

2.7 Experimental Parameter Optimised for Ni Coating

Ni electroplating was conducted by using conventional Watt's bath which contain nickel sulphate (NiSO$_4$, 6H$_2$O): 300 g/L, Nickel chloride (NiCl$_2$, 6H$_2$O): 60 g/L and boric acid (H$_3$BO$_3$) 40 g/L and solution pH was 4.0. Three different current density was selected for Ni electroplating which were 100 A/m^2, 400 A/m^2, 700 A/m^2 and varies two different time (5, 8 min) for each current density. Total experimental chart has showed in Table 2.

Table 2 Experimental parameter of Ni electroplating

Current density (A/m^2)	Ni plating time, minute	Coating appearance, visual
100	5	Black
	8	Black
400	5	No black area, shaded brown color
	8	No black area, shaded brown color
700	5	Bubble mark observed at surface and granular coating at edges
	8	More bubble mark and granular coating surface at edges

3 Result and Discussion

3.1 Microstructural Analysis of As-Received Samples: Give Details of Starting Sample

Cross-section microstructure of steel clearly shows the ferrite-perlite structure (Fig. 1) and perlite percentage are very less (4–5%) and rest 95% are ferrite which give very low hardness at as cast condition. Cross-section image of GA sample shows some rough surface at top of the coating (Fig. 2a) and those are more visible after Ni electroplating (Fig. 2b).

3.2 Process Optimization of Degreasing

Initial cross-sectional microstructure of GA coated steel was characterized by optical microscopy and it was found that top surface of GA coating was not uniform, small crack present and coating thickness was 9–11 μm. Conventional degreasing solution (NH_4Cl) (25 gm/lit) of pH 4 was used to clean the GA sample before Ni electroplating and Ni electroplating was done by using "Watt bath" for 5 and 8 min. Ni Plating time was increased to protect the interface of GA and Ni coating as GA coating is brittle in nature and top surface may damage during sample preparation of cross-section. Crack of GA coating are visible after Ni electroplating (Fig. 2b). It is also clearly visible on SEM image (Fig. 3) and from point analysis of the crack region, it has been found that high amount of oxygen is present along with zinc (Table 3). Point analysis done at top surface of the GA coating (Fig. 4) and it was found that zinc oxide was present (Table 4) which was not removed after cleaning by normal alkaline solution.

Fig. 3 Cross-section EDS image of Ni coated GA (5 min) under SEM
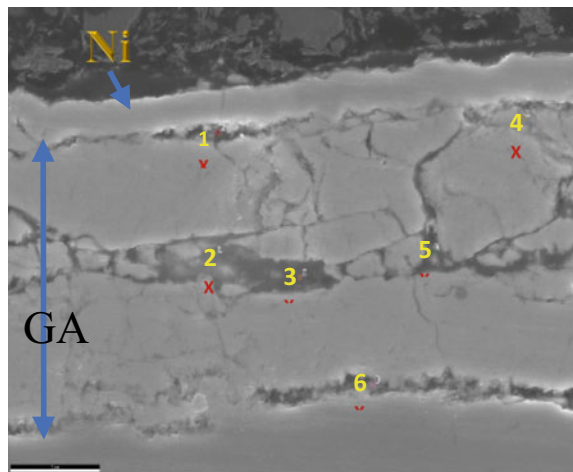
Table 3 Compositional analysis of Fig. 3 by EDS in wt%

Points	Chemical composition by EDS analysis of Ni coated GA (wt%)				
	OK	FeK	NiK	ZnK	ClK
1	8.17	7.14	48.03	36.67	–
2	17.82	7.42	–	72.22	2.54
3	18.72	8.74	6.29	65.12	1.13
4	13.65	10.33	5.73	70.29	–
5	15.36	12.01	–	70.63	–
6	8.15	30.42	4.43	57	–

Fig. 4 Top surface of as received GA coating under SEM
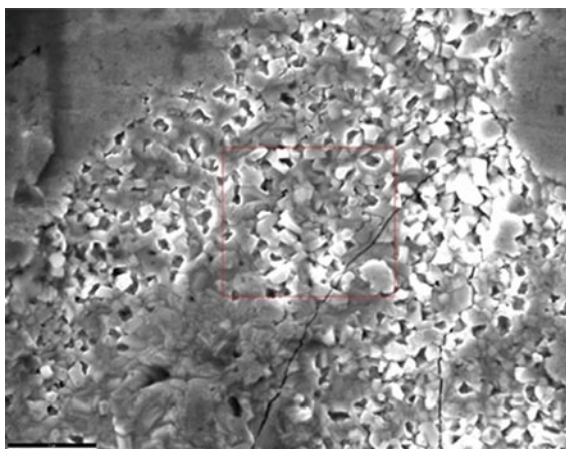
Table 4 Compositional analysis of Fig. 4 by EDS in wt%

Area	Chemical composition by EDS analysis of GA top surface (wt%)		
	OK	FeK	ZnK
1	7.22	11.92	80.86

High temp bending test was conducted and it was observed that Ni plating coating was peeled off from GA surface (Fig. 5a). EDS also done on peel off coating of top surface (Fig. 5b) and zinc was not present (Table 5), that means interface bonding between Ni and GA has not formed properly i.e. no adhesion formed between the coating, so Ni coating is unable to diffuse into GA coating and results in peeling off the coating during heating and bending.

It is vividly understood that zinc oxide will not be removed or dissolve by conventional degreasing solution. Pourbaix diagram of the zinc showed that zinc oxides will not dissolved where solution pH below 12.0 but oxides will be removed above 12.0 pH (Fig. 6) [10]. Hence concentration of degreasing solution was increased
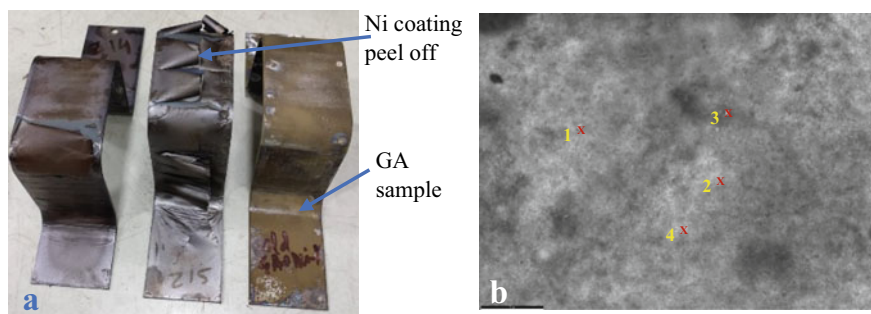
Fig. 5 a High temp 90° bending sample of Ni coated GA and GA sample without Ni plating, b Ni peel off coating under SEM

Table 5 Compositional analysis of Ni peel of coating by EDS in wt%, Fig. 5b

Points	Chemical composition by EDS analysis of Ni peel off (wt%)			
	O K	AlK	FeK	NiK
1	23.46	0.51	6.42	69.61
2	25.51	0.7	4.9	68.89
3	21.57	0.49	4.02	73.92
4	26.32	0.85	5.65	67.17
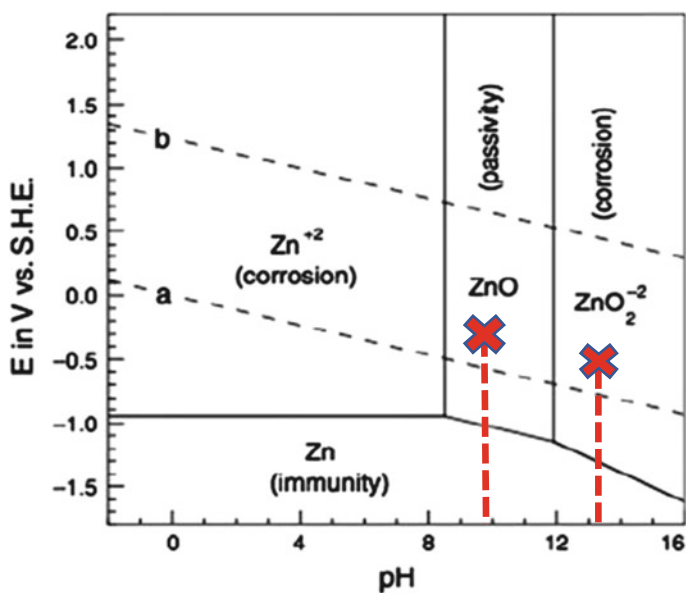
Fig. 6 Pourbaix diagram of zinc

(70–80 gm/lit) to reach the solution pH level above 12.5–13.5. Ni electroplating was done after using this high concentration degreasing solution and followed by pickling, rinsing. Cross-section of the Ni plated sample after using high pH solution during degreasing process showed that significant decrease of crack (Fig. 7a) and EDS also done inside the coating (Fig. 7b). EDS analysing of Fig. 7b showed that significant decrease of oxide present inside the coating (Table 6). This coating adhesion also improves and the coating didn't show any peel off issue after high temperature process and bending test. There was no such significant difference at top surface between without alkali clean and after high concentration alkali clean sample (Fig. 8a–c) at low magnification. But top surface had showed small difference between without alkali clean and after high concentration alkali clean sample (Fig. 8b–d) at higher magnification. Black spot was more on without alkali clean
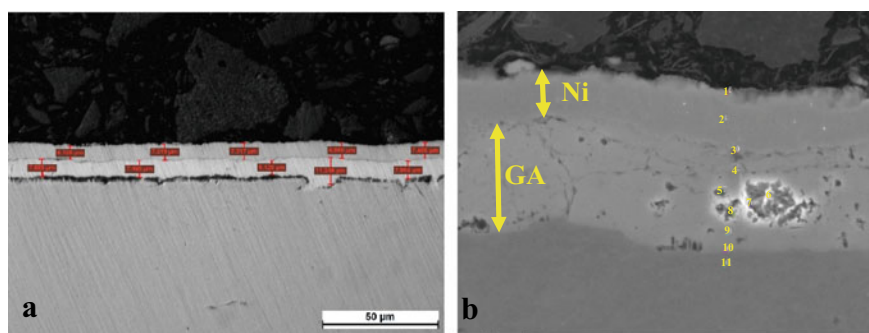
Fig. 7 Ni electroplating on GA after decreasing by pH 12.5 solution: **a** Optical, **b** SEM image

Table 6 Compositional analysis of Ni electroplated coating by EDS in wt%, Fig. 7b

Points	Chemical composition by EDS analysis of Ni coated GA (wt%), after degreasing solution pH 12.5			
	O K	FeK	NiK	ZnK
1	7.3	5.22	87.48	–
2	–	5.61	94.39	–
3	5.6	9.9	42.55	41.95
4	2.68	12.37	7.7	77.25
5	–	14.43	3.78	81.79
6	15.94	15.94	3.67	67.2
7	13.06	13.06	14.05	60.62
8	–	15.25	2.95	81.8
9	–	18.85	–	81.15
10	–	81.19	–	18.81
11	–	98.69	–	–

(a) GA-before alkaline clean, 200X

(b) GA-before alkaline clean, 1000X

(c) GA-after high concentration
alkaline clean, 200X

(d) GA-after high concentration
alkaline clean, 1000X
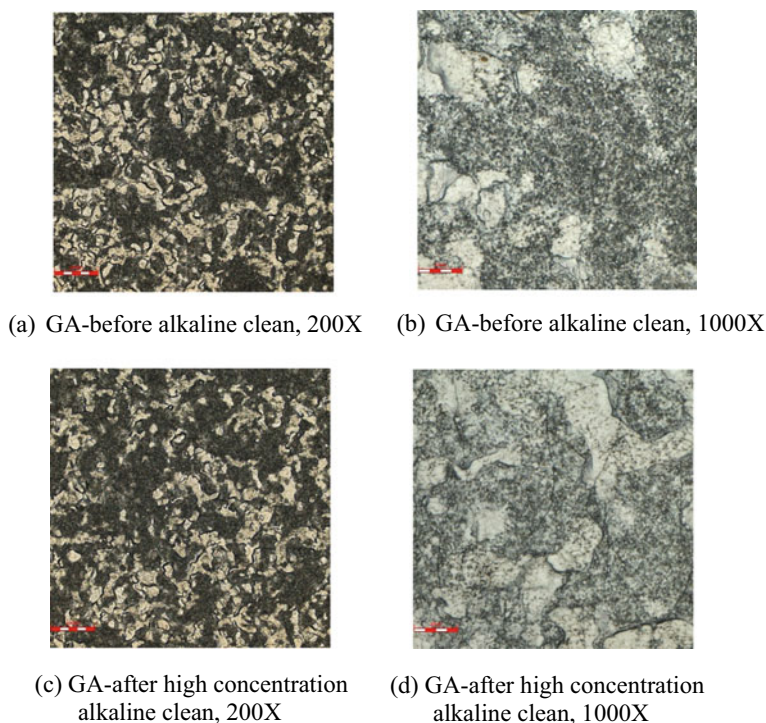
Fig. 8 Top surface optical image before alkaline clean (**a**, **b**) and after high concentration alkaline clean (**c**, **d**)

GA (Fig. 8b) and black spot was comparatively less (Fig. 8d) on alkaline cleaned GA sample. The dissolution of zinc oxide occurred at nanometric level which fully unable to trace through optical microscopy. But improvement of adhesion property between GA and Ni coating interface indicates the efficiency of high concentration alkali solution which remove the oxide from GA coating surface.

3.3 Process Optimization of Ni Coating

It was seen that at lower current density (100 A/m^2) coating were not uniform and coating appearance was slight blackish (Table 2). Coating uniformity and appearance was good at current density of 400 A/m^2. Coating thickness was good at 700 A/m^2 current density but coating appearance at top surface was not good. Many hydrogen bubbles were visible and granular coating surface forms at edges. So, it was decided to do Ni coating by using current density of 400 A/m^2 which gives uniform coating thickness as per requirement. Coating thickness was checked by optical microscopy. Coating thickness was 1.2–2 μ and ununiform coating was observed for 100 A/m^2
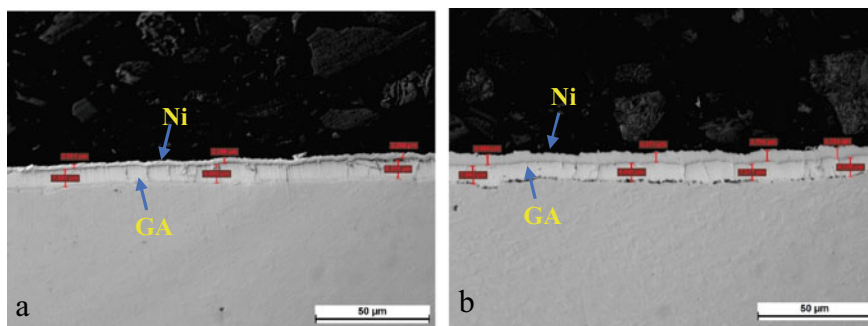
Fig. 9 Ni electroplating on GA at 400 A/m^2 current density: **a** 5 min, **b** 8 min

current density. 8–12 μ coating thickness was appeared for 700 A/m^2 current density but top surface of the coating showed some bubble mark and coating was peeled off or broken during cutting as high current density increases the stress inside the Ni coating. But coating had no issue which was done by using 400 A/m^2 current density. Coating thickness was 2.3–3.5 μ (5 min) and 4.5–7 μ (8 min) (Fig. 9) and surface appearance also improved significantly. GA coating thickness was 7.5–8.5 μ.

3.4 Adhesion

Coating interface between GA and Ni electroplating showed a significant difference if compare between Figs. 2b and 9. Crack at interface was not observed. Coating was heat treated at high temperature and no Ni coating peel off was seen after 90° bend test (Fig. 10). It is now established that the higher concentration of degreasing solution enhances the dissolution of the zinc oxide layer which enables the Ni ion deposited on GA surface and make better bonding between GA and Ni electroplating layer. This in turn enables the inter-diffusion of nickel and GA during high temperature application and no coating peel off happened during 90° bend test.

4 Conclusions

1. The surface preparation process before conventional electroplating of nickel on steel does not yield proper adhesion of galvannealing coating and nickel coating.
2. The new surface preparation parameters are optimized to improve the dissolution of zinc oxide from surface but without damaging the underlying galvannealing coating.

Fig. 10 Ni electroplating on GA after high temperature 90° bend test

No Ni coating peel off
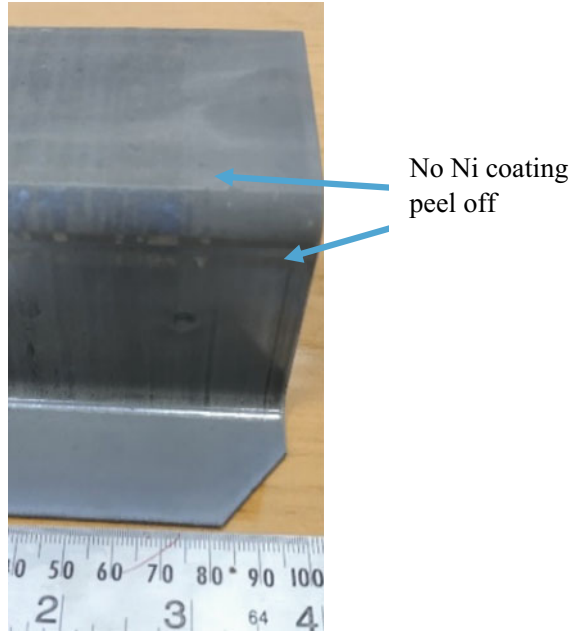
3. The nickel coating is performed through electrodeposition and with the use of live current to suppress the dissolution of zinc from galvanneal coating to the plating bath.
4. The revised surface preparation and electroplating process exhibit uniform nickel coating thickness and improved nickel coating adhesion as tested from high temperature heating and bending experiments.

References

1. Marder AR (2000) The metallurgy of zinc-coated steel. Prog Mater Sci 45:191–291. https://doi.org/10.1016/S0079-6425(98)00006-1
2. Howe P, Kelley SC (1988) A comparison of the resistance spot weldability of bare, hot-dipped, galvannealed and electrogalvanized DQSK sheet steels, SAE technical paper no. 880280, SAE, Warrendale, PA
3. Landriault JP, Harrison FW (1987) Comparison of thermally alloyed Zn-Fe coatings produced by mechanical wiping to those produced by post-coating annealing. CIM Bull 80(904):71–78
4. White CL, Lu F, Kimchi M, Dong P (1998) Resistance welding electrode wear on galvannealed steels, zinc-based steel coating systems: production and performance. In: Goodwin FE, (ed) TMS, Warrendale, PA, p 219
5. Campos A, Guerreo-Mata MP, Colas R, Gazra R (2002) Weldability of galvannealed interstitial free steel. ISIJ Int 42(8):876–881. https://doi.org/10.2355/isijinternational.42.876
6. Hada T, Fujiwara T, Kanamaru T, Nakayama M, Horita T (1985) ASM Met./Mater. Technol. Ser. Pap., No. 8512-005

7. Satoh N (1987) Effects of heavy metal additions and crystal modification on the zinc phosphating of electrogalvanized steel sheet. Surf Coat Technol 30(2):171–181. https://doi.org/10.1016/0257-8972(87)90141-1

8. Narayanan TSNS (2005) Surface pretreatment by phosphate conversion coatings–a review. Rev Adv Mater Sci 9:130–177

9. Pradhan D, Dutta M, Venugopalan T (2016) Ni-flash-coated galvannealed steel sheet with improved properties. JMEPEG 25:4996–5006. https://doi.org/10.1007/s11665-016-2290-2

10. McCafferty E (2009) Thermodynamics of corrosion: pourbaix diagrams, introduction to corrosion science pp 95–117

Innovation in Optimization of Mixing and Nodulizing Drum for Reducing Energy Consumption at Sinter Plant, Tata Steel

Dhirendra Prasad, Renu Kumari, Bikash Kr. Chatterjee, Mazhar Ali, Amit Kr. Singh, and Surajit Sinha

1 Introduction

Steel industry is known for its high impact on carbon foot print because of large amount of energy is required for its several processes starting from mining of raw materials to iron making and steel manufacturing. As per published report, in India during 2018–19, the total National Energy Consumption was 5,69,537 ktoe (Kilo Tonne of oil Equivalent) [1]. Out of the total final energy consumption, the industrial sector consumed 55.90%. Within the industry sector, the most energy intensive industries were iron and steel which accounted for 17.68% of the industrial energy use followed by Chemicals and petrochemicals 4.41% and construction 2.38%. Sinter making is no exception within the iron and steel industry. Sinter Plant is an energy intensive unit in any integrated steel plant [2]. Therefore, any work towards energy saving will have positive impact on overall energy scenario and environment. Sintering is a process of agglomeration of iron ore fines along with crushed fluxes, solid fuel and solid wastes etc. These materials are mixed together and granulated in mixing and nodulizing drum (MND), thereafter it is charged on to sintering machine where sinter mix is fired and sintering takes place at >1300 °C [3]. Conventionally, solid fuel like coke breeze is the main source of heat in sintering process. Along with solid fuel, electrical power consumption contributes to a major portion of energy

D. Prasad · R. Kumari (✉)
Department of Metallurgical and Materials Engineering, National Institute of Technology, Jamshedpur, India
e-mail: renu.met@nitjsr.ac.in

D. Prasad · B. Kr. Chatterjee · A. Kr. Singh
Sinter Plant, Tata Steel Limited, Jamshedpur, India

M. Ali
Iron Making Electrical Maintenance, Tata Steel Limited, Jamshedpur, India

S. Sinha
Chief Agglomerates, Tata Steel Limited, Jamshedpur, India

consumption in iron ore sintering process. There are several high electrical-power consuming equipment in a sinter plant. This provide immense opportunities to optimize these equipment to save electrical energy. Mixing and nodulizing drum (MND) is one of the high electrical-power consuming unit and is used for mixing of base mix with trimming flux and solid fuel along with calcined lime and water. Mixing and Nodulizing Drum (MND) causes increase in mean size of sinter mix due to ball formation (quasi particles) during its rotating movement. While the coarser fractions of the base mix form the nucleus, the finer fractions collect around the nuclei to form these quasi-particles [4–6]. Higher mean size of sinter mix increases sinter bed permeability which leads to faster sintering and higher sinter machine productivity [7]. Therefore, Granulation Index (GI) is an important parameter that measures the effectiveness of granulation/balling where the objective is to minimize the finer fractions, and also to produce quasi-particles of a narrow size range. Higher granulation gives better air permeability through 'sinter mix bed' during sintering. Better permeability leads to faster rate of sintering [8]. This finally enables higher sinter production either by increasing the speed of sintering machine or by increasing the sinter bed height on sintering strand.

Several innovative experiments were conducted at Sinter Plant (SP) 3 of Tata Steel Jamshedpur to optimize the speed of MND to save electrical energy without effecting sinter plant productivity and product sinter quality. At sinter plant, Mixing and Nodulizing Drum (MND) generally rotates at fixed RPM (rotation per minute) with the help of high tension (HT) motor. At SP3, MND runs at constant motor RPM 1400. So, there is possibility to reduce motor RPM to increase retention time of sinter mix in MND which may improve Granulation Index (GI) of sinter mix which is an indicator balling efficiency of MND. To establish this variable-voltage/variable-frequency (VVVF) drive installed in MND at SP3 and experiments were conducted with MND motor reduced RPM to improve GI and saving of electrical power energy.

2 Experimental Procedures

Mixing and nodulizing drum is a large equipment in sinter plant used for granulation of sinter mix. In sinter plant 3 at Tata Steel Jamshedpur, its main dimensions are 4000 mm diameter and 5000 mm length. It is designed for interior to act as mixing drum 33% of total length and nodulizing of sinter mix remaining 67% of total length. MND rotates at speed of 5.5 RPM.

2.1 Sampling

A large quantity of base mix sample (before MND) was collected from conveyor belt (cutting across the breadth of conveyor belt at 6 different points) before the mixing & nodulizing drum from sinter plant 3 at authors' works. These samples were taken

Table 1 Raw materials used for making base mix

Raw material	Iron ore fines	Flux materials	Solid wastes	Solid fuels	Return fines
%	58.9	13.0	8.8	3.1	15.5

before the trimming addition of calcined lime. Raw materials used for making base mix are given in Table 1. Similar way green mix samples (after MND) were collected from conveyor belt after the mixing and nodulizing drum.

Quantity of base mix sample was reduced by riffle divider to get samples for moisture, size spectrum and chemical analyses. Moisture content of base mix sample was determined by drying it till constant weight in an air oven maintained at 200 °C. Size spectrum analysis was carried out by sieve shaker using 10, 5, 3.15, 1, 0.25 and 0.15 mm opening sieves. Chemical analyses of base mix were conducted by using Inductively Coupled Plasma Spectrometry (ICP) method. Loss on ignition of base mix sample was determined in a muffle furnace. Carbon content of sample was measured by Leco CS200.

2.2   Drying Time Temperature Curves for Base Mix and Green Mix

Drying time temperature curve for base mix was prepared by taking 500 gm of sample from any one base mix sample with the help of riffle divider collected before mixing and nodulizing drum. In case of green mix, 500 gm sample was taken from green mix samples collected after the mixing and nodulizing drum. The selected 500 gm sample was put in a microwave oven and heated at 100 ± 5 °C for 1 min. Sample was taken out and weight loss occurred in 1 min was calculated by weighing it in an electronic balance. This step gives moisture removed from sample in 1 min. Again, sample was put back in oven and heated for 1 min in 100 ± 5 °C and weight loss occurred in 1 min is calculated. These steps were repeated until the moisture removed during particular drying step was less than 5% of moisture removed during the first minute. Data of moisture removed in each minute were tabulated. Cumulative time of drying verses percentage moisture in the base/green mix was plotted. The plot was used as a reference to estimate the time required to dry the sample up to 3% moisture level.

2.3   Determination of Granulation Index (GI) of Green Mix

From the preserved base mix sample (before MND), 500 gm was taken with the help of riffle divider. Sample was put in microwave oven and heated at 100 ± 5 °C for the time (T1) required (calculated earlier in drying time temperature curve for base mix)

to bring down moisture content to $3.0 \pm 5\%$ in sample. Sample was then removed from oven and screened for one minute using the 1ow tap (sieve size 10, 5, 2, 1, 0.5, 0.25 mm). Weights of different fractions of screened materials were measured (by putting the fines adhered to the back side of the screen into the screen of the succeeding grade).

In the same manner, 500 gm samples from various prepared green mix samples (after NMD) were taken and dried in oven to get $3.0 \pm 5\%$ moisture in sample for the time (T2) (time T2 required to get 3% moisture were already calculated in drying time temperature curve for these green mix samples). After drying samples were screened for one minute using the low tap (sieve size 10, 5, 2, 1, 0.5, 0.25 mm). Weights of different fractions of screened materials were measured (by putting the fines adhered to the back side of the screen into the screen of the succeeding grade).

Granulation index (GI) of green mix was calculated using the following formula:

$$GI_{0.25} = \frac{W_a - W_b}{W_a} \times 100$$

where,

W_a weight of -0.25 mm particles in the base mix (before MND)
W_b weight of -0.25 mm particles in the green mix (after MND)

$$GI_{0.50} = \frac{W_c - W_d}{W_c} \times 100$$

where,

W_c weight of -0.50 mm particles in the base mix (before MND)
W_d weight of -0.50 mm particles in the green mix (after MND)

2.4 Installation of Variable-Voltage/variable-Frequency (VVVF) Drive in MND at SP3

At SP3, MND runs at constant motor RPM 1400. To optimize the motor speed to get maximum output from MND in terms of increase in granulation index and reduce electrical power energy, variable-voltage/variable-frequency (VVVF) drive was installed in MND HT motor at SP3. MND motor rpm reduced in steps of 25 rpm from 1400 to 1250.

2.5 Measurement of Reduction Degradation Index (RDI) and Tumbler Index (TI) of Product Sinter

Sinter samples were collected from auto sampler fitted on conveyor belt used for dispatching product sinter to blast furnaces. Sinter sample quantity was reduced with help of riffle divider and final samples were taken to laboratory for RDI, TI and other analysis on product sinter. For RDI, 10–15 mm sample was selected and dried in air oven at 105 °C for 2 h. After drying, 500 gm sample was put in RDI Testing Furnace and temperature of furnace increased to 550 °C under N_2 gas flow. At 550 °C, (CO: 30% + N_2: 70%) gas passed at 15 L/minute through the RDI sample for 30 min. After cooling in N_2 atmosphere, RDI sample is rotated at 30 RPM for 900 revolutions in small RDI drum having length 200 mm and diameter 130 mm fitted with lifter of 5 mm. After rotation of RDI sample in RDI drum, sample is sieved in 3.15 mm sieve and −3.15 mm weight fraction reported as sinter RDI in percentage. Determination of Tumbler Index of product sinter was carried out by IS 6495 (1984).

3 Results and Discussion

Moisture and chemical analyses of raw materials used for base mix is given in Table 2. Size spectrum and chemical analysis of collected sinter base mix samples are shown in Tables 3 and 4 respectively. The Drying time temperature curves for base mix and green mix samples are depicted in Fig. 1. In these curves, T1 and T2 are the time required to heat the fresh samples of base mix and green mix respectively at 100 ± 5 °C in micro wave oven to reduce the moisture content to approximately 3% level.

Trial started with installed variable-voltage/variable-frequency (VVVF) drive from 10th April 2020. MND HT motor rpm reduced in steps of 25 rpm from 1400 to 1250. Initially, MND RPM reduced from 1400 to 1375 and process parameters were monitored. Gradually RPM reduced to 1250 till 29th April 2020. Electrical power consumption in kWh and granulation index (GI) with reduced level of MND motor speed were monitored and tabulated in Table 5.

Reduction in MND HT motor RPM with the help of variable-voltage/variable-frequency (VVVF) drive is shown in Fig. 2. Granulation index (0.25) and (0.50) measured over long period before and after installation of variable-voltage/variable-frequency (VVVF) drive in MND motor at SP3 are depicted in Figs. 3 and 4 respectively. Increase in sinter production enabled by increase in granulation index of sinter mix due to lowering of MND motor RPM is presented in Fig. 5. Reduction in electrical power consumption for MND is shown in Fig. 6. Improvement in sinter reduction degradation index (RDI) and Tumbler Index (TI) is represented in Figs. 7 and 8 respectively.

From Figs. 3 and 4 it can be observed that granulation index (GI) of sinter mix improved from 72–74 to 75–79% in case of GI (0.25) and it has improved from

Table 2 Raw materials used for making base mix

Raw materials	(%) Qty	(%) Silica	(%) CAO	(%) PHOS	(%) MGO	(%) Alumina	(%) C	(%) LOI	(%) Moisture
1. Iron ore fine	58.90	2.52	0.08	0.090	0.04	2.47	0.00	2.61	7.48
1a. IRON_ORE_JODA_FINES_DIRECT	28.40	2.22	0.08	0.100	0.02	2.45	0.00	2.86	7.56
1b. _ORE_JODA_FINES_RECLAIMED	5.80	2.26	0.08	0.100	0.06	2.42	0.00	3.35	8.44
1c. IRON_ORE_NOA_FINES_DIRECT	24.70	2.93	0.08	0.070	0.05	2.52	0.00	2.15	7.16
2. Flux	13.00	7.81	38.81	0.000	10.81	0.53	0.00	37.95	0.00
2a. Dolomite	3.20	4.55	29.77	0.010	20.16	0.73	0.00	43.48	0.00
2b. Lime stone	7.70	1.64	52.61	0.000	0.52	0.41	0.00	42.68	0.00
2c. Pyroxenite	2.20	34.05	3.80	0.010	33.15	0.63	0.00	13.44	0.00
3. Revert	8.80	5.13	13.51	0.350	1.61	1.80	9.37	5.39	9.29
3a. LD slag	1.30	12.40	51.83	1.580	5.39	0.92	0.00	0.00	0.00
3b. Processed solid wastes	7.40	3.81	6.54	0.120	0.92	1.96	11.07	6.38	10.98
4. Solid fuel	3.10	9.40	1.13	0.100	0.30	4.69	79.71	0.00	8.25
4a. Coke breeze	3.10	9.40	1.13	0.100	0.30	4.69	79.71	0.00	8.25
5. Return fines	15.50	4.90	12.59	0.100	2.29	2.42	0.00	0.00	0.00
5a. Sinter return	15.50	4.90	12.59	0.100	2.29	2.42	0.00	0.00	0.00
6. End cone	0.70	4.12	8.13	0.110	1.92	2.32	3.37	6.85	5.49
6a. END_CONE	0.70	4.12	8.13	0.110	1.92	2.32	3.37	6.85	5.49
Cumulative Base Mix Chem	**100.00**	**4.04**	**8.33**	**0.100**	**1.95**	**2.22**	**3.35**	**7.01**	**5.52**
Cumulative Sinter Chem (Without Trimming)		**4.39**	**9.34**	**0.109**	**2.19**	**2.35**	**3.68**		
Sinter Chem (Cumulative + Recomendation)		**4.40**	**9.32**	**0.110**	**2.19**	**2.37**	**3.70**		

Table 3 Size spectrum of base mix

Size analysis	−0.15 MM	+0.25 MM	+0.15 MM	+1.0 MM	+3.15 MM	+8 MM	+10 MM
%	6.3	25.6	4.4	26.2	28.2	4.7	4.5

62–69% to 70–74% in case of GI (0.5). This improvement in GI is attributed to increase in retention time of sinter mix in MND. Higher retention time of sinter mix in MND due to lowering of NMD motor RPM facilitated better nodulizing of sinter mix which resulted in improvement in GI. Higher GI of sinter mix helped to achieve higher sinter production ~50 ton/shift as shown in Fig. 5. This higher sinter production was realized, despite of operating with lower calcined lime trimming (1%) against average of 1.5% throughout the trial period. Increase in sinter production was enabled by better sinter bed permeability due to increase in sinter feed mix GI. Higher sinter bed permeability allows faster rate of sintering and higher sinter production rate. Increase in sinter plant productivity attained was approximately 1 t/m^2/day. In Fig. 6, it can be seen that lowering the speed of HT motor of MND facilitated reduction of electrical power consumption by ~150 kWh / Shift. As bed permeability improved with increase in sinter mix GI, waste gas fan RPM reduced from 930 to 900 which also runs with help of HT motor. This further contributed in reducing the overall electrical power consumption in sinter making. From Figs. 7 and 8, it can be observed that with increase in sinter mix GI due to reduction in MND motor speed helped in maintaining and improving the product sinter quality like RDI & TI as per blast furnaces' (customers') requirements. Better product sinter quality was achieved because of homogeneous and complete sintering due to improved sinter bed permeability.

4 Conclusions

In an attempt to reduce the electrical power consumption in sinter making by improving granulation of sinter feed mix, a variable-voltage/variable-frequency (VVVF) drive installed in MND at SP3 and experiments were conducted with reduced MND motor RPM to improve GI and saving of electrical power energy. Experiments were conducted in a running sinter plant. Following conclusions could be made from the present work:

- Granulation of sinter feed mix improves with optimization of MND motor RPM.
- With higher sinter feed mix Granulation Index (GI), sinter production and productivity was increased.
- Lowering of MND motor RPM resulted in reduction of electrical power consumption.
- Product sinter quality was maintained as per the requirements of blast furnaces.

Table 4 Chemical analysis of base mix

Chemical Analysis	Fe(T)	FeO	CaO	SiO_2	S	MgO	MnO	Al_2O_3	TiO_2	Cr_2O_3	K_2O	LOI	Na_2O	C	P
%	50.6	3.3	8.34	4.76	0.03	1.86	0.06	2.50	0.16	0.01	0.06	10.15	0.02	4.27	0.07
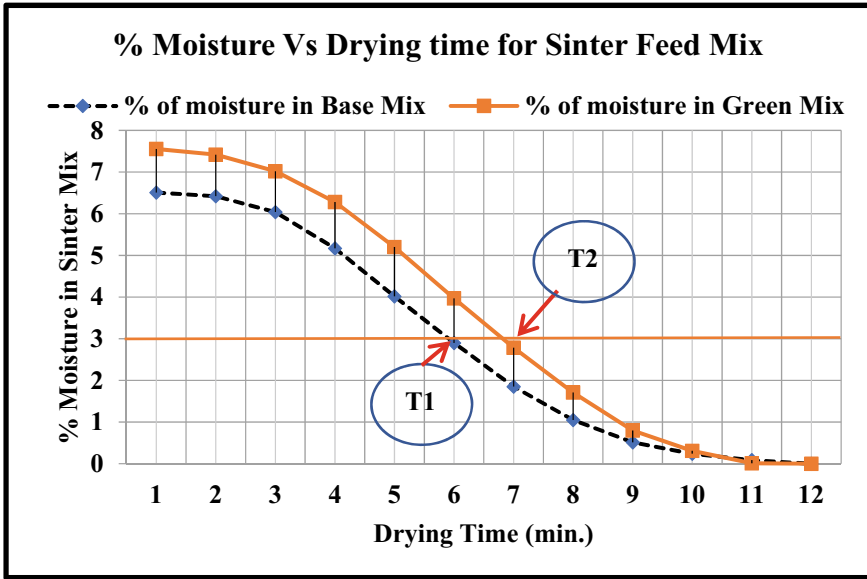
Fig. 1 Drying time temperature curve for base mix (before MND) and green mix (after MND)

Table 5 Electrical power consumption in kWh and granulation index (GI) with reduced level of MND motor speed

Date	Shift (8 hr)	MND RPM	Production rate (tonnes per shift)	MND kWh (Shift AVG)	GI_0.25	GI_0.50
10.04.20	Base	1400	2700	190.5	73.53	67.95
10.04.20	A	1375	2710	185.2		
10.04.20	B	1350	2720	183.7		
10.04.20	C	1350	2720	185.8		
11.04.20	A	1350	2720	188.4	74.63	68.85
11.04.20	B	1350	2740	185.8		
11.04.20	C	1350	2730	182.3		
12.04.20	A	1350	2750	183.1		
12.04.20	B	1350	2720	185.2		
12.04.20	C	1350	2750	186.5		
13.04.20	A	1350	2800	187	74.89	69.57
13.04.20	B	1325	2850	189.05		
13.04.20	C	1325	2750	181.69		

Table 5 (continued)

Date	Shift (8 hr)	MND RPM	Production rate (tonnes per shift)	MND kWh (Shift AVG)	GI_0.25	GI_0.50
14.04.20	A	1325	2850	185.06	76.93	70.14
14.04.20	B	1325	2750	184.79		
14.04.20	C	1325	2800	181.69		
15.04.20	A	1325	2800	180.29		
15.04.20	B	1325	2800	182.54		
15.04.20	C	1325	2800	183.21		
16.04.20	A	1325	2775	175.25	77.69	70.77
16.04.20	B	1300	2800	177.95		
16.04.20	C	1300	2775	182.72		
17.04.20	A	1300	2800	180.96	77.41	70.26
17.04.20	B	1300	2675	168.12		
17.04.20	C	1300	2800	179.05		
18.04.20	A	1300	2800	180.13		
18.04.20	B	1300	2800	180.36		
18.04.20	C	1300	2800	180.63		
19.04.20	A	1300	2850	183.47		
19.04.20	B	1300	2850	183.75		
19.04.20	C	1300	2800	181.86		
20.04.20	A	1300	2850	182.28	79.33	73.22
20.04.20	B	1300	2850	179.27		
20.04.20	C	1300	2700	174.08		
21.04.20	A	1300	2800	175.94		
21.04.20	B	1300	2750	171.8		
21.04.20	C	1300	2800	178.81		
22.04.20	A	1300	2750	178.95	78.94	72.43
22.04.20	B	1300	2800	181.57		
22.04.20	C	1300	2850	181.08		
23.04.20	A	1300	2800	178.86	78.25	73.17
23.04.20	B	1300	2820	173.73		
23.04.20	C	1300	2850	174		
24.04.20	A	1300	2700	171.53		
24.04.20	B	1300	2750	171.75		
24.04.20	C	1300	2850	170.79		
25.04.20	A	1275	2800	173.26	77.21	71.31
25.04.20	B	1275	2800	171.8		

Table 5 (continued)

Date	Shift (8 hr)	MND RPM	Production rate (tonnes per shift)	MND kWh (Shift AVG)	GI_0.25	GI_0.50
25.04.20	C	1275	2850	172		
26.04.20	A	1275	2800	171.77	78.40	71.48
26.04.20	B	1275	2850	170		
26.04.20	C	1275	2820	170.53		
27.04.20	A	1250	2850	169.04		
27.04.20	B	1250	2830	169.5		
27.04.20	C	1250	2865	169.5		
28.04.20	A	1250	2850	169.85	76.59	71.58
28.04.20	B	1250	2900	170		
28.04.20	C	1250	2850	169.9		
29.04.20	A	1250	2850	169.8	79.66	73.98
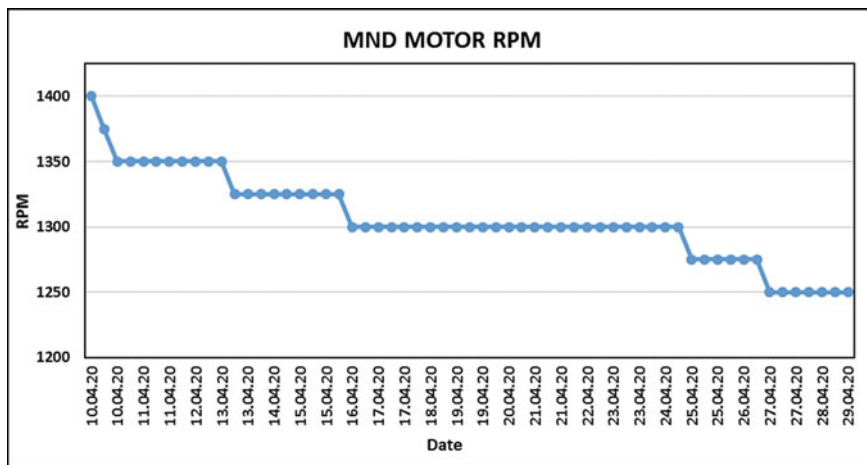
Fig. 2   Reduction in MND motor RPM with the help of VVVF drive
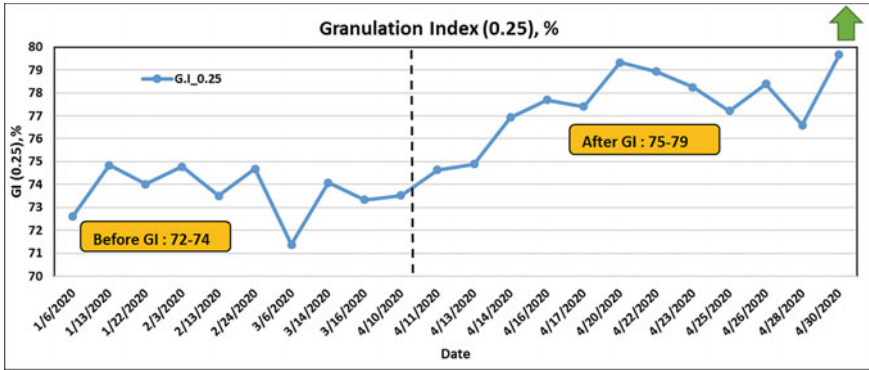
Fig. 3 Granulation index (0.25) before and after installation of (VVVF) drive
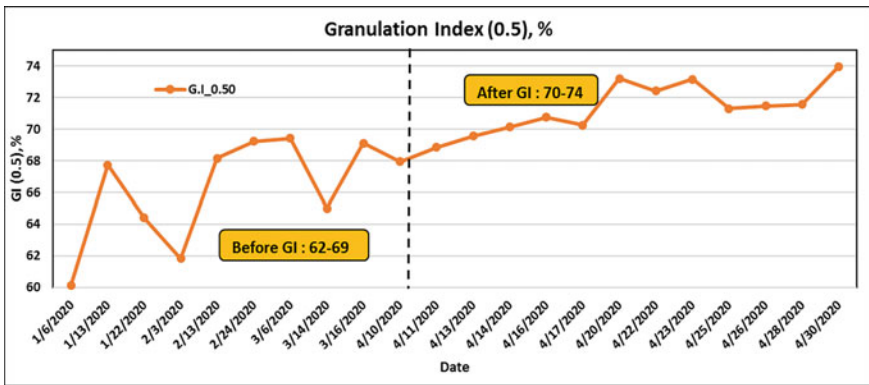
Fig. 4 Granulation index (0.5) before and after installation of (VVVF) drive
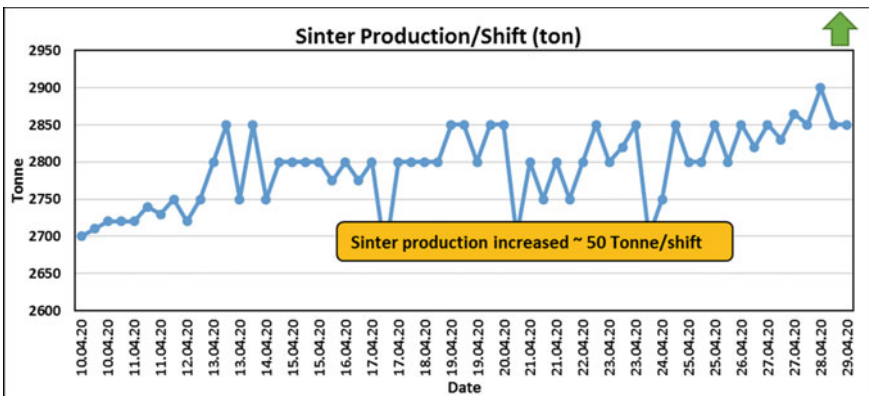
Fig. 5 Increase in sinter production enabled by increase in GI of sinter mix
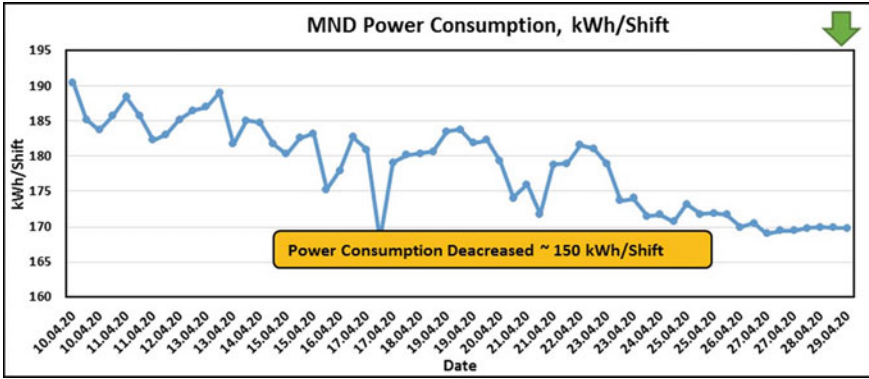
Fig. 6 Reduction in electrical power consumption for MND
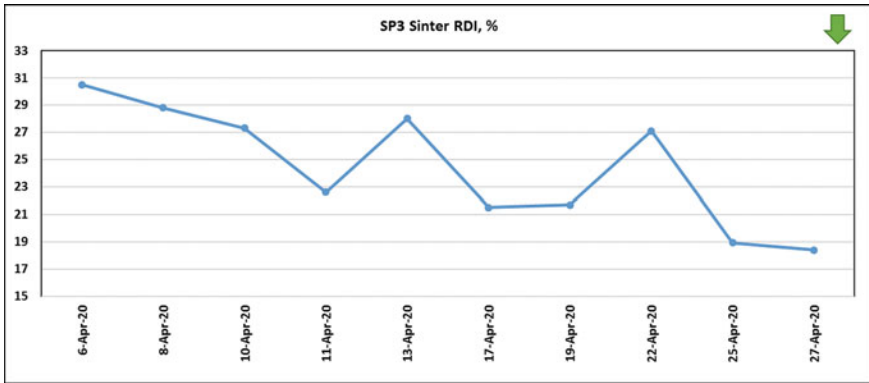
Fig. 7 Improvement in sinter reduction degradation index (RDI)
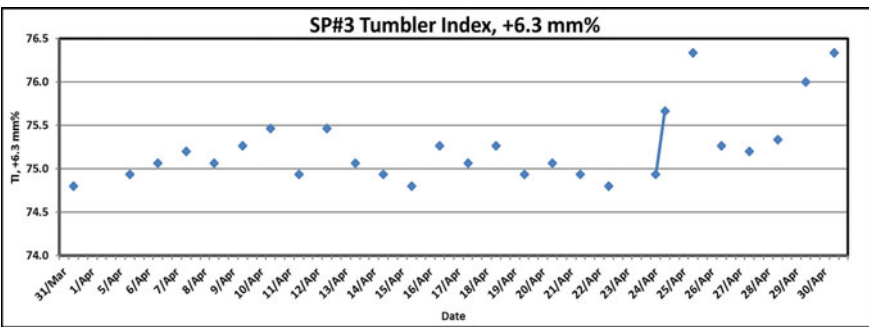
Fig. 8 Improvement in sinter Tumbler Index (TI)

References

1. Energy Statistics (2020) by National statistical office, ministry of statistics and programme implementation, Government of India, New Delhi. http://www.mospi.gov.in/sites/default/files/publication_reports/ES_2020_240420m.pdf. Downloaded on 13/07/20
2. Cheng Z, Tan Z, Guo Z, Yang J, Wang Q (2020) Recent progress in sustainable and energy-efficient technologies for sinter production in the iron and steel industry. Renew Sustain Energ Rev 131(2020):110034, 1–16
3. Fernández-González D, Piñuela-Noval J, Verdeja LF, Iron ore agglomeration technologies provisional chapter iron ore agglomeration technologies. https://doi.org/10.5772/intechopen.72546
4. Furui T, Sugawara K, Kagawa M, Uno S, Kawazu S, Fugiwara T, Sawamura A (1977) Nippon Steel Tech. Rept Overseas 10:36
5. Hida Y, Sasaki M, Sato K, Kagawa M, Miyazaki T, Soma H, Naito H, Taniguchi M (1987) Nippon Steel Tech. Rep Overseas 35:59–67
6. Wu S, Kasai E, Omori Y (Oct 1990) In: 6th International iron and steel cong. proceeding, nagoya, iron and steel institute of Japan (Japan), pp 15–22
7. Fernández-González D, Ruiz-Bustinza I, Mochón J, González-Gasca C, Verdeja LF (2017) Iron ore sintering: raw materials and granulation. Miner Process Extr Metall Rev 38(1):36–46. https://doi.org/10.1080/08827508.2016.124459
8. Loo CE (1998) In: ISS iron making conference proceedings vol 57, pp 1299–1316

Investigation of the Selective Oxidation Process for High Strength Steels

Suman Sadhu, Anindita Chakraborty, Shiv Brat Singh, and Arup Kumar Halder

1   Introduction

Advanced high strength steels (AHSS) are being used widely owing to their superior combination of strength and formability. Combinations of this properties are obtained by adding various alloying elements like aluminium, manganese, chromium, silicon etc. However, the corrosion property is of equal importance. A protective Zn coating has been applied on to the surface by continuous Hot-Dip Galvanizing Process, in order to protect AHSS from corrosion [1]. So, the challenge is not only to produce AHSS having high strength and superior ductility, but also to protect it from corrosion by applying Zn coating on it.

Before entering into the molten Zn bath, the steel strips are passed through annealing furnace to obtain desired final microstructure. The furnace section consists of 1. Direct Fired Furnace (DFF), 2. Radiant Tube Furnace (RTF) and 3. Jet Cooled furnace (JCF). In the direct fired furnace, the sample is rapidly heated up to 650 °**C** followed by annealing at radiant tube furnace at the temperature range of 750–820 °**C**. Then cooled to 460 °**C** prior to dipping into the molten Zn bath. Generally, the annealing atmosphere used for many commercial units is 5% H_2 + N_2 with -30 °**C** dew point [2]. This atmosphere is reducing for iron but oxidizing for the other alloying elements (Mn, Si, Cr, Al etc.) that are present in AHSS. Those alloying elements, will be oxidised to form different oxides (MnO, SiO_2, Cr_2O_3, $MnAl_2O_4$, $MnCr_2O_4$ etc.). This phenomenon is called selective oxidation. The oxides cover the surface of the steels, resulting in poor wetting ability with molten Zn. Therefore, adhesion of molten Zn with the substrate reduces, causing bare spot formation on the galvanised sample [2–4]. In order to achieve better adhesion, the surface is oxidised at first to form FeO layer on the top surface. Oxides of other alloying elements are

S. Sadhu (✉) · S. B. Singh
Department of Metallurgical and Material Engineering, IIT Kharagpur, Kharagpur, India

A. Chakraborty · A. K. Halder
Research and Development, Tata Steel Limited, Jamshedpur, India

embedded within the FeO layer or lie under the FeO layer. In the next step, the FeO is reduced in a reducing atmosphere to form pure Fe layer on the surface.

A number of researches has been done on the selective oxidation to understand the influence of alloying elements and oxidation atmosphere. Liu et al. [5] and Maderthaner et al. [6] showed the effect of dew point on the sub surface segregation of alloying elements, oxide morphology. Influence of alloying elements and annealing temperature on selective oxidation has been reported by I. Olefjord et al. [7] and Swaminathan et al. [8]. First theoretical model of internal oxidation has been developed by Wagner [9]. However, it is limited for binary alloys and oxidation in single oxidant only. Based on Wagner model a number of extended solutions has been proposed by Huin et al. [10], Whittle et al. [11] and Rapp [12]. These works used analytical solutions to solve the problem.

In this present work, the focus is on developing a numerical model to simultaneously simulate the diffusion of the chemical species and precipitation of the oxide in the steel matrix. The depth of Internal Oxidation Zone (IOZ) has been obtained as a function of the furnace atmosphere, annealing temperature and the alloy composition so that it would be possible to choose the suitable annealing atmosphere for different alloy compositions without doing extensive trial and error type experiment. Also a few sets of TGA experiment has been done for Fe-1.58 wt.% Mn in order to know the Wustite formation kinetics. The composition is so selected that it covers the Mn composition range that is typically used from steels with 600–1200 MPa steels in general.

2 Numerical Model of Oxide Formation Kinetics

A 1 D implicit has been developed which will simulate simultaneous diffusion of chemical species and precipitation of oxides (as shown in Fig. 1). Concentration profile of the alloying element from surface to the bulk has been obtain as a function of dew point, furnace atmosphere, furnace temperature and alloy composition. This model is based on few assumptions: 1. Fe, which provides the matrix phase is

Fig. 1 Schematic diagram of elementary volume
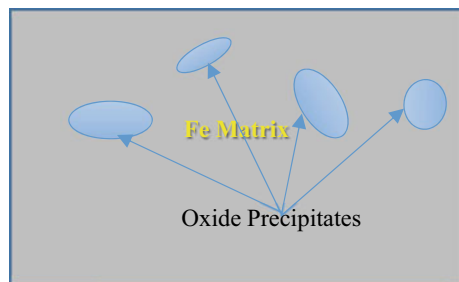
considered as a noble metal, and it won't combine with other chemical species, 2. Sufficiently large elementary volume has been considered which will contain both matrix and precipitate phase, 3. Only local thermodynamic equilibrium has been considered.

2.1 Numerical Algorithm and Boundary Condition

A total domain length of 1 μm has been considered which is then discretise into 101 grid points. During the simulation the steel surface will be in contact with the annealing atmosphere at a constant dew point. It is assumed that on the surface oxygen and the steel substrate are in local equilibrium and the dissolve oxygen concentration of the surface will remain constant (for isothermal annealing) during the whole iteration.

X_o represent the surface nodes and X_n is the node which lie inside the sample in between nodes are termed as X_i (where i = 0, 1, 2,……) (as shown in Fig. 2). And the distance between consecutive grid point is termed as ΔX (=X_{i+1}-X_i). For sake of simplicity this distance is considered to be identical here. In practise, to obtain more accurate distribution of concentration profile the mesh is refined near the surface.

It is assumed that at the nth node (X_n, the node lies deep inside the sheet) the concentration of oxygen and the alloying element is fixed, so boundary condition at nth grid point we have

$$C_0(X_n) = 0; \quad and \quad C_i(X_n) = C_i^{Core}$$

where subscript "o" denotes the oxidising elements (i.e. oxygen) and subscript "i" represents the alloying element (like Mn, Si, Cr, Al etc.). C_i^{Core} define the concentration of the oxidizable element at the core or nth grid point which is equals to the bulk composition of that element with in that steel grade. As oxygen concentration is zero at nth grid point, so, there is no precipitates forming, so $P_\alpha(X_n) = 0$. Where, P_α is the mass fraction of the precipitate α. And total concentration of the oxidizable
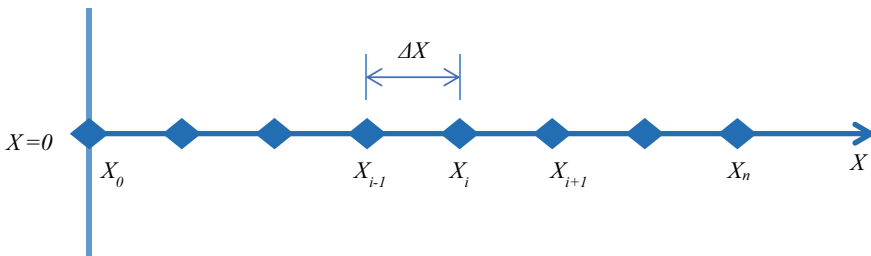
Fig. 2 Discretisation of 1dimensional space

element $W_i(X_n)$ is equal to the dissolve concentration of that element at that grid point [i.e., $W_i(X_n) = C_i(X_n)$].

At the surface node, the dissolve concentration of the oxygen is given by the equilibrium partial pressure of oxygen at the furnace atmosphere. And for isothermal annealing which is assumed to be constant during the whole annealing process. And it is assumed that there is no outward flux of the oxidizable elements through the surface node. So, the boundary condition for X_0 grid point (i.e., the surface grid point) are

$$C_0(X_n) = C_0^{Surf}; \quad and \quad \left(\frac{\partial C_i}{\partial x}\right)_{x_0} = 0$$

2.2 Numerical Solution

Solution of the above model requires **1.** Consideration of local thermodynamic equilibrium at each grid point, **2.** Mass balance and **3.** Generating discretise equation for diffusion at eacgripnt a solving them numerically using implicit scheme.

Thermodynamic Equilibrium. The condition for the precipitation depends on the solubility product equation i.e.

$$\prod_{i=1}^{n} C_i^{N_{i\alpha}} \geq k_\alpha^{S_P} \tag{1}$$

where,

C_i is the dissolve concentration of the oxidizable eminent, $N^{i\alpha}$ is the stoichiometric coefficient of element i in the precipitate phase (α). And n is the number of element present with in the oxide phase, K_α^{sp} denotes the solubility product of the precipitate phase.

So, when the multiplication of the dissolve concentration raised to the power of stoichiometric ratio of the element present in the precipitates is less then K_α^{sp}, then no precipitate will form ($P_\alpha = 0$).

Mass Balance. Total number of atoms of an element can be equated with the summation of the number of elements presents in all their possible form, such as dissolve in the matrix or embedded in the precipitate phase.

If total mass fraction of the element i is denoted as.

W_i and their molar mass is denoted by.

M_i then the mass balance equation can be written as.

$$\frac{W_i}{M_i} = \frac{C_i}{M_i} + \sum_{\alpha=1}^{n\alpha} N_{i\alpha} \frac{P_\alpha}{M_\alpha} \tag{2}$$

where, M_α is the molar mass of the precipitate phase α and n_α is the number of precipitate phase, and P_α is the fraction of the precipitate phase α.

Combining the Eqs. (1) and (2) one can get a polynomial equation of P_α which then can be solved using Newton Raphson method to obtain equilibrium amount of precipitate that will form at each grid point for that time step.

Discretise Equation for Diffusion. Fick's second law is used as governing equation for generating discretise equation for the diffusion.

$$\frac{\partial C}{\partial t} = D\frac{\partial^2 C}{\partial x^2} \tag{3}$$

Equation (3) is then discretised by applying Taylor's theorem and we obtain

$$\frac{C_i^n - C_i^{n-1}}{\Delta t} = Di\left[\frac{C_{i-1}^n - 2C_i^n + C_{i+1}^n}{(\Delta x)^2}\right] \tag{4}$$

where, superscript n denotes the present time step and Di is the diffusivity of the element i. Although there is no limitation on selecting time step as the algorithm is implicit, but for better accuracy small time step ($\sim 10^{-5}$ s) is used.

Further expansion of Eq. (4) gives the discretise equation for i^{th} grid point (where $i = 1, 2, 3, \ldots$).

$$C_i^n - C_i^{n-1} = \frac{Di \times \Delta t}{(\Delta x)^2}\left[C_{i-1}^n - 2C_i^n + C_{i+1}^n\right]$$

$$C_i^n - C_i^{n-1} = \lambda \times C_{i+1}^n - 2 \times \lambda \times C_i^n + \lambda \times C_{i-1}^n \text{ taking,}$$

$$\lambda = \frac{Di \times \Delta t}{(\Delta x)^2}$$
$$-\lambda C_{i-1}^n + (1 + 2\lambda)C_i^n - \lambda C_{i+1}^n = C_i^{n-1}$$

Discretise equation for boundary grid point also be obtain by applying the above-mentioned boundary condition. All the discretise equation obtained for each element (for oxidant and for oxidizable elements) are then solve by Tridiagonal Matrix Algorithm (TDMA) solver.

3 Experiment

Fe-1.58 wt.% Mn alloy has been melted in induction melting furnace followed by hot and cold rolling. Both side of the steel sheet is first polished up to 4000 grade emery paper followed by diamond polishing. After polishing the sheet was cut into small pieces having 50–100 mg weight. After that thermogravimetric analysis has been

done to understand Wustite formation kinetics for those sample at three different oxidising temperature, which has been maintained by maintaining CO_2/CO ratio 1,2 and 3 in the furnace. For each oxidizing atmosphere the samples were first heated to three different peak temperatures (650 °C, 750 °C and 850 °C) with heating rate of 15 K/min. then the samples were hold at the peak temperatures for 2 h. And then finally cooled down to the room temperature with cooling rate of 15 K/min. During heating and cooling only Ar gas (40 ml/min) was purged and during holding period CO_2 and CO gas mixture was purged along with Ar. The gas mixture of Ar + CO + CO_2 is used to simulate the industrial atmosphere. As the oxygen required is very less and is difficult to control precisely that level of partial pressure of oxygen during experiment, so only O_2 is not used here as oxidising atmosphere.

4   Results and Discussions

4.1   Simulation Results

Isothermal Annealing (Binary Alloy). The isothermal annealing of Fe-1.58 wt.% Mn steel at isothermal holding temperature of 800 °C for 90 s at dew point of −40 °C has been considered, which involves diffusion of Mn and O to form MnO. 5%H_2 + 95% N_2 was used as furnace atmosphere during the whole annealing treatment.

The equilibrium partial pressure of oxygen and C_o^{Surf} values corresponding to the above-mentioned condition was calculated as following. Initially the partial pressure of the saturated water vapour in the furnace $\left(p_{sat}^{H_2O} \right)$ is calculated by the data provided by thermodata bank [13].

$$\log_{10} p_{sat}^{H_2O} = \frac{9.80DP}{273.8+DP} - 2.22 \text{ Dew Point (DP)} \leq 0\,°C$$
$$\log_{10} p_{sat}^{H_2O} = \frac{7.58DP}{240+DP} - 2.22 \text{ Dew Point (DP)} > 0\,°C$$

The equilibrium partial pressure of oxygen is then calculated by the relation provided by Rist et al. [14]. Where,

p_{H_2} is the partial pressure of H_2 in the furnace.

$$\log_{10} p_{O_2} = 6.0 - 26176/T + 2\log \frac{p_{Sat}^{H_2O}}{p_{H_2}}$$

Finally, the dissolve mass fraction of oxygen at the surface is given by Swisher and Turkdogan's [15] formula.

$$log_{10}C_0^{Surf} = 1.0 - 9398/T + 1/2log\ pO_2$$
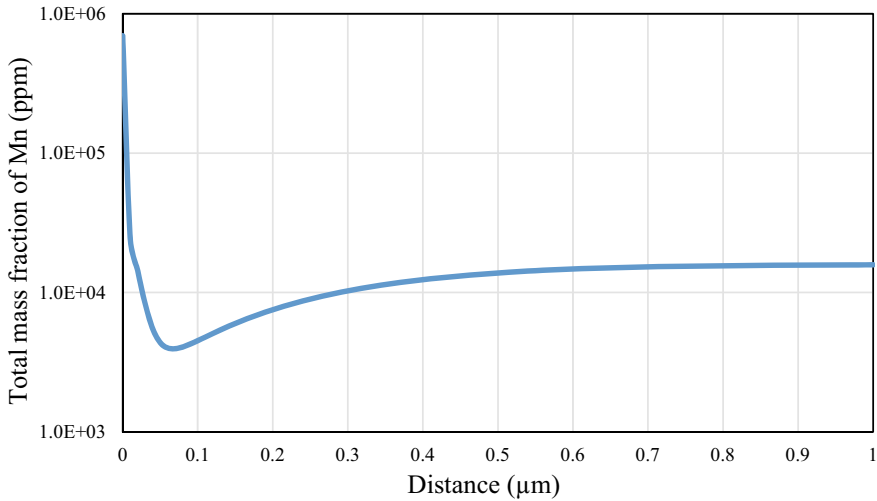
Fig. 3 Concentration profile of total mass fraction of Mn (isothermal annealing, precipitation of MnO)

Diffusion coefficient of the elements (in $\mu m^2 s^{-1}$) are obtained from the following formula taken from Oikawa et al. [16]**.** Where T is in K.

$$D_O = 2.44 \times 10^5 exp(-11078/T)$$
$$D_{Mn} = 7.56 \times 10^7 exp(-26983/T)$$
$$D_{Si} = 7.35 \times 10^7 exp(-26439/T).$$

The values of diffusion coefficients of Mn and O at the above-mentioned temperature are 9.06×10^{-4} $\mu m^2 s^{-1}$ and 8.01 $\mu m^2 s^{-1}$ respectively and $C_o^{Surf} = 9.23 \times 10^{-3}$ ppm. The following profile of total mass fraction of Mn and dissolve mass fraction of oxygen. Depth of Internal Oxidation Zone (IOZ) obtain is 0.41 μm (Figs. 3 and 4).

The same model has been run at different dew point temperature, keeping all other variable same. It has been observed that with increasing dew point the depth of internal oxidation zone increases exponentially and at the same time the total mass fraction of Mn decreases at the surface. This is because of increasing inward flux of oxygen with increasing dew point. Therefore, prone of oxidation of interior grid point increases, which results both in increase of depth of IOZ and decrease of total Mn concentration at the surface. So, to obtain higher depth of IOZ it is more preferable to increase the dew point rather than increasing annealing time. The profile for total mass fraction of Mn at three different dew point has been shown in the Fig. 5. The effect of dew point on the depth of IOZ and total Mn concentration at the surface has been shown in the Fig. 6(a and b) (Table 1).
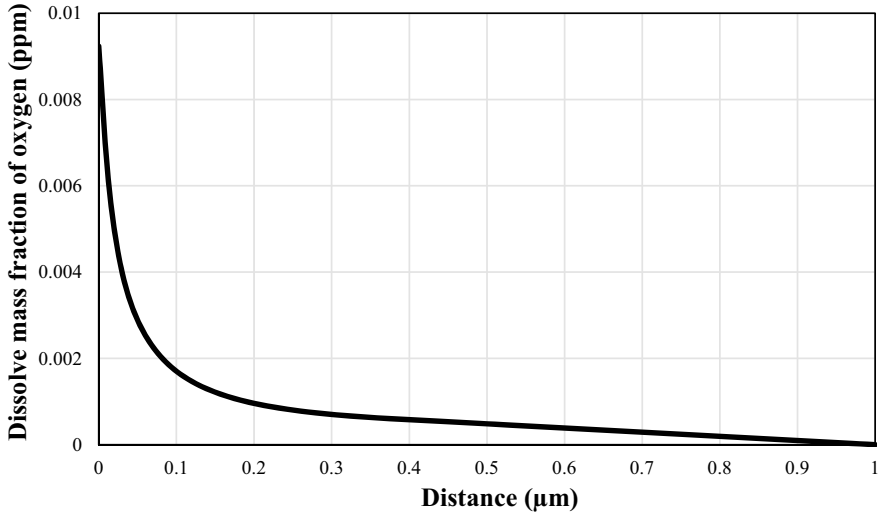
Fig. 4 Concentration profile of dissolve mass fraction of oxygen (isothermal annealing, precipitation of MnO)
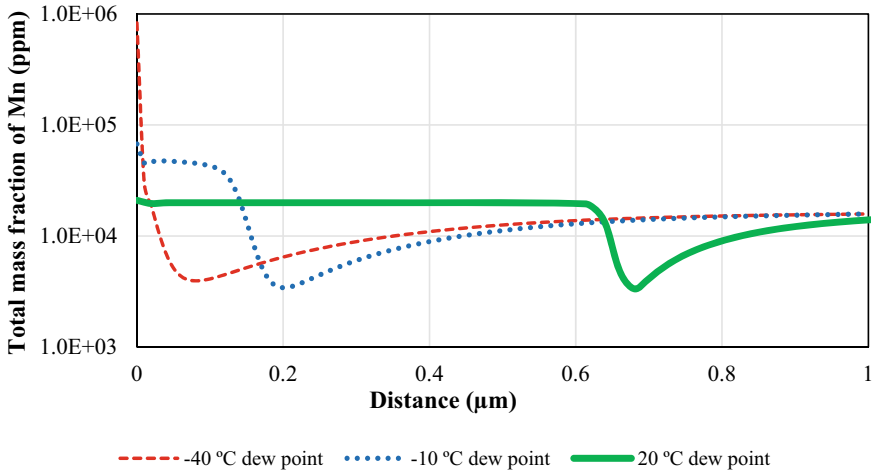
Fig. 5 Total mass fraction of manganese vs distance for isothermal annealing of Fe-1.58 wt.% Mn at 800 °C

Isothermal Annealing (Ternary Alloy). Now the isothermal annealing of a 1.58 wt.% Mn and 0.1 wt.% Si steel, involving diffusion of Mn, Si, and O and precipitation of simple oxide MnO and SiO_2 has been considered. The temperature of the annealing furnace is 800 °C and the dew point is -40 °C. The values of the diffusion coefficients, solubility products of the elements are $D_{Mn} = 9.06 \times 10^{-4}$ $(\mu m)^2/\text{sec}$, $D_{Si} = 1.48 \times 10^{-3}$ $(\mu m)^2/\text{sec}$, $D_O = 8.01 \times 10$ $(\mu m)^2/\text{sec}$, $K_{MnO}^{sp} = 7.19$
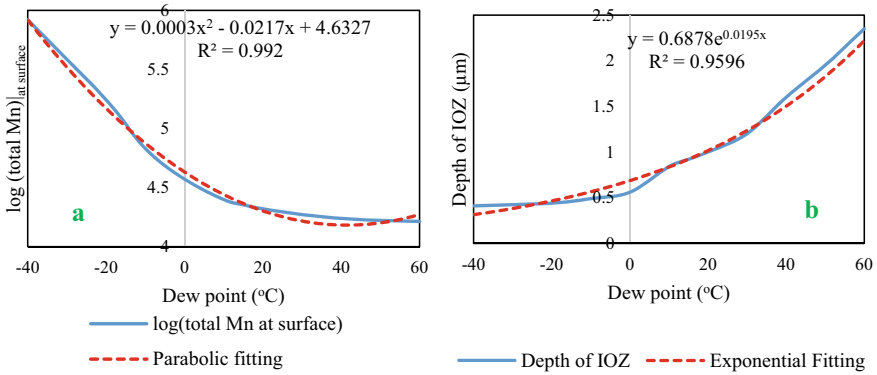
Fig. 6 Effect of dew point on **a** total mass fraction of Mn at the surface, **b** depth of IOZ

Table 1 Variation of depth of IOZ and total mass fraction of Mn at the surface with dew point

Dew Point (°C)	−40	−10	20	40	60
Depth of IOZ (μm)	0.41	0.49	1	1.6	2.35
log (total Mn) $|_{\text{at surface}}$	5.92	4.83	4.32	4.24	4.21

ppm^2, $K_{SiO2} = 3.07 \times 10^{-5}$ ppm^3. As Si has more prone to oxidation as compared to Mn, it has been assumed that SiO$_2$ will form first and then followed by MnO formation (if $C_{Mn} \times C_O > K_{MnO}^{sp}$ satisfy) (Fig. 7).

Due to the large solubility product of MnO precipitation of MnO occur over a much smaller distance than precipitation of SiO$_2$. It has been also observed that enrichment of Si occurs over a large distance whereas precipitation of MnO occur solely at the surface nodes. After surface nodes there is sudden drop of total Mn concentration at the next node.

Anisothermal Annealing. Anisothermal annealing of Fe-1.58 wt.% Mn binary alloy has been considered at annealing temperature of 750 °**C** at two different dew point of + 20 °**C** and + 30 °**C**. Heating cycle is: (i) temperature will continuously rise from 25 °**C** to 750 °**C** at heating rate of 15 K/s, (ii) isothermal holding at 750 °**C** for 90 s and (iii) finally cooled to room temperature from 750 °**C** at a cooling rate of 30 K/s. Total mass fraction of Mn vs distance at different stages of anisothermal annealing of Fe-1.58 wt.% Mn at 750 °**C** temperature and dew point of + 30 °**C** has been plotted on Fig. 8.

As the curves have different minima it is not possible to deduce them from each other by dilation or contraction of space. Mn enrichment at the surface and depletion of Mn concentration observed at the end of heating cycle itself. Depth of depletion and IOZ has been increase at the end of isothermal stages and depletion level increases little more during cooling period. Which suggest that heating and cooling rate will have effect on the final depth of IOZ. The corresponding values of depth of IOZ at each stage are listed below in the table (Table 2).
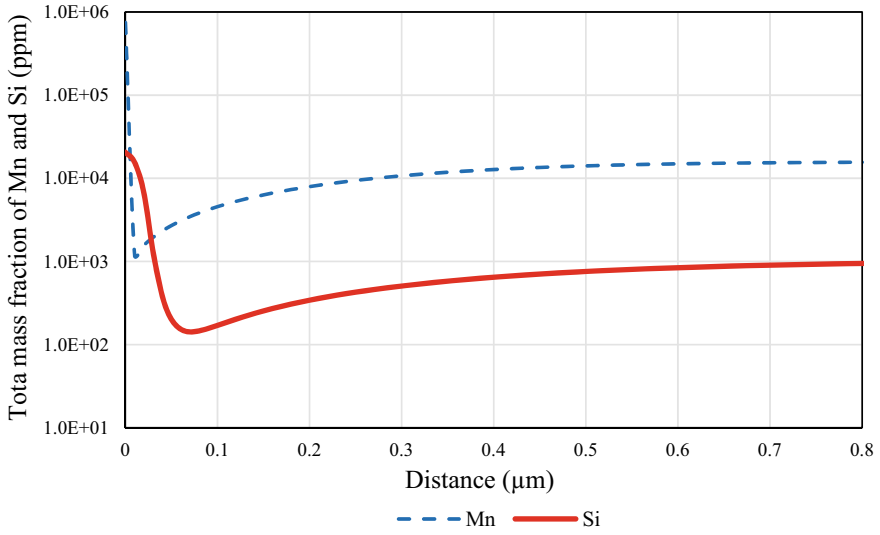
Fig.7 Total mass fraction of Mn and Si for isothermal annealing of Fe-1.58 wt.% Mn-0.1 wt.% Si steel (precipitation of MnO and SiO$_2$)
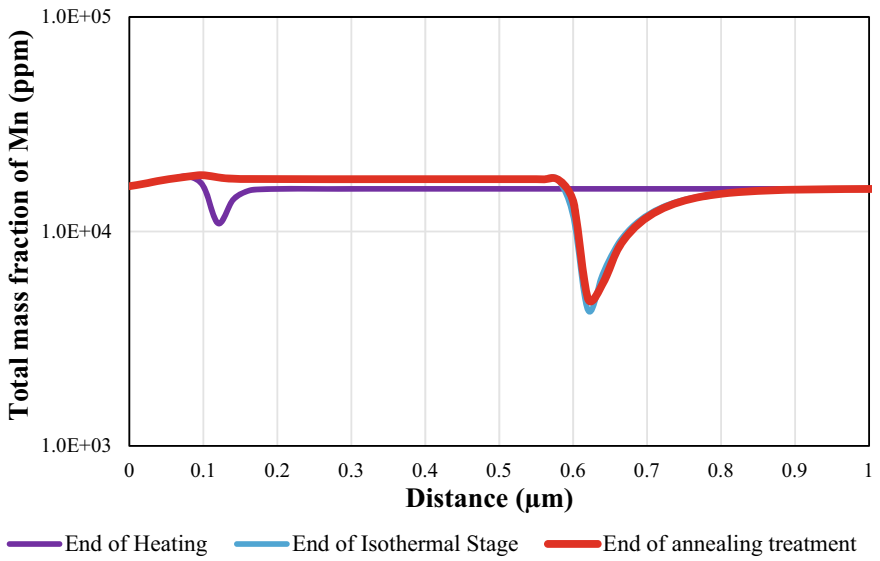
Fig. 8 Anisothermal annealing of Fe-1.58 wt.% Mn, oxidised at 750 °C at dew point of + 30 °C

Table 2 Depth of IOZ at different stages of annealing

Stages of annealing	End of heating	End of isothermal stage	End of annealing treatment
Depth of IOZ (μm)	0.16	0.8	0.84
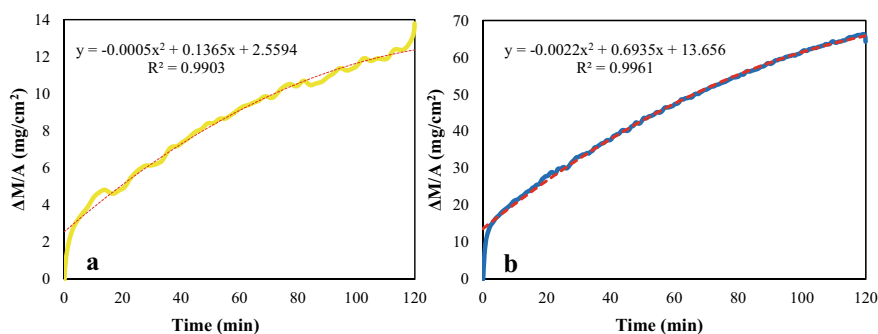
Fig. 9 Weight gains vs time for Fe-1.58 wt.% Mn for oxidation at **a** 750 °C, $CO_2/CO = 2$, **b** 850 °C, $CO_2/CO = 2$

4.2 Oxidation Kinetics

From the TGA plot of the sample oxidised at different oxidising atmosphere and peak temperature, it has been observed that the oxide growth kinetics follows parabolic law. It has been observed that with increasing temperature the curve tends to follow nearly linear path. The weight gains vs time for the holding period of the sample oxidized at 850 °C and 750 °C for CO_2/CO ratio 2 has been shown in the Fig. 9.

Oxide Morphology. The top surfaces of the oxidized sample were analysed using Scanning Electron Microscopy (SEM). The top surface images of the oxidized sample at different temperatures and CO_2/CO ratios are shown in the Fig. 10. It is observed that the top surface of the oxidised sample is fully covered with the oxide layer. The different in contrast is observed in Fig. 10(a–f) due to the porous structure of the oxide layer. It has been observed that with increasing temperature the oxide morphology changes from lump shaped to island shaped oxide. The sample oxidised at 650 °C and 750 °C has lump shaped oxide while oxidation occurs at high temperature (850 °C) showed island like oxide particle surrounded by a network of oxide. The EDS of top surfaces of the samples shows same composition (62–68% Fe, 30–36% O and 1.16 to 3.78% Mn) on both the contrast (network and island). Which suggest that different contrast observed in Fig. 9(g–i) is due to the different oxidation kinetics in the grain boundary as compared to the grain body. With increasing CO_2/CO ratio the particle size of the oxide is found to be increase.
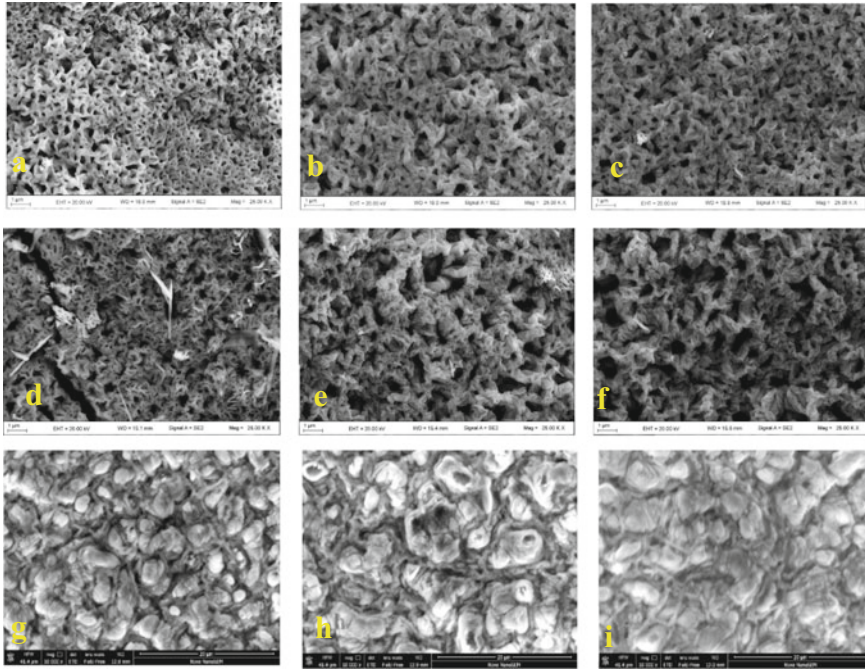
Fig. 10 SEM images of the top surfaces of the oxidized samples at different temperature and CO_2/CO ratio **a** 650 °C, $CO_2/CO = 1$, **b** 650 °C, $CO_2/CO = 2$, **c** 650 °C, $CO_2/CO = 3$, **d** 750 °C, $CO_2/CO = 1$, **e** 750 °C, $CO_2/CO = 2$, **f** 750 °C, $CO_2/CO = 3$, **g** 850 °C, $CO_2/CO = 1$, **h** 850 °C, $CO_2/CO = 2$, **i** 850 °C, $CO_2/CO = 3$

5   Conclusion

From the result of numerical simulation and the oxidation experiment the following conclusion can be made.

1. Low dew point (near about -40 °C), which provides reducing environment for Fe, forms higher amount of MnO near the surface and causes poor adhesion of the coating with the substrate.
2. Increasing dew point increases the inwards flux of the oxygen which causes increase in the depth of IOZ (exponentially).
3. Increasing dew point temperature causes decrease in the surface oxidation, and it Increases the depth of IOZ. So, if in case high depth of IOZ is needed it is more desirable to achieve it by increasing dew point rather than increasing time.
4. From the modelling it is observed that amount of surface oxidation decreases with increasing dew point. So, increasing dew point during annealing increases the equilibrium partial pressure of oxygen which may provide suitable oxidising atmosphere (ranges can be obtain from Ellingham diagram) for Fe to form FeO

    and at the same time it reduces the amount of MnO on the surface as it increases the inward flux of oxygen.

5. For the alloy having more than one alloying elements, the oxide of the alloying element having lower affinity towards oxygen will precipitate out near the surface and the oxide of the alloying element having higher affinity toward oxygen will be distributed over a large region.

6. Anisothermal annealing of Fe–Mn binary alloys show enrichment of Mn near the surface and the depletion of dissolve Mn occurs during the heating period itself, and the large growth of the IOZ occur during the isothermal holding period, and it grows a lIttle bit during cooling periods. So, we can say that heating and cooling rate will have effect on the final depth of IOZ of the oxidised sample.

7. Thermogravimetric analysis data shows parabolic growth of the oxide layer. And at higher temperature the growth started with a parabolic growth region and it tends to be flattened and follows nearly linear growth.

8. Oxide formed at 650 °C and 750 °C has lump shaped oxide while the oxide formed at higher temperature (850 °C) show island shaped oxide.

9. Size of the oxide particle increases with increasing the CO_2/CO ratio.

References

1. Marder A (2000) The metallurgy of zinc-coated steel. Prog Mater Sci 45:191–271. https://doi.org/10.1016/S0079-6425(98)00006-1
2. Li F, Liu H, Shi W, Li L (2011) Thermodynamic consideration on selective surface oxidation of high strength steels prior to hot-dip galvanizing. J Coat Technol Res 8:639–647. https://doi.org/10.1007/s11998-011-9334-1
3. Maki J, Mahieu J, De Cooman B, Claessens S (2003) Galvanisability of silicon free CMnAl TRIP steels. Mater Sci Technol 19:125–131
4. Gong Y, Kim H, De Cooman B (2008) Formation of surface and subsurface oxides during ferritic, intercritical and austenitic annealing of CMnSi TRIP steel. ISIJ Int 48:1745–1751
5. Liu H, He Y, Swaminathan S, Rohwerder M, Li L (2011) Effect of dew point on the surface selective oxidation and subsurface microstructure of TRIP-aided steel. Surf Coat Technol 206:1237–1243
6. Maderthaner M, Jarosik A, Angeli G, Haubner R (2017) Effect of dew point on the selective oxidation of advanced high strength steels. Mater Sci Forum 891:292–297
7. Olefjord I, Leijon W, Jelvestam U (1980) Selective surface ace oxidation during annealing of steel sheets in H2/N2. Appl Surf Sci 6:241–255
8. Swaminathan S, Spiegel M (2008) Effect of alloy composition on the selective oxidation of ternary Fe–Si–Cr, Fe–Mn–Cr model alloys. Surf Interface Anal 40:268–272
9. Wagner C (1959) Zeitschrift fur Elektrochemie 63:772 (in German)
10. Huin D, Lanteri V, Loison D, Autesserre P, Gaye H (eds) (1997) In microscopy of oxidation—3, newcomb and little. The Institute of Metals, London, pp 573–586
11. Whittle D, Gesmundo F, Bastow B, Wood G (1981) The formation of solid solution oxides during internal oxidation. Oxid Met 16:159
12. Rapp R (1965) Kinetics, microstructures and mechanism of internal oxidation—its effect and prevention in high temperature alloy oxidation. Corrosion. 21:382–401
13. Thermodata (2005) Electronic data bank for thermodynamic quantities, address. http://thermodata.online.fr

14. Rist A, Ancey-Moret MF, Gatellier C, Riboud PV (1974) Équilibres thermodynamiques dans l'élaboration de la fonte et de l'acier. Techniques de l'ingénieur. Matériaux métalliques 2(M1730):1–42
15. Swisher JH, Turkdogan ET (1967) Transactions of the metallurgical society of AIME 239:426
16. Oikawa H (1982) Lattice diffusion in iron-a review. Trans Iron Steel Inst Japan 68:1489

Microstructure Evolution in Medium Mn, High Al Low-Density Steel During Different Continuous Cooling Regimes

Biraj Kumar Sahoo, Suman Sadhu, Avanish Kumar Chandan, Gaurav Kumar Bansal, V. C. Srivastava, and S. G. Chowdhury

1 Introduction

Automotive vehicles are one of the major sources of greenhouse gas emissions in the world because of which stringent environmental norms to control emissions have been implemented globally in recent years [1–4]. There is an imminent requirement for weight saving in the body-in-white (BIW) of conventional vehicles and to compensate for the weight of batteries/cells in upcoming electric or hybrid vehicles. A weight saving of 10% results in a 6–8% improvement in fuel economy and eventually reduces emission [5]. As steel comprises, 50–70% weight of the vehicle, an approach that can be adopted, is to make the steel lighter without compromising the required mechanical properties. In this context, Al (density = 2.7 g/cc) has emerged as the chief alloying element for density reduction in steel. For every 1% addition of Al, there is a decrease in density of 1.3% due to the combined effect of lower atomic weight and lattice dilatation [6]. The development of low-density steel by alloying with high aluminum seems to be a viable option.

The addition of a high amount of Al to steel expands the ferrite phase field, as a result, the δ-ferrite formed during solidification remains untransformed and retained at room temperature [7, 8]. To make the phase transformation feasible, the addition of austenite stabilizers like Mn, C is done in these steels. The austenite transformation helps to tailor the microstructure and imparts necessary formability to the steel. Based on the relative amount of Al and (Mn + C), low-density steels could be single-phase

B. K. Sahoo (✉) · A. K. Chandan · G. K. Bansal · V. C. Srivastava · S. G. Chowdhury
Academy of Scientific and Innovative Research (AcSIR), Ghaziabad 201002, India
e-mail: biraj@nmlindia.org

Materials Engineering Division, CSIR National Metallurgical Laboratory, Jamshedpur 831007, India

S. Sadhu
Department of Metallurgical and Materials Engineering, Indian Institute of Technology, Kharagpur 721302, India

ferritic or multiphase such as the duplex steel (ferrite and austenite), or triplex steel (ferrite, austenite, and *k*-carbide), depending on the stable phase formed at room temperature [1]. It has been reported that a maximum of 11 wt.% of aluminum is feasible to add in ferritic low-density steels. Addition of excess aluminum leads to the formation of a brittle intermetallics like iron aluminides [4, 7, 9]. While with the addition of austenite stabilizers like Mn, C, the amount of Al addition can be increased. Also, the addition of a minor amount (<1 wt.%) of Si in these alloys has a beneficial effect as it accelerates the kinetics of *k*-carbide formation. The presence of Si increases the activity of C in austenite and thus increases its partitioning to *k*-carbide, which has a direct effect on increasing the strength of the alloy [10]. Recently, the addition of Ni in high Al has also been explored. Nickel has been found to be effective in forming B2 Ni–Al type precipitates that impart necessary strength to the alloy [11–13]. The Fe-Mn-Al-C steel has a promising application in automotive because of its low density, high strength, and good ductility [4, 6].

In the present work, a high Al steel composition, Fe-13 Al-12 Mn-4.8 Ni-0.8 C-0.35 Si wt.% is taken up for the study. The thermodynamic assessment of the alloy is done to understand the partitioning behavior of the elements. The study focuses on the phase evolution and *k*-carbide precipitation in the alloy, after two-phase heat treatment, followed by continuous cooling to room temperature through different cooling regimes i.e. water quenching, air cooling and furnace cooling.

2   Materials and Methods

The alloy preparation was done at a laboratory scale in a 2 kg vacuum induction melting furnace. High purity alloying elements were used for the alloy preparation. The composition of the alloy obtained is shown in Table 1. Thermodynamic analysis of the alloy was carried out in Themo-Calc software using the TCFE9 database.

The as-cast ingot was given homogenization treatment at 1200 °C for a duration of 3 h followed by hot forging to a plate of 20 mm thickness and then quenched in water. The as-forged alloy samples were then reheated to a two-phase ferrite–austenite region at a temperature of 1150 °C for 30 min. Samples were then cooled to room temperature through different cooling regimes viz. water quenching (WQ), air cooling (AC), and furnace cooling (FC). The approximate average cooling rate in WQ, AC and FC samples are 100 °C/s, 10 °C/s and 0.05 °C/s respectively. The schematics of the heat treatment and cooling schedule is shown in Fig. 1.

Table 1 Chemical composition (wt.%) analysis of the steel used in the study

Elements	C	Mn	Al	Ni	Si	S	P	Fe
wt.%	0.80	12.40	12.60	4.8	0.35	0.01	0.02	Bal
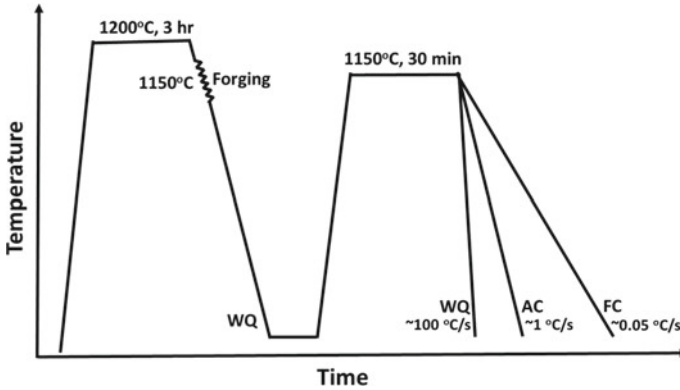
Fig. 1 Schematics of the heat treatment schedule

The heat-treated samples were mechanically grinded and prepared using standard metallography techniques followed by etching in a 6% Nital solution for 2–3 min. Microstructural characterization of the samples was done using Leica DM 2500 optical microscope and FEI Nova Nano 430 field emission scanning electron microscope (FESEM). Composition analysis of the phases in the microstructure was carried out using Bruker energy dispersive spectrometry (EDS) detector attached to Hitachi S3400 SEM. To characterize the phases and their spatial distribution, electron backscattered diffraction (EBSD) analysis of the samples was carried out with a step size of 0.1–0.2 μm in EDAX-EBSD attached to FEI Nova Nano 430 SEM. For EBSD analysis the samples were polished in fine colloidal silica of 0.05 μm size. The post-processing of the EBSD data was carried out in TSL OIM software version 7. For bulk phase analysis, the X-ray diffraction (XRD) measurements of the samples were carried out in Burker D8 XRD using Cu-Kα radiation ($\lambda = 1.5408$ Å).

3 Results and Discussion

3.1 *Thermodynamic Analysis*

The variation of equilibrium volume (%) of the phases with temperature obtained from Thermo-Calc is shown in Fig. 2a. The major phases in the alloy are ferrite, austenite, and *k*-carbides. The austenite phases start to form at a temperature of 925 °C and reach a maximum of ~45 vol.% at 1130 °C, thereafter it decreases with an increase in temperature. As the equilibrium volume of the austenite phase doesn't go beyond 45% it implies that a major amount of δ-ferrite formed during solidification will remain untransformed and retained at room temperature. A large fraction (~19 vol.%) of *k*-carbides i.e. (Fe, Mn)$_3$AlC was found to form in the alloy, which dissolves
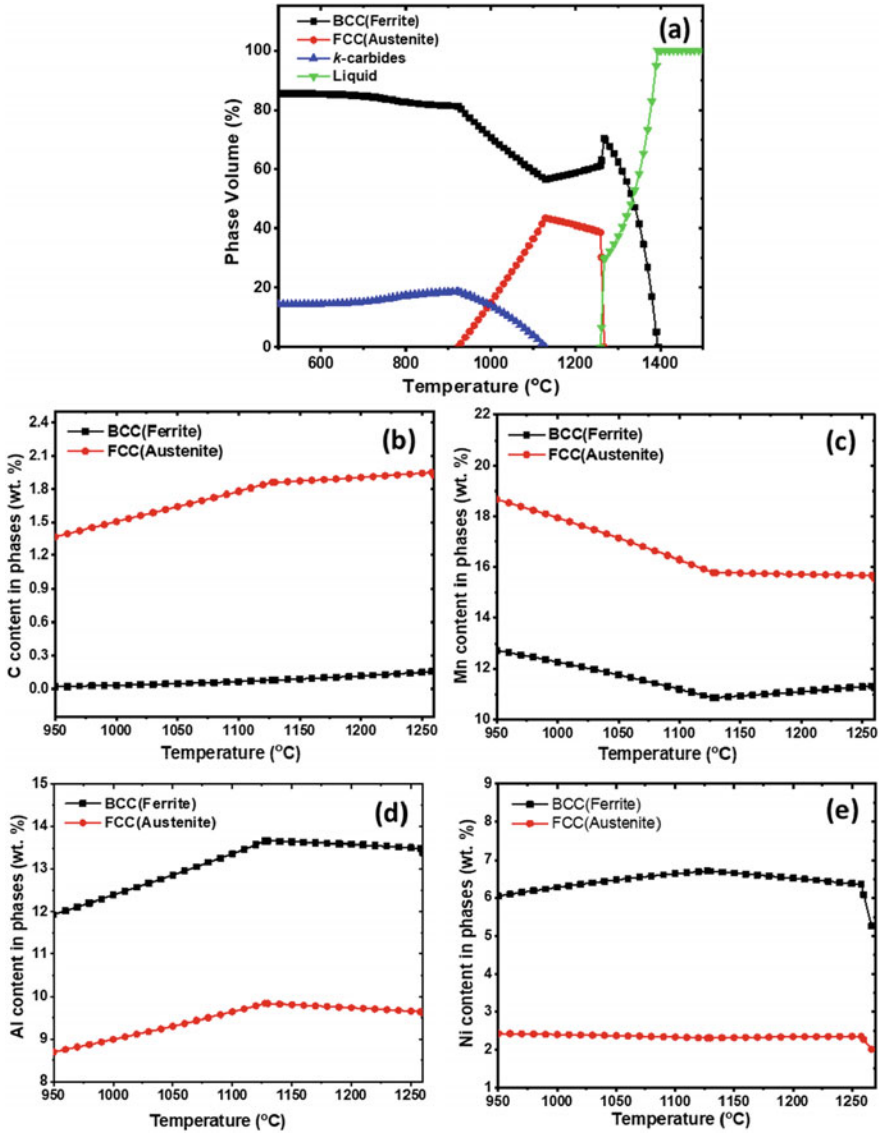
Fig. 2 Thermodynamic analysis of the alloy from Thermo-Calc software **a** Equilibrium phase fraction vs temperature plot; **b**, **c**, **d** and **e** Composition of C, Mn, Al, and Ni respectively in ferrite and austenite

around 1130 °C. The *k*-carbide formation is the result of the eutectoid decomposition of austenite into α-ferrite and carbides [7].

The partitioning behavior of the major elements in the alloy was studied through Thermo-Calc. The concentration of C, Mn, Al, and Ni in the two-phase region of austenite and ferrite has been shown in Fig. 2b-e. It can be seen that C and Mn being austenite stabilizer partitions to austenite as the composition (wt.%) of C, Mn is higher in the austenite phase as compared to ferrite. The C composition (Fig. 2b) in austenite was found to initially increase with temperature due to the gradual dissolution of *k*-carbides (Fig. 2a), thereafter beyond 1130 °C, it becomes nearly constant. The Mn composition (Fig. 2c) in austenite initially decreases because of an increase in austenite vol.%, and at a temperature beyond 1130 °C, the Mn composition profile in austenite nearly becomes constant. Aluminum being a ferrite stabilizer was found to partition to ferrite (Fig. 2d). Nickel was also found to partition to ferrite as shown in Fig. 2e. Ni in general is an austenite stabilizer, however, it has been shown that in steels containing high Al content, Ni has a higher tendency to partition to the ferrite phase [12] as it forms more stable phases like (Ni, Fe)Al within ferrite [14].

3.2 As-Forged Microstructure

The microstructure of the alloy after forging and cooling is shown in Fig. 3. The optical micrograph (Fig. 3a) shows the presence of two phases having bright and dark contrast. The phases were identified through EBSD analysis, as shown in Fig. 3b. The bright and dark phases in the optical micrographs are δ-ferrite and austenite respectively. The fraction of austenite phase was found to be around 51% (Fig. 3b). A large number of annealing twins were found to form in the austenite grains due to high deformation and temperature during forging operation. As the alloy was directly water quenched after forging, no carbides were found to be present in the microstructure.

The elemental mapping of the elements in the forged and WQ microstructure is shown in Fig. 3c. The brighter areas in the elemental maps show a higher concentration of elements. Mn was found to be enriched in austenite grains. While Ni and Al were found to be enriched in ferrite grains. These results corroborate the Thermo-Calc prediction (Fig. 2), where Ni was found to partition to ferrite along with Al.

3.3 Microstructure Evolution During Different Continuous Cooling Regimes

The SEM micrographs of the alloy after heat treatment followed by different cooling regimes i.e. WQ, AC, and FC are shown in Fig. 4. The alloy after water quenching (WQ) shows a duplex microstructure consisting of δ-ferrite and austenite (Fig. 4a,
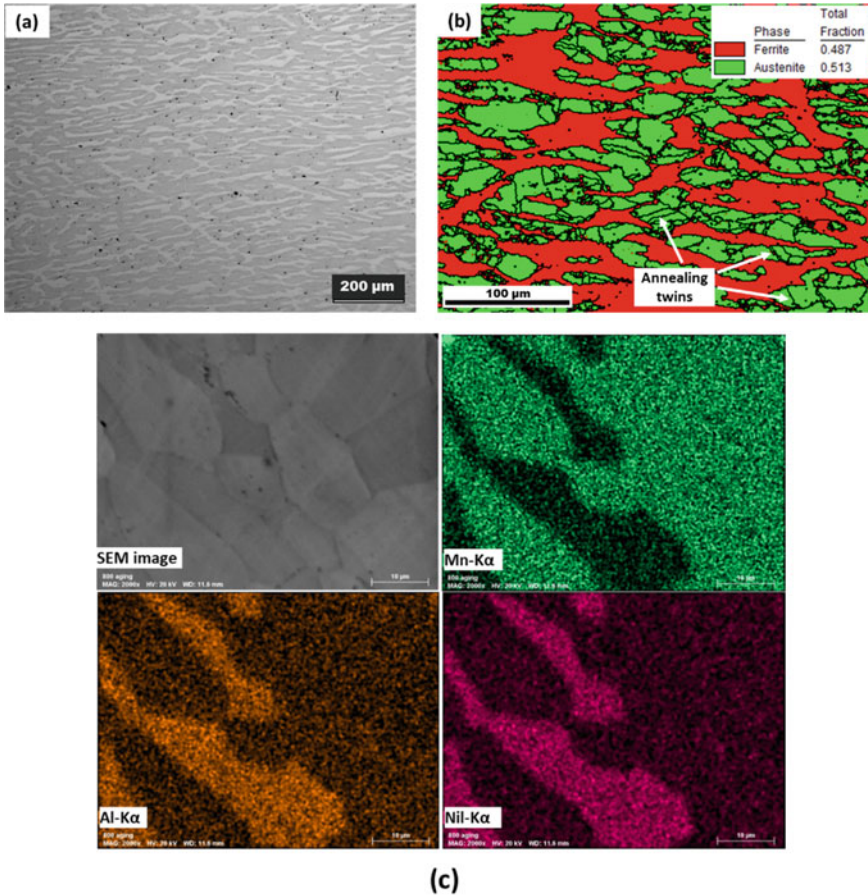
Fig. 3 Microstructure of the alloy after forging and water quenching **a** Optical micrograph, **b** EBSD phase map, and **c** Elemental mapping of Mn, Al and Ni

b). The topology of the phases appears to be smooth and no considerable formation of carbides or ordering was detected. After air cooling (AC), the microstructure constituted primarily of austenite and δ-ferrite, along with a small amount of α-ferrite (Fig. 4c, d). The α-ferrite was found to form inside the austenite phase as indicated in Fig. 4c, d. Also, the surface topology of the austenite grains was found to be granular, possibly due to the formation of fine intragranular k-carbides within it. In the furnace cooled (FC) sample (Fig. 4e, f), along with δ-ferrite and austenite, a considerable amount of lamellar/blocky α-ferrite and k-carbides was formed. Due to the slow cooling rate during furnace cooling, most of the austenite underwent eutectoid decomposition into α-ferrite and k-carbides. Also, the surface topology of the remaining austenite phase (Fig. 4f) appears to be regularly arranged indicating the occurrence of ordering within the austenite phase. The austenite phase formed
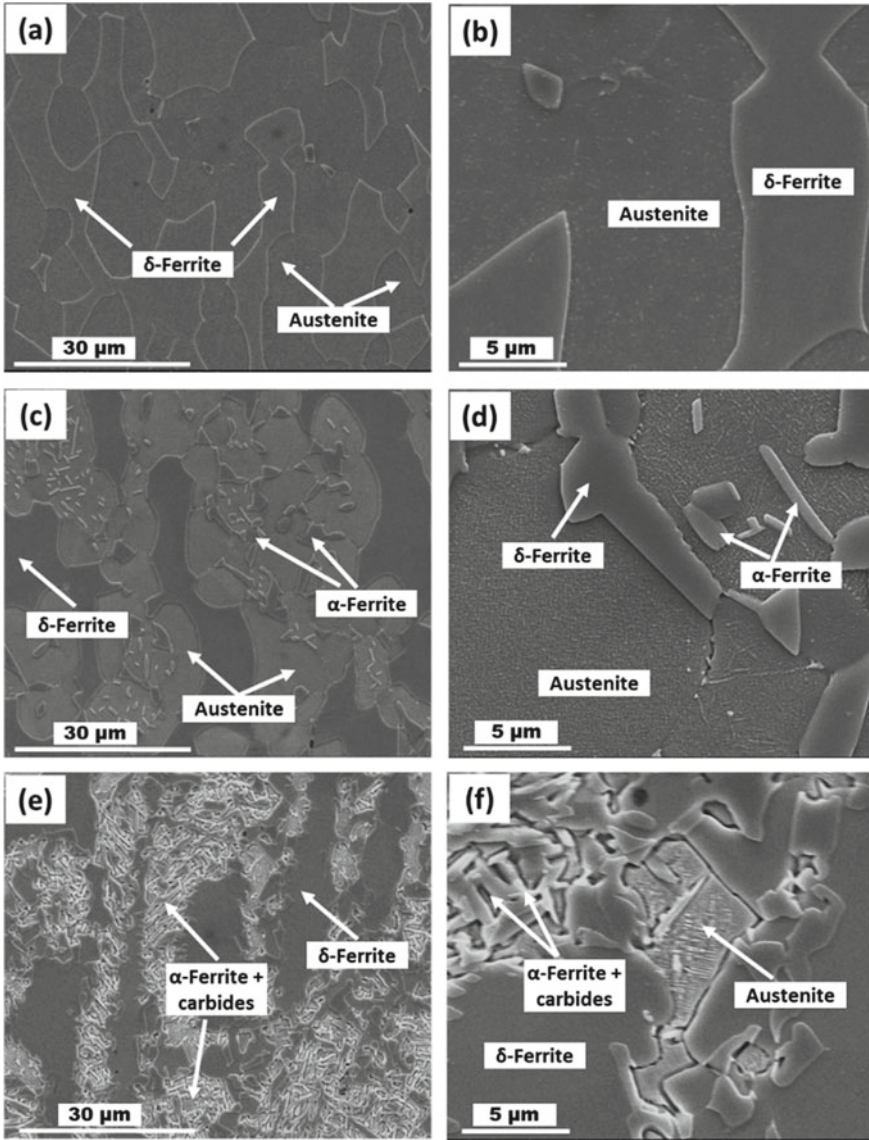
Fig. 4 SEM micrographs of the heat-treated samples cooled through different cooling regimes **a** and **b** Water quenching; **c** and **d** Air cooling; **e** and **f** Furnace cooling

here seems to show the typical modulated type cuboidal structures of *k*-carbides as found in Fe-Mn-Al-C steel [15, 16]. The *k*-carbides has precipitated inside the austenite as well, giving rise to a regularly arranged modulated structure. It has been reported that during continuous cooling of high Al duplex steels, austenite forms from δ-ferrite, and k-carbides is precipitated at the inter-phase boundaries of ferrite and austenite. But during slow cooling rates as in furnace cooling, the decomposition of austenite takes place through eutectoid reaction resulting in ferrite and lamellar carbides. However, if this reaction is incomplete the k-carbides precipitates inside the austenite grains giving rise to a modulated structure [17, 18].

The X-ray diffraction analysis of the WQ, AC, and FC samples is shown in Fig. 5. In the WQ sample (Fig. 5a), diffraction peaks of only austenite and ferrite are observed. In the AC sample (Fig. 5b), predominant peaks of ferrite and austenite are observed, but a minor splitting of the (111) austenite peak was seen (indicated by the arrow). While in the FC sample, the split in the (111) and (200) austenite peaks are very distinct as illustrated by the arrows in Fig. 5c. This splitting in the austenite peaks is due to the formation of *k*-carbide. This is because *k*-carbide has an FCC structure and its lattice parameter is very similar to that of the austenite phase [19], and thus its XRD peaks nearly overlaps or are close to the austenite peaks.
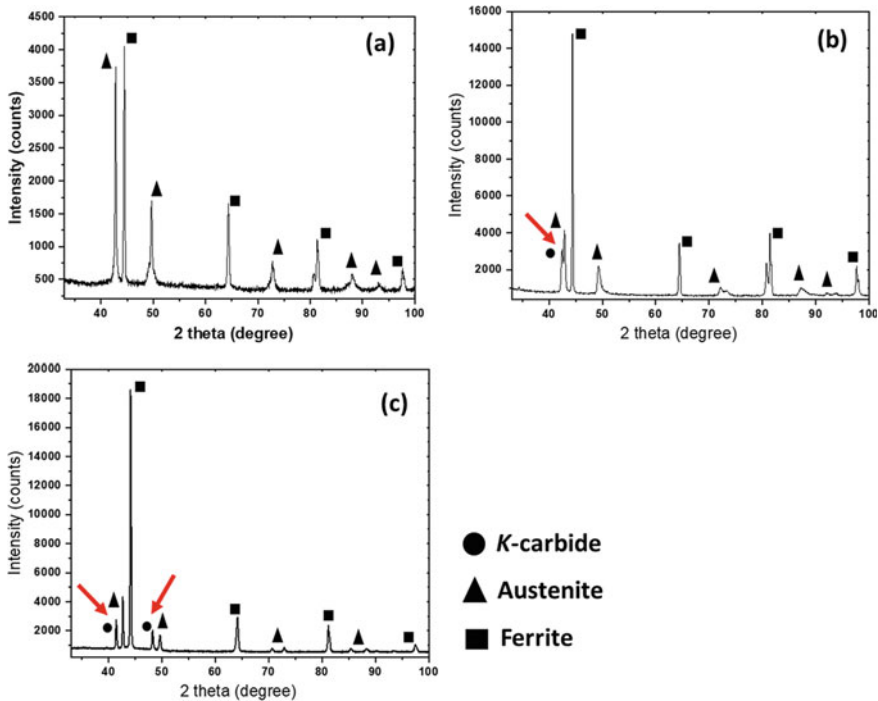
Fig. 5 X-ray diffraction patterns of the heat-treated samples cooled through different cooling regimes **a** Water quenching, **b** Air cooling, and **c** Furnace cooling

The signature of *k*-carbides (minor splitting of austenite peak) in the XRD results of AC samples confirms the presence of intragranular *k*-carbide in the AC sample as observed in SEM micrograph (Fig. 4d). Also, the *k*-carbide peaks in the XRD data of FC samples are in accordance with the SEM results, where the extensive presence of lamellar and intragranular *k*-carbides is observed.

The phase fraction of the austenite in the WQ, AC, and FC samples was quantified form the EBSD data. The retained austenite volume was found to be 58–60 vol.% in the WQ and AC samples; while in the FC sample it decreased to 36 vol.% due to extensive formation of α-ferrite and *k*-carbide. To further illustrate the formation of the phases, a magnified view of the EBSD phase map of the samples has been shown in Fig. 6. In the WQ condition (Fig. 6a), very fine α-ferrite grains were found to nucleate inside the austenite grains, notably along austenite twin boundaries and at the triple junction. These α-ferrite grains were not detectable in the SEM micrograph (Fig. 4a, b). After AC (Fig. 6b) the α-ferrite grains grew and stringers of α-ferrite were found along the austenite twin boundaries. The twin boundaries and triple junctions
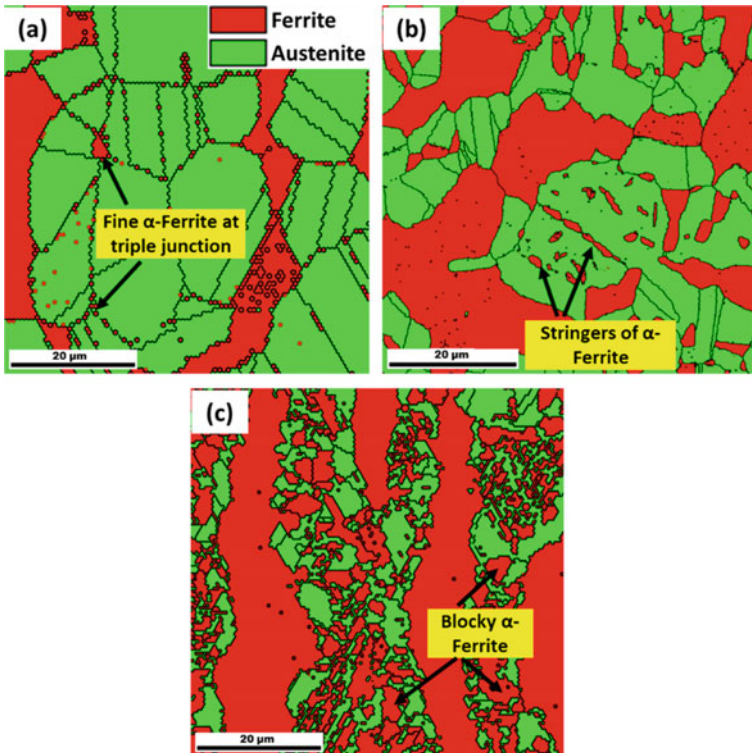
Fig. 6 EBSD phase map of the heat-treated samples cooled through different cooling regimes **a** Water quenching, **b** Air cooling, and **c** Furnace cooling

have high interfacial energy and serve as potential sites for α-ferrite nucleation and growth. While, in the FC sample (Fig. 6c), the α-ferrite grains were lamellar and blocky due to extensive transformation and growth of the α-ferrite, formed from the austenite.

4 Conclusion

The study presented the microstructure evolution in Fe-12Mn-13Al-4.8Ni-0.8C-0.35Si steel subjected to two-phase heat treatment and cooled to room temperature adopting different cooling regimes i.e. water quenching (WQ), air cooling (AC) and furnace cooling (FC). In the WQ sample, a duplex microstructure was obtained consisting mainly of δ-ferrite and austenite along with a minor amount of fine α-ferrite formed at austenite twin boundaries and triple junction. In the AC sample besides δ-ferrite and austenite, a small amount of α-ferrite and intragranular *k*-carbide was found to form. Stringers of α-ferrite were found to grow along austenite twin boundaries in the AC sample. In the FC sample, a significant amount of α-ferrite and *k*-carbide was formed due to the decomposition of austenite owing to the slow cooling rate of furnace cooling. The *k*-carbide formed in the FC sample was modulated intragranular type (inside austenite grain) as well as in the lamellar form. The phase fraction of austenite was found to reduce to 36 vol% in the FC sample as compared to 58–60 vol% in the WQ and AC sample.

These high Al lightweight steels seem to be promising candidates for future automotive applications [1, 4, 20]. Future research and investigation are required for optimizing the composition, microstructure, and mechanical properties. As well, work should be carried out in overcoming the challenges for industrial production that include: inclusion control and re-oxidation during steelmaking, clogging during continuous casting due to reaction of Al with mold slag, and occurrence of cracks during cold rolling.

References

1. Rana R, Liu C, Ray RK (2013) Low-density low-carbon Fe-Al ferritic steels. Scr Mater 68:354–359. https://doi.org/10.1016/j.scriptamat.2012.10.004
2. Rana R, Liu C, Ray RK (2014) Evolution of microstructure and mechanical properties during thermo mechanical processing of a low-density multiphase steel for automotive application. Acta Mater 75:227–245. https://doi.org/10.1016/j.actamat.2014.04.031

3. Rana R, Liu C, Ray RK (2014) Recrystallization in a low-density low-alloy Fe-Mn-Al-C duplex-phase alloy. Philos Mag Lett 94:127–134. https://doi.org/10.1080/09500839.2013.878046

4. Suh DW, Kim NJ (2013) Low-density steels. Scr Mater 68:337–338. https://doi.org/10.1016/j.scriptamat.2012.11.037

5. Joost WJ (2012) Reducing vehicle weight and improving US energy efficiency using integrated computational materials engineering. JOM 64:1032–1038. https://doi.org/10.1007/s11837-012-0424-z

6. Kim H, Suh DW, Kim NJ (2013) Fe-Al-Mn-C lightweight structural alloys: a review on the microstructures and mechanical properties. Sci Technol Adv Mater 14. https://doi.org/10.1088/1468-6996/14/1/014205

7. Rana R, Lahaye C, Ray RK (2014) Overview of lightweight ferrous materials: strategies and promises. JOM 66:1734–1746. https://doi.org/10.1007/s11837-014-1126-5

8. Pramanik S, Suwas S (2014) Low-density steels: the effect of Al addition on microstructure and properties. JOM 66:1868–1876. https://doi.org/10.1007/s11837-014-1129-2

9. Gutierrez-Urrutia I, Raabe D (2013) Influence of Al content and precipitation state on the mechanical behavior of austenitic high-Mn low-density steels. Scr Mater 68:343–347. https://doi.org/10.1016/j.scriptamat.2012.08.038

10. Bartlett LN, Van Aken DC, Medvedeva J, Isheim D, Medvedeva NI, Song K (2014) An atom probe study of kappa carbide precipitation and the effect of silicon addition. Metall Mater Trans A Phys Metall Mater Sci 45:2421–2435. https://doi.org/10.1007/s11661-014-2187-3

11. Rahnama A, Spooner S, Sridhar S (2017) Control of intermetallic nano-particles through annealing in duplex low density steel. Mater Lett 189:13–16. https://doi.org/10.1016/j.matlet.2016.11.020

12. Rahnama A, Kotadia H, Sridhar S (2017) Effect of Ni alloying on the microstructural evolution and mechanical properties of two duplex light-weight steels during different annealing temperatures: experiment and phase-field simulation. Acta Mater 132:627–643. https://doi.org/10.1016/j.actamat.2017.03.043

13. Zhang BG, Zhang XM, Wang GD, Liu HT (2019) Age-hardening medium Mn steel with high strength and large ductility. Mater Sci Eng A 756:35–40. https://doi.org/10.1016/j.msea.2019.04.019

14. Drouven C, Song W, Bleck W (2019) Phase-specific precipitation of intermetallic phases in Fe Al Mn Ni C duplex steels. Steel Res Int 90. https://doi.org/10.1002/srin.201800440

15. Lin CL, Chao CG, Bor HY, Liu TF (2010) Relationship between microstructures and tensile properties of an Fe-30Mn-8.5Al-2.0C Alloy. Mater Trans 51:1084–1088. https://doi.org/10.2320/matertrans.M2010013

16. Zhao C, Song R, Zhang L, Yang F, Kang T (2016) Effect of annealing temperature on the microstructure and tensile properties of Fe-10Mn-10Al-0.7C low-density steel. Mater Des 91:348–360. https://doi.org/10.1016/j.matdes.2015.11.115

17. Choo WK, Kim JH, Yoon JC (1997) Microstructural change in austenitic Fe-30.0 wt% Mn-7.8 wt% Al-1.3 wt% C initiated by spinodal decomposition and its influence on mechanical properties. Acta Mater. 45:4877–4885. https://doi.org/10.1016/S1359-6454(97)00201-2

18. Sato K, Tagawa K, Inoue Y (1989) Spinodal decomposition and mechanical properties of an austenitic Fe-30 wt.% Mn-9 wt.% Al-0.9 wt.% C alloy. Mater. Sci. Eng. A. 111:45–50. https://doi.org/10.1016/0921-5093(89)90196-2

19. Ha MC, Koo JM, Lee JK, Hwang SW, Park KT (2013) Tensile deformation of a low density Fe-27Mn-12Al-0.8C duplex steel in association with ordered phases at ambient temperature. Mater Sci Eng A 586:276–283. https://doi.org/10.1016/j.msea.2013.07.094

20. Chen S, Rana R, Haldar A, Ray RK (2017) Current state of Fe-Mn-Al-C low density steels. Prog Mater Sci 89:345–391. https://doi.org/10.1016/j.pmatsci.2017.05.002

Phonon Dynamics and Collective Excitations in $Cu_{60}Zr_{20}Hf_{10}Ti_{10}$ Bulk Metallic Glass

Alkesh L. Gandhi and Aditya M. Vora

1 Introduction

The *Cu* based BMGs have good mechanical strength, high ductility, large super-cooled region and high thermal stability against crystallization. Since the element *Zr* in a BMG maintains thermal stability and offers resistant to fracture and brittleness, the material is used in the high-field superconducting magnets applications [1–5]. The $Cu_{60}Zr_{20}Hf_{10}Ti_{10}$ BMG is a typical multi application amorphous alloy amongst quaternary *Cu-Zr-Hf-Ti* BMG family having good Glass Forming Ability (*GFA*) and fracture strength above 2000 MPa [6]. Wang et al. [7] had investigated the crystallization and *GFA* of $Cu_{60}Zr_{20}Hf_{10}Ti_{10}$ BMG by *XRD* and other characterization techniques and also measured its elastic properties from the acoustic velocities and density using the ultrasonic pulse-echo technic. They confirmed its glass transition temperature (T_g) between *721* and *763 K* [8]. Agarwal [9] has theoretically investigated this BMG. Borja Soto et al. have calculated the shear modulus (G) of $Cu_{60}Zr_{20}Hf_{10}Ti_{10}$ BMG [10].

The Pseudo Alloy Atom (*PAA*) model is used here instead of Vegard's law [1–5]. The collective dynamics of the longitudinal and transverse phonon modes have been studied at room temperature in terms of the Eigen frequencies of the localized collective excitations. The self-consistent phonon scheme is attempted to apply the model pseudopotential formalism by involving phonon eigenfrequencies and multiple scattering. Such frequencies can be expressed in terms of interatomic pair potential [*V(r)*] [11] and many-body pair-correlation functions (*PCF*) [*g(r)*], which are the vital components to represent the propagation velocity of elastic waves by longitudinal and transverse modes of phonon dispersion curves (PDCs) from which various thermodynamic and elastic properties can be estimated.

A. L. Gandhi (✉)
Department of Physics, C. U. Shah University, Surendranagar, Gujarat, India

A. M. Vora
Department of Physics, Gujarat University, Ahmedabad, Gujarat, India

Here, Shaw's optimized constant core model pseudopotential [12] is effectively used with five versatile local field correlation functions viz. Hartree [13], Taylor [14], Itchimaru and Utsumi [15], Farid et al. [16], and Sarkar et al. [17] to study the screening effects on the vibrational dynamics of the BMG. The dielectric function plays an important role in the assessment of the potential due to screening of the electron gas and hence, these screening functions help to study the relative effects of exchange and correlation in the properties of the BMG. The well famous computational approach given by Hubbard-Beeby [18] is exploited so that the phonon frequency expressions reproduce the essential characteristic features of the PDCs. Presently, very first time $Cu_{60}Zr_{20}Hf_{10}Ti_{10}$ BMG is studied here using Shaw's model potential with five screening functions under the pseudopotential approach. Such a study involves computational approximations of collective density waves at larger momenta for the BMG material and the dynamical structure factors are generated up to very large wave vectors. According to *HB*-approach [18], the product of the second-order derivative of the pair potential and static PCF [*g(r)*] peaks near the hard-core radius. Applying the random phase approximation, the collective motion in a BMG is studied as a generalization of phonon theory. The results for the elastic constants like Isothermal Bulk modulus (B_T), Rigidity modulus (G) Poisson's ratio (σ), Young's modulus (Y), Debye temperature (θ_D) have been reported at room temperature (R_T) [1–5] and compared with the theoretical or experimental data, whatever, available in the literature.

2   Computational Methodology

The expression for the pair potential in a BMG is adopted from the Wills-Harrison model [11] in which the angular interaction due to partially filled d-bands in transition metals are ignored.

$$V(r) = \left\{ \frac{Z^2 e^2}{r} + \frac{\Omega_0}{\pi^2} \int F(q) \left[\frac{\sin(qr)}{(qr)} \right] q^2 \mathrm{dq} \right\}$$
$$+ \left\{ -Z_d \left[1 - \frac{Z_d}{10} \right] \left(\frac{12}{N_c} \right)^{\frac{1}{2}} \left(\frac{28.6}{\pi} \right) \left(\frac{2\, r_d^3}{r^5} \right) \right\}$$
$$+ \left\{ Z_d \left(\frac{450}{\pi^2} \right)^2 \left(\frac{r_d^6}{r^8} \right) \right\} \tag{1}$$

The PCF [*g(r)*] [1–5] can be obtained experimentally by either x-ray or neutron diffraction technique. In the current work, they have been computed theoretically from the effective pair potentials [*V(r)*].

$$g(r) = \exp \left[\left(\frac{-V(r)}{k_B T} \right) - 1 \right] \tag{2}$$

Show's optimized constant core model pseudopotential, employed here, is,

$$W(q) = -\left(\frac{8\pi Z}{\Omega_0 \boldsymbol{q}^2}\right)\left[\frac{\sin \boldsymbol{q}r_c}{\boldsymbol{q}r_c}\right] \tag{3}$$

The single parametric potential i.e. model potential parameter is,

$$\boldsymbol{r_c} = (0.51)r_S Z^{-1/3} \tag{4}$$

The longitudinal and transverse phonon eigenfrequencies proposed by Hubbard and Beeby in their *HB*-approach are given by, [18–20].

$$\omega^2_{L_{HB}}(q) = \omega^2_E\left[1 - \frac{\sin(q\sigma)}{q\sigma} - 6\frac{\cos(q\sigma)}{(q\sigma)^2} + 6\frac{\sin(q\sigma)}{(q\sigma)^3}\right] \tag{5}$$

$$\omega^2_{T_{HB}}(q) = \omega^2_E\left[1 + 3\frac{\cos(q\sigma)}{(q\sigma)^2} - 3\frac{\sin(q\sigma)}{(q\sigma)^3}\right] \tag{6}$$

$$\omega^2_{E_{HB}}(q) = \left(\frac{4\pi\rho}{3M}\right)\int_0^\infty g(r)V''(r)r^2 dr \tag{7}$$

Formulations for the longitudinal and transverse sound velocities (v_L and v_T) are carried out with,

$$\omega_L = v_L.q \tag{8}$$

$$\omega_T = v_T.q \tag{9}$$

$$v_L(HB) = \omega_E\left(\frac{3}{10}\sigma^2\right)^{1/2} = (0.5477)\omega_E\sigma \tag{10}$$

$$v_T(HB) = \omega_E\left(\frac{1}{10}\sigma^2\right)^{1/2} = (0.3162)\omega_E\sigma \tag{11}$$

The elastic and thermodynamic physical properties have been computed from,

$$\text{Isothermal bulk modulus, } B_T = \rho_M\left(v_L^2 - \frac{4}{3}v_T^2\right) \tag{12}$$

$$\text{Modulus of rigidity, } G = \rho_M v_T^2$$

$$\text{Poisson's ratio, } \sigma = \frac{1}{2}\left\{\frac{1 - 2\left(v_T^2/v_L^2\right)}{1 - \left(v_T^2/v_L^2\right)}\right\} \tag{13}$$

Table 1 Input parameters and constants

Z	Z_S	Z_d	R_d (au)	R_s (au)	Ω_0 (au)^3	N_C	M amu	r_c (au)
2.20	1.50	6.70	1.77	2.18	105.84	12.00	79.01	0.8847

$$\text{Young's modulus, } Y = 2G(\sigma + 1)$$

$$\text{Debye temperature, } \theta_D \quad = \frac{\hbar\,\omega_D}{k_B} = \frac{\hbar}{K_B} \; 2\pi \left(\frac{9\rho}{4\pi}\right)^{\frac{1}{3}} \left(\frac{1}{v_L^3} + \frac{2}{v_T^3}\right)^{-\frac{1}{3}}. \tag{14}$$

The theories, equations and expressions, parameters, variables, constants etc. with specific units and detailed computational methodology are well-defined and discussed in respective literature. The input parameters used in the present work are furnished in Table 1.

The entire computational software for generating data regarding interatomic pair potentials, pair correlation functions, PDCs and Elastic-Thermodynamic properties has been developed in FORTRAN-77.

3   Results and Discussion

The screening dependency for $Cu_{60}Zr_{20}Hf_{10}Ti_{10}$ BMG is plotted by the interatomic pair potential curves wherein the pair potential *[V(r) (Ryd.)]* versus interatomic distance *r(au)* is plotted as shown by Fig. 1. The shape and pattern of pair potentials are in fair agreement with those of other BMGs [1–5]. The shape, oscillation, the first zero $V(r = r_0)$, the first minima (well-depth) with its minimum position $V(r_{min})$, well-width etc. are seemingly affected by the nature of the screening function [1–5] as shown in Table 2.

Inclusion of a screening function hardly changes the nature of the pair potentials, except the $V(r_{min})$,. The first zero for all screening potentials occur nearly *3.60 au.* The well-depth is seen maximum at around *4.72 au* for *IU*-function and minimum at around 4.17 au for *T*-function. The potential energy holds negative value within larger *r*-region. Though the graph pattern is according to our expectation, potential $V(r)$ fluctuates with increasing interatomic distances and hence the graph shows minor oscillations after a certain value of *r*. A particular part of the $V(r)$, which indicates coulomb repulsive potential, dominates the oscillations due to the electron-ion-electron interactions resulting in minor or negligible oscillations after the first depression. In the attractive zone, $V(r)$ does not become zero but converges to narrow finite values. All $V(r)$ curves display the of *s*- and *d*- electrons combined effect under which the attractive part is drawn deeper while the repulsive part is drawn lower as $V(r)$ is shifted towards the lower *r* values. Thus, the derived results seem to support the *d*-electron effect [21].

Fig. 1 Ineratomic pair potential curves
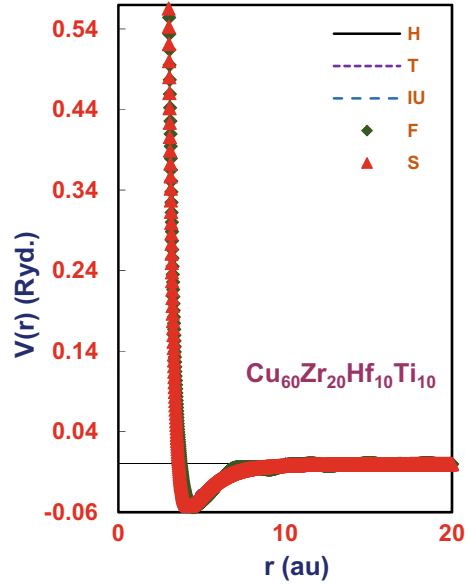
Table 2 Observations of interatomic pair potential curves

Maximum depth position (au)					For all local field correction functions	
H	T	IU	F	S	1st zero V ($r = r_0$) for all screening functions (au)	Waving shape starting point (au)
4.31	4.17	4.72	4.51	4.23	3.60	6.96

The PDCs are generated attempting HB-approach [18] as graphically represented by Fig. 2 and the comparative observations are highlighted in Table 3. The screening influence on longitudinal and transverse phonon eigenfrequencies using H-, T-, IU-, F- and S- screening functions [13–17] based on Shaw's optimized constant core model pseudopotential [12].

In each PDC, the peak height is strongly dependent on the pseudopotential approach and selected screening function employed in this computational study. The longitudinal phonon mode oscillations seem to be more prominent than those due to transverse mode, which confirms the collective excitations at the larger momentum transfer due to the longitudinal phonons only and the instability of the transverse phonons due to the anharmonicity of the atomic vibrations in the BMG. The transverse mode eigenfrequencies increase with the wave vector q and then gets saturated at some value that supports Thorpe theory [22], which describes that there are finite liquid clusters in the glassy structure. The transverse phonons are absorbed for such phonon frequencies which are larger than the smallest eigenfrequencies of the biggest cluster. The phonon dispersion spectra display a minimum, where the static structure

Fig. 2 Phonon dispersion curves
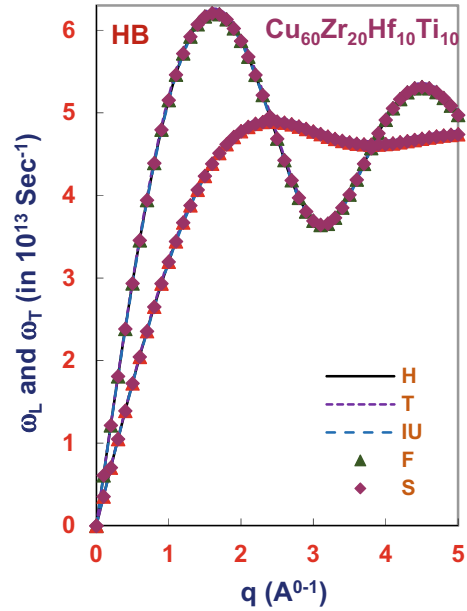
Table 3 First maxima and minima for different screening functions in the PDCs

Phonon frequencies	Maxima minima positions $q(\text{Å}^{-1})$	H	T	IU	F	S	[10]
Longitudinal (ω_L)	Maxima	1.6	1.6	1.6	1.6	1.6	1.8
	Minima	3.1	3.1	3.1	3.1	3.1	3.7
Transverse (ω_T)	Maxima	2.4	2.4	2.4	2.4	2.4	2.3
	Minima	3.8	3.8	3.8	3.8	3.8	4.0

factor $S(q)$ shows its first maximum value. The first and second crossover positions of the ω_L and ω_T are seen at 2.4 au and 1.2 au respectively.

The thermodynamic and elastic properties of $Cu_{60}Zr_{20}Hf_{10}Ti_{10}$ BMG, computed from the longitudinal and transverse long-wavelength limits, are reported in Table 4. As expected, the presently calculated results show some upside deviation than the same properties of its crystalline counterpart. The presently estimated results overperform a little than the experimentally observed data. This is because we have not used any kind of 'fitting formula' to get the expected results. The physical conditions like temperature etc., adopted while experimental work, maybe different is another reason for a minor difference between the calculated and observed results. The computational work can be carried out by other than the pseudopotential method or using different combinations of another computational approach with screening functions and pseudopotential model potential. But, still, the advantage of the present computational work is that it has generated the theoretical sets of data, which may be very useful to provide important information regarding this BMG.

Table 4 Thermodynamic and elastic properties of $Cu_{60}Zr_{20}Hf_{10}Ti_{10}$ BMG

Approach	Screening function	$v_L \times 10^5 \left(\frac{cm}{s}\right)$	$v_T \times 10^5 \left(\frac{cm}{s}\right)$	$B_T \times 10^{11} \left(\frac{dyne}{cm^2}\right)$	$G \times 10^{11} \left(\frac{dyne}{cm^2}\right)$	σ	$Y \times 10^{11} \left(\frac{dyne}{cm^2}\right)$	$\theta_D(K)$
HB	H	6.13	3.54	17.44	10.46	0.25	26.16	467.30
	T	6.18	3.57	17.73	10.64	0.25	26.60	471.20
	IU	6.11	3.53	17.35	10.41	0.25	26.02	466.06
	F	6.13	3.54	17.43	10.46	0.25	26.15	467.18
	S	6.12	3.54	17.42	10.45	0.25	26.13	467.00
Other theoretical [10, 23, 24, 23–26]		4.62	2.11	12.23 12.82	3.69 4.14 4.42	0.34 0.36 0.37	10.11 10.27 10.31 10.70 11.50 11.77 14.20	282.00
Experimental [8, 25, 26, 19, 20]		–	–	12.82	3.69	0.37	10.10	–
Crystalline state [8, 20]		4.80	2.34	13.13	4.59	–	12.33	312.00

4   Conclusion

The present work supports the pseudopotential theory and PAA model. Such a study can be carried for any multicomponent BMG. The work confirms the applicability of the proposed model potential, screening functions and computational approach. The presently selected Shaw's optimized constant core model pseudopotential along with HB-computational approach working under the screening influence of H, T, IU, F and S localized correlation functions—all together successfully reproduce main characteristics of the interatomic pair potential, PCFs and PDCs as they could generate a complete and comparable data of the BMG under investigation.

References

1. Gandhi AL, Vora AM (2019) Theoretical study of thermodynamic and elastic properties of $Ti_{50}Be_{34}Zr_{16}$ BMG—a pseudopotential method. Int J Trend Sci Res Dev 3:1076–1080. https://doi.org/10.31142/ijtsrd21550
2. Vora AM, Gandhi AL (2019) Collective dynamics of Zr-based bulk metallic glasses. Chinese J Phys 62:284–295. https://doi.org/10.1016/j.cjph.2019.10.013
3. Gandhi AL, Vora AM (2020) A theoretical study of vibrational dynamics of $Ti_{60}Zr_{16}V_9Cu_3A_{13}Be_9$ hexanary bulk metallic glass by pseudopotential theory and estimation of thermodynamic and elastic properties using BS approach. AIP Conf Proc 2224:030010(1)–030010(5). https://doi.org/10.1063/5.0000487
4. Vora AM, Gandhi AL (2021) Phonon dynamics of $Zr_{67}Ni_{33}$ and $Fe_{80}B_{20}$ binary glassy alloys. BIBECHANA 18:33–47. https://doi.org/10.3126/bibechana.v18il.28760
5. Vora AM (2008) Phonon dispersion in binary metallic glasses. Glass Phys Chem 34(6):671–682
6. Wang ZX et al (2004) Crystallization mechanism of Cu-based supercooled liquid under ambient and high pressure. Phys Rev B 46(092202):1–4
7. Wang ZX et al (2003) Formation and crystallization of CuZrHfTi BMG under ambient and high pressure. J Phys: Condens Matter 15:5923–5932
8. Wang ZX (2006) Elastic properties of $Cu_{60}Zr_{20}Hf_{10}Ti_{10}$ BMG under high pressure. Mater Lett 60:831–833
9. Agarwal PC (2005) Dynamics of BMG $Cu_{60}Zr_{20}Hf_{10}Ti_{10}$. Mater Sci Eng-A 404(1–2):301–304
10. Borja Soto CE et al (2016) Composition, elastic property and packing efficiency predictions for BMGs in binary. Ternary Quat Syst Mat Res 19(2):285–329
11. Wills JM, Harrison WA (1983) Interionic interactions in transition metals. Phys Rev B 28:4363–4373
12. Shaw RW (1968) Optimum form of a modified Heine-Abarenkov model potential for the theory of simple metals. Phys Rev 174(3):769–781
13. Harrison WA (1999) Elementary electronic structure. World Scientific, Singapore
14. Taylor R (1978) A simple, useful analytical form of the static electron gas dielectric function. J Phys F: Metal Phys 8:1699–1702
15. Ichimaru S, Utsumi K (1981) Analytic expression for the dielectric screening function of strongly coupled electron liquids at metallic and lower densities. Phys Rev B 24(12):7385–7388
16. Farid B et al (1993) Extremal properties of the Harris-Foulkes functional and an improved screening calculation for the electron gas. Phys Rev B 48(16):11602–11621
17. Sarkar A et al (1998) Static local field factor for dielectric screening function of electron gas at metallic and lower densities. Mod Phys Lett B 12(6):639–648
18. Hubbard J, Beeby JL (1969) Collective motion in liquids. J Phys C: Solid State Phys 2(3):556–571

19. HaiBo KE et al (2015) Structural heterogeneity and deformation rheology in metallic glasses. Sci China Technol Sci 58:47–55
20. Li S et al (2005) Formation and properties of new heavy rare-earth-based bulk metallic glasses. Sci Tech Adv Mater 6:823
21. Bretonnet JL, Derouiche A (1990) Variational thermodynamic calculations for liquid transition metals. Phys Rev B 43:8924–8929
22. Thorpe MF (1983) Continuous deformation in random networks. J Non-Cryst Solids 57(3):355–370
23. Wang WH et al (2004) Bulk metallic glasses. Mater Sci Eng 44:45–89
24. Rouxel T (2007) Elastic properties and short-to-medium range order in glasses. J Am Ceram Soc 90(10):3019–3039
25. Wang WH (2011) The elastic properties, elastic models and elastic perspectives of metallic glasses. Prog Mater Sci 57(3):487–656
26. Wang WH (2006) Correlation between elastic moduli and properties in bulk metallic glass. J Appl Phys 99(093506):1–10

Microstructure and Texture Study of High Temperature Upset Forged 304LN Stainless Steel

Matruprasad Rout, Shiv B. Singh, Ravi Ranjan, and Surjya K. Pal

1 Introduction

The austenitic group of stainless steel is an important group of material for nuclear, petro-chemical and fertilizer industries [1]. These steels possess exceptional corrosion resistance and higher strength at high temperatures [2] which makes them the material of choice under these severe environment. Usually produced through thermo-mechanical processes [3], these single-phase steels [4] undergo microstructural changes which largely influence their final properties. These microstructural changes are described by recovery, recrystallization and grain growth which are mainly controlled by the process parameters viz. strain, strain rate and temperature [5]. For low static fault energy (SFE) material, such as 304 austenitic stainless steel [6, 7], the microstructural changes during deformation are primarily driven by the discontinuous dynamic recrystallization (dDRX) [8–10]. A good number of work describing the hot deformation behavior of this material have been reported in the literature where the compression tests were carried out in the lower strain rate range of 0.0001–10 s^{-1} [11–17]. However, axial compression or upset forging of bulk material at a low strain rate can significantly affect the production rate, as the strain rate is controlled by the velocity of the forging press die [18]. Hence, forging at a

M. Rout (✉)
Department of Production Engineering, National Institute of Technology Tiruchirappalli, Tiruchirappalli 620015, India

S. B. Singh
Department of Metallurgical and Materials Engineering, Indian Institute of Technology Kharagpur, Kharagpur 721302, India

R. Ranjan
Research and Development Division, TATA Steel, Jamshedpur 831001, India

S. K. Pal
Department of Mechanical Engineering, Indian Institute of Technology Kharagpur, Kharagpur 721302, India

113
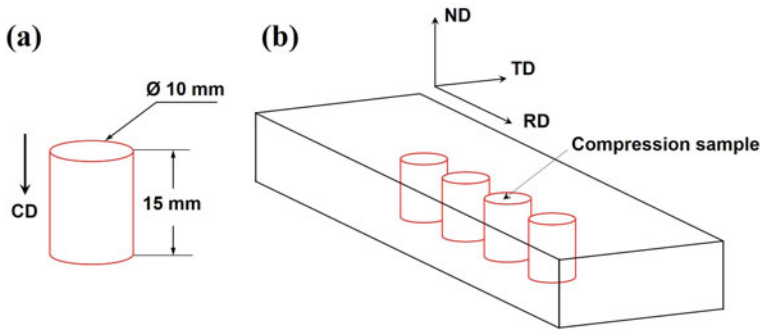
Fig. 1 **a** Dimensions of compression sample and **b** orientation of compression samples on the as-received plate

higher strain rate is required to improve the productivity. However, the strain rate significantly affects the material behavior, microstructure and texture development, especially at higher temperatures [5, 17, 19]. So, in the present work, an attempt has been made to study the development of microstructure and texture in an austenitic stainless steel subjected to hot deformation at a strain rate of 100 s^{-1}.

2 Experimental Details

2.1 Compression Test

The considered 304LN austenitic stainless steel material (Ni-8.04, Cr-18.29, C-0.035, Si-0.384, Mn-1.5, Mo-0.17, N-0.09 wt. %) was obtained as a hot rolled and solution annealed plate. Cylindrical samples of 10 mm diameter and 15 mm height (Fig. 1a), with orientation as shown in Fig. 1b, were cut from the as-received material. The uniaxial compression tests at strain rate of 100 s^{-1} were performed on Gleeble 3800 system. Samples were heated (at the rate of 5 °C/s) to various required test temperatures (900 °C, 1000 °C, 1100 °C and 1200 °C) and held at a particular temperature for 5 min for uniform heating. Compressive load was then applied along the thickness direction of the samples to deform them to a true strain of ~0.4. Samples were then rapidly cooled to room temperature so that the deformed microstructure can be retained for further analyses.

2.2 Characterization

The compressed samples were cut along the thickness direction and were subjected to mechanical polishing followed by electro-polishing. Metallographic observations
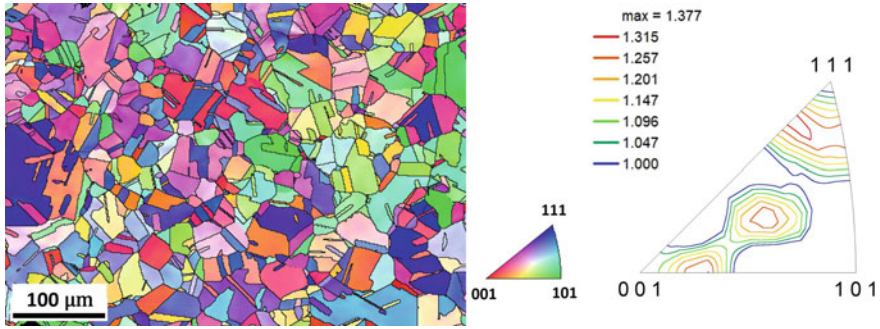
Fig. 2 IPF map and [100] IPF of as-received material

viz. microstructure and crystallographic texture were studied at the center volume (on RD-ND surface) of the compressed samples through electron back scatter diffraction (EBSD). The EBSD scans, with a step size of 0.7 μm, were performed on FIB-SEM operated at 25 kV. Obtained scan data were analyzed on TSL OIM software. Before analyses, scan data were subjected to the standard grain-dilation clean-up procedure for a single iteration. The developed microstructures are represented in the form of inverse pole figure (IPF) map and the grain boundaries were characterized, based on the misorientation angle (θ), as follows: very low angle boundaries (VLABs, $2° \leq \theta \leq 5°$), low angle boundaries (LABs, $5° < \theta \leq 15°$) and high angle grain boundaries (HAGBs, $\theta > 15°$). For the study of coincidence site lattice (CSL) boundaries, Brandon criterion [20] was followed. For texture analysis, orthotropic sample symmetry was considered to compare the compression developed texture with the as-received material texture. The ND of as-received material is taken as the compression direction (CD) for compression test samples. The crystallographic texture, of the as-received and the deformed samples, is represented in the form of [100] inverse pole figure (IPF) and the texture intensities are presented in terms of maximum of random distribution (MRD). Figure 2 shows the microstructure and the [100] IPF of as-received 304LN austenitic stainless steel. The material was in solution annealed condition and hence annealing twins can be seen from the microstructure. The average grain size, calculated by area fraction method, was found to be ~27 μm.

3 Results and Discussions

3.1 Microstructure

Figure 3(a–d) shows the IPF map for the samples compressed at 900 °C, 1000 °C, 1100 °C, and 1200 °C with 100 s^{-1} strain rate. Whereas, Fig. 3(e–h) shows the corresponding phase map. For 900 °C deformed grains can be observed and a color gradient across the grains indicating the change in orientations can be seen. Except for
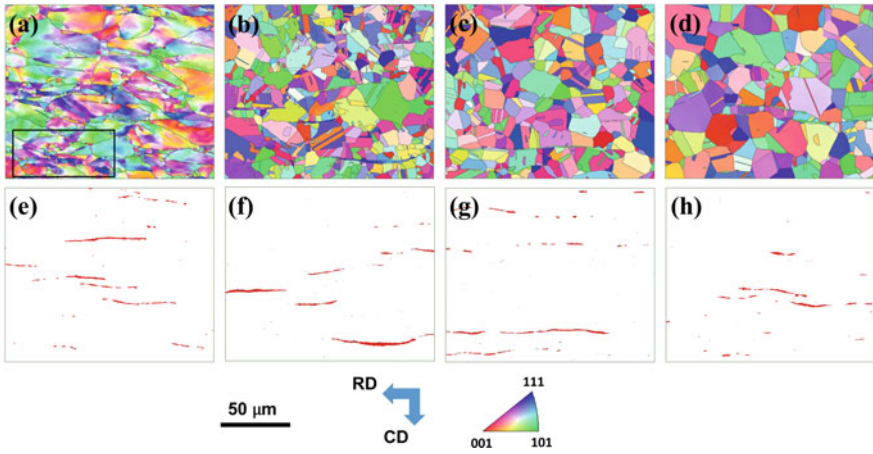
Fig. 3 IPF maps for samples compressed at 100 s^{-1} **a** 900 °C, **b** 1000 °C, **c** 1100 °C, **d** 1200 °C and **e**–**h** corresponding phase map (color code: white–austenite, red–delta ferrite)

900 °C, at all other temperatures the resultant microstructure contains recrystallized grains. However, there is an increase in grain size with increase in the deformation temperature can be observed. The average grain size (area fraction method) was found to be 18 µm (±11.26 µm), 9.5 µm (±4.75 µm), 11.75 µm (±5.57 µm) and 15.18 µm (±7.8 µm) for 900 °C, 1000 °C, 1100 °C, and 1200 °C, respectively. For grain size calculation, twin boundaries were included in the high angle grain boundaries.

A magnified view of the IPF map of the sample deformed at 900 °C is shown in Fig. 4a. It can be noted that the initial microstructure (Fig. 2) was in annealed condition and the effect of deformation on the microstructure can be easily identified from Fig. 4a. The grains got elongated as they are constrained by the surrounding grains and hence, accommodate strain. The grain boundaries also got serrated. Apart from the large deformed grains, small equi-axed grains can be seen which might
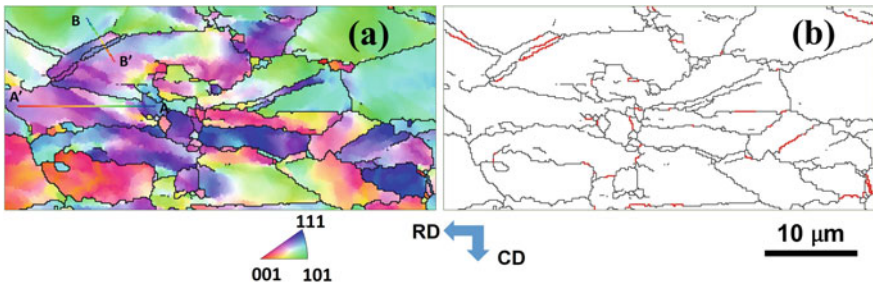
Fig. 4 a Magnified view of the highlighted area of the Fig. 3a, and **b** the corresponding grain boundary map (black line–HAGBs and red line–Σ3 CSL boundaries)
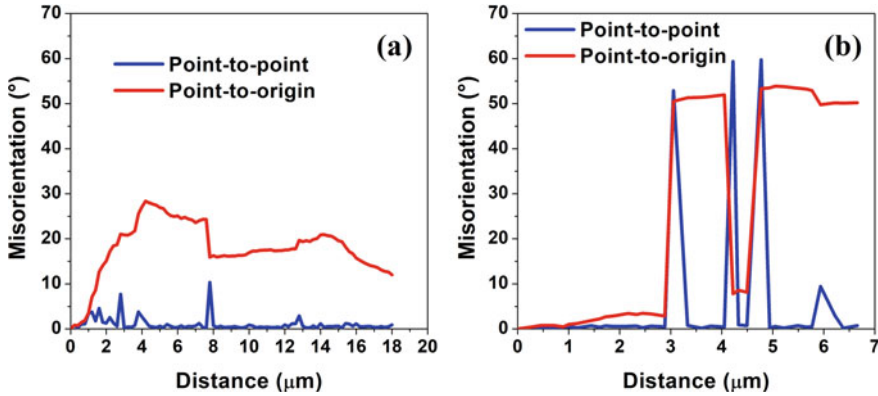
Fig. 5 Misorientation profile along **a** AA′ (i.e. within the grain) and **b** BB′ (i.e. across the grain)

be formed due to dynamic recrystallization (DRX). These strain-free grains can be seen at the serrated grain boundaries indicating bulging as the mechanism of nuclei formation for DRX. The DRX for deformation at lower strain rates (0.01 to 1 s^{-1}) was also explained by the bulging mechanism [5].

The accumulated strain within the grain is analyzed by plotting the variation of the misorientation angle within a grain (along AA′) and is shown in Fig. 5a. Here the misorientation along AA′ is represented both by point-to-point and point-to-origin (A as origin). The point-to-point misorientation variation is having a low value with two distinct peaks ($5° < \theta \leq 15°$). These two peaks represent the formation of LABs. On the other hand, the point-to-origin profile is having a gradual increase in misorientation value. This shows the misorientation formation of the same nature, resulting in the accumulation of θ value. However, at the second peak of the point-to-point misorientation profile, the point-to-origin profile drops sharply indicating the misorientation formed to be of opposite nature [21]. A similar misorientation profile plot has also been plotted across the grain boundaries (along BB′) and is shown in Fig. 5b. Sharp peaks (θ close to 60°) can be seen for the point-to-point misorientation profile. This indicate the formation of $\Sigma3$ CSL boundaries (60° around $\langle 111 \rangle$). The same can also be seen from Fig. 4b ($\Sigma3$ boundaries are shown in red color).

3.2 Formation of δ Ferrite

Figure. 3(e–h) shows the different phases present in the deformed microstructure. The presence of a small fraction of the BCC phase can be observed. These are considered to be δ ferrite and observed near the austenite grain boundaries as can be seen from the corresponding IPF maps (Fig. 3(a–d)). The as-received material (Fig. 2) does not show any trace of δ ferrite. This indicates that the formation of δ ferrite is the result of the deformation. It can be noted that the microstructure has been taken at the center

region of the deformed samples which experience the highest strain and the chance of formation of δ ferrite is more in the region of higher strain [22]. The development of δ ferrite in austenitic stainless steel during high-temperature deformation at high strain rate has been reported earlier [23–26]. Sundararaman et al. [23] and Venugopal et al. [26] observed the δ ferrite in 304L austenitic stainless steel after the deformation at 1200 °C with 100 s^{-1} strain rate. However, in the present case, the δ ferrite is observed for each deformation temperatures i.e. 900 °C, 1000 °C, 1100 °C and 1200 °C. This can be noted that, for the studied material, δ ferrite has not been observed in the lower strain rate range i.e. 0.01 to 1 s^{-1} [3, 5, 27]. In addition to deformation at high-temperature and high strain rate, the composition of the 304 austenitic stainless steel also plays an important role in the formation of δ ferrite [22]. The 304 stainless steel with higher chromium equivalent to nickel equivalent ratio develops more δ ferrite during high temperature deformation. However, above 1050 °C the effect of carbon on the deformation characteristic of the 304 stainless steel material is negligible. The development of δ ferrite in 304 stainless steel can be possible through adiabatic heating during the plastic deformation and/or flow-induced transformation [25]. The temperature rise (ΔT) due to adiabatic heating during deformation can be calculated from the following equation [28]

$$\Delta T = \frac{0.95\eta}{\rho C_p} \int\limits_0^\varepsilon \sigma \, d\varepsilon$$

where, η is the thermal efficiency, ρ is the density, C_p is the specific heat, σ is the flow or true stress and ε is the true strain. For the present work, the calculated values of ΔT at $\varepsilon = 0.4$ varies from ~12 °C to 22 °C. This small rise in temperature is insufficient for the δ ferrite transformation. Hence, the development of δ ferrite is a result of deformation. The transformation of austenite to ferrite is enhanced by the dislocation interaction leading to an increase in dislocation density which eases the transformation [29]. This transformation is observed in the region of intense shear [26]. Also, the development of twins and twin bands at higher strain rate provides the additional nucleation sites for the δ ferrite formation [25].

3.3   Grain Boundary Character Distributions

The fraction of different kind of grain boundaries developed after processing is shown in Fig. 6a. As seen from the IPF map (Fig. 3a), sample compressed at 900 °C has deformed grains. Hence a higher fraction of boundaries with θ < 15° is expected. The same can be seen from Fig. 6a as the fraction of boundaries with θ < 15° is ~0.71, highest among all the samples. For other three temperatures high fraction (~0.96–0.98) of HAGBs is developed. This can be noted that the HAGBs also includes the CSL boundaries in which Σ3, among others, contributes a large fraction (~0.457–0.522). However, the fraction of Σ3 boundaries slightly decreases when the deformation temperature increases (Fig. 6b). A similar kind of observation can
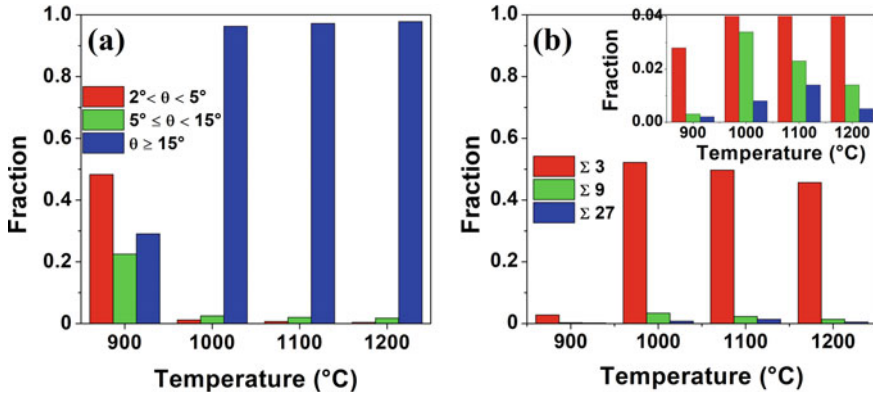
Fig. 6 **a** Grain boundary character distribution and **b** fraction of Σ3, Σ9 and Σ27 boundaries for samples compressed at 900 °C, 1000 °C, 1100 °C and 1200 °C

also be seen for Σ9 boundaries (38.94° around ⟨110⟩). On the other hand there is an increase in fraction of Σ27 boundaries (Σ27a–31.58° around ⟨110⟩ and Σ27b–35.42° around ⟨210⟩), except at 1200 °C. The Σ9 and Σ27 boundaries are formed by multiple twinning where two twins interact with each other. Intersection of two Σ3 boundaries results in the formation of Σ9 and interaction Σ3 and Σ9 leads to the formation of Σ27 boundaries. However, interaction of two CSL, governed by the following rule, may also results in the dissociation of CSL [30].

$$\Sigma A \times \Sigma B \rightarrow \Sigma(A \times B) \text{ or } \Sigma A \times \Sigma B \rightarrow \Sigma(A/B)$$

So, interaction of Σ3 and Σ9 may either form Σ27 or Σ3 CSL boundaries. A low fractions of Σ9 and Σ27 boundaries observed in Fig. 5b indicate fewer interaction of twin boundaries. These low energy configured Σ-CSL boundaries can alter the grain boundary dependent properties of the material like corrosion [31].

3.4 Texture Evolutions

The texture of the as-received material and the texture developed by the compression at different temperatures are shown by [100] IPF in Fig. 7(a–e). No trace of delta ferrite (BCC) was observed in the as-received material, hence only FCC texture corresponding to the austenite phase is shown in Fig. 7a. For compression at 900 °C, BCC texture intensities can be observed near [001] and scatter towards [101]. With an increase in deformation temperature [101] crystal axes align with the compression axis however, a decrease in texture intensities (maximum MRD ~9.14 to ~7.29) with the increase in temperature can be seen. In the FCC phase, deformation at 900 °C produces grains with [111] and [001] parallel to CD. From the IPF map (Fig. 4a) it
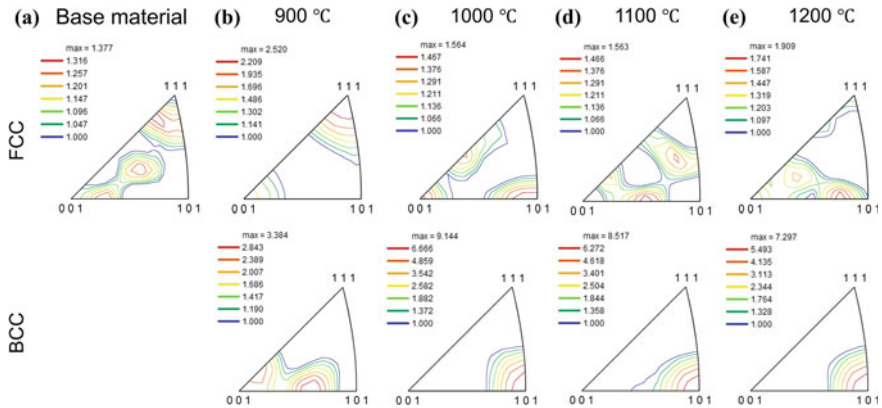
Fig. 7 [100] IPF for **a** base material and for samples deformed with strain rate $100\,\mathrm{s}^{-1}$ at temperature **b** 900 °C, **c** 1000 °C, **d** 1100 °C, and **e** 1200 °C

is clear that compression at 900 °C results in deformed grains. So, the [111] ‖ CD and [001] ‖ CD represents the deformed texture. With an increase in the temperature the [111] ‖ CD texture component disappears, however at 1200 °C low intensity can be observed. At these temperatures, recrystallized grains are developed. However, these recrystallized grains do not exhibit any preferred growth directions as can be seen from the IPFs (Fig. 7(c–e)). This random texture development is usually attributed to the formation of annealing twins. The presence of annealing twins in the microstructure can be seen from the corresponding IPF maps shown in Fig. 3(a–d).

4   Summary and Conclusions

Microstructure and texture of the 304LN stainless steel upset forged at $100\,\mathrm{s}^{-1}$ have been studied through EBSD. The following conclusions can be made from the above study.

i.   Deformation at 900 °C produces deformed grains however deformation at 1000 °C to 1200 °C produces fully recrystallized microstructure with increase in grain size with increase in deformation temperature.

ii. The Σ3 CSL boundary largely contributes to the high angle grain boundaries formed by recrystallization.

iii. Deformation at $100\,\mathrm{s}^{-1}$ strain rate produces δ ferrite with orientation [101] ‖ to the deformation direction. No specific orientation, for deformation at all the temperature, has been observed for the FCC austenite phase.

References

1. Chowdhury SG, Das S, De PK (2005) Cold rolling behaviour and textural evolution in AISI 316L austenitic stainless steel. Acta Mater 53:3951–3959. https://doi.org/10.1016/j.actamat.2005.05.006

2. Fang X, Zhang K, Guo H, Wang W, Zhou B (2008) Twin-induced grain boundary engineering in 304 stainless steel. Mater Sci Eng A 487:7–13. https://doi.org/10.1016/j.msea.2007.09.075

3. Rout M, Biswas S, Ranjan R, Pal SK, Singh SB (2018) Deformation behavior and evolution of microstructure and texture during hot compression of AISI 304LN stainless steel. Metall Mater Trans A 49:864–880. https://doi.org/10.1007/s11661-017-4447-5

4. Paggi A, Angella G, Donnini R (2015) Strain induced grain boundary migration effects on grain growth of an austenitic stainless steel during static and metadynamic recrystallization. Mater Charact 107:174–181. https://doi.org/10.1016/j.matchar.2015.07.003

5. Rout M, Ranjan R, Pal SK, Singh SB (2018) EBSD study of microstructure evolution during axisymmetric hot compression of 304LN stainless steel. Mater Sci Eng A 711:378–388. https://doi.org/10.1016/j.msea.2017.11.059

6. Taylor AS, Hodgson PD (2011) Dynamic behaviour of 304 stainless steel during high Z deformation. Mater Sci Eng A 528:3310–3320. https://doi.org/10.1016/j.msea.2010.12.093

7. Simmons JW (1996) Overview: high-nitrogen alloying of stainless steel. Mater Sci Eng A 207:159–169

8. Mirzadeh H, Cabrera JM, Najafizadeh A, Calvillo PR (2012) EBSD study of a hot deformed austenitic stainless steel. Mater Sci Eng A 538:236–245. https://doi.org/10.1016/j.msea.2012.01.037

9. Wahabi M, Gavard L, Cabrera JM, Prado JM, Montheillet F (2005) EBSD study of purity effects during hot working in austenitic stainless steels. Mater Sci Eng A 393:83–90. https://doi.org/10.1016/j.msea.2004.09.064

10. Wahabi ME, Gavard L, Montheillet F, Carbera JM, Prado JM (2005) Effect of initial grain size on dynamic recrystallization in high purity austenitic stainless steels. Acta Mater 53:4605–4612. https://doi.org/10.1016/j.actamat.2005.06.020

11. Mirzadeh H, Parsa MH, Ohadi D (2013) Hot deformation behavior of austenitic stainless steel for a wide range of initial grain size. Mater Sci Eng A 569:54–60. https://doi.org/10.1016/j.msea.2013.01.050

12. Wahabi M, Cabrera JM, Prado JM (2003) Hot working of two AISI 304 steels: a comparative study. Mater Sci Eng A 343:116–125. https://doi.org/10.1016/S0921-5093(02)00357-X

13. Dehghan-Manshadi A, Barnett MR, Hodgson PD (2008) Recrystallization in AISI 304 austenitic stainless steel during and after hot deformation. Mater Sci Eng A 485:664–672. https://doi.org/10.1016/j.msea.2007.08.026

14. Kim S-I, Yoo Y-C (2001) Dynamic recrystallization behavior of AISI 304 stainless steel. Mater Sci Eng A 311:108–113. https://doi.org/10.1016/S0921-5093(01)00917-0

15. Wang C, Feng H, Zheng W, Song Z, Yong Q (2013) Dynamic recrystallization behavior and microstructure evolution of AISI 304N stainless steel. J Iron Steel Res Int 20:107–112. https://doi.org/10.1016/S1006-706X(13)60185-5

16. Belyakov A, Miura H, Sakai T (2000) Dynamic recrystallization in ultra fine-grained 304 stainless steel. Scr Mater 43:21–26. https://doi.org/10.1016/S1359-6462(00)00373-0

17. Belyakov A, Miura H, Sakai T (1998) Dynamic recrystallization under warm deformation of a 304 type austenitic stainless steel. Mater Sci Eng A 255:139–147. https://doi.org/10.1016/S0921-5093(98)00784-9

18. Switzner NT, Van Tyne CJ, Mataya MC (2010) Effect of forging strain rate and deformation temperature on the mechanical properties of warm-worked 304L stainless steel. J Mater Process Technol 210:998–1007. https://doi.org/10.1016/j.jmatprotec.2010.01.014

19. Ferdowsi MRG, Nakhaie D, Benhangi PH, Ebrahimi GR (2014) Modeling the high temperature flow behavior and dynamic recrystallization kinetics of a medium carbon microalloyed steel. J Mater Eng Perform 23:1077–1087. https://doi.org/10.1007/s11665-013-0815-5

20. Brandon DG (1966) The structure of high-angle grain boundaries. Acta Metall 14:1479–1484. https://doi.org/10.1002/pssb.19690310123
21. Jorge-Badiola D, Iza-Mendia A, Gutiérrez I (2007) Evaluation of intragranular misorientation parameters measured by EBSD in a hot worked austenitic stainless steel. J Microsc 228:373–383. https://doi.org/10.1111/j.1365-2818.2007.01850.x
22. Soleymani S, Ojo OA, Richards N (2015) Effect of composition on the formation of delta ferrite in 304L austenitic stainless steels during hot deformation. J Mater Eng Perform 24:499–504. https://doi.org/10.1007/s11665-014-1290-3
23. Sundararaman D, Divakar R, Raghunathan V (1993) Microstructural features of a type 304L stainless steel deformed at 1473 K in the strain rate interval $10–3$ s^{-1} to 102 s^{-1}. Scr Metall Mater 28:1077–1082. https://doi.org/10.1016/0956-716X(93)90013-I
24. Sundararaman D, Divakar R, Raghunathan VS (1994) Reply to comments on "Microstructural features of a type 304L stainless steel deformed at 1473 K in the strain rate interval $10–3$ s^{-1} to 102 s^{-1}." Scr Metall Mater 30:1617–1622. https://doi.org/10.1016/0956-716X(94)90318-2
25. Venugopal S, Mannan SL, Prasad YVRK (1996) Influence of strain rate and state-of-stress on the formation of ferrite in stainless steel type AISI 304 during hot working. Mater Lett 26:161–165. https://doi.org/10.1016/0167-577X(95)00215-4
26. Venugopal S, Ravishankar C, Mannan SL, Prasad YVRK (1994) Comments on the paper entitled "Microstructural features of a type 304L stainless steel deformed at 1473 K in the strain rate interval $10–3$ to 102 s^{-1}." Scr Metall Mater 30:1611–1616
27. Rout M, Singh SB, Pal SK (2020) Microstructure and texture evolution in austenitic stainless steel during low strain rate deformation at elevated temperature. Int J Mater Form 13:605–621. https://doi.org/10.1007/s12289-019-01500-8
28. Goetz RL, Semiatin SL (2001) The adiabatic correction factor for deformation heating during the uniaxial compression test. J Mater Eng Perform 10:710–717. https://doi.org/10.1361/105994901770344593
29. Cahn RW, Haasen P (1996) Physical metallurgy by cahn and haasen.pdf. North-Holland, Amsterdam
30. Randle V (2004) Twinning-related grain boundary engineering. Acta Mater 52:4067–4081. https://doi.org/10.1016/j.actamat.2004.05.031
31. Shimada M, Kokawa H, Wang ZJ, Sato YS, Karibe I (2002) Optimization of grain boundary character distribution for intergranular corrosion resistant 304 stainless steel by twin-induced grain boundary engineering. Acta Mater 50:2331–2341. https://doi.org/10.1016/S1359-6454(02)00064-2

Sol-gel Preparation and Characterization of ZnCaAl$_2$O$_4$ Composite Nanoparticles

Sekhar Didde, R. S. Dubey , and Sampad Kumar Panda

1 Introduction

Communication is classified in to two categories, one is wired communication, and another one is wireless communication. Due to the improvement in the technology, the wireless communication must be present with qualified functions and provide small dimensions with an antenna. In the Global positioning system, antenna becomes a crucial matter as growing the operating frequencies. Nanoceramic compounds are significant for the wireless communications with their low-dimension, low-process cost, and minimum loss through the components. Further, these materials possess high quality factor and controlled dielectric permittivity therefore, considered to be promising as the choice as global positioning system patch antenna materials. Microwave dielectric ceramics has performed significant roles in the global telecommunications sector over the past several decades, with a large variety of applications from land to satellite. Dielectric ceramics are commonly employed in the devices working in the frequency range from 300 MHz and 300 GHz. The nanoceramic material is highly suited and efficient to produce smaller devices by enhancing the dielectric constant in a reasonable range. In current scenario, the microwave operating frequency regime is getting widening to have a broad spectrum of millimeter-wave applications.

S. Didde
Department of ECE, Swarnandhra College of Engineering and Technology, Narsapur,
Andhra Pradesh 534275, India

R. S. Dubey (✉)
Department of Nanotechnology, Swarnandhra College of Engineering and Technology, Narsapur,
Andhra Pradesh 534275, India

S. K. Panda
Department of ECE, KL University, Greenfields, Vaddeswaram, Guntur, Andhra Pradesh, India

In this context, there is a demand of suitable ceramic materials that can improve the performance and size of global positioning system and therefore, the ceramic materials should have high dielectric permittivity. The nanoceramic materials not only reduce the size of the device but also cost with the enhanced characteristics of the material [1, 2]. In current trends zinc aluminate ($ZnAl_2O_4$) based microwave ceramics have excellent dielectric properties which also have improved thermal stability along with a better mechanical resistance and surface sharpness. Recently several dielectric-ceramic materials have been investigated such as $MgCoTiO_3$-$NaNdTiO_3$, $ZnTa_2O_6$-TiO_2, $MgCoTiO_3$-$NaNd$, (1-x)$Ca(Mg_{1/3}Nb_{2/3})O_3$-x$(Ca_{0.8}Sr_{0.2})TiO_3$, $CaTiO_3$-$Sm(Mg_{1/2}Ti_{1/2})O$, $LaMg_{12}Ti1_2O_3$-$CaSrTiO_3$, (1-x)$(Mg_{0.95}Co_{0.05})TiO_3$-x$(Na_{0.5}Nd_{0.5})TiO_3$, $Nd(Mg_{12}Ti_{12})O_3$-$SrTiO_3$, ZrO_2-ZnO-Ta_2O_5-TiO_2, $MgZnTiO_3$-$CaNdTiO_3$, $ZnAl_2O_4$-Co_2TiO_4, $ZnAl_2O_4$-xMg_2TiO_4, $0.75ZnAl_2O_4$-$0.25TiO_2$-$MgTiO_3$ and $(Mg_{(1-x)}Cox)2SnO_4$ [3–12]. For the synthesis, various techniques like thermal decomposition, sol–gel, Hydrothermal, Solvothermal, microwave-assisted, and so on are recognized. In spite of these methods, the sol gel method well suited for the synthesis of compound nanoceramics due to its easy handling, low-cost and non-hazardous process which produces nanoparticles with the better stoichiometry and homogeneity.

In this work, we present the synthesis and characterization of calcium zinc aluminate ($ZnCaAl_2O_4$) composite nanoparticles by sol–gel route and studied the dielectric permittivity. Section 2 presents the experimental approach of composite nanoparticles and results are discussed in Sect. 3. Finally, Sect. 4 summarizes the paper.

2 Experimental Details

Zinc acetate, aluminum nitrate nonahydrate and calcium nitrate tetrahydrate were used as the source of Z, Al and Ca without any further purification. At first, aluminum nitrate nonahydrate was mixed in 40 ml absolute ethanol under a constant stirring and then 0.33 ml ethylene glycol was added as the chelating agent in the above mixture. Later, 5.868 gm zinc acetate and 2.83 gm calcium nitrate tetrahydrate were added in this solution. This solution was stirred for 1 h while maintaining 75 °C and later 0.24 ml nitric acid dropped in order to get the homogeneous solution. After attaining this, the solution thermally treated under constant stirring for 1 h. The obtained the gel was dried at 180 °C in hot air oven for nearly 2 h to get the powder and later calcined in muffle furnace at temperature 700 °C. Finally, the calcined sample was ground to get the fine powder of $ZnCaAl_2O_4$. The as prepared sample was examined by X-ray diffraction (XRD), Fourier-Transform Infrared Spectroscopy (FTIR), Scanning Electron Microscopy (SEM), Energy Dispersive Spectroscopy (EDS), finally dielectric property was studied.

3   Results and Discussion

Figure 1 depicts the XRD pattern of $ZnCaAl_2O_4$ nanoceramic compound particles calcined at temperature 700 °C for 1 h. The XRD pattern demonstrates the presence of mixed crystalline phases of $ZnAl_2O_4$ and $ZnCaAl_2O_4$.

The $ZnAl_2O_4$ peaks originated at Bragg angle $2\Theta = 31.3°$, 36.3°, 44.6°, 47.6°, 55.6° and 59.7° were indexed to the planes (220), (311), (400), (331), (422), and (511) respectively. The intense peaks located at $2\Theta = 31.3°$ and 36.3° were assigned to the face-centered cubic structure of $ZnAl_2O_4$ while the small peak originated at $2\Theta = 26.6°$ was assigned to the attributed to the $ZnCaAl_2O_4$ of the plane (422). The diffraction peaks were coincided with the JCPDS File Nos. 01-087-0265 and 00-050-0426 corresponding to the $ZnCaAl_2O_4$ and $ZnAl_2O_4$ respectively. One can also notice a ZnO impurity peak of the plane (002) [1, 5, 12]. We can notice that an addition of calcium did not disturb the crystallinity of the host material.

Figure 2 shows the Fourier-Transform Infrared Spectroscopy (FTIR) spectra of calcined $ZnCaAl_2O_4$ recorded in the wave number range from 400 to 4000 cm^{-1}. The FTIR spectra depicts the various vibration peaks of $ZnCaAl_2O_4$ nanoceramic particles originated at wave number values 654, 1410, 1744, 2318, 3446 and 3743 cm^{-1}. A broad peak from 3446 to 3743 cm^{-1} is attributed to the O–H stretching mode while another peak at 2318 cm^{-1} is found associated with the presence of water molecules. The stretching vibration mode of Al-O can be assigned to a peal originated at 1410 cm^{-1}. The other vibration peak at 654 cm^{-1} was ascribed to the inorganic material. The FTIR vibration peaks was found consistent with the reported literature [1, 5, 12].

We have investigated the morphology of nanoceramic nanoparticles using scanning electron microscopy (SEM). Figure 3 depicts the SEM micrographs of $ZnCaAl_2O_4$ nanoparticles. Figure 3a, b shows SEM images at the scale 2 micron

Fig. 1 XRD pattern of $ZnCaAl_2O_4$ nanoparticles prepared by sol–gel process
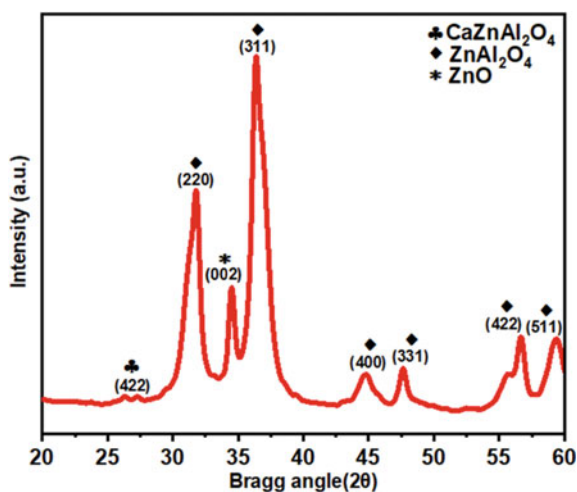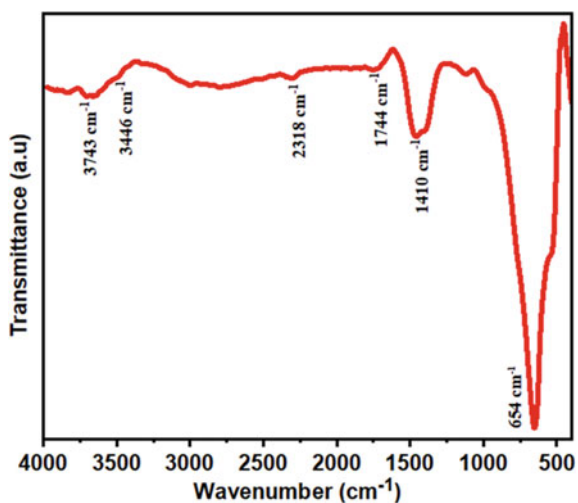
Fig. 2 FTIR spectra of ZnCaAl$_2$O$_4$ thin films annealed at 700 °C for one hour
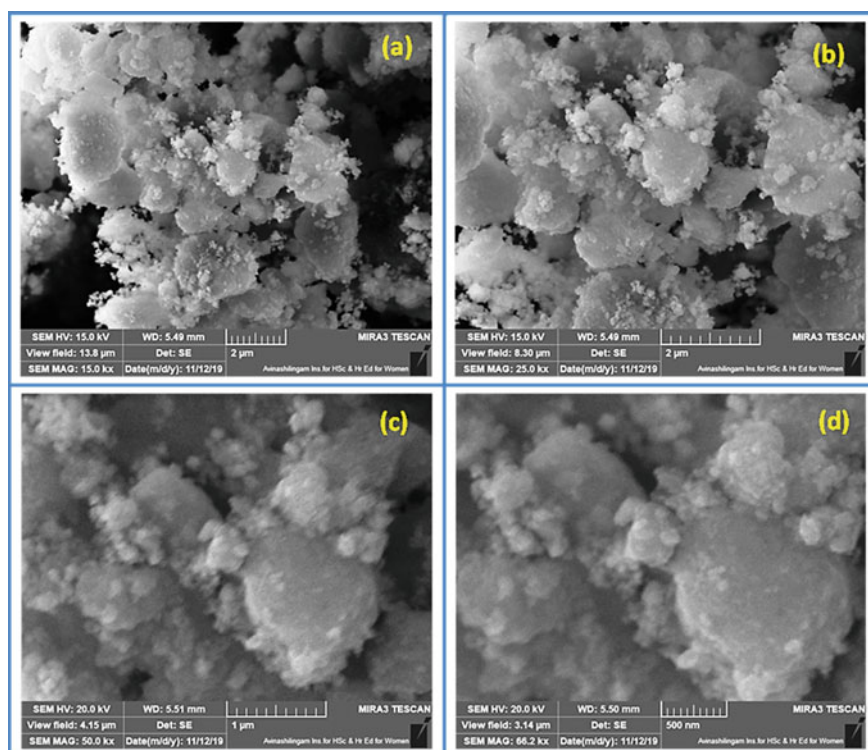
Fig. 3 Depicts the SEM micrographs of ZnCaAl$_2$O$_4$ nanoceramic particles calcined at temperature 700 °C.

however, second image is recorded at high magnification which evidenced the preparation of spherical nanoparticles of $ZnCaAl_2O_4$. Similarly, Fig. 3c, d shows the SEM images recorded at resolution 1 micron and 500 nm respectively. The SEM investigation demonstrates the formation of agglomerated nanoparticles. The estimated mean diameter of the nanoparticles was found to be 50 nm.

EDS investigation is useful approach to study the elemental compositions present in the prepared sample. It works on a simple phenomenon of the interaction of X-ray with the specimen. With this tool, the element mapping can be carried out in the form of images which demonstrate the spatial distribution of various elements existing in the sample. To know the compositional elements in $ZnCaAl_2O_4$ sample, we have carried out the element mapping which is shown in Fig. 4. We can observe the various images shown in Fig. 4a–d corresponding to the elemental mapping of Zn, Ca, Al, and O. The overlay mapping image of all these elements is shown in Fig. 4e which demonstrated the homogeneous distribution in the prepared sample. The quantitative analysis of all elements is endorsed in Fig. 4f with the presence of Zn, Ca, Al, and O having their weight percentage 53.42%, 9.92%, 20.31%, and 34.27%, respectively. Figure 4g depicts EDS spectra of $ZnCaAl_2O_4$ prepared by sol–gel process, which shows the elemental peaks of Zn, Ca, Al and O at 1.00 eV, 3.80 eV, 1.50 eV and 0.50 eV respectively.

The variation of the dielectric permittivity of $ZnCaAl_2O_4$ nanoparticles as a function of with applied frequency from 100 KHz to 5 MHz is plotted in Fig. 5. The dielectric permittivity was calculated by using the following formula.

$$\varepsilon_r = \frac{Cd}{\varepsilon_o A}$$

Here, ε_r is the dielectric permittivity of the sample under the test, C is the capacitance, d is the thickness of the sample and A is the cross-sectional area of the sample. It can be observed that the dielectric permittivity increases with the decrease in the applied frequency. At initial frequency value, the dielectric permittivity was of 23.4 and then decreased to 21.33 at applied frequency 1 MHz. From 1 MHz frequency to 2 MHz, again the dielectric permittivity was decreased to 21. From 2 to 4 MHz the dielectric permittivity was increased up to 23.7. Finally, dielectric permittivity was decreased to 21 at 5 MHz. The increased dielectric permittivity at applied frequency 4 MHz can be assigned to the more relaxation time of the dipoles.

Presently, $ZnCaAl_2O_4$ composite nanoparticles are employed for their broad applications in microwave resonators, circulators, oscillators, telecommunications, GPS and direct broad cast satellites and so on [6, 8]. The addition of Ca in $ZnAl_2O_4$ is important to increase the dielectric permittivity which is beneficial to decrease the size of the GPS patch antenna [1, 4, 5].
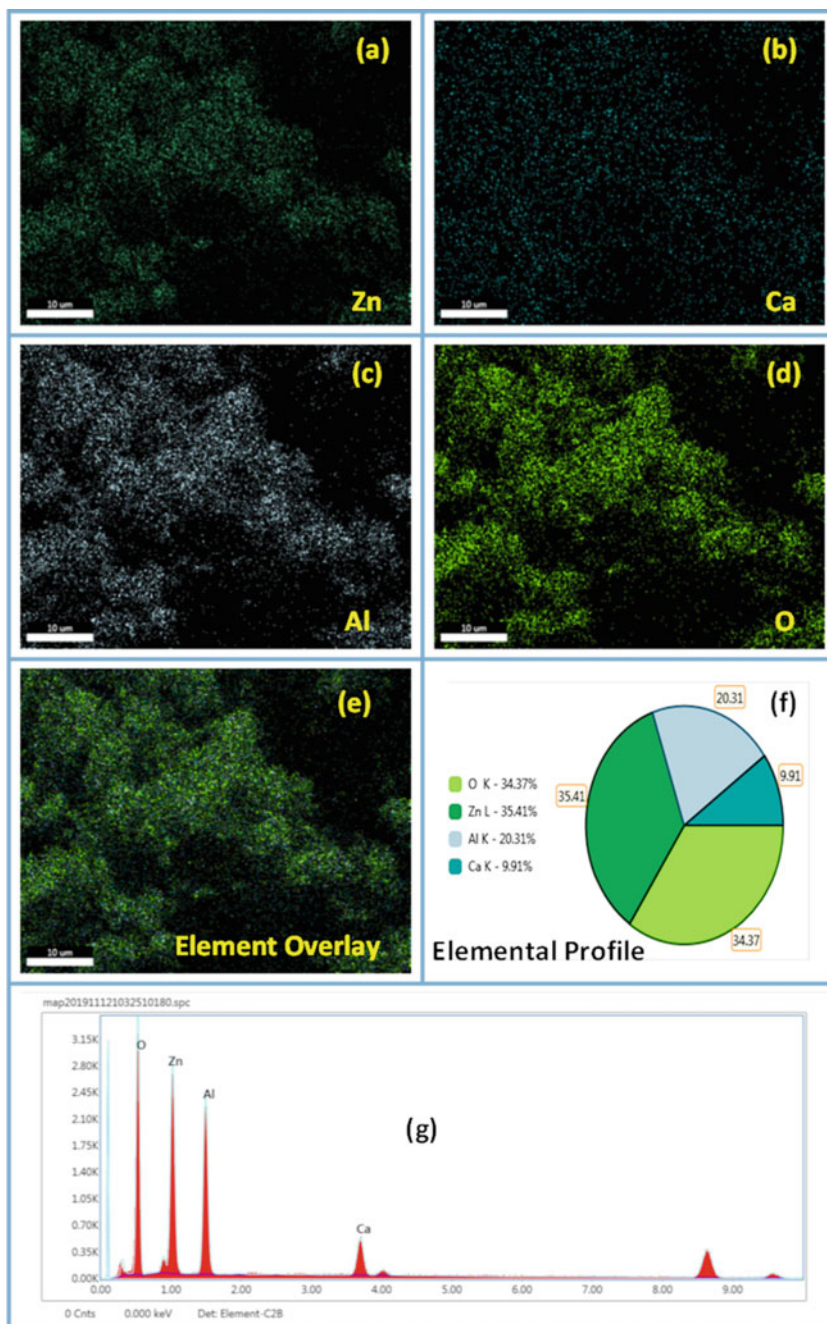
Fig. 4 EDS element mapping and EDS spectrum of ZnCaAl$_2$O$_4$ nanoparticles
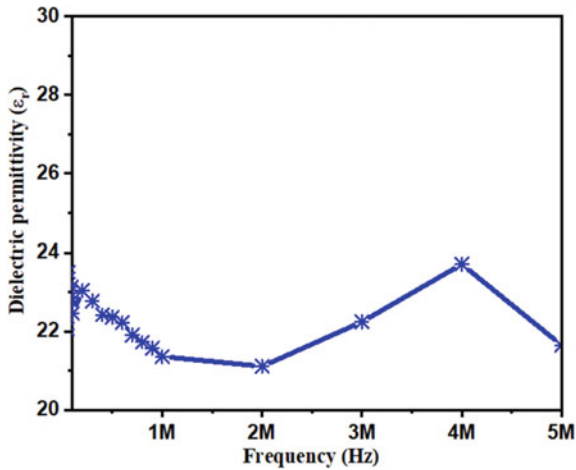
Fig. 5 Dielectric permittivity of $ZnCaAl_2O_4$ nanoparticles

4   Conclusions

By employing the sol–gel route, we have synthesized and characterized the $ZnCaAl_2O_4$ nanoceramic nanoparticles and studied by using XRD, FTIR, SEM and EDS mapping. The investigation by XRD pattern endorsed the presence of mixed phases of $ZnCaAl_2O_4$ and $ZnAl_2O_4$ which represents the polycrystalline nature of the prepared nanoparticles. The FTIR measurement demonstrated the various vibrational peaks correspond to the functional compositions exhibited in the sample. The SEM study evidenced the preparation of spherical nanoparticles of $ZnCaAl_2O_4$ with agglomeration. The EDS mapping exhibited the homogeneous distribution of Zn, Ca, Al and O in the prepared nanoceramic particles of $ZnCaAl_2O_4$. Finally, we performed the study of dielectric permittivity and observed decreased with the increased of operating frequency. This study has the scope to optimize the structural and morphological properties of nanoceramic nanoparticles by changing the concentration of calcium in order to improve their dielectric properties suited for the application in fabricating the GPS patch antenna.

References

1. Nasarudin W, Jalal W, Abdullah H, Zulfakar MS, Tariqual IM, Bais B, Sahbuddin S (2014) GPS patch antenna performance by modification of $Zn_{(1-x)}Ca_xAl_2O_4$ based microwave dielectric ceramics. https://doi.org/10.1007/s10971-014-3397-2
2. Zawadzki M, Wrzyszcz J (2000) Hydrothermal synthesis of nanoporous zinc aluminate with high surface area. Mater Res Bull 35(1):109–111. https://doi.org/10.1016/SOO25-5408(00)00185-9

3. Huang C-L, Chen J-Y and Tseng Y-W (2010) High-dielectric-constant and low-loss microwave dielectric in the Ca(Mg1/3Ta2/3)O$_3$–(Ca0.8Sr0.2)TiO$_3$ solid solution system. Mater Sci Eng B 167:142–146

4. Zulfaka MS , Abdullah H, Tariqul IM, Nasarudin W, Jalal W, Zainuddin Z, Sahbudin S (2014) Performance effect of ZnAl$_2$O$_4$—SiO$_2$ thin film for wireless patch antenna application. J Nano Res 28:141–150. https://doi.org/10.4028/www.scientific.net/JNanoR.28.141© Trans Tech Publications, Switzerland. Online: 2014-06-06, ISSN: 1661-9897

5. Abdullah H, Nasarudin W, Jalal W, Zulfakar MS (2013) Miniaturization of GPS patch antennas based on novel dielectric ceramics Zn(1–x)MgxAl$_2$O$_4$ by sol–gel method, journal of sol-gel science and technology. J Sol-Gel Sci Technol 69:429–440. https://doi.org/10.1007/s10971-013-3239-7

6. Nasarudin W, Jalal W, Abdullah H, Zulfakar MS, (2013) Characterization and dielectric properties of novel dielectric ceramics CaxZn(1-x)Al$_2$O$_4$ for GPS patch antennas. Int J Appl Ceram Technol, 1–11. https://doi.org/10.1111/ijac.12193

7. Zawadzki M, Staszak W, López-Suárez FE, Illán-Gómez MJ, Bueno-López A (2009) Preparation, characterisation and catalytic performance for soot oxidation of copper-containing ZnAl$_2$O$_4$ spinels. Appl Cataly A General 371(1–2):92–98

8. Nasarudin W, Jalal W, Abdullah H, Zulfakar MS, Bais B, Sahbudin S, Mohammad Thariqul IM, ZnAl$_2$O$_4$-based microwave dielectric ceramics as GPS patch antenna: a review. Trans Indian Ceramic Soc 72(4):215–224. https://doi.org/10.1080/0371750X.2013.868323

9. Abdullah H, Zulfakar MS, Nasarudin W, Jalal W, Tariqul IM, Sahbudin S (2014) Synthesis and fabrication of (1-x)ZnAl$_2$O$_4$–xSiO$_2$ thin films to be applied as patch antenna. J Sol-Gel Sci Technol 69:183–192. https://doi.org/10.1007/s10971-013-3202-7

10. Zulfakar MS, Abdullah H, NasarudinW, Jalal W, Zainuddin Z, Sarada I (2014) Study of (1/2x)ZnAl$_2$O$_4$–xSiO$_2$ spinel structures as microwave dielectric material. Received: 23 Dec 2013/Accepted: 8 May 2014 Springer Science+Business Media New York

11. Abdullah H, Nasarudin W, Jalal W, Zulfakar MS, Badariah B, Sahbudin S, Tariqul IM, Sarada I (2015) Effects of Mg contents on ZnAl$_2$O$_4$ thin films by sol gel method and its application. In: Ohji T, Singh M, Mathur S (eds) Advanced processing and manufacturing technologies for nanostructured and multifunctional materials. The American Ceramic Society

12. Abdullah H, Nasarudin W, Jalal W, Zulfakar MS, Tariqul IM, Bais B (2015) Characterization of TixZn(1-x)Al$_2$O$_4$ thin films by sol-gel method for GPS patch antennae. J Korean Phys Soc 66(1): 41–45

Effect of Surface Pockets on the Performance of Journal Bearings

Shazee Rahmani and Faisal Rahmani

1 Introduction

In heavy rotating machines, journal bearings are widely used owing to its capability to bear heavy loads, lower power consumption, and better damping properties. Pressure developed inside the thick lubricating film supports the rotor. However, the lubricating oil offers resistance due to viscous shearing of the oil, which in turn increases the temperature and this effect is further augmented under high speed and heavy loading conditions. The increased temperature diminishes the viscosity of the oil and hence the load carrying capacity is mitigated [1, 2]. For an efficient operation of the system, it is imperative that friction and power consumption is reduced. Previous works evinced that some modifications in the form of dimples, grooves and pockets has improved the performance of journal bearings [3, 4]. This modification of the surface of bearing alters the pressure distribution leading to increase in load carrying capacity and reduction in power consumption.

Several studies have been reported for textured journal bearings [5–13]. Tala-Ighil et al. [5] carried out one of the earliest studies on textured journal bearings employing spherical dimples. It was shown that surface texturing can be beneficial as well as detrimental on the performance owing to the distribution of textures. Therefore, it is crucial to design the texturing properly. In a later study [6] by the same researchers, 25 different texturing design were investigated for journal bearing performance using cylindrical dimples. It was found that bearing performance can be improved if partial texturing is provided near the declining portion of pressure profile, whereas full texturing is detrimental. Tala-Ighil et al. [7] studied both the thermal and texturing effect on the static characteristics of journal bearings. It was reported that the optimum design of texturing depends on the geometrical parameters and operating conditions. Ausas et al. [8] investigated the effect of texture depth on the performance of journal bearings with fully textured rectangular dimples. A slight

S. Rahmani (✉) · F. Rahmani
Birla Institute of Technology, Mesra, Ranchi, India

131

increase in minimum film thickness and frictional torque was found. Kango et al. [9, 10] studied the influence of spherical dimples and transverse grooves on the performance of journal bearings considering thermal effect and mass conserving algorithm. They observed that partial texturing may increase load carrying capacity and reduce the average temperature.

Olver et al. [14] demonstrated that a simple parallel pad bearing can support load if a closed pocket is provided. Fouflias et al. [15] studied four types of sector-pad thrust bearing: (a) open pocket, (b) closed pocket, (c) tapered land, and (d) partially textured with rectangular dimples. A better performance of open pocket bearing compared with other types was found. Brajdic-Mitidieri [16] carried out CFD analysis of a pocketed pad bearing and reported that significant reduction in friction coefficient can be obtained in the presence of closed pockets. Rahmani et al. [17, 18] carried out studies on the static and dynamic characteristics of pocketed journal bearings using powder lubricants. Different shapes of pockets: rectangular, trapezoidal, elliptical, and parabolic were taken for study and it was found that a rectangular pocket is best for improving the static as well as dynamic characteristics of journal bearings.

The performance of textured journal bearings wherein surface textures in the form of dimples and grooves of various shapes have been investigated in the recent past, and it has been found that surface texturing is a useful method to improve the performance. However, there is a dearth of studies using pockets in the bearing nevertheless pocketed bearings may improve the performance better than dimpled or grooved bearings. The objective of present work is to investigate the influence of pocket on the performance parameters mainly load carrying capacity and power loss. In the present work, the bearing bore surface has been provided with a rectangular pocket. A numerical study is carried out for both conventional and pocketed bearings. It is found that if the location of pocket is suitably chosen (generally at the declining portion of pressure profile), the performance of the journal bearing is improved. In the present work, a rectangular pocket is given in the bearing after the position of minimum film thickness. A decrease in eccentricity ratio in the range of 1–3% is achieved in compared with conventional bearing. Power loss is significantly reduced by 4–37% as compared with conventional bearing.

2   Mathematical Model

The schematic of a journal bearing, and unwrapped bearing surface is shown in Fig. 1. The expression for nondimensional film thickness is given by Tala-Ighil et al. [6], as shown in Eq. (1).

$$\bar{h} = 1 + \varepsilon \cos \theta + \bar{\delta} \tag{1}$$
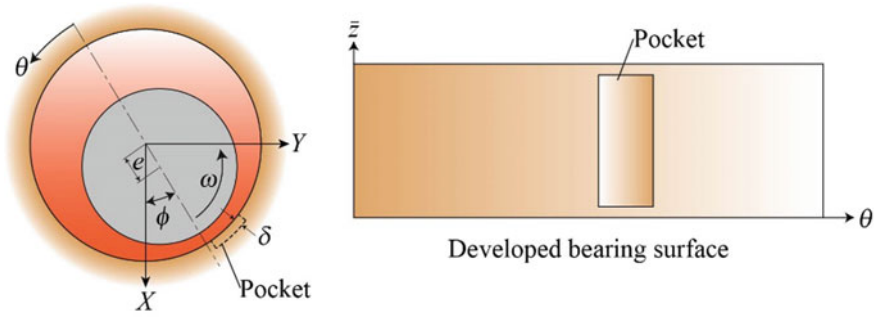
Fig. 1 Schematic of journal bearing

where c is the radial clearance, $\varepsilon = \frac{e}{c}$ is eccentricity ratio, and $\bar{\delta} = \frac{\delta}{c}$ is nondimensional pocket depth applicable only in the region of pocket and zero elsewhere [6].

The Reynold's equation used for evaluating the steady state pressure distribution is given by Khonsari and Booser [1], as shown in Eq. (2).

$$\frac{\partial}{\partial\theta}\left[\bar{h}^3\frac{\partial\bar{p}}{\partial\theta}\right] + \left(\frac{R}{L}\right)^2\frac{\partial}{\partial\bar{z}}\left[\bar{h}^3\frac{\partial\bar{p}}{\partial\bar{z}}\right] = 6\frac{\partial\bar{h}}{\partial\theta} \tag{2}$$

Non-dimensional bearing forces, $\bar{F}_X$ in vertical (X), and $\bar{F}_Y$ in horizontal (Y) directions, non-dimensional load capacity $(\bar{W})$, non-dimensional frictional force $(\bar{F}_s)$ at the journal surface and non-dimensional power loss $(\bar{E}_P)$ are given by Khonsari and Booser [1],

$$\bar{F}_X = \int\limits_0^1\int\limits_0^{2\pi}\bar{p}\cos\theta\, d\theta\, d\bar{z} \tag{3}$$

$$\bar{F}_Y = \int\limits_0^1\int\limits_0^{2\pi}\bar{p}\sin\theta\, d\theta\, d\bar{z} \tag{4}$$

$$\bar{W} = \int\limits_0^1\int\limits_0^{2\pi}\bar{p}\, d\theta\, d\bar{z} \tag{5}$$

$$\bar{F}_s = \int\limits_0^1\int\limits_0^{2\pi}\frac{c}{R}\left(\frac{1}{\bar{h}} - \frac{\bar{h}}{2}\frac{\partial\bar{p}}{\partial\theta}\right)d\theta\, d\bar{z} \tag{6}$$

$$\bar{E}_P = \bar{F}_s\bar{U} \tag{7}$$

where $\bar{W} = \frac{W}{\mu U L}\left(\frac{c}{R}\right)^2$, $\bar{F}_s = \frac{F_s}{\mu U L}\left(\frac{c}{R}\right)^2$, and $\bar{U} = \frac{U}{c\omega}$. Equation (2) is discretized using finite difference method. The resulting algebraic equations are solved for pressure using Gauss-Seidal iterative method.

3   Computational Procedure

The Reynold's equation (Eq. (2)) is discretized using finite difference technique. The bearing surface is developed and divided into rectangular grids. Equation (2) is solved for pressure using Gaus-Seidal iterative technique. A flowchart of the computational procedure is given in Fig. 2. Convergence criteria is taken as,

$$\frac{\sum_{i=1}^{m} \sum_{j=1}^{n} \left|(\bar{p}_{i,j})_{k+1} - (\bar{p}_{i,j})_{k}\right|}{\sum_{i=1}^{m} \sum_{j=1}^{n} \left|(\bar{p}_{i,j})\right|} \leq 10^{-5} \tag{8}$$

where, i, j are the grid points in θ and z direction, m, n are the number of grid points, and k is the iteration number.

3.1   Boundary Conditions

Equation (1) is solved for pressure using finite difference method pertaining to the Reynolds boundary condition:
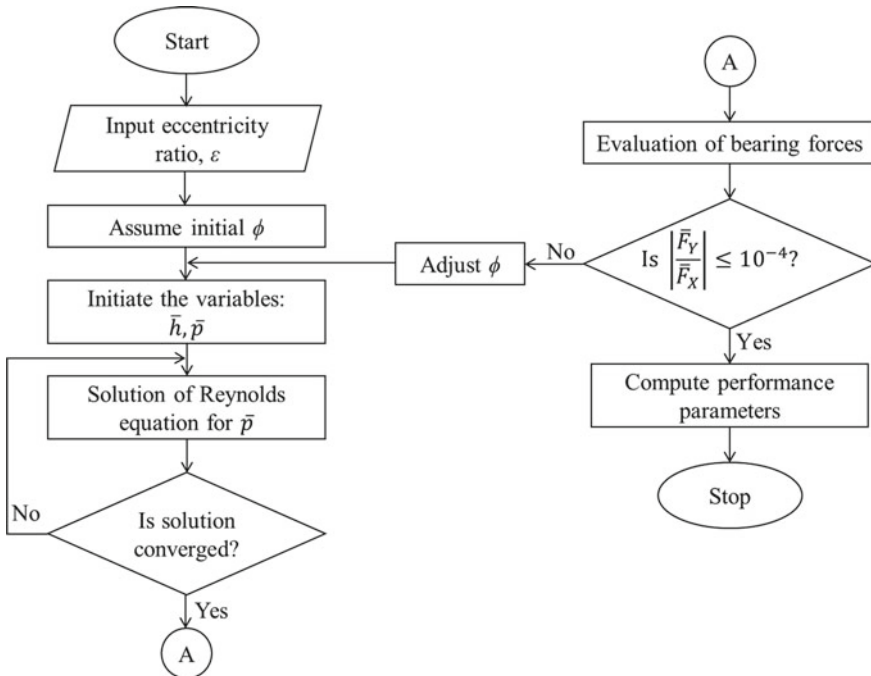
Fig. 2 Flow chart of computation procedure

(i) $\bar{P} = 0$, at $\theta = 0, \bar{z} = 0$, and $\bar{z} = 1$ (which refers to extremities of the bearing)

(ii) $\bar{p} = \frac{\partial \bar{p}}{\partial \theta} = 0$, when pressure becomes negative.

4 Results and Discussions

A finite bearing ($L/D = 1$) is taken for numerical study. The location of rectangular pocket is from $\theta = 185°$ to $230°$ in the circumferential direction and $\bar{z} = 0.12$ to 0.88 in the axial direction. The location of pocket has been decided by finding performance parameters for various configurations. The nondimensional pocket depth ($\bar{\delta}$) is taken as 0.5. Figure 3 shows the three-dimensional pressure distribution on the unwrapped bearing surface for conventional and pocketed bearings for an eccentricity ratio of 0.6. It can be seen that positive pressure is distributed over a larger area in case of pocketed bearing. This phenomenon is more obvious when the pressure at the mid-plane ($\bar{z} = 0.5$) is seen in Fig. 4. It shows the pressure profile at the mid-plane of bearing for four different eccentricity ratios ($\varepsilon = 0.2, 0.4, 0.6,$ and 0.8).
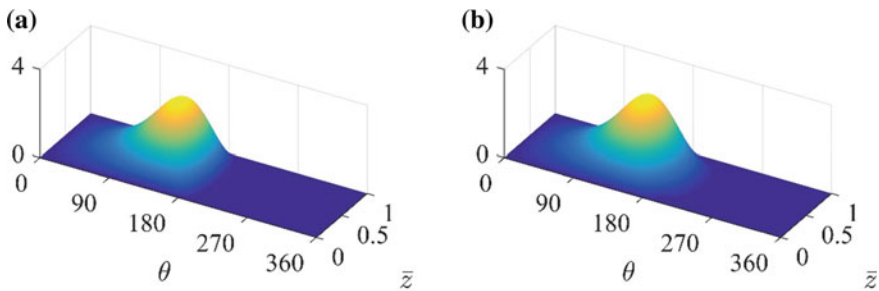
Fig. 3 Pressure profile for **a** Conventional, and **b** Pocketed bearing at $\varepsilon = 0.6$

Fig. 4 Pressure at the bearing mid plane ($\bar{z} = 0.5$)
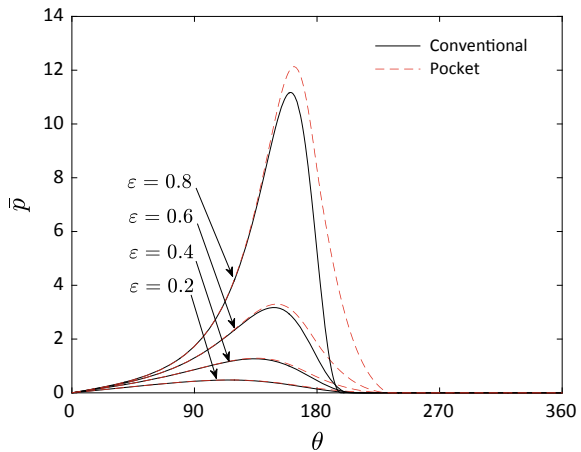
For each eccentricity ratio, pressure profile is more expanded in case of pocketed bearing. This is because pocket is given at the declining part of the pressure curve and extends beyond the cavitation angle (θ_{cav}), resulting in a slightly larger area for pressure distribution. Moreover, the maximum pressure is also increased with pocketed bearing. This leads to a higher load capacity at the given eccentricity ratio.

Sommerfeld number, $S = \left(\frac{\eta N_s LD}{W}\right)\left(\frac{R}{c}\right)^2$ is a non-dimensional number which depends upon the operating parameters. A higher value of 'S' indicates higher speed of operation or a lower load. The variation of eccentricity ratio, power loss, and improvement percentage with 'S' is shown in Fig. 5. A decrease in eccentricity ratio for a particular 'S' indicates an increase in load carrying capacity. It is clear from Fig. 5a eccentricity ratio is reduced by incorporating pocket for same operating conditions for all values of 'S'. Figure 5b represents the steady state journal center position for different eccentricities. It is seen that pocketed bearing has lower attitude angle than conventional bearing. In Fig. 5c, the maximum pressure is plotted against Sommerfeld number. With increase in Sommerfeld number there is a decrease in maximum pressure. If the load is fixed, an increase in S means an increase in speed of the shaft. With an increase in speed, pressure will be distributed over a larger area resulting in a decrease in maximum pressure. Another observation from Fig. 5c is that pocketed bearing reduces the maximum pressure for fixed S. In other words, for same maximum pressure the value of S with pocketed bearing is lower than conventional bearing. This means that to support same load, pocketed bearing can be run at lower speeds. In Fig. 5d it is clearly seen that power loss is significantly reduced in case of pocketed bearing. Figure 5e, f shows the variation of location of maximum pressure (θ_{max}) and cavitation angle (θ_{cav}) with Sommerfeld number S. With pocketed bearing θ_{max} is slightly higher compared with conventional bearing. θ_{cav} is also significantly higher for pocketed bearing as compared with conventional bearing implying that pressure is distributed over a larger area.

Figure 6 represents the improvement percentage in eccentricity ratio and power loss with Sommerfeld number. It clearly shows that, introduction of pocket in the bearing leads to a decrease in eccentricity ratio ranging from 1 to 3%, whereas power loss is reduced by 4–37%. Better improvements are seen for lower values of S, which is the case of heavy load or lower speed.

5   Conclusions

A numerical study for conventional and pocketed journal bearings is carried out to investigate the effect on the load carrying capacity and power loss. Pocketed bearing alters the pressure distribution which changes the performance parameters significantly. Load capacity can be increased, and power loss can be decreased by suitably choosing the location of the pocket, which is found to be at the declining part of the pressure profile. Pocketed bearing significantly reduces power loss. It is found that a decrease in eccentricity ratio ranges from 1 to 3%, whereas power loss is
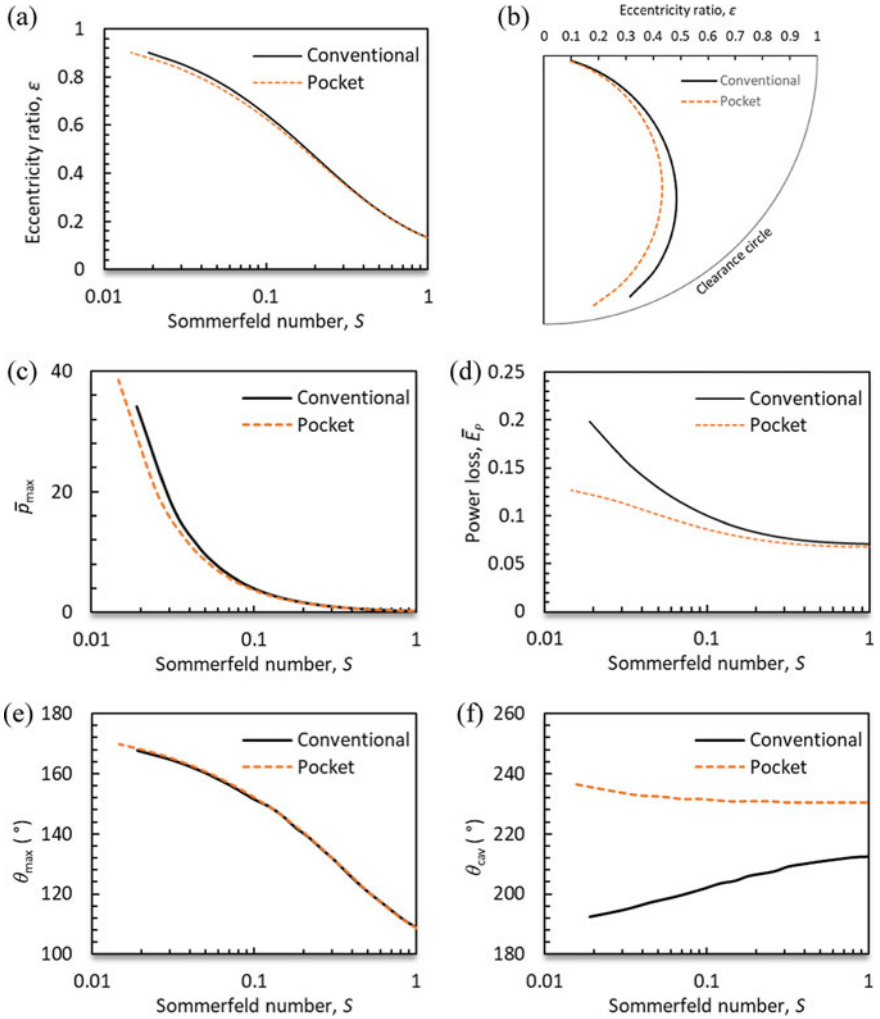
Fig. 5 **a** Eccentricity ratio versus S, **b** Journal trajectory, **c** $\bar{p}_{max}$, versus S and **d** Power loss $\bar{E}_P$ versus S, **e** θ_{max} versus S, **f** θ_{cav} versus S

reduced by 4–37%. Thus, pocketed bearing can be used as a better performer when load capacity and power loss is a concern.

Fig. 6 Improvement
percentage in eccentricity
ratio and power loss with
Sommerfeld number
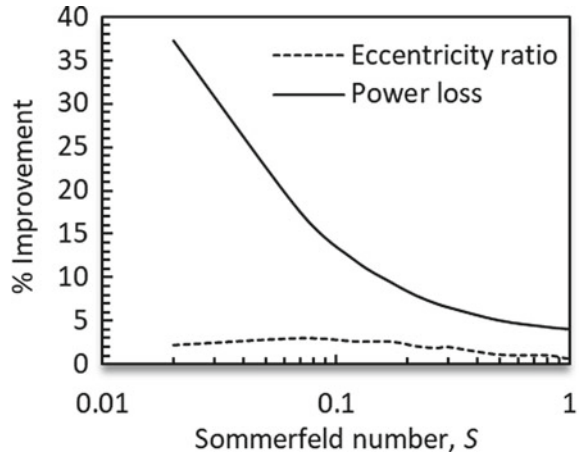
References

1. Khonsari MM, Booser ER (2008) Applied tribology: bearing design and lubrication, 2nd edn. John Wiley & Sons, Ltd
2. Stachowiak G, Batchelor AW (2013) Engineering tribology. Butterworth-Heinemann
3. Gropper D, Wang L, Harvey TJ (2016) Hydrodynamic lubrication of textured surfaces: a review of modeling techniques and key findings. Tribol Int 94:509–529. https://doi.org/10.1016/j.triboint.2015.10.009
4. Etsion I (2005) State of the art in laser surface texturing. ASME J Tribol 127:248–253. https://doi.org/10.1115/1.1828070
5. Tala-Ighil N, Maspeyrot P, Fillon M, Bounif A (2007) Effects of surface texture on journal-bearing characteristics under steady-state operating conditions. Proc Inst Mech Eng Part J J Eng Tribol 221:623–633. https://doi.org/10.1243/13506501JET287
6. Tala-Ighil N, Fillon M, Maspeyrot P (2011) Effect of textured area on the performances of a hydrodynamic journal bearing. Tribol Int 44:211–219. https://doi.org/10.1016/j.triboint.2010.10.003
7. Tala-Ighil N, Fillon M (2015) A numerical investigation of both thermal and texturing surface effects on the journal bearings static characteristics. Tribol Int 90:228–239. https://doi.org/10.1016/j.triboint.2015.02.032
8. Ausas RF, Ragot P, Leiva J, Jai M, Bayada G, Buscaglia GC (2007) The impact of the cavitation model in the analysis of microtextured lubricated journal bearings. ASME J Tribol 129:868–875
9. Kango S, Sharma RK, Pandey RK (2013) Comparative analysis of textured and grooved hydrodynamic journal bearing. Proc Inst Mech Eng Part J J Eng Tribol 228:82–95. https://doi.org/10.1177/1350650113499742
10. Kango S, Singh D, Sharma RK (2012) Numerical investigation on the influence of surface texture on the performance of hydrodynamic journal bearing. Meccanica 47:469–482
11. Lu X, Khonsari MM (2007) An Experimental investigation of dimple effect on the Stribeck curve of journal bearings. Tribol Lett 27:169–176. https://doi.org/10.1007/s11249-007-9217-x

12. Cupillard S, Glavatskih S, Cervantes MJ (2008) Computational fluid dynamics analysis of a journal bearing with surface texturing. Proc Inst Mech Eng Part J J Eng Tribol 222(2):97–107. https://doi.org/10.1243/13506501JET319
13. Brizmer V, Kligerman Y (2012) A laser surface textured journal bearing. ASME J Tribol 134(3): 031702
14. Olver AV, Fowell MT, Spikes HA, Pegg IG (2006) 'Inlet Suction', a load support mechanism in non-convergent, pocketed, hydrodynamic bearings. Proc Inst Mech Eng Part J J Eng Tribol 220(2):105–108. https://doi.org/10.1243/13506501JET168
15. Fouflias DG, Charitopoulos AG, Papadopoulos CI, Kaiktsis L, Fillon M (2015) Performance comparison between textured, pocket, and tapered-land sector-pad thrust bearings using computational fluid dynamics thermohydrodynamic analysis. Proc Inst Mech Eng Part J J Eng Tribol 229(4):376–397
16. Brajdic-Mitidieri P, Gosman AD, Ioannides E, Spikes HA (2005) CFD Analysis of a low friction pocketed pad bearing. ASME J Tribol 127(4):803–812. https://doi.org/10.1115/1.2032990
17. Rahmani F, Pandey RK, Dutt JK (2018) Performance studies of powder-lubricated journal bearing having different pocket shapes at cylindrical bore surface. ASME J Tribol 140:031704-1–12. https://doi.org/10.1115/1.4038678
18. Rahmani F, Pandey RK, Dutt JK (2020) Stability of rotor supported on powder lubricated journal bearings with surface pockets. Proc Inst Mech Eng Part C J Mech Eng Sci Online first. https://doi.org/10.1177/0954406220957369

Effect of Tin as Alloying Element on Grey Iron Automobile Casting

Himanshu Shekhar Mishra, Rina Sahu, and D. S. Padan

1 Introduction

Grey iron is widely used for making components for automobile parts, valve fittings, machine bed, turbine blades, electrical components etc. Iron has properties like, thermal conductivity, lubrication, damping capacity and wear resistance. This is due to graphite flakes present in the matrix. It has good mechanical properties like tensile, hardness, toughness due to pearlite and ferrite present in the matrix [1]. Grey iron castings proportions in total casting production is 50% and among 50%, automobile castings proportion is 32% [2, 3]. Grey iron is an iron-carbon alloy consisting of mainly carbon (2.5–4.0%), silicon (1–3 %) and other elements like Sulphur, phosphorous, manganese, chromium and minor elements like Pb(lead), Zn(zinc), vanadium, titanium [3–5]. Sulphur and phosphorous must be at lower level for making automobile component. Chromium is necessary for hardness and corrosion resistance [5, 6].

Properties of grey cast irons are influenced by a number of factors including graphite morphology, matrix structure, base iron compositions, section size, heat treatment, thermal properties of mould, casting geometry and alloying additions [7–9]. In most cases, minor alloying is done to increase strength and promote formation of pearlite. Minor elements normally used in grey iron are chromium, copper, nickel, molybdenum, vanadium and tin [10–12]. Tin in the range of 0.025–0.1% is a strong pearlite stabilizer. It does not appear to increase the strength of a fully

H. S. Mishra (✉) · D. S. Padan
Foundry Divison, Tata Motors Ltd, Jamshedpur, Jharkhand 831010, India
e-mail: himanshu@tatamotors.com

D. S. Padan
e-mail: devinder.padan@tatamotors.com

H. S. Mishra · R. Sahu
Department of Metallurgical & Materials Engineering, NIT, Jamshedpur, Jharkhand 831014, India
e-mail: reenasahu.met@nitjsr.ac.in

141

pearlitic grey iron. It increases small strength due to pearlitic matrix otherwise matrix would be ferrite. Additions above this level is avoided to prevent embrittlement [13, 14]. Cast irons with 0.1–0.15% Sn is the only practical way to avoid the ferritic matrix in stable eutectoid transformation and develop fully pearlitic matrix in the metastable eutectoid transformation system [15, 16]. Copper increases the tensile strength by promoting a pearlitic matrix. Its effects is pronounced at lower addition levels, 0.25–0.5%, whereas at higher addition rates, its effects are not dramatic due to fully pearlitic matrix. In ferrite and ferrite- pearlite combination matrix expectation is to increase tensile strength and hardness. Copper has mild graphitizing effect and does not promote carbide in light sections. Copper addition improves graphitization and structure refinement of the matrix. Cast iron have various engineering properties competes with steel and other material for its superior wear, abrasion and corrosion resistance when it is alloyed. Properties of grey cast iron components depends on microstructure of the material and which is related by the chemistry and processing technique of cast iron [2]. The mechanical and physical properties of grey iron is controlled by varying the amounts of ferrite, graphite and pearlite in the structure [5]. Graphite shape and amount of ferrite/pearlite ratio depends either on casting composition or by cooling rate. Since grey irons normally silicon, which acts as a graphitizer and also promotes ferrite. Control of the ferrite/pearlite ratio is normally fulfilled by additions of elements that promote pearlite formation [8, 9]. These elements increase pearlite formation by enhancing eutectic and eutectoid carbide formation (Cr, Mn) or decreasing the rate of carbon diffusion (Cu, Sn) in austenite [17–19]. Manganese (Mn) can be as low as 0.1% for ferritic irons and as high as 1.2% for pearlitic irons because manganese is a strong pearlite promoter. The percentage of sulphur and phosphorous must be less than 0.05 for making automobile castings. The optimum ratio between manganese and Sulphur for an FeS—free structure is %Mn = 1.7(%S) + 0.3% [20, 21].Combined effect of copper and tin promotes pearlite in the matrix and increases tensile strength and hardness [22, 23]. Inocualtion of grey iron is done to take care of shape, size or distribution of graphite in the casting and thereby increasing the mechanical properties. Amount of effective element remains in the iron is usually very small [22]. Graphite type, size is described as per ASTM A247 [2].

Present study of tin along with fixed percentage of copper has been done. Tin % in the base iron is varied keeping copper 0.5% in all of the samples made for studies. This study has been done to make higher grade cast iron for automobile application.

2 Experimental Procedure

2.1 Metal and Samples Preparation

Liquid grey iron metal was prepared in medium frequency induction furnace of capacity 5 MT. Furnace was charged with steel scrap by weight approx. 60–70% and

Table 1 Charge materials composition, size, percentage and purity

Steel scrap (medium carbon steel)	Foundry returns	Ferro-silicon	Petroleum coke (carburizers)	Ferro-silicon for inoculation in sample dry sand mould	Tin for alloying in ladle
0.1% C & 0.1% Si	3.25–3.40% C, 1.80–2.20% Si	70% Silicon(Si) in lump form	Carbon-80% in granular form	70% silicon &-18 + 50 mesh size (0.2–0.6 mm)	Commercial tin % 99.5

30–40% foundry returns (running systems, scrap casting from foundry and machine shops) of total charge shown in Table 1. Charge was melted by applying power up to 3800 KW.

Composition of metal was made up by adding carburizers(petroleum coke) and ferro silicon alloys. Metal temperature was raised upto 1500 °C. Slag was removed. Wedge chill and carbon equivalent were taken. Spectrometer sample was taken before pouring metal. Temperature was raised up to 1510–1520 °C before tapping into ladle. Ladle metal was transferred to holding furnace by forklift. Slag was removed before transferring metal into holding furnace. Holding furnace is beneficial for getting homogenised metal with base iron composition shown in Table 2. Liquid metal was tapped into 3 MT (metric tonne) ladle.

First base iron sample was taken in copper mould for knowing base chemistry.C alculated amount of tin in the range (0.030–0.050%) was added into ladle and copper 0.5% weight was also taken.T est bar sample poured. Spectral sample in copper mould was also taken before pouring each test bar mould. Similarly, third, fourth and fifth samples were taken following tin ranges and copper fixed % in all the samples made depicted in Table 3. Inoculation of 30 gm (0.2% Fe-Si) was given in each test mould before pouring. Test bars were knocked down from mould at atmospheric temp. Test bars were given for machining for making tensile test bars (3 nos.), impact test bar (3nos.) for charpy test (notched) 3 nos as per ASTM standard.

2.2 Sample Preparation for Microstructural Properties

For microstructural studies, samples were cut from tensile specimen just behind the fractured surface and it was made plain by grinding on belt type emery paper of 80 grit size. Samples were ground on different emery papers of mesh sizes 600 grade to 1500 grade from rough to finish polishing. Samples were dry polished on cloth polisher. Liquid alumina ($Al_2 o_3$) was added on cloth during polishing and samples were washed with acetone. Polished sample was checked on optical microscope with a magnification of $100\times$. First sample was seen without etching for graphite flakes types, size and distribution in the matrix and matrix was seen after etching the sample with 2% nital for phases ferrite, pearlite and cementite. This process was repeated

Table 2 Base iron composition

% C	% Mn	% Si	% S	% P	% Cr	% Cu	% Sn	% Ni	% Mo	% V	% Al	% Ti	% Pb	% B	% Fe
3.38	0.75	1.89	0.053	0.039	0.091	0.11	0.010	0.026	0.005	0.004	0.003	0.006	0.001	0.001	93.42

Table 3 Effect of Sn percentage variation in grey iron on tensile strength

Sample no.	Composition			UTS (MPa)			Average UTS (MPa)
	% Sn range	Actual % Sn	% Cu	a	b	c	
1 (Base Iron)	0.00–0.000	0.010	0.11	250	257	249	253.00
2	0.030–0.050	0.036	0.5	305.28	270.48	244.27	273.34
3	0.050–0.070	0.066	0.5	301.55	320.50	281.29	301.11
4	0.070–0.090	0.079	0.5	344.41	406.38	377.55	376.11
5	0.090–0.110	0.104	0.5	217.61	274.09	237.32	243.00

for each sample with and without etching. Micrographs were taken for each sample under study.

2.3 Mechanical Properties Testing Procedure

2.3.1 Tensile test was done on universal tensile testing machine as per sample size in Fig. 1. Three samples were tested and average reading taken shown in Table 3.

2.3.2 Hardness test was done on Brinell hardness tester machine (Briviskop 3000D Georg Reicherter Esslin gen/Neckar) with 5 mm diameter ball with load of 750 kg and applied for 10 s for each test. Three readings were taken at each specimen given in Table 4.

2.3.3 Charpy test was done on impact testing machine make FIE. Testing had been done on notched bar specimen as per size given in Fig. 2. Three specimens were tested and average readings taken has been shown in Table 5.
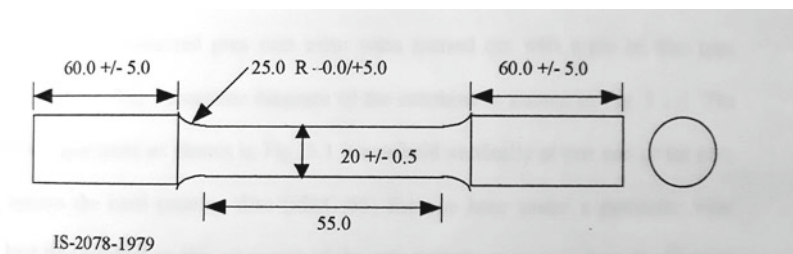
Fig. 1 Line diagram for tensile testing specimen for grey cast iron

Table 4 Effect of Sn percentage variation in grey iron on hardness

Sample no.	Composition			Hardness (BHN)			Average hardness (BHN)
	% Sn range	Actual % Sn	% Cu	a	b	c	
1 (Base Iron)	0.00–0.000	0.010	0.11	170	175	174	173
2	0.030–0.050	0.036	0.5	207	206	210	207.66
3	0.050–0.070	0.066	0.5	225	217	219	220.33
4	0.070–0.090	0.079	0.5	224	222	220	222.00
5	0.090–0.110	0.104	0.5	211	217	215	214.33
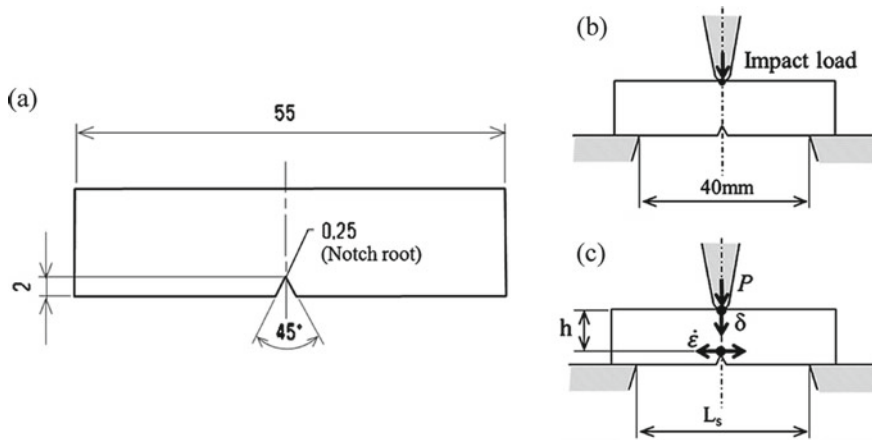
Fig. 2 Line diagram for charpy test specimen (a), (b) & (c) dimension for grey cast iron

Table 5 Effect of Sn percentage variation in grey iron on impact strength

Sample no.	Composition			Impact strength (J)			Average impact strength (J)
	% Sn range	Actual %Sn	% Cu	a	b	c	
1 (Base Iron)	0.00–0.000	0.010	0.11	3.5	4.0	4.0	3.83
2	0.030–0.050	0.036	0.5	3.5	4.0	3.5	3.66
3	0.050–0.070	0.066	0.5	3.5	4.5	4.0	4.00
4	0.070–0.090	0.079	0.5	2.5	3.0	2.5	2.66
5	0.090–0.110	0.104	0.5	3.5	4.0	3.5	3.66

3   Results and Discussions

3.1   Microstructural Properties

Figure 3a, b Shows without etch and with etch micrograph taken on optical microscope for base iron.

Graphite flake is in finer size and longer in shape at lower level of tin 0.1%. As the tin percentage increases, size and shape reduces. Finer flake reduces in length and becomes thicker in shape. Distribution of graphite flake in the lower percentage of tin is randomly and uniformly distributed in the matrix as precipitate. Matrix contains ferrite and pearlite. Distance between ferrite and cementite is more in lamellar pearlite. A type graphite flake with some D type are also present there.

Figure 4a (0.036% Sn) Without etch shows, graphite flake fineness reduces, edge of flake becomes round and it is thicker in size due to diffusion and graphitization process occurring as the cooling rate decreases.

Figure 4b (0.036% Sn) With etch shows matrix contain pearlite and ferrite, lamellar(ferrite and cementite) spacing is more.

Figure 5a (0.066% Sn) Without etch, shows more thicker graphite and it is uniformly distributed and randomly oriented.

Figure 5b (0.066% Sn) With etch, matrix contain pearlite and ferrite and lamellar spacing is lesser when Sn % increases.

Figure 6a Shows (0.079% Sn) Without etch shows more thicker graphite flake, uniformly distributed and randomly oriented.

Figure 6b Shows (0.079% Sn) with etch, matrix with pearlite and ferrite, lamellar spacing reduces as % Sn increases.

Figure 7a Shows (0.104% Sn), Without etch, shows graphite flake in smaller in size, thicker and uniformly distributed and randomly oriented.
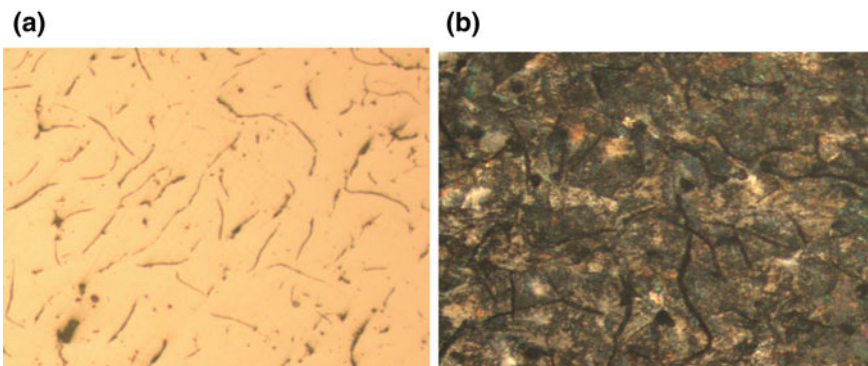
Fig. 3 **a** Without etch (0.010% Sn) 100× magnification, **b** With etch (0.010% Sn) 100× magnification
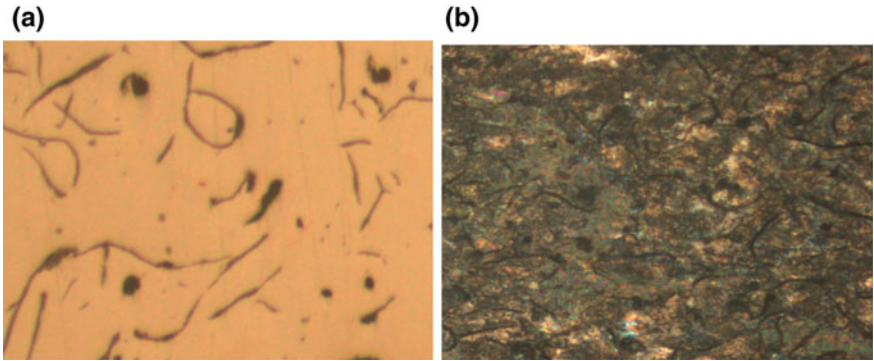
Fig. 4 a Without etch (0.036% Sn) 100× magnification, **b** With etch (0.036% Sn) 100× magnification
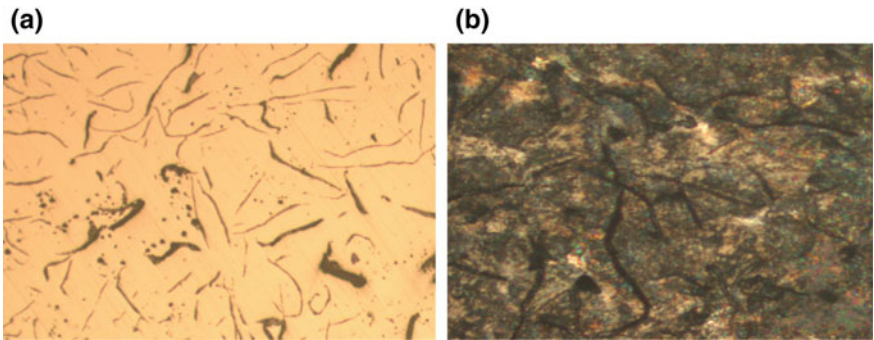
Fig. 5 a Without etch (0.036% Sn) 100× magnification, **b** With etch (0.036% Sn) 100× magnification
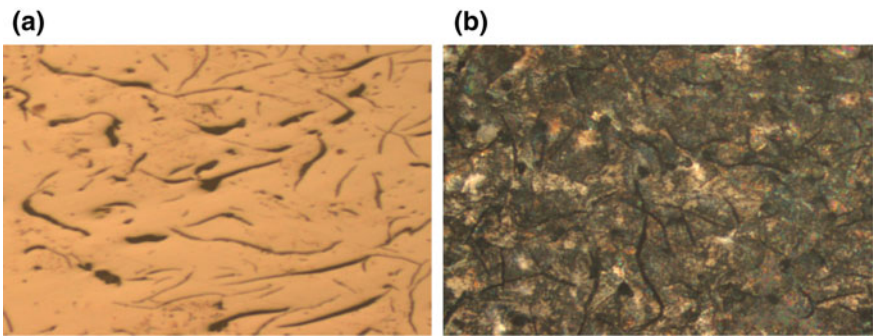
Fig. 6 a Without etch (0.079% Sn) 100× magnification, **b** With etch (0.079% Sn) 100× magnification
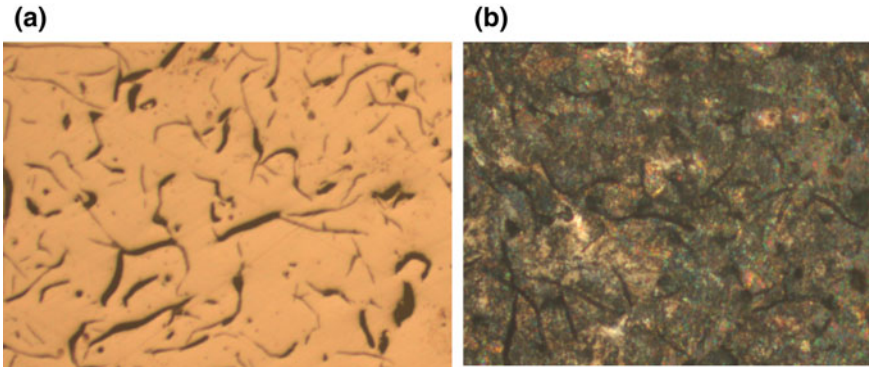
Fig. 7 Without etch (0.104% Sn) 100× magnification, **b** with etch (0.104% Sn) 100× magnification

Figure 7b Shows (0.104% Sn) With etch shows pearlite and ferrite in matrix, finer lamellar spacing and more ferrite percentage which reduces tensile and hardness.

Graphite flake size formation depends on cooling rate in casting, as the flake size develops, diffusion process occurs and graphitization increases. Flake (l/d ratio) (length of flake/thickness of the flake) decreases as the tin percentage increases [17]. Pearlite percentage is increased as tin % increased and also lamellar spacing in pearlite decreases, since tin is a pearlite stabilizer [12, 17, 19].

3.2 Mechanical Properties

3.2.1 Tensile strength data has been given in Table 3 and trend graph for tensile given in Fig. 8. It shows that when tin % is increased, tensile strength is also increased.
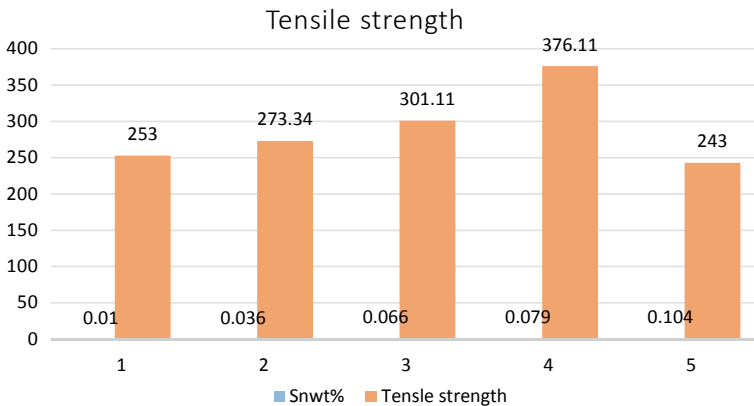
Fig. 8 Trend chart for tensile strength
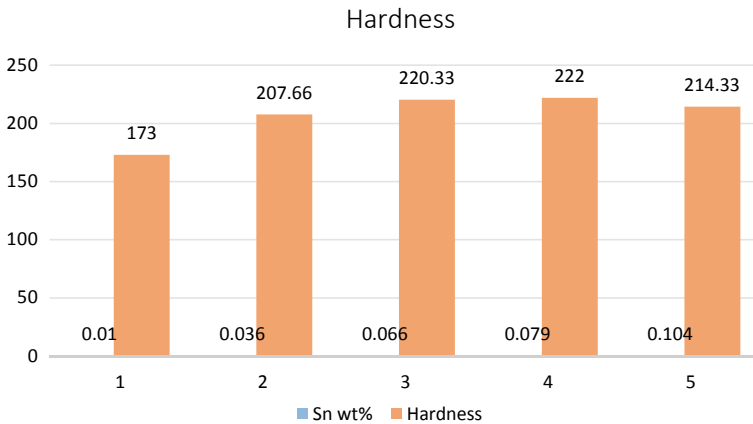
Hardness

Fig. 9 Trend graph for hardness

Strength is increasing and increases upto 0.079% Sn. This is due to pearlite present in the matrix and reduces further, due to the presence of more pearlite and pearlite characteristics changes due to embrittlement phenomena occurring in the case of 0.104% Sn. Literature says that tensile strength increases upto 0.2% Sn but after 0.080%, embrittlement in the casting occurs [11] and this casting is practically of no use for automobile parts. As the percentage of pearlite increases, the reduction in percentage of ferrite decreases with the percentage of tin added into grey iron. Pearlite becomes finer when we add more percentage of tin. Fine and long graphite flakes reduces in length and increases in width by increasing the tin percentage in the solution. Graphite flake reduces in size and end portion becomes round with the increase of copper percentage. Graphite flake is precipitate in solution [3, 13].

3.2.2 Hardness data showed in Table 4 and trend graph in Fig. 9. Hardness is in increasing trend as the percentage tin increases in grey iron upto 0.079% Sn and reduces further a little bit at 0.0104% Sn due to ferrite presence in matrix and also characteristic of pearlite changes with embrittlement phenomena after 0.080% Sn. It is directly related with the tensile strength. Hardness is increased due to complete dissolution of tin in the alloy giving α-solid solution. Tin refines pearlite (inter lamellar spacing decreasing) and hardens ferrite phase in solid solution [17].

3.2.3 Impact strength data shown in Table 5, as tensile and hardness is increasing as the tin percentage increasing, impact strength is decreasing and when both tensile and hardness is decreasing from 0.079% Sn to 0.104% Sn shown in Fig. 10. That iron will absorb less energy. As the hardness and tensile will increase, impact energy will be less [11, 24].
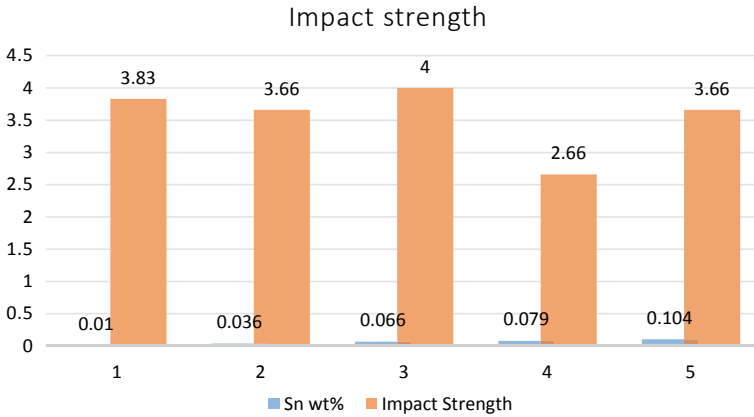
Fig. 10 Trend graph for impact strength

4 Conclusions

Based on the above discussions, following points have been concluded.

1. Metallographic studies show that as the percentage of tin increases graphite flakes in microstructure reduces from fineness to coarser side. Matrix is also changed in percentage of ferrite and pearlite. As the percentage of tin increases, pearlite increases and ferrite reduces. After 0.080% Sn, characteristics of pearlite changes due to embrittlement phenomena occurring in the casting.
2. Tensile strength increases with the increase in the percentage of tin in grey iron upto 0.079 and decreases after. This is due to more pearlite in the matrix and changes in the characteristics of pearlite due to embrittlement phenomena occurring after 0.080%.
3. Hardness also increases with tensile strength with the increase of tin percentage in grey iron and reduces following the tensile strength trend.
4. Impact strength decreases as hardness and tensile strength increases as the tin % in alloy increases and follow the same trend as the tensile and hardness decreases, impact strength increases.

References

1. Heine RW, Rosenthal PC, Principal of metal casting 195. McGraw –Hill Book Co., pp 497–516
2. Elliot R (1988) Cast iron technology. Butterworth, London
3. Bihari B, Kumar R, Singh AK (2014) Effect on the mechanical properties of gray cast iron with variation of copper and molybdenum as alloying elements. IJERT 3(5)
4. Riposan L, Chisamera M, Stan S (2014) New developments in high quality grey cast iron, special report, vol 11, no 4. Politechnica University of Bucharest, Romania
5. Xue W, Li Y (2016) Pretreatmemts of gray cast iron with different inoculants. J Alloys Compd 689:408–415
6. Davis JR, Davis and Associates (2001) Alloying understanding the basics. ASM International
7. Kus R, Akgul B (2018) Experimental investigation on the effect of tin in gray cast iron to impact strength hardness and microstructure
8. Naseef A, El-Nasr A-BAA (2007) Influence of copper additions and cooling rate on mechanical and tribological behavior of grey cast iron, conference paper
9. Indian Foundry Journal (2006)
10. Modern casting (2017)
11. Rooney TC, Wang CC, Rosenthal PC, Loper CR, Heine RW (1971) Tin and Cu in gray cast iron. AFS Trans 71:189
12. Xu W, Ferry M, Wang Y (2005) Influence of alloying elements on as-cast microstructure and strength of gray cast iron. Mater Sci Eng A 390(1–1):326–333
13. Siswanto A, Widodo R, Ardiansyah E (2019) Effect of interlamellar spacing on tensile strength gray cast iron. Published under licence by IOP Publishing Ltd. J Phys Conf Ser 1450. In: International conference on applied science and technology (iCAST on Engineering Science), 24–25 Oct 2019, Bali, Indonesia
14. Stefanescu DM (2002) Science and engineering of casting solidification. Kluwer Academic/Plenum Publishers, New York, Boston, Dordecht, London, Moscow
15. Messina CJ (1975) The effect of tin on the mechanical and physical properties of gray cast iron. Theses and Dissertations, paper
16. Lacaze J, Sertucha J (2017) Effect of tin on the phase transformations of cast irons. J Phase Equilibria Diffusion, pp 1–7. ISSN 1547-7037
17. Abdou SMI, El Nasser GA (2003) The tribological behaviour of grey cast iron at different additions of Cu. PSERJ Faculty of Engineering Port Said, Suez Canal University 7(1):44–54
18. Abu El-Aini HM, Abd El-Mageed AM, Abdel-Rahman M (1999) Mechanical properties and corrosion behaviour of grey cast iron with Cu additions. In: 2nd International conference on mechanical engineering advanced technology for industrial production, Assuit University, Assuit, Egypt, 2–4 Mar 1999, pp 67–77
19. Abbasi HR, Bazdar M, Halvaee A (2007) Effect of phophorous as an alloying lement on microstructure and mechanical properties of pearlitic gray cast iron. Mater Sci Eng A 444(1–2, 25):314–317
20. Kidao (1970) Application of copper in automotive iron castings. Copper in Cast Iron, pp 13–18
21. Li P, Wang JJ, Ge DC, Sui GH, Chen GH, Yang GW, Wang DS, Tang B, Tang WM, Microstructures and mechanical properties of grey irons by adding high-content steel scrap. Int J Cast Metals Res. https://doi.org/10.1080/13640461.2016.1155024
22. Fras E, Go MYM, Lopez HF (2005) The transition grom gray to white iron during solidification, part I – theoretical background. Metall Mater Trans A 36A:3075–3082
23. Shea MM (1978) Influence of cooling rate and manganese and copper content on hardness of As-cast Ductile Iron. AFS Trans, pp7–12
24. Zhradeen M (2016) Effects of copper addition and section thickness on some mechanical and the morphology of graphite flakes in grey cast iron. Department of Metallurgical and Materials Engineering, Faculty of Engineering, Ahmadu Bello University, Zaria, Nigeria

Influence of Roll Wear in Hot Rolling of Steel at Hot Strip Mills

Purnanand Pathak, Ghanshyam Das, and Sanjay Kumar Jha

1 Introduction

In a Hot Strip Mill (HSM), steel slabs are plastically deformed between pairs of rotating rolls to achieve hot rolled (HR) coils of desired size, shape and mechanical properties. HR coils are widely used in construction, fabrication, pipe, container and other industries. A large proportion of HR coils are further rolled to thinner gauge coils in cold rolling mills. These cold rolled (CR) strips are used in white goods, automobiles, barrel, roofing, packaging and many other applications. Stringent market demands on cost and quality of the rolled products put proportional thrust on HSM to improve its performance. It is therefore required to explore measures for improving techno-economic parameters of the mill.

Roll is considered as backbone of the rolling mills as all the deformations of the material take place between pairs of rolls. Energy required for deformation is transferred to the material through these rolls [1]. However, it is one of the costliest consumables of the rolling mills and, besides huge production loss on account of frequent roll-changes, around 5–15% of the cost of production of the rolled material is directly related to the rolls [2]. Quality of the rolled products is also very much dependent on performance of rolls. It is therefore pertinent to discuss and to explore possibilities of saving rolls and improving their performance.

In any HSM deformation of material is divided primarily into two groups of mill-stands known as roughing mills and finishing mills (Fig. 1). Roughing mills have horizontal as well as vertical (edger) stands for subjecting steel slab to thickness

P. Pathak (✉)
R&D Centre for Iron and Steel, Steel Authority of India Ltd, Ranchi, Jharkhand, India
e-mail: ppathak@sail.in

G. Das
National Institute of Foundry and Forge Technology, Hatia, Ranchi, Jharkhand, India

S. K. Jha
Birla Institute of Technology, Mesra, Ranchi, Jharkhand, India
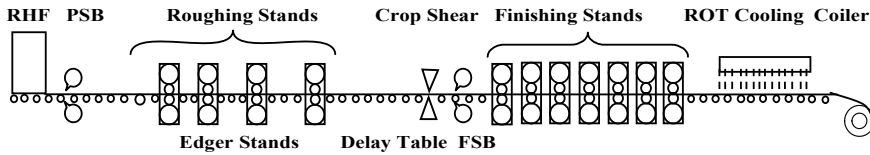
Fig. 1 Schematic layout of a typical HSM (RHF: Reheating furnace; PSB: Primary scale breaker; FSB: Finishing scale breaker; ROT: Run-out table)

and width reductions, respectively. Finishing mills have series of horizontal stands with sophisticated control mechanisms to achieve desired thickness reduction and dimensional quality of the HR strips. All the horizontal stands are mostly of 4-Hi configuration with two work rolls and two backup rolls. Each vertical stand uses a pair of edger rolls for controlling width of the HR strips.

Friction is the need of rolling and therefore tribology plays a great role in controlling mill operation. In HSM, rolls are subjected to arduous conditions due to various heat transfers, fire cracks, high compressive and shear stresses, abrasive iron oxides, etc. Under such conditions wear of the work rolls become inevitable. With higher wear, the contour of roll gap becomes uneven making it unfavourable for obtaining desired shape and surface quality of the HR coils. Rolls are therefore changed frequently at shorter campaign sizes however at the cost of loss in production. After every cycle of operation, rolls are ground to regain their original profile. Roll life is thus reduced on three accounts—roll wear in each campaign, material loss during grinding and occasional marks, spalling or sudden failure of roll.

This paper brings together various aspects related to wear performance of rolls. Few cases are discussed to show influence of wear during rolling at industrial HSM.

2 Roll Wear in HSM

2.1 Rolls Used in HSM

HSM uses various types of rolls as the operating conditions in terms of strain, strain rate, temperature, roll force, torque, type of scale, etc. varies significantly from roughing to finishing mills. Most commonly used rolls of HSM are listed in Table 1 [3]. Besides requirement of strength to withstand high mechanical loads, higher wear resistance has been the driver for successive developments in roll materials and their manufacturing technology. In-depth research on wear performance of different roll materials has been carried out by various researchers [4–9]. Roughing mills are required to impart heavy reductions to the slabs and therefore rolls in these stands need to possess high strength. Forged alloy steel rolls with suitable heat treatment are preferred in these stands to meet the service requirements. In contrary, the finishing stands of HSM imparts desired surface finish and dimensional accuracy to

Table 1 Various types of rolls used in HSM [3]

Material	Forged or cast	Roll	C (%)	Si (%)	A* (%)	B** (%)	Carbide (%)	Hardness (HV)
Hypo-eutectic steel	Forged/cast	BUR, Edger	0.4–1.0	0.3–1.0	1–6	<0.5	0–2	180–700
ICDP	Cast	WR: FM	2.0–4.0	0.4–1.0	6–9	0–4	30–40	600–700
High chrome iron	Cast	WR	2.0–4.0	0.4–1.0	14–22	<0.5	20–30	500–700
High chrome steel	Cast/forged	WR: RM, FM	1.0–2.2	0.4–0.8	8–12	<0.5	10–20	500–700
Adamite (hyper eutectic steel)	Cast	Edger roll	1.0–2.2	0.4–0.8	<4	<0.5	6–15	300–450
High speed steel (HSS)	Cast/forged	WR: FM	1.0–2.2	0.4–0.8	<6	8–15	3–5	600–750
Semi-HSS	Cast	WR: FM, RM	0.4–1.0	0.3–1.0	5–8	5–10	2–5	500–700

*A $= \sum$(Cr, Mn, Mo, Ni, Co); **B $= \sum$(V, W, Ti, Nb)
BUR: Backup roll; WR: Work roll; RM: Roughing mill; FM: Finishing mill

the HR strips, and, therefore, the rolls in these stands need to possess superior resistances towards wear, thermal cracking and breakages. Accordingly, high chromium (Hi-Cr) iron and other cast iron grade rolls are used in these stands.

On account of higher temperature and tertiary scales, the initial few finishing stands of HSM are observed to have more roll wear compared to the later stands. Some of the mills therefore use Hi-Cr rolls in the initial stands and Indefinite Chilled Double Pour (ICDP) cast iron rolls in the later stands. Some of the mills have also tried using high speed steel (HSS) rolls at initial stands. Wear resistance of HSS rolls have been found 3 to 4 times superior than that of Hi-Cr rolls [10]. Application of HSS or semi-HSS work rolls in roughing mills is also found beneficial over chromium steel rolls [11]. However, there are some limitations in using HSS rolls. Such rolls increase friction at roll bite and they are more susceptible to failure in case proper roll cooling and maintenance practices are not in place.

2.2 Wear of Work Rolls in HSM

As friction is the need of rolling, there are significant interactions among asperities of rolls and the workpiece. In such interactions asperities either get deformed or get torn out depending on several factors related to materials and operating conditions. This way interacting surfaces have progressive loss of materials, which is called wear.

The wear of steel strip does not carry much significance as there is constant generation of new surfaces during rolling. However, wear of roll surfaces has significant consequences on process as well as on quality of the rolled products. It has adverse effects on life of rolls and on techno-economics of rolling. Classically, wear happens in different modes such as abrasive wear, adhesive wear, fatigue wear, corrosive wear, erosive wear, etc. In rolling also wear of rolls takes place through most of these modes. However, abrasion, adhesion and fatigue are the main modes of roll wear. Mechanisms of these modes of wear are well explained in published literatures [12].

When wear takes place due to sliding of hard surface projections relative to another contacting surface under load, it is called abrasive wear. In this case ploughing action or micro-cutting by hard particles produces loose wear particles. When the hard particles are part of one of the surfaces, it is called two-body wear and when these are loosely held between the two surfaces, it is called three-body wear. Abrasive wear may be accelerated in presence of subsurface cracks, generated by the hard particles under load. When a softer material is rolled, the abrasive action of the debris is the prime cause for roll wear. Here scale or oxides and the inter-metallic of precipitation hardened alloys constitute the main abrasive particles.

Adhesive wear occurs when surfaces slide against each other and the pressure between the mating asperities is high enough to cause local plastic deformation and adhesion. It is reported that the atomic bond between the mating asperities is higher than the strength of the parent materials [12]. This results in metal transfer or pickup from one surface to the other. When the material is picked up by rolls, the size of the adherent particles grows with subsequent adhesions and there may also be strain hardening of these particles under rolling load. These particles finally get separated from the rolls, through the process of fatigue or by shearing action, generating loose particles. It is also suggested that at elevated temperature some of the alloying elements of the roll get diffused into the workpiece, which reduces strength of the roll leading to its wear [12]. Adhesive roll wear is expected when harder materials are rolled. In this case, often rolls are visible with banded or peeled off surface.

Fatigue wear is the most severe type of wear of HSM rolls. During rolling work rolls are heated at roll bite and are water-cooled immediately after the roll bite. Alternate heating and cooling of the roll surface leads to generation of compressive and tensile stresses in the rolls at a frequency set by rolling speed. Above this, the roll material is also subjected to cyclic mechanical loading which adds to the complexity of stresses in the roll. After processing several coils, when the fatigue limit of the material is reached, there is nucleation of fine cracks on the surface of rolls, network of which is termed as fire-cracks [2]. With progress of rolling or with any external factor the crack can be so deep to destroy the hard surface layer of roll (spalling).

In light of the above discussions it is evident that performance of the roll depends on many factors including roll material and quality, roll utilization and maintenance practices and above all on the operating conditions in the mill. The inferior performance of rolls does not only lead to increased roll consumption but also leads to increased mill delays as a result of any in-service roll failure. It is therefore pertinent

to discuss critical operating conditions affecting roll performance. These conditions include temperature, roll force, scale, etc.

2.3   Selected Parameters Affecting Roll Wear

Heat transfer with work rolls. Work rolls are exposed to high material temperature typically in the range of 1150–1050 °C at roughing mills and 1000–850 °C at finishing mills during rolling of carbon steels. Simultaneously, rolls are cooled with water spray to avoid their overheating. There is also conductive heat transfer within the roll in radially inward direction. While cyclic conductive heating and convective cooling of the work rolls causes thermal fatigue of the roll material, a thermal stress field is also created in its subsurface layers. Heat transfer coefficient at roll bite also has significant effect on thermal fatigue degradation [13]. At higher temperature, despite taking all cooling cares, there is generation of fine fire-cracks on the roll surface, whose intensity is more in the roughing mills than in the finishing mills. Both thermal fatigue and fire-cracks accelerate wear rate of work rolls.

Mechanical loading of work rolls. During deformation of material there are high roll separating forces of the order of few mega Newton at different stands. Under such condition roll surface is subjected to severe cyclic mechanical load. The workpiece at roll bite is having normal compressive force, tangential frictional force and may also have tensile forces due to inter-stand tensions. As the velocity of material under deformation keeps on increasing at the roll bite, the direction of frictional forces gets reversed at neutral point. Difference in linear velocities of material and roll generates forward and backward slips. Material also tries to spread in width direction which is obstructed by frictional forces between workpiece and roll.

Under such conditions, there is a complex stress field generated at the roll bite. Consequently, the work roll is also subjected to a similar stress filed, which is mainly comprised of compressive and shear stresses that too in cyclic manner [1, 12]. It may also be noted that in hot rolling the friction may not be in slipping mode. Rather sticking friction is more prevalent at higher temperature, which may lead to shearing of material at subsurface level. Rolls are also subjected to bending forces due to its mechanical and thermal crown and external roll bending applied for controlling profile of the rolled materials. Additionally, there is significant influence of inter-roll pressure between work roll and backup roll and profiles of the two rolls also play an important role [14, 15]. Under the influence of cyclic mechanical load, high friction, high slip ratio and shear stress at roll bite, the work rolls wear out at faster rates.

Surface oxides on steel strip. Besides thermal and mechanical loads, the third most critical parameter affecting life of the rolls is presence of iron oxides or scale over the steel surface. Although the primary scale formed during heating of slabs inside the reheating furnace is removed through high pressure hydraulic descaling, there is generation of secondary scale during rolling at high temperature in roughing mills. Further, the secondary scale is removed hydraulically before the finishing mills.

However, there is formation of tertiary scale during rolling in finishing mills. Thus work rolls of roughing and finishing mills are constantly interacting with secondary and tertiary scales, respectively. Friction and wear at roll bite have strong dependence on oxides [16–18].

The effects of scale on rolls and in rolling process depend on its constitution. Invariably, the scale has different thicknesses of all the three iron oxides, that is, hematite (Fe_2O_3), magnetite (Fe_3O_4) and wustite (FeO). With highest oxygen %, hematite forms the outermost layers and with the lowest oxygen %, wustite forms the innermost layers. Magnetite layers remain in between. Hardness and proportion of these oxides are quite different and they strongly depend on temperature of steel. Among them, hematite is the hardest oxide and wustite is the softest one. Some of the researchers found hardness of FeO, Fe_3O_4 and Fe_2O_3 as 460, 540 and 1050 HV, respectively, at room temperature [19], and 105, 366 and 516 HV, respectively, at 900 °C [20]. It is also reported that above 900 °C, proportions of hematite and magnetite in scale increase with increasing temperature whereas at the same time proportion of the wustite decreases [21].

From the above facts it is clear that at higher temperatures while oxides lose their hardness, there is increase in proportion of the harder constituent of the oxides. Wear rate of rolls in abrasion mode should normally be higher with harder oxides. At the same time the softer oxide is sticky and may contribute in enhancing adhesive wear. Thus the mechanism of effect of scale on wear rate of rolls is a bit complex and besides temperature it should also depend on chemistry of the steel being rolled.

3   Experimental

Large numbers of studies on wear have been carried out by limited physical simulations in laboratory or through numerical or mathematical modelling of the actual process [18, 22–29]. Very less industrial research is found in this area. In the present work, investigations were carried out directly at industrial HSMs to study influence of roll wear on the following parameters without the use of any roll bite lubrication:

(a)   Campaign size of rolling,
(b)   Roll consumption, and
(c)   Surface quality of HR coils.

While studies related to campaign size and roll consumption were carried out at an HSM with 6 finishing stands (HSM-1), the study on surface quality was carried out at another HSM with 7 finishing stands (HSM-2). Salient details of these HSMs are given in Table 2.

Table 2 Salient details of HSMs where experiments were carried out

Parameters	HSM-1	HSM-2
Slab thickness (mm)	200–220	200–250
HR coil size (mm)	1.8–12.0 × 700–1580	1.6–16.5 × 750–1850
Material	All carbon and alloy steels	All carbon and alloy steels
Reheating furnace	Walking beam	Walking beam
Roughing mills		
• Roughing stands	2-reversing, 1-continous	1-reversing, 3-continous
• Edger stands	With each roughing stand	With each roughing stand
• Delay table	Coil box	Heat shield
Finishing mills		
• Finishing stand	6 No., 4-Hi, 1700 mm	7 No., 4-Hi, 2000 mm
• Work roll diameter, mm	760–710 (F1), 664–612 (F2-F6)	810–750 (F1–F7)
• Backup roll size, mm	1310–1180 × 1700	1610–1460 × 2000
• Work roll material	Hi-Cr (F1), ICDP (F2–F6)	Hi-Cr (F1–F3), ICDP (F4–F7)
• Backup roll material	Alloy forged steel (3% Cr)	Alloy forged steel (3% Cr)
• Max. speed, m/s	12.75	20.0
Run-out-table cooling	Laminar	Laminar
Down coiler	2	4

3.1 Study on Campaign Size of Rolling

Effect of wear on campaign size of work rolls was studied at the finishing mills of HSM-1. Here the campaign size was measured in terms of tonnage of steel rolled with one set of rolls at the mills. As per the practice, the campaign size of rolling was formed in coffin shape, i.e., width of the coils in a campaign was increased from narrow to wider and then again it was reduced to narrow size. It is well known that wear of work rolls has direct effect on strip crown of the rolled HR coils. Thus an optimum campaign size would be one within which the HR coils have acceptable level of strip crown.

Accordingly, crown of the rolled HR coils was evaluated at different production or tonnage processed in a campaign. For this, thickness of strip along width of the HR strip was measured using ultrasonic thickness gauge and strip crown was calculated as

$$Strip\ crown = \frac{t_c - t_e}{t_c}$$

where, t_c is the strip thickness at centre line and t_e is the average strip thicknesses 25 mm away from the two edges. The strip crown study was carried out for two strip sizes, one in narrower coils having width of 940 mm and thickness of 2.2 mm and

another in wider coils having width of 1280 mm and thickness of 2.8 mm. Finally, variation of strip crown with increasing rolled tonnage was plotted to visualise the effect of wear on strip crown and in turn on the campaign size of rolling.

3.2   Study on Roll Consumption

In another study, effect of wear on specific roll consumption was studied at Finishing Mills of the HSM-1. The F1 stand was using work rolls of Hi-Cr cast iron of higher diameter (760–710 mm) whereas the F2–F6 stands were using work roll of ICDP cast iron (diameter 664–612 mm). Midpoint diameter of the ground work roll was measured before and after the use at each stand to calculate amount of roll material loss due to wear during operation. It was termed as "mill wear". Roll dressing of the used work rolls was carried out at grinding machine to remove unevenness caused by wear and to provide proper profile to the ground rolls. Sum of the mill wear and the grinding off-take was the total material loss or roll consumption primarily on account of wear. The total wear loss was studied for over 1250 rolls at different finishing stands in a study period of 3 months. Tonnage rolled in each campaign was also noted for each set of rolls and ratio of total wear loss and campaign size was calculated to arrive at specific roll consumption. Comparisons of wear loss and specific roll consumption were made stand wise as well as for Hi-Cr and ICDP rolls.

3.3   Study on Surface Quality of HR Coils

Separate studies were carried out at HSM-2 where occurrence of surface defects like ridge and rolled-in-scale were observed in the rolled strips. It is often considered that one of the reasons of such defect is uneven wear of the work rolls in the finishing mills. Accordingly, an attempt was made to identify if there was any correlation between campaign size of rolling and the level of defects. As campaign size was linked to the wear of rolls, the study indirectly tried to find out if there was any direct relation between wear and these defects in HR coils.

During the study, HR coils diverted on account of the said surface defects were inspected and historical operating data of those coils were collected from level-2 computer of the HSM. Data were analysed and a plot of defect level against campaign size of rolls was drawn to see if there was any direct correlation between them.

4 Results and Discussion

4.1 *Effect of Roll Wear on Campaign Size of Rolling*

The campaign size of rolling in the mill is commonly decided based on acceptable tolerances for dimensional and surface quality parameters. One of such parameters is strip crown. Figure 2 shows variation of strip crown with increasing tonnage of rolled HR coils in a campaign for two sizes of strips. It was clearly evident that strip crown increased with the increasing tonnage of rolled strip, which was attributed to loss of roll profile on account of wear. In this case it was desired to have strip crown within 50–60 μm. Higher crown was undesirable for cold rolling of the HR coils and further application of the rolled products. It was observed that for limiting the strip crown to maximum 50–60 μm, the campaign size of rolling had to be fixed to around 2000–2500 ton for this mill. In other words, the campaign size was limited to a maximum value due to roll wear.

From Fig. 2 it was also observed that the rate of increase in strip crown of wider coils (2.8 mm × 1280 mm) suddenly increased after rolling around 2000 tons in the mill. The critical tonnage for narrower coil (2.2 mm × 940 mm) was slightly higher (3000 ton). It indicated that there was a steep rise in wear rate after reaching a critical campaign size of rolling. This value of the campaign size was considered as its optimum value. There was possibility of increasing the optimum campaign size by decreasing wear rate of rolls.

Restricting the campaign size at lower level due to high wear rate of rolls had significant economic implication for the mill. Lower the campaign size meant more number of roll changes for the given production level. Each roll change was causing a delay of around half an hour and thus significant amount of production loss. Besides, after each roll change, rolls were dressed for next campaign at the cost of increase in roll consumption. Thus any measure for reduction in wear rate of rolls and in turn for increase in campaign size of rolling was most welcome.

Fig. 2 Effect of roll wear on strip crown at finishing mills of HSM-1
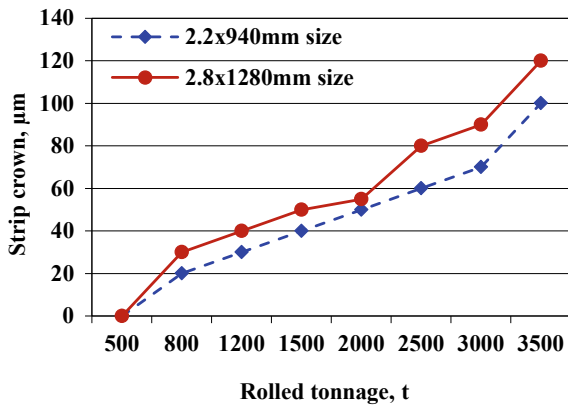
4.2 Effect of Roll Wear on Roll Consumption

Roll wear parameters namely mill wear (loss of material during rolling), grinding off-take (loss of material to remove effect of wear) and specific roll consumption were studied for over 1250 work rolls used in several normal campaigns at all the six finishing stands (F1–F6) of HSM-1. Average values of these parameters per roll per campaign at different stands are plotted in Fig. 3. Breakup of the mill wear and the grinding off-take for top and bottom work rolls at different stands are shown in Figs. 4 and 5, respectively. These data are only for normal roll changes made during three months of study period. Data related to abnormal roll changes, say for roll mark, dent mark, fire cracks, roll neck failure, etc., were filtered out during the analysis. The total loss of roll material was calculated as sum of the values of mill wear and grinding off-take of the same roll. The specific roll consumption was calculated by dividing total wear loss with average campaign size of rolling for each roll.
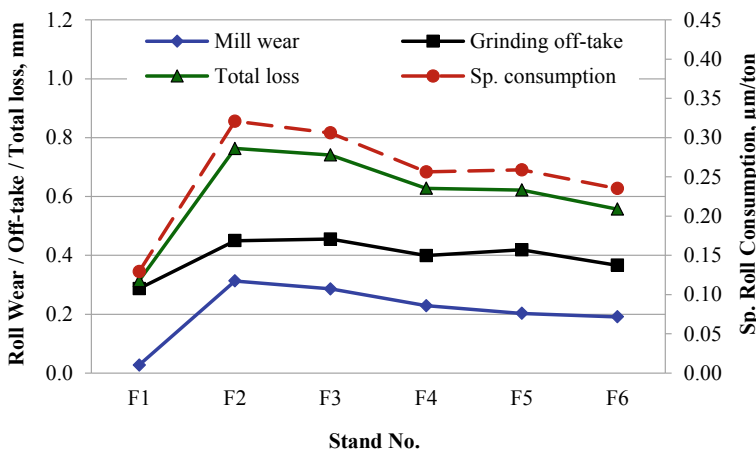
Fig. 3 Variation of roll wear parameters at finishing stands F1–F6 of HSM-1

Fig. 4 Average mill wear of top (T) and bottom (B) work rolls per campaign at finishing stands F1–F6 of HSM-1
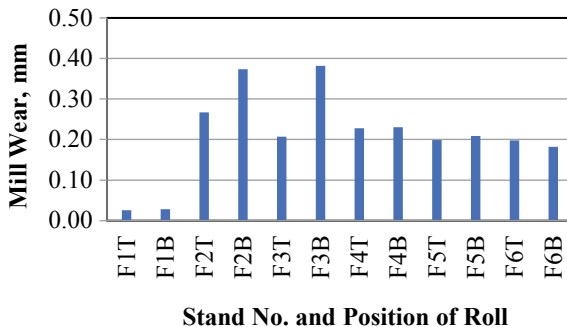
Fig. 5 Average grinding off-take of top (T) and bottom (B) work rolls per campaign at finishing stands F1–F6 of HSM-1
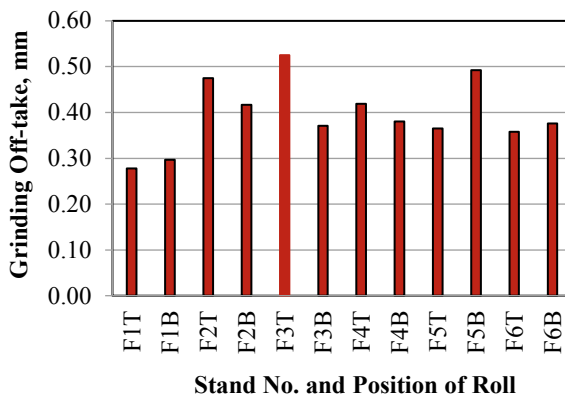
It may also be reemphasised that while the first finishing stand (F1) was using Hi-Cr cast iron rolls of larger diameter, the other finishing stands (F2–F6) were using ICDP rolls comparatively of lower diameters. It may also be noted that as per requirements of shape and profile control of HR coils, the top work rolls were provided a positive crown of 0.15–0.35 mm (convex profile) at different stands, the bottom rolls at all the stands were of cylindrical shape (without any crown). Hardness of the rolls varied in the range of 70–82 Shore. Analysis of wear parameters led to the following observations:

(a)   Average campaign size of rolling at different finishing stands varied in the range of 2300–2500 ton. In order to save delay for roll change, generally work rolls of all the stands were changed at the same time. However, sometimes due to rolling of special steels with stringent quality requirements, work rolls of last two stands were changed at lower campaign sizes.

(b)   Mill wear of Hi-Cr work rolls at F1 stand was significantly lower than that of the ICDP rolls at F2–F6 stands. While the average mill wear of Hi-Cr rolls was of the order of 0.027 mm at F1 stand, it was 0.313 mm, over 10 times higher, for the ICDP rolls at the next stand (F2). Average mill wear for all the ICDP rolls at F2–F6 stands was 0.227 mm per roll per campaign. These values would be higher if all the rolls with mill defects like fire cracks, roll marks, dent marks, etc. were included in the analysis.

(c)   As the amount of wear with the Hi-Cr rolls was lesser, there was also requirement of lesser roll dressing to remove the adverse effect of wear over the roll barrel. That is why average grinding off-take with Hi-Cr rolls (0.287 mm) was around 30% lower than that with the ICDP rolls (0.407 mm).

(d)   Combining the mill wear and the grinding off-take, the total roll material loss on account of wear for the Hi-Cr rolls was 50–60% lower than that of ICDP rolls. Similarly, as the campaign size of rolling for both types of rolls was kept of the same order, the average specific roll consumption of Hi-Cr rolls (0.13 μm/ton) was also lower by 50–60% from that of the ICDP rolls (0.24–0.32 μm/ton).

Fig. 6 Typical roll force for some of the coils rolled at Finishing Stands of HSM-1
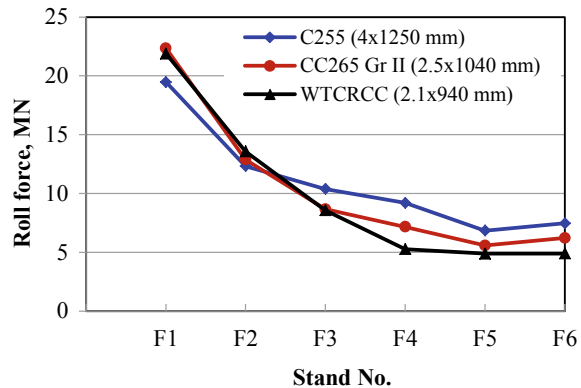
(e)   Figure 6 shows typical distribution of roll force for some of HR coils in different grades and sizes. It exhibited that there was decreasing order of roll force from the first stand to the last stand. The F1 stand had roll force almost double to that at the F2 stand. Obviously, the strip temperature was also in decreasing order from F1 to F6. From this it was clearly evident that the improved anti-wear performance of the Hi-Cr rolls at F1 stand was despite the fact that this stand had maximum roll force and temperature conditions. It thus justified the concept of using Hi-Cr rolls or superior wear resistant rolls at the initial finishing stands.

(f)   From Fig. 3 it was also revealed that for the same type of rolls (ICDP rolls of similar diameters), all the three roll wear parameters (mill wear, grinding off-take and specific roll consumption) were in decreasing order from F2 to F6 stands. It matched with the trend of roll force (Fig. 6) and temperature at these stands. That is, roll wear was higher at stands with higher roll force and strip temperature. It could be possible for multiple reasons; firstly, at higher load and temperature the effect of fatigue and adhesive wear would be more; secondly, at higher temperature friction would tend into sticky friction mode; thirdly, and most importantly, at higher temperature above 900 °C, growth of the harder oxides (Fe_2O_3 and Fe_3O_4) would shoot up [20, 21] leading to more abrasive wear.

(g)   From the Figs. 4 and 5, it was observed that there was a general pattern that wear of bottom work roll was slightly higher than that of the top roll of the same stand. It could be due to slightly higher temperature of the bottom rolls. In fact, top surface of a strip is exposed to atmosphere and cooling water more than that of its bottom surface. It was therefore possible to have slightly higher temperature of strip at its bottom surface. Accordingly, bottom work rolls would have higher temperature leading to higher wear rate.

4.3 *Effect of Roll Wear on Surface Quality of HR Coils*

Two surface defects namely ridge and rolled-in-scale were observed in HR coils at HSM-2. Ridge is a buckle defect which is visible in thinner CR coils, however, it is considered to have source in HR coils. The defect becomes prominent after rolling of HR coils at tandem mill and finishing at the skin pass mill. The ridge consists of sinusoidal waveforms located in one or two bands and runs mostly in full length of the coil [30]. It is a protuberance above the ideal thickness profile as shown in Fig. 7. CR coils with ridge may impact manufacturing operation at the customer's end adversely and is therefore downgraded or discarded depending upon severity of the defect.

Some of the literatures suggest that ridge is generated due to metallurgical reasons such as variations in microstructure, grain size or crystallographic texture along width of HR strips, which may cause differential deformation in cold rolling and subsequent operations [31]. However, in a recent research it could not be confirm experimentally [32]. The other school of thought, a more logical one, is that the ridge is generated due to uneven wear of work rolls in the HSM [30, 32]. It is understood that the work rolls with uneven wear make the roll gap contour irregular leading to heterogeneous deformation along the width direction of strip. The heterogeneity in deformation is not noticeable at HR stage because the difference in thickness is negligible compared to the average thickness of the HR strip. It becomes noticeable during cold rolling as the strip becomes thinner and possibly gets further aggravated during tempering due to higher coiling tension.

In order to test this concept, hot rolling parameters of 100 number of CR coils having ridge defects were analysed. Results of the analysis could not fully substantiate the theory of uneven wear of work rolls being the sole reason of the ridge formation. Generally, once the unevenness is introduced in the roll profile, it may

Fig. 7 Photograph of outer layer of a CR coil having ridge defect

last for several coils being rolled with it. Under such condition, ridge would appear in series of the coils rolled in a sequence. However, this evidence was not observed in the analysed coils. There was large gap between two consecutive coils having ridge defects.

Secondly, it is also a proven fact that unevenness of the wear profile of work rolls is more towards end of the campaign, that is, wear rate increases with increasing number of coils being rolled with the same rolls. The ridge defect should therefore be generated mostly in the coils hot rolled at higher campaign size. This trend was also not visible in the above analysed coils. Rather most of the defective coils were rolled either at the beginning or in the middle of the campaign (Fig. 8). At the HSM-2, the campaign size was measured in length of coils rolled and the standard campaign size was of the order of 100 km. Over 70% of the coils with ridge defect were rolled within 60 km of the campaign size. It was thus revealed that although uneven roll wear was the logical reason of the ridge defect, it might not be the only reason.

Similarly, level of rolled in scale (RIS) defect in the HR coils could not be correlated with the campaign size of rolling. As shown in Fig. 9, it was found that with

Fig. 8 Level of ridge defect at different campaign size of rolling at HSM-2
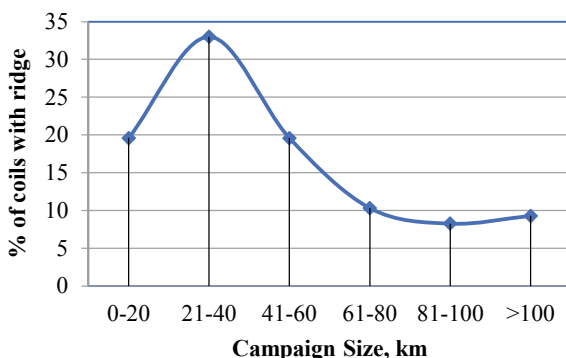
Fig. 9 Campaign size of rolling and level of rolled-in-scale (RIS) defect in some of the months at HSM-2
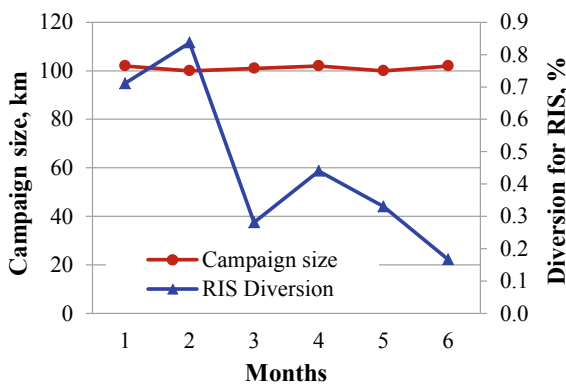
the same level of campaign size in some of the months, there was wide variation in the diversion of coils on account of rolled-in-scale defect in those months. Thus in addition to the wear of rolls, there must be some other reasons for generation of this defect.

5 Conclusions

Work rolls of hot steel strip mills suffer high amount of wear through abrasive, adhesive and fatigue modes. Abrasive oxide, high temperature adhesion and cyclic thermal and mechanical loads promote high wear rate of rolls. Studies carried out at finishing stands of the two HSMs reveal that with increasing amount of steel rolled with a set of rolls in a campaign, the strip crown increases due to progressive wear rate. In order to produce HR strips of given crown, campaign size is limited by roll wear. Rolling at lower campaign sizes is uneconomical due to higher frequency of roll change, production loss during roll change delay and higher specific roll consumption.

The studies also confirm the fact that the Hi-Cr rolls have much superior anti-wear performance compared to the ICDP rolls. Initial finishing stands are found prone to higher roll-wear and therefore Hi-Cr or superior rolls may be used at these stands. Wear rate, grinding off-take and specific roll consumption for the same type of work rolls have decreasing trends from the first to the last finishing stand due to decreasing trends of roll force and strip temperature at these stands. Bottom work roll is generally found to have slightly higher wear rate compared to the top roll in the same stand.

High or uneven wear of the work rolls is considered to be one of the reasons of the ridge and the rolled-in-scale defects associated with HR coils. However, the studies do not confirm genesis of the defects directly related with campaign size of rolling or with wear of the rolls.

References

1. Roberts WL (1988) Flat processing of steel. Marcel Dekker Inc., New York
2. Spuzic S, Strafford KN, Subramanian C, Savage G (1994) Wear of hot rolling mill rolls: an overview. Wear 176:261–271
3. Schroder KH (2003) A basic understanding of the mechanics of rolling mill rolls. ESW-Handbook, EisenwerkSulzau-Werfen
4. Pellizzari M, Molinari A, Straffelini G (2005) Tribological behaviour of hot rolling rolls. Wear 259:1281–1289

5. Tchuindjang JT, Lecomte-Beckers J (2008) Investigation on retained delta ferrite occurrence and its influence on HSS and semi HSS strengthening after thermomechanical routes. In: Pellizzari M (ed) Proceeding of ABRASION2008, abrasion wear resistant alloyed cast irons for rolling and pulverizing mills. University of Trento, Italy

6. Pellizzari M, Cescato D, De Flora MG (2009) Hot friction and wear behaviour of high speed steel and high chromium iron for rolls. Wear 267:467–475

7. Tremea A, Grespi M, Esteban A, Martinez W (2012) The work roll surface damaging study: a key factor in using HSS alloys in hot rolling. In: Proceedings 19th rolling conference, IAS, Rosario, Santa Fe, Argentina

8. Shinde GD, Raut LP (2015) An optimal design approach for adamite hot rolling mill roll. Int J Adv Eng Res Dev (IJAERD) 2(2):161–169

9. Inoue T, Uchida S, Ogawa S (2016) Characteristics of wear and rolling on fibre reinforced metal at high temperature. Nippon Steel & Sumitomo Metal Tech. Report, 111, pp 67–72

10. Tahir M, Widell B (2003) Roll wear evaluation of HSS, HiCr and IC work rolls in hot strip mill. Steel Res 74(10):624–630

11. Lecomte-Beckers J, Sinnaeve M, Tchuindjang JT (2012) Current developments of alloyed steels for hot strip roughing mills: characterization of high-chromium steel and semi-high speed steel. Iron Iron Steel Technol 9(2):33–40

12. Schey JA (1983) Tribology in metalworking—friction, lubrication and wear. American Society for Metals, Ohio

13. Legrand N, Weisz-Patrault D, Horsky J, Luks T, Labbe N, Picard M, Ehrlacher A (2013) Characterization of roll bite heat transfers in hot steel strip rolling and their influence on roll thermal fatigue degradation. Key Eng Mater 554–557:1555–1569

14. Dong Q, Cao J, Wen D (2015) Spalling prevention and wear improvement of rolls in steel strip hot-rolling process. J Fail Anal Prev 15:626–632

15. Servin R, Arreola SA, Calderón I, Perez A, San Miguel SM (2019) Effect of crown shape of rolls on the distribution of stress and elastic deformation for rolling processes. Metals 9(11), 1222, pp 1–16

16. Vergne C, Boher C, Gras R, Levaillant C (2006) Influence of oxides on friction in hot rolling: exp. investigations and tribological modelling. Wear 260(9–10):957–975

17. Joos O, Boher C, Vergne C, Gaspard C, Nylen T, Rezai-Aria F (2007) Assessment of oxide scales influence on wear damage of HSM work rolls. Wear 263:198–206

18. Zhu H, Zhu Q, Tieu AK, Kosasih B, Kong C (2013) A simulation of wear behaviour of high-speed steel hot rolls by means of high temperature pin-on-disc tests. Wear 302:1310–1318

19. Luong LHS, Heijkoop T (1981) The influence of scale on friction in hot metal working. Wear 71:93–102

20. Lundberg S-E, Gustafsson T (1994) The influence of rolling temperature on roll wear, investigated in a new high temperature test rig. J Mater Process Technol 42:239–291

21. Tominaga J, Wakimoto KY, Mori T, Murakami M, Yoshimura T (1982) Manufacture of wire rods with good descaling property. Trans Iron Steel Inst Jpn 22(8):646–656

22. Wang B (1996) A simulation of roll wear in hot rolling processes. Master of Engineering (Hons.) thesis, Department of Mechanical Engineering, University of Wollongong, https://ro.uow.edu.au/theses/2508.

23. Turk R, Fazfar P, Robic R, Perus I (2002) Prediction of hot strip mill roll wear. Metalurgija 41(1):47–51. ISSN 0543-5846

24. Tahir M (2003) Some aspects on lubrication and roll wear in rolling mills. Doctoral thesis, Division of Materials Forming, Dept. of Prod. Eng., Royal Institute of Technology, KTH

25. Jonsson M (2006) TM-rolling of heavy plate and roll wear. Thesis, Division of Material Mechanics, Department of Applied Physics and Mechanical Engineering, Lulea University of Technology, Lulea, Sweden. ISSN: 1402-1757

26. Jonsson M (2007) Modelling the work roll wear contour in a four-high mill. Steel Res Int 78(4):333–339

27. Byon SM, Lee Y (2008) A study of roll gap adjustment due to roll wear in groove rolling: experiment and modelling. Proc IMechE Part B J Eng Manuf 222:875–885

28. Dohda K, Boher C, Rezai-Aria F, Mahayotsanun N (2015) Tribology in metal forming at elevated temperatures. Friction 3(1):1–27. ISSN 2223–7690
29. Liu Z, Guan Y, Wang F (2017) Model development of work roll wear in hot strip mill. IOP Conf Ser Mater Sci Eng 207(012022):1–4
30. Zhu HT, Tieu AK, Dippenaar RJ, Careter CD, Ziegelaar J (2010) Effect of hot coil profile containing ridges on ridge-buckle defects of cold rolled thin strip. Int J Mater Form 3(1):21–27
31. Takeehi H, Kato H, Sunami T, Nakayama T (1967) The mechanism of ridging formation in 17%-chromium stainless steel sheets. Trans JIM 8:233–239
32. Melfo WMC (2006) Analysis of hot rolling events that lead to ridge-buckle defect in steel strips. Ph.D. thesis, School of Mechanical, Materials and Mechatronics Engineering, University of Wollongong

Tribological Performance of Heat Treated 0.6% C Steel

Renu Kumari, Ajit Behera, Priyanka Bharti, and Deepak Kumar Sethi

1 Introduction

The wide application of medium carbon steel in automotive, aerospace, agriculture and structural application due to its good mechanical properties. Most of the steel in the structural application observed wear, such as, steel shaft observed sliding wear in journal bearing application. In the past several research were done on the effect of heat treatment on the microstructure and mechanical properties [1–4]. Effect of quenching and tempering of austenitic steel with 5% manganese on microstructure, hardness and wear properties were analyzed by Garcia et al. [2]. And found that increased hardness after wear test in as received, air quenched and oil quenched sample. This trend was not obtained in water quenched and tempered sample. Fadare et al. [3] investigated the effect of heat treatment on microstructure and mechanical properties of NST 37–2 steel. Result obtained that annealed sample consisted mainly ferrite phase along with lowest strength and hardness, while hardened sample consisted marten site phase, which showed highest tensile strength and hardness. The effect annealing and normalizing during hot rolling process on microstructure and hardness of steel was studied by Dahiwade et al. [4]. They found that annealing gave coarse perlite with low hardness and normalized gave fine pearlite with high hardness. The effect of annealing on the microstructural characterization and mechanical properties was studied by Onwuamaeze et al. [5]. And showed that significant modification in microstructure

R. Kumari (✉)
Department of Metallurgical and Materials Engineering, NIT Jamshedpur, Jamshedpur, Jharkhand, India

A. Behera
Department of Metallurgical and Materials Engineering, NIT Rourkela, Rourkela, Odisha, India

P. Bharti
Department of Mechanical Engineering, BCE Bhagalpur, Bhagalpur, Bihar, India

D. K. Sethi
Department of Metallurgical and Materials Engineering, NIFFT, Ranchi, Jharkhand, India

171

Table 1 Composition of steel specimen

Elements	C	Si	Mn	P	S	Cr	Mo	Ni	Al	Cu	Fe
Content (%)	0.60	0.25	0.74	0.01	0.01	0.10	0.02	0.13	0.01	0.18	Balance

and mechanical properties. Ismail et al. [6] studied that the effect of heat treatment on the hardness and impact properties of medium carbon steel. Result showed that highest hardness in quenched steel, on the other hand, tempered sample showed good mechanical properties due to increased ductility and toughness. Mudashiru and Adio [7] investigated the effect of heat treatment on hardness and microstructure of welded low carbon steel. Microstructure showed that predominately pearlite phase and less ferrite phase after heat treatment. There was a significant improvement in ductility, toughness and grain refinement, on the other hand, decreased in hardness and brittleness. Saha et al. [8] investigated the effect of cyclic heat treatment of 0.6 wt% carbon steel and found an excellent combination of strength and ductility.

From the aforementioned literature, it was found that in the past many work was done on effect of various heat treatment on microstructure and mechanical properties. However, a very few work was done on 0.6% C steel. So the present work focus on effect of heat treatment (mainly annealing and normalizing) on microstructure, phase, hardness and tribology behavior have been analyzed.

2 Methodology

In this study, 0.6% carbon steel rod was used and the composition is mentioned in Table 1. The samples were cut by using abrasive cutter by 10 mm × 10 mm × 6 mm dimension. Heating of the samples were done at 910 °C for 2 h than furnace cooling (annealing) and air cooling (Normalizing) were done. Followed by heat treatment, microstructure analysis was done by using optical microscopy. X-ray diffraction techniques (D8 Advance, Bruker, using Cu K $\propto$ radiation) was used to analyze the phase of as received and heat treated 0.6% C. The wear test was done by using a pin-on-disk wear tester at an applied load 10 kg for 600 s time at ambient condition as per ASTM G99.

3 Results and Discussions

Microstructure analysis were done for as received and heat treated sample. Figure 1 shows the optical micrographs of as received 0.6%C steel at different magnification (a) 100X (b) 200X (c) 400X (d) 1000X. From Fig. 1, it is observed that presence of ferrite and pearlite. High magnification view shows that presence of fine lamella of pearlite in Fig. 1(c, d).

Fig. 1 Optical micrographs of as received 0.6% C steel at different magnification **a** 100X, **b** 200X, **c** 400X, **d** 1000X

Figure 2 shows the optical micrographs of annealed 0.6% C steel at (a) 100X, (b) 200X, (c) 400X, (d) 1000X magnification. From Fig. 2, it is observed that presence of ferrite and pearlite grains.

Figure 3 shows optical micrographs of normalized 0.6% C steel at different magnification (a) 100X, (b) 200X, (c) 400X, and (d) 1000X. From Fig. 3 it is observed that there is ferrite and pearlite grains. Phase analysis has been done by using X-ray diffraction technique and results are summarized in Table 2. From Table 2 it is observed that presence of ferrite and carbide phase in as received 0.6% C steel. Presence of ferrite and carbide phase have been also observed in annealed and normalized 0.6% C steel.

Figure 4 shows the variation of micro-hardness of as received and heat treated 0.6% C steel. From Fig. 4 it is observed that the hardness value decreases from 548 HV for as received 0.6% C steel to 256 HV for annealed sample and 412 HV for normalized samples (Fig. 4). This is may be due to formation of coarser lamella in pearlite after heat treatment as compared to presence of fine lamellae pearlite in as received 0.6% C steel. A close comparison of hardness of annealed and normalized samples shows that the hardness of annealed steel is less than normalized samples. Which may be due to annealing heat treatment gives coarse pearlite. Biswas et al. [9] reported the hardness of 508 BHN for quenched, 155 BHN for annealed and 259 BHN for normalized EN9 Steel.
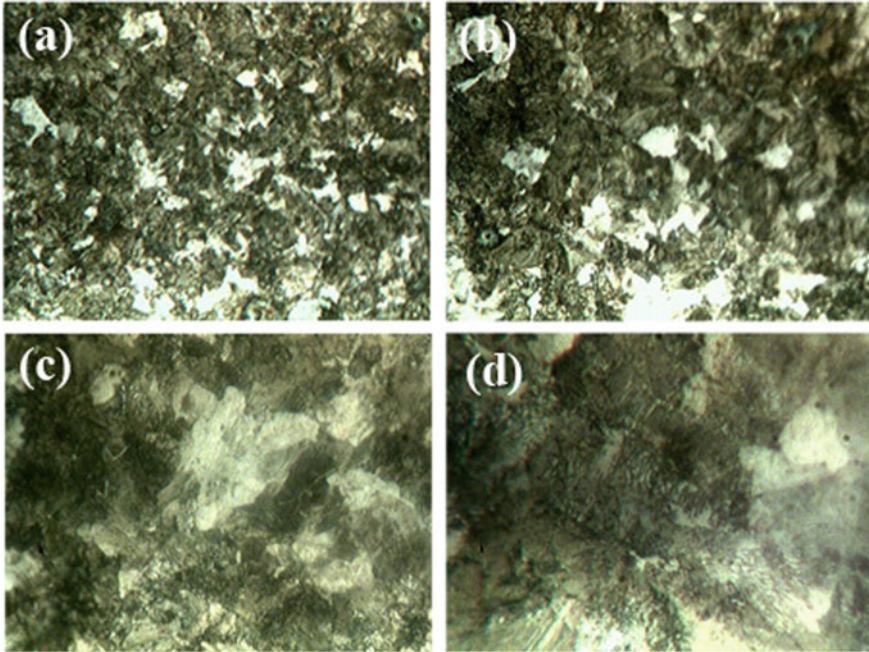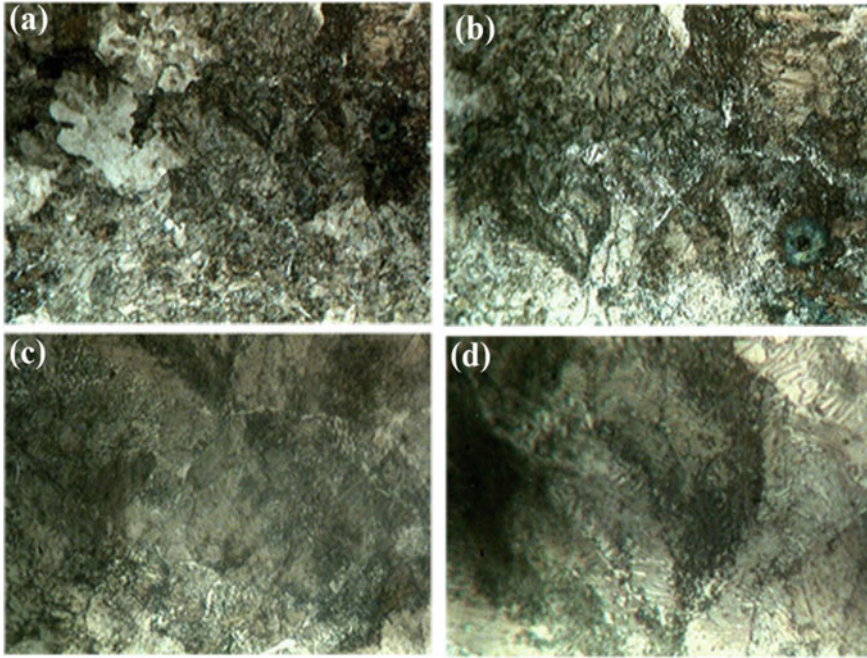
Fig. 2 Optical micrographs of annealed 0.6% C steel at different magnification **a** 100X, **b** 200X, **c** 400X, and **d** 1000X

Figure 5 shows that the variation of wear depth with time for as received (plot 1), annealed (plot 2) and normalized (plot 3) 0.6% C Steel. From Fig. 5 it is clearly observed that the wear depth of as received 0.6% C steel is 20 µm. On the other hand, the wear depth of normalized sample is 390 and 410 µm for annealed sample. The low wear depth of as received sample is due to high hardness as compared to heat treated sample [10, 11].

Figure 6 shows the variation of coefficient of friction (COF) with time for as received (plot 1), annealed (plot 2) and normalized (plot 3) 0.6% C steel. From Fig. 6 it is observed that the coefficient of friction of as receive sample varies from 0.052 to 0.062 for 600 s interaction time. On the other hand, coefficient of friction varies from 0.052 to 0.062 for 600 s interaction time for normalized sample and varies from 0.062 to 0.073 for 600 s interaction time for annealed sample. Coefficient of friction is more in case of normalized sample as compared to as recieved and annealed sample, which may be due to fine grain size and formation of smooth surface [11, 12].
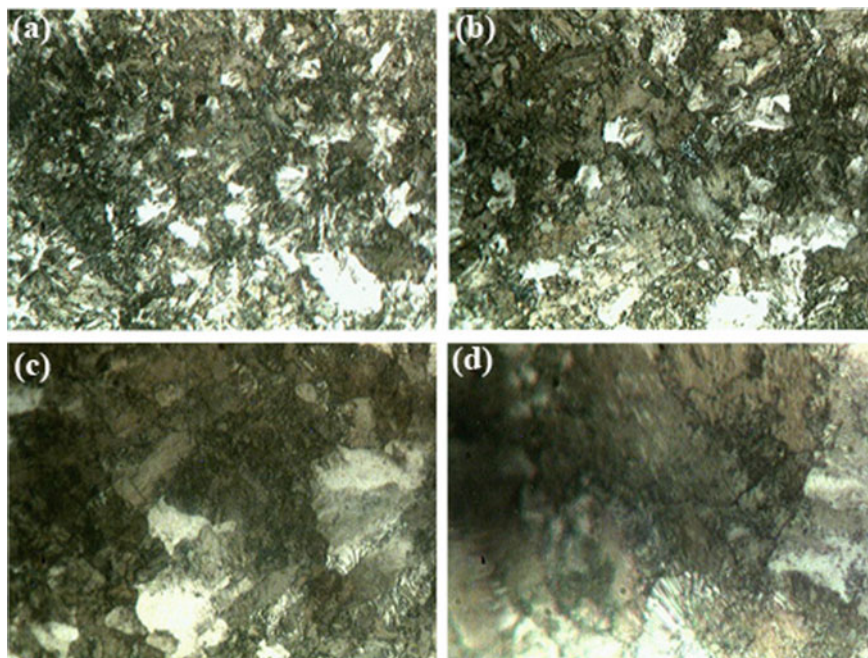
Fig. 3 Optical micrographs of normalized 0.6% C steel at different magnification **a** 100X, **b** 200X, **c** 400X, **d** 1000X

Table 2 Summarized phases, hardness and wear depth of as received and heat treated 0.6% C steel

Sample	Phase	Hardness	Wear depth
As received 0.6% C steel	Ferrite, carbide	548 (HV)	20 (μm)
Normalized 0.6% C steel	Ferrite, carbide	412 (HV)	390 (μm)
Annealed 0.6% C steel	Ferrite, carbide	256 (HV)	410 (μm)

Fig. 4 Bar-chart showing the variation of micro-hardness of as received and heat treated 0.6% C steel
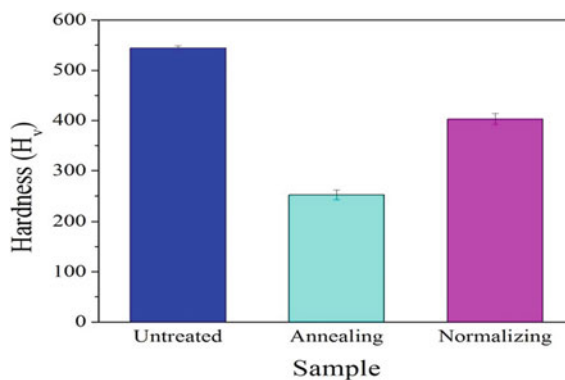
Fig. 5 Variation of wear depth with time for as received (plot 1), annealed (plot 2) and normalized (plot 3) 0.6% C Steel
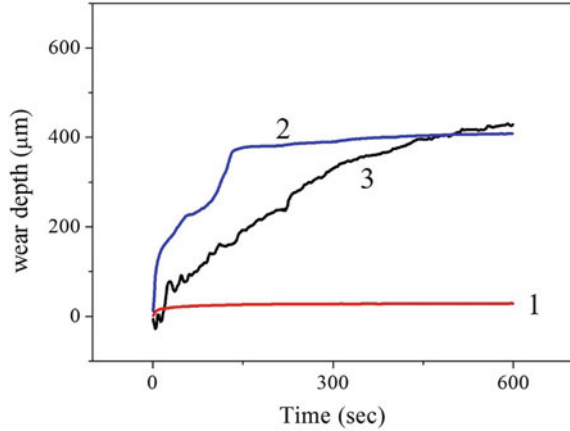
Fig. 6 Variation of coefficient of friction with time for as received (plot 1), annealed (plot 2) and normalized (plot 3) 0.6% C steel
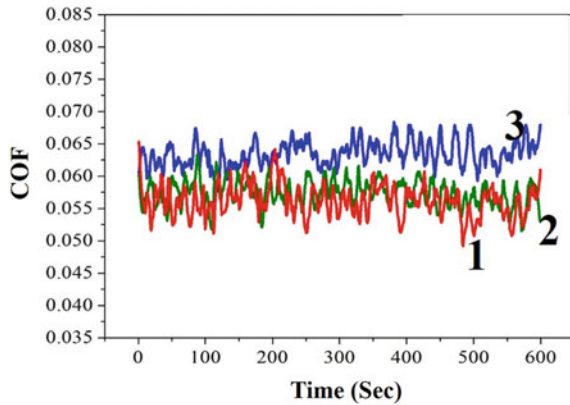
4   Conclusions

In this study, tribological performance of heat treated 0.6% C steel have been analysed. A detailed study of microstructure, hardness and wear have been done. And following conclusion have been drawn: (1) Presence of predominantly pearlite grains and less ferrite grains in as received and heat treated sample. (2) Phase analysis shows the ferrite and carbide phase in as received and heat treated sample. (3) Microhardness value decreases from 548 HV for as received 0.6% C steel to 256 HV for annealed 0.6% C steel sample and 412 HV for normalized 0.6% C steel. (4) The wear resistance of as received sample is good as compared to annealed and normalized sample. The wear depth is 20 μm for as received, on the other hand, 390 μm for normalized sample and 410 μm for annealed sample. (5) The coefficient of friction of as received sample varies from 0.052 to 0.062, on the other hand, coefficient of

friction varies from 0.052 to 0.062 for normalized sample and 0.062 to 0.073 for annealed sample.

References

1. Czichos H, Habig KH (1986) Wear of medium carbon steel: a systematic the influence of materials and operating parameters. Wear 110:389–400
2. Garcia A, Varela A, Garcia L et al (2005) Comparing the tribological behaviour of an austenitic steel subjected to diverse thermal treatments. Wear 258:203–207
3. Fadare DA, Fadara TG, Akanbi OY (2011) Effect of heat treatment on mechanical properties and microstructure of NST 37–2 Steel. J Miner Mater Characterizat Eng 10(3):299–308
4. Dahiwade PA, Shrivastava S, Sagar NK (2014) study the effect of hardness of steel by Annealing and normalizing during hot rolling process. IJIRT1 (2). ISSN-2349–6002
5. Onwuamaeze IP, Oyejide JO, Salisu S et al (2018) The effect of annealing on the microstructure and mechanical environmental science 3(1):96–102
6. Ismail NM, Khatif NAA, Kecik MAKA, Shaharudin MAH (2016) The effect of heat treatment on the hardness and impact properties of medium carbon steel. IOP Conf Ser Mater Sci Eng 114:012108. https://doi.org/10.1088/1757-899X/114/1/012108
7. Mudashiru LO, Adio TA (2013) Study of effects of heat treatment on the hardness and microstructure of welded low carbon steel pipes. Innov Syst Des Eng 4(9). ISSN 2222–1727
8. Saha A, Mondal DK, Maity J (2010) Effect of cyclic heat treatment on microstructure and mechanical properties of 0.6wt% carbon steel. Mater Sci Eng A 527(16–17):4001–4007
9. Biswas P, Kundu A, Mondal D (2017) An experimental investigation on hardness and microstructure of heat treated EN 9 steel. IOP Conf Ser Mater Sci Eng 225:012055
10. Priyadarshini M, Behera A, Biswas CK (2020) Effect of sub-zero temperatures on wear resistance of AISI P20 tool steel. J Braz Soc Mech Sci Eng 42:212
11. Priyadarshini M, Biswas CK, Behera A (2019) Grey-Taguchi optimization of Wire-EDM parameters for P20 tool steel. In: ICMRE'19: proceedings of the 5th international conference on mechatronics and robotics engineering, pp 5–8
12. Priyadarshini M, Biswas CK, Behera A (2019) Machining of sub-cooled low carbon tool steel by wire-EDM. Mater Manuf Processes 34(12):1316–1325

Improvement in Adhesion of Electroless Coating on Plastic Substrates: A Review

Budhram Boipai and **Tushar Banerjee**

1 Introduction

Plastics are synthetic or semi-synthetic organic compounds that are malleable and suitable shapes may be imparted to them. Recently, demand for plastics is on the rise due to low cost as well as their ability to be molded into complex shape and size with good accuracy and surface finish. Plastics may be a good alternative option for certain parts/applications in automobile like door knobs [1], electromagnetic interference shielding textiles [2] and flexible circuits [3] in electronic industries, urinary catheters [4] in medical field. The plastics have low density, and have good strength-to-weight ratio. But, due to non-metallic property, they cannot be used as electrically conductive, abrasive resistant, and thermally conductive material. In order to impart such properties, metallic coatings may be deposited on the surface of plastic components and it may result in replacement of metallic parts in certain industrial applications. The coating of metals on plastic substrate is called metallization. Metallization of plastic substrate is necessary for various application areas such as decoration, printed circuits, automotive, aerospace, and microelectronics industries [5, 6].

Currently, many techniques are used for depositing coating on plastic surface such as vacuum deposition [7], flame and arc spraying [8], sputter coating [9], electroless coating [10] etc. Electroless coating is a suitable selection for the development of the technology and its distinct characteristics include uniformly thickness of deposit, bath temperature below the melting point of plastic, low investment, and manufacturing cost [11]. The electroless coated films or layers serve important functions such as providing electrically conducting surface layer on the plastic substrate [12], improving wear resistance of the product and providing a secure bonding layer

B. Boipai · T. Banerjee (✉)
Department of Production and Industrial Engineering, NIT Jamshedpur, Jamshedpur, India
e-mail: tbanerjee.prod@nitjsr.ac.in

between the plastic surface and metal [13]. There are several advantages of electroless coating process such as control of plating thickness, substrate volume, chemical replacement, process monitoring [5]. However, the main hurdle is ensuring proper adhesion between the metallic layer to the plastic surface [14–18].

This article reviews different methods being investigated by researchers, for improving adhesion of electroless deposited layer with plastic substrate.

2 Basic Conditions for Electroless Coating on Plastic Substrate

Electroless coating on plastic surface involves a series of steps such as cleaning, etching, neutralization, activation, acceleration and finally deposition of the functional layer [19]. The steps are briefly discussed below.

(i)   Cleaning: This is the process to remove dust, oil, and grease from the plastic surface. Micro-roughness is also developed by the cleaning process which increases the coating surface area. Generally, brushing or scouring with sand paper is used to accomplish cleaning [20]. The alkaline solution is also used [21]. Recently, ultrasonic agitation in anhydrous ethanol and distilled water has also been found to be effective to clean plastic substrates [22].

Some factors to be considered about the cleaning process includes the following.

(a)   Choice of cleaner,
(b)   Cleaning medium temperature,
(c)   Concentration and composition of cleaning medium,
(d)   Cleaning duration,
(e)   Level of agitation in the cleaner,
(f)   Cleanliness of the cleaner.

(ii) Etching: Etching is the most significant step in the substrate pretreatment process which is mainly responsible for achieving high bonding strength between plastic and metal. The substrate surface is etched chemically and pores are developed to increase the plating surface regions in order to enhance coating-substrate bonding. In this phase, the polymer or plastic material is immersed in the oxidant solution. The oxidant solution is generally H_2CrO_4 mixed with aqueous H_2SO_4 or HF with H_2SO_4 on the basis of the surface to be coated [13]. Generally, the solution of H_2O (41%), H_2SO_4, and CrO_3 used for the etching process. The etching process is conducted for 5–15 min and temperature of bath is maintained between 60 and 65 °C.

(iii) Neutralization: In this stage, the remaining extra residual acid present in the hole and gap of the plastic substrate after etching is removed. Such residual acid adversely affects the coating process and may corrode if not removed from the plastic surface. For this purpose, acidic as well as the basic solutions are used [13].

(iv) Activation: In this stage, activating of the etched plastic surface is carried out on by immersing in an activator solution. The activator is a solution of palladium/tin (Pd/Sn). The activation process introduces the metal particles to the substrate surface to act as seeds for metal deposition. This process is generally carried out at 45 °C for 5 min [21].

(v) Acceleration: In this stage, activated plastic substrate is immersed in the acceleration solution which increases the absorptive capacity. Acceleration solution may be an acid [23] or basic solution and it absorbs the excess activator and frees the plastic substrate from it. Generally, the activated surface is washed with distilled water and subjected to an acceleration bath for 5 min [23].

(vi) Electroless deposition: This is the last stage of the electroless coating process. In this stage, the activated plastic substrate is immersed into solution usually containing metal salts and reducing agent (sodium hypophosphite) [11]. The medium may be either acidic or basic. The redox reaction starts taking place and coating is deposited on activated substrate surface. Bath temperatures normally maintained at 50–60 °C [21].

The steps involved and their corresponding medium and operating conditions regarding deposition of electroless copper on acrylonitrile butadiene styrene substrate is presented in Table 1.

Table 1 Bath compositions and deposition conditions for electroless plating on the ABS (acrylonitrile butadiene styrene) substrate [21]

Step	Composition	Conditions
Degreasing	Sodium hydroxide 16 g/L, Sodium carbonate 18 g/L, Trisodium phosphate 14 g/L, Emulsifier 5–8 ml	70 °C, 15 min
Etching	Nitric acid 187.5 ml/L Sulfuric acid 187.5 ml/L Nickel (II) sulfate 50 g/L	50 °C, 20 min 60 °C, 20 min 70 °C, 20 min
Swelling	Sodium hydroxide 90 g/L, 1-methyl-2-pyrrolidone 50 ml/L and 2-Butoxy ethanol 20 ml/L	70 °C, 20 min
Activation	Colloidal palladium solution	45 °C, 5 min
Dispergation	HCl 100–120 ml/L	35 °C, 2 min
Electroless copper plating	Copper (II) sulfate pentahydrate 10 g/L, Formaldehyde 3 ml/L, Ethylenediaminetetraacetic acid 30 g/L, 2, 2'-pyridine 15 mg/L, PEG (Mw = 1000) 0.5 g/L, pH 11–13	50–60 °C For 2–10 min

3   Methods for Enhancing Adhesion of Electroless Coating on Plastic Substrate

The main problem associated with electroless coating on plastic/polymer is generally low chemical affinity for metals, which results in weak bonding strength between metal and polymer. Several authors have investigated the issue of enhancing adhesion between electroless coating and plastic substrate. Hoffman [24] reviewed the surface activation method such as (a) physical method (b) chemical method (c) mechanical methods (d) biological methods, on polymer. These methods help to modify the surface of the polymer. Wang et al. [25] developed the Sn-free process and improved the adhesion between copper and PRMC (phenolic resin matrix composite). They employed the wet chemical etching process for modification of surface of phenolic resin matrix composite. Chen et al. [26] introduced layer-by-layer (LbL) electroless coating process to enhance adhesion of metallic coatings on plastic. This method depends on procedures for modifying the polymer substrate. They used P-TES and N-TES solutions to improve the adhesion strength. Lu [12] studied the ultrasonic-assisted electroless deposition of copper thin film on to PET (polyethylene terephthalate) with the modification of silane and reported improvement in adhesion of copper plating. Hou et al. [27] sequentially immersed the UV/ozonolysis irradiated PET samples on to the cupric citrate solution and $NaBH_4$ solution and observed high adhesive strength under the optimized condition. They found that peel adhesion strength was up to 39 N/cm. Sahoo et al. [28] introduced the environmentally friendly electroless copper coating on acrylonitrile–butadiene–styrene (ABS). They eliminated the etching and palladium activation process. For copper deposition, five different acidic baths were used. Schaubroeck et al. [29] studied the influence of surface modification, epoxy roughness and electroless copper deposition temperature on the polyamine surface. They introduced wet—chemical modification on the surface of polyamine. They studied the adhesion strength of electroless copper coating on polyamine substrate. Rytlewski et al. [30] introduced copper (II) L-tyrosine as precursor for selective activation of polymer and subsequent deposition of electroless copper coating. ArF excimer laser of wavelength 193 nm was used to irradiate the precursor to modify its structure and thereby to improve the adhesion of the coating. Analysis by EDX showed that more copper was deposited on the substrate with increasing irradiation of laser. Vasconcelos et al. [31] achieved strong adhesion between silver film and thermoplastic by first immersing it into the solution of polyvinylpyrrolidone in dimethyl sulfoxide, and then create a polyvinylpyrrolidone rich network on to the thermoplastic polyurethane surface by the help of surface-physical-interpenetrating-network method. Charbonnier and Romand [32] focused on surface modification on the surface of polypropylene (PP) and poly (bisphenol A carbonate) (PC) using Nd: YAG laser and incoherent excimer lamp operating in an oxygenated environment. They analysed the chemical interaction of catalysts with the grafted surface by X-ray photoelectron spectroscopy. A review of the literature on improvement of adhesion of electroless coating on plastic substrate indicates four main processes as discussed below in detail.

Table 2 Composition and conditions of copper polyalloy bath [27]

Composition	Condition
Cobalt sulphate heptahydrate	0.08–0.12 M
pH	9.0–11.0
Plating temperature	30–40 °C
Coating time	25–45 min
Copper (II) sulphate pentahydrate	0.1 M
Sodium hydroxide	0.56 M
Potassium sodium tartrate	0.8 M

(i) **UV-ozonolysis irradiation for improving adhesion of copper polyalloy coating**

Ultraviolet lights are extremely helpful in cleaning surfaces of plastic substrate and free it from any carbonaceous residue, which results in excellent adhesion between plastic and metallic layer. Therefore, electroless plating with combination of UV/ozonolysis irradiation is an excellent method to achieve good adhesion between metal and plastic surface. Hou et al. [27] used this method to improve adhesion between polyethylene terephthalate (PET) and electroless copper layer. The selection of PET was owing to excellent mechanical strength and good thermal stability [33]. In this process, the PET sheet was washed ultrasonically and then exposed to ultraviolet light (using mercury lamp) in ozone atmospheric condition for 1 h. The irradiation power was generally 5 mWcm^2. After that ultraviolet/ozonolysis-treated plastic substrate was immersed for 10 min in the aqueous cupric citrate solution for activation and then soaked on NaBH$_4$ aqueous solution for 10 min at room temperature again for activation. After that sample was rinsed with distilled water and put in an oven for 30 min at 60 °C for the purpose of drying. The activated Cu-seeded polyethylene terephthalate sheet was put in the copper polyalloy coating bath. The composition and conditions of copper polyalloy bath is presented in Table 2.

Finally, the copper polyalloy coated PET is dried with warm air stream. The adhesion strength is found up to 39 N/cm, which is in acceptable limit. The basic procedure of electroless copper coating on PET is shown in Fig. 1.
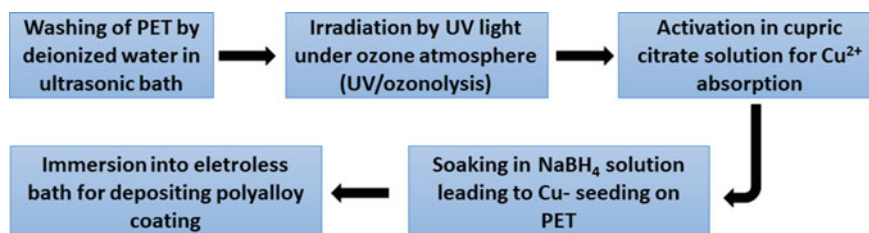

Fig. 1 The process of electroless copper polyalloy coating with UV/ozonolysis irradiation [27]
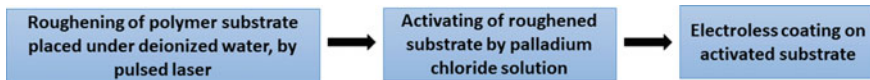
| Roughening of polymer substrate placed under deionized water, by pulsed laser | ➡ | Activating of roughened substrate by palladium chloride solution | ➡ | Electroless coating on activated substrate |

Fig. 2 Step of the Laser-induced selective activation (LISA) method [34]

(ii) **Laser-induced selective activation (LISA) method**

Laser can be the most efficient tool for coating on the plastic. It is generally used to clean, roughen, and activate to the plastic surface. In this section laser-induced selective activation metallization on the plastic is reviewed.

Laser-induced selective activation method is the technique that can be used for depositing positional selective coating on the surface of plastic or polymer substrate. In this method, there are three primary steps such as (a) Laser treatment: The laser ray modifies the plastic or polymer surface in a medium of deionized water. In this step, a thin molten surface layer is produced on the plastic substrate by laser pulse energy. After that plastic substrate is instantly cooled down with water so that polymer solidifies quickly and sponge-like structure is created. The sponge-like structure ensures good mechanical engagement between metal and polymer, thereby improving adhesion. After multiple passes of laser, the surface becomes rough and porous. (b) Activation: The laser modified plastic surface is activated by immersing it into a palladium solution. The palladium atoms attach to the rough surface of the plastic. (c) Metal plating: Metallic coating is deposited on the surface of activated plastic by electroless route. Zhang et al. [34] used this method to coat copper on the polycarbonate substrate. In the first step, they irradiated the plastic surface, immersed in deionized water, with Nd: YAG laser. Beam velocity and average power was 60 mm/s and 3.4 W respectively. In the second step, mixture of $SnCl_2$ and $PdCl_2$ solution was used for the activation process. In the final step, the autocatalytic copper coating was done on the activated plastic surface. They found the average adhesion strength of the copper layer to be 2.79 MPa. Figure 2 illustrates the steps involved in the laser-induced selective activation method.

(iii) **Novel coating with assisted super-critical CO_2**

To achieve high adhering performance, anchoring effects are needed between adequate interfacial areas. This method introduced an interlocking phenomenon between metal to the polymer substrate. In this method, there are two steps as follows.

(a) Catalyst impregnation (pre-treatment of substrate): In this step, first the catalyst precursor Pd (II) hexafluoroacetylacetonate ($Pd(hfa)_2$) is dissolved in the super-critical carbon dioxide ($scCO_2$), which is followed by exposure of plastic substrates to $scCO_2$ in order to infuse the precursor. The catalyst impregnation is done in a high pressure vessel at temperature of about 80 °C. The substrate and $Pd(hfa)_2$ are placed in the pressure vessel. The substrate is kept on a small

Fig. 3 Procedure of electroless coating on polymer substrate with assisted super-critical CO_2 [35]

metallic table and the $Pd(hfa)_2$ powder is put below so that it infuses into the polymer by diffusion only. Now, carbon dioxide at high pressure (up to 10 MPa) is loaded into the chamber to dissolve $Pd(hfa)_2$ and to do substrate impregnation. This process is carried up to 30 min. The impregnated $Pd(hfa)_2$ is subjected to temperature of 120 °C in presence of CO_2 for 30 min in order to decompose thermally. Impregnation of catalyst precursor into the polymer substrate is done to create anchoring effect. Now plastic sample is dried on vacuum chamber up to 24 h for remove the CO_2.

(b)   Electroless coating: In this step, the impregnated polymer substrate is put into the electroless coating bath. Ethanol and CO_2 are then added to the bath to plasticize the substrate and promote mass transfer of the coating solution into the substrate. Now metal is grown on the polymer substrate through auto-catalytic reaction. A composite layer of metal/polymer is developed on the surface, owing to penetration of bath solution in the plasticized polymer. This composite layer acts as metal anchors and enhances coating-substrate adhesion [35]. Adachi et al. [35] drastically improved adhesion up to 19.5 N/cm by this process. Tengsuwan and Ohshima [36] achieved the average adhesion strength of 8.8 ± 1.8 N/cm on polypropylene blend substrate by electroless plating. Figure 3 illustrates the steps involved in the process.

(iv)   **Molecular bonding followed by electroless spray-coating**

This is the newest method of electroless coating to enhance adhesion. Yang et al. [37] used this method to improve the adhesion between metallic coating to the polymer substrate. This method consists of three steps.

(a)   Degreasing
(b)   UV-grafting and self-assemble of P-TES and N-TES respectively
(c)   Sensitizing, followed by electroless plating

In this method, the substrate is annealed at 60 °C for 2 h for relieving stress. To degrease the substrate, it is immersed into the solution of NaOH and Na_2CO_3 at 30 °C for 1 h. Now again the substrate material is cleaned in ultrasonic cleaner for 5 min with ethanol. The substrate is then dried for few minutes and then immersed into an alcoholic solution with P-TES for 20 s. Now the substrate is exposed to UV radiation with a wavelength of 365 nm for 5 min and then washed several times with distilled water. The UV-grafted substrate is immersed into the solution of N-TES for 30 min and then cleaned and dried.

The modified substrate is immersed into the solution of $SnCl_2$ and hydrochloric acid for 5 min to sensitize and then it is washed with distilled water. The substrate is then dried for a few seconds. Then solution A ($AgNO_3$, $NH_3·H_2O$, and 1 L distilled
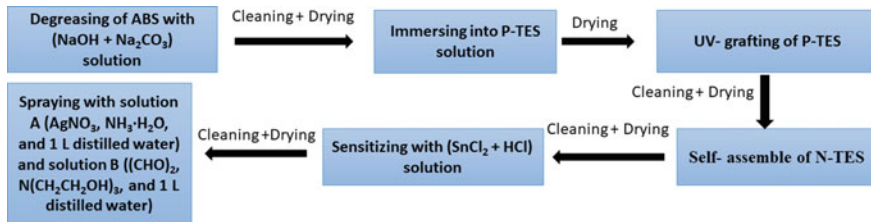
Fig. 4 Step diagram of molecular bonding followed by electroless spray-coating [37]

water) and B ((CHO)$_2$, N(CH$_2$CH$_2$OH)$_3$, and 1 L distilled water) is sprayed on the substrate in the glove box. Finally, the substrate is rinsed with distilled water and dried [37]. The adhesion strength is found to be in acceptable limit. Chen et al. [26] modified the acrylonitrile butadiene styrene (ABS) by P-TES and N-TES molecules and enhanced the adhesion strength up to 25 N/cm. Kang et al. [38] modified the flexible PET sheet by P-TES and N-TES molecules, and increase the adhesion strength up to 12 N/cm. Figure 4 shows the steps involved in the process.

The summary of four different methods for enhancing adhesion is presented in Table 3.

4 Conclusions

Plastics may be good option as compared to metals for certain applications. Specific application are decorative items like knobs for automobile sector, electromagnetic interference (EMI) shielding textiles and flexible circuits in electronic industries, urinary catheters in medical field etc. However, certain applications need metallic characteristics, which necessitates deposition of metallic coating on plastic substrates. Electroless coating is a suitable method for plating on the plastic surface. But the problem associated with electroless coating on plastic is poor adhesion. This article reviewed different methods of increasing adhesion strength between the electroless coating and plastic substrate. In this article four methods are discussed (i) UV/ozonolysis irradiation for improving adhesion of copper polyalloy coating, (ii) Laser-induced selective activation (LISA) method, (iii) Novel plating with assisted super-critical CO$_2$ (iv) Molecular bonding and electroless spray. Every method is characterised by unique pretreatment processes, which are mainly responsible for enhancing the adhesion.

The ultraviolet lights are extremely useful in cleaning the surfaces of plastic substrate and free it from any carbonaceous residue, which in turn results in excellent adhesion between plastic and metal. The adhesion strength could be achieved to the order of 39 N/cm, which is an acceptable limit.

The laser can be the most efficient tool for selective activation of the plastic substrate surface. It is generally used to clean, roughen, and activate to the plastic

Table 3 Summary of methods discussed in this article for improving adhesion of electroless coating on plastic substrate [27, 34, 35, 37]

Process	Adhesion improvement methods			
	Electroless copper polyalloy plating assisted with UV/ozonolysis irradiation	Laser-induced selective activation	Novel plating with assisted super-critical (sc) CO_2	Molecular bonding and electroless spray-plating
Pretreat-ment	Washing (ultrasonic), UV/ozonolysis surface modification, Activation (cupric citrate (0.059 M) solution), Re-activation (0.1 M Sodium tetrahydridoborate aqueous solution)	Roughing the surface (laser treatment), activation (mixture of $SnCl_2$ and $PdCl_2$ solution)	Ultrasonic cleaning (acetone), Supercritical CO_2 pretreatment	Degreasing (NaOH + Na_2CO_3), UV-molecular grafting and self-assembly of P-TES and N-TES respectively, Sensitizing ($SnCl_2$ + HCl)
Electroless coating	Copper polyalloy plating bath, (0.08–0.12 M cobalt sulphate hep-tahydrate, pH 9.0–11.0, plating temperature 30–40 °C, plating time 25–45 min, copper (II) sulphate pentahydrate-0.1 M, sodium hydroxide-0.56 M, potassium sodium tartrate-0.8 M)	Copper bath (40 g/L ethylenediaminetetraacetic acid (EDTA) + 4.2 g/L $CuCl_2$ + 3.0 g/L concentrated formaldehyde + 10 mg/L NaCN (pH-12.2 by NaOH) at 60 °C for a few minutes.) and (10.5 g $NiSO_4$ + 10.6 $Na_2H_2PO_2$ + 17.1 mL conc. Acetic acid diluted in 400 mL water, pH-4.5 by NH_4OH at 90 °C)	Electroless plating reaction (Three different solution added to bath as follows: (a) 0% ethanol, non-CO_2, (b) 40% ethanol, non-CO_2 and (c) 40% ethanol, 10 MPa-CO_2	Spraying (solution A (20 g $AgNO_3$, 15 mL $NH_3 \cdot H_2O$ and 1 L distilled water) and solution B (60 mL $(CHO)_2$, 15 mL N $(CH_2CH_2OH)_3$ and 1 L distilled water))
Adhesion strength	39 N/cm (Peel test)	2.79 MPa (Tensile adhesion test)	19.5 N/cm (Peel test)	25 N/cm (Peel test)

surface. The adhesion strength has been reported of the order of 2.79 MPa on an average. The solution of catalyst precursor and super-critical CO_2 creates pores on polymer substrate which is mainly responsible for achieving anchoring effect on polymer and metal surface. The adhesion strength can be achieved up to 19.5 N/cm. The UV-grafting and self-assembly of P-TES and N-TES respectively, generate good bonding strength between plastic and metal surface. The adhesion strength can be of the order of 25 N/cm.

References

1. Hepfer IC, Drive WS (1968) Electroless plating on non-conductive materials. United States Patent No. 3370974, Feb 27
2. Jiang SX, Guo RH (2011) Electromagnetic shielding and corrosion resistance of electroless Ni-P/Cu-Ni multilayer plated polyester fabric. Surf Coatings Technol 205:4274–4279. https://doi.org/10.1016/j.surfcoat.2011.03.033
3. Park SJ, Ko TJ, Yoon J, Moon MW, Oh KH, Han JH (2017) Copper circuit patterning on polymer using selective surface modification and electroless plating. Appl Surf Sci 396:1678–1684. https://doi.org/10.1016/j.apsusc.2016.12.007
4. Guo R, Yin G, Sha X, Wei L, Zhao Q (2015) Effect of surface modification on the adhesion enhancement of electrolessly deposited Ag-PTFE antibacterial composite coatings to polymer substrates. Mater Lett 143:256–260. https://doi.org/10.1016/j.matlet.2014.12.125
5. Mallory G (1990) Electroless plating—fundamentals and applications. William Andrew Publishing, Noyes, pp1–56https://doi.org/10.1007/s004420050568
6. Woo BH, Sone M, Shibata A, Ishiyama C, Edo S, Tokita M, Watanabe J, Higo Y (2010) Impregnation of Ni-P metal into polymer substrate via catalyzation in Sc-CO_2 and electroless plating in Sc-CO_2 emulsion. Surf Coatings Technol 204:1785–1792. https://doi.org/10.1016/j.surfcoat.2009.11.010
7. De Bruyn K, Van Stappen M, De Deurwaerder HH, Rouxhet L, Celis JP (2003) Study of pretreatment methods for vacuum metallization of plastics. Surf Coatings Technol 163–164:710–715. https://doi.org/10.1016/S0257-8972(02)00684-9
8. Jia Z, Liu Y, Wang Y, Gong Y, Jin P, Suo X, Li H (2017) Flame spray fabrication of polyethylene-Cu composite coatings with enwrapped structures: a new route for constructing antifouling layers. Surf Coatings Technol 309:872–879. https://doi.org/10.1016/j.surfcoat.2016.10.071
9. Wei QF, Xu WZ, Ye H, Huang FL (2006) Surface funtionalization of polymer fibers by sputter coating. J Ind Text 35:287–294.https://doi.org/10.1177/1528083706060783
10. Wang W, Ji S, Lee I (2013) A facile method of nickel electroless deposition on various neutral hydrophobic polymer surfaces. Appl Surf Sci 283:309–320. https://doi.org/10.1016/j.apsusc.2013.06.108
11. Luan B, Liu XY, Nagata J, Cheong WJ (2005) Residual stress analysis—an important consideration for coating of stereolithography polymers. Surf Coatings Technol 192:323–330. https://doi.org/10.1016/j.surfcoat.2004.07.083
12. Lu Y (2010) Improvement of copper plating adhesion on silane modified PET film by ultrasonic-assisted electroless deposition. Appl Surf Sci 256:3554–3558. https://doi.org/10.1016/j.apsusc.2009.12.153
13. Krulik GA (1978) Electroless plating of plastics. J Chem Educ 55:361–365. https://doi.org/10.1021/ed055p361
14. Ranucci E, Sandgren S, Andronova N, Albertsson AC (2001) Improved polyimide/metal adhesion by chemical modification approaches. J Appl Polym Sci 82:1971–1985. https://doi.org/10.1002/app.2043

15. Fang F, Huang GW, Xiao HM, Li YQ, Hu N, Fu SY (2018) Largely enhanced electrical conductivity of layer-structured silver nanowire/polyimide composite films by polyaniline. Compos Sci Technol 156:144–150. https://doi.org/10.1016/j.compscitech.2018.01.001
16. Kim SH, Na SW, Lee NE, Nam YW, Kim YH (2005) Effect of surface roughness on the adhesion properties of Cu/Cr films on polyimide substrate treated by inductively coupled oxygen plasma. Surf Coatings Technol 200:2072–2079. https://doi.org/10.1016/j.surfcoat.2005.05.021
17. Huang J, Tian C, Wang J, Liu J, Li Y, Liu Y, Chen Z (2018) Fabrication of selective electroless copper plating on PET sheet: effect of PET surface structure on resolution and adhesion of copper coating. Appl Surf Sci 458:734–742. https://doi.org/10.1016/j.apsusc.2018.07.119
18. Yu Q, Zhou T, Jiang Y, Yan X, An Z, Wang X, Zhang D, Ono T (2018) Preparation of graphene-enhanced nickel-phosphorus composite films by ultrasonic-assisted electroless plating. Appl Surf Sci 435:617–625. https://doi.org/10.1016/j.apsusc.2017.11.169
19. Equbal A, Dixit NK, Sood AK (2013) Electroless plating on plastic. Int J Sci Eng Res 4https://doi.org/10.2307/1310387
20. Rantell A (1969) The influence of surface chemistry on the adhesion of copper deposited on plastic substrates. Trans IMF 47:197–202. https://doi.org/10.1080/00202967.1969.11870113
21. Han X, Wang G, He Y, Wang Y, Qiao Y, Zhang L (2018) Surface modification of ABS with Cr^{6+} free etching process in the electroless plating. J Adhes Sci Technol 32:2481–2493. https://doi.org/10.1080/01694243.2018.1488460
22. Zhang H, Kang Z, Sang J, Hirahara H (2018) Surface metallization of ABS plastics for nickel plating by molecules grafted method. Surf Coatings Technol 340:8–16. https://doi.org/10.1016/j.surfcoat.2018.02.005
23. Dev A, Tandon S, Jha P, Singh P, Dutt A (2020) Investigation of process parameters in electroless copper plating on polystyrene. Sadhana—Acad Proc Eng Sci 45.https://doi.org/10.1007/s12046-020-01377-3
24. Hoffman AS (1996) Surface modification of polymers: physical, chemical, mechanical and biological methods. In: Macromolecular symposia, pp 443–454
25. Wang Y, Bian C, Jing X (2013) Adhesion improvement of electroless copper plating on phenolic resin matrix composite through a tin-free sensitization process. Appl Surf Sci 271:303–310. https://doi.org/10.1016/j.apsusc.2013.01.188
26. Chen D, Zhang Y, Bessho T, Sang J, Hirahara H, Mori K, Kang Z (2016) Layer by layer electroless deposition: an efficient route for preparing adhesion-enhanced metallic coatings on plastic surfaces. Chem Eng J 303:100–108. https://doi.org/10.1016/j.cej.2016.05.114
27. Hou L, Bi S, Zhao H, Xu Y, Mu Y, Lu Y (2017) Electroless plating Cu-Co-P polyalloy on UV/ozonolysis irradiated polyethylene terephthalate film and its corrosion resistance. Appl Surf Sci 403:248–259. https://doi.org/10.1016/j.apsusc.2017.01.182
28. Sahoo SK, Sahu AK, Mahapatra SS (2017) Environmental friendly electroless copper metallization on FDM build ABS parts. Int J Plast Technol 21:297–312. https://doi.org/10.1007/s12588-017-9185-4
29. Schaubroeck D, Mader L, Dubruel P, Vanfleteren J (2015) Surface modification of an epoxy resin with polyamines and polydopamine: adhesion toward electroless deposited copper. Appl Surf Sci 353:238–244. https://doi.org/10.1016/j.apsusc.2015.06.114
30. Rytlewski P, Jagodziński B, Malinowski R, Budner B, Moraczewski K, Wojciechowska A, Augustyn P (2020) Laser-induced surface activation and electroless metallization of polyurethane coating containing copper(II) L-tyrosine. Appl Surf Sci, 505.https://doi.org/10.1016/j.apsusc.2019.144429
31. Vasconcelos B, Vediappan K, Oliveira JC, Fonseca C (2018) Mechanically robust silver coatings prepared by electroless plating on thermoplastic polyurethane. Appl Surf Sci 443:39–47. https://doi.org/10.1016/j.apsusc.2018.02.229
32. Charbonnier M, Romand M (2003) Polymer pretreatments for enhanced adhesion of metals deposited by the electroless process. Int J Adhes Adhes 23:277–285. https://doi.org/10.1016/S0143-7496(03)00045-9
33. Yan H, Chen Z, Zheng Y, Newman C, Quinn JR, Dotz F, Kastler M, Facchetti A (2009) A high-mobility electron-transporting polymer for printed transistors. Nature 457:679–686. https://doi.org/10.1038/nature07727

34. Zhang Y, Tang PT, Hansen HN, Nielsen JS (2009) Electroless plating on plastic induced by selective laser activation. Natl Assoc Surf Finish Annu Tech Conf 2009, SUR/FIN 2009, pp 188–198

35. Adachi H, Taki K, Nagamine S, Yusa A, Ohshima M (2009) Supercritical carbon dioxide assisted electroless plating on thermoplastic polymers. J Supercrit Fluids 49:265–270. https://doi.org/10.1016/j.supflu.2008.12.010

36. Tengsuwan S, Ohshima M (2014) Supercritical carbon dioxide-assisted electroless nickel plating on polypropylene—the effect of copolymer blend morphology on metal-polymer adhesion. J Supercrit Fluids 85:123–134. https://doi.org/10.1016/j.supflu.2013.11.012

37. Yang S, Kang Z, Guo T (2020) Preparation and conductive property of cu coatings and cu-graphene composite coatings on ABS substrate. Nanotechnology 31:195710.https://doi.org/10.1088/1361-6528/ab703e

38. Kang Z, Zhang Y, Zhou M (2019) AgNPs@CNTs/Ag hybrid films on thiolated PET substrate for flexible electronics. Chem Eng J 368:223–234. https://doi.org/10.1016/j.cej.2019.01.005

Computational Analysis of the Effect of Boron and Nitrogen Dopants on the Mechanical Properties of Graphene with Single Vacancy Defects

Dhrumil M. Purohit and **Ashish B. Deoghare**

1 Introduction

In the last decade, a single-atom layer sheet of carbon, monolayer Graphene (Gr), acquired significant recognition owing to its planar (2-D) crystal structure and extraordinary thermal, electrical and mechanical properties [1–5]. The Gr sheet has a wide range of applications in nano-composites [6], transistors [7], nanosensors [8] and nanoelectronics [9] due to its unique features.

However, according to the second law of thermodynamics, certain disorders and defects exist in crystalline materials [10]. Different types of defects in Gr also arise during the fabrication process, which is unavoidable. These defects can alter the topology, curvature and the structure of Gr [11]. These inevitable defects modify the mechanical properties besides the electrical and thermal conductivities [12] of Gr and Gr-based nano-composites [13]. Defects in Gr can be classified into two groups prominently as intrinsic and extrinsic defects. Intrinsic defects include non-sp^2 orbital hybrid carbon atoms in Gr. The extrinsic defects are induced by the presence of non-hexagonal rings surrounded by hexagonal rings or the crystalline order is disturbed with non-carbon atoms in Gr [14]. Common types of defects include grain boundaries [15], Stone–Wales (SW) [16], single vacancy (SV) [17, 18], double vacancy (DV) [17, 18], carbon adatoms [19], etc. The SW defects are caused by the rotation of a single pair of carbon atoms by 90°, arising to neighboring pairs of heptagonal and pentagonal rings in Gr. Hence, these defects do not cause any removal or addition of carbon atoms [20]. SV defect occurs when a carbon atom is missing in the carbon hexagon ring of Gr [21]. Similar to a SV defect, if another carbon atom is missing, it is known as a DV defect [22]. Missing carbon atoms resulting from SV and DV defects may not get completely lost from the Gr plane. Rather, after dissociating from the original carbon hexagon ring, these carbon atoms relocate on the surface of the Gr. Novel defects may be caused when these atoms interact with a pure Gr layer.

D. M. Purohit (✉) · A. B. Deoghare
National Institute of Technology Silchar, Silchar, Assam, India

Such defects known as carbon adatoms, will disrupt the original planar structure of Gr and form a three-dimensional structure [15].

However, all these defects can be useful in some applications, as they help to tailor the local properties of Gr and achieve new functionalities [23–26]. Dopant atoms such as Boron (B) and Nitrogen (N) are proved to be efficient in improving the semiconducting properties of Gr and thus its performance in nanoelectronics and nanodevices [27, 28]. Method control is used for deliberately adding the B and N atoms in Gr [29]. In addition, B-doped and N-doped Gr have excellent conductivity and catalytic activity [30]. The electron cloud around Gr in the local area changes due to the addition of B and N atoms. Also, this phenomena causes the local regions to be more active [31]. Besides that, the doping of heteroatoms in the Gr also enhances its performance in aspect of adsorption properties [32]. However, these dopant atoms distort the original sp^2 hybridization in carbon atoms and modifies the local mechanical, chemical, and electronic properties of Gr [28, 33].

Hence, a good comprehension of the defects and dopants induced in Gr would be beneficial for enhancement in Gr based nano applications. Till now various attempts were made to investigate the overall effects of various dopants and vacancy defects on the mechanical properties of Gr [34–36]. Also, the effects of Boron and Nitrogen doping on mechanical properties of the Gr, Gr nano ribbons and carbon nanotube, considering the various doping configurations with SW defects have been thoroughly investigated [37–41]. However, the effects of SV defect and dopants like B and N atoms, at various defect and doping concentrations, on the mechanical properties of Gr have not be explored yet to the best of the authors' knowledge. In the present study, the effects of SV defects and dopants as B and N atoms, on the fracture strength, fracture strain and Young's modulus of Gr were determined and comparative analysis of their results was performed. Computational study of graphene using Molecular Dynamics (MD) is preferred over experimental study due to cost effectiveness, modelling flexibility, faster analysis and large number of tests.

2 Molecular Dynamics Simulation

2.1 Methodology

The MD simulation starts with modelling the system topology by arranging the initial position of constituent atoms. As the MD simulator, an open source code LAMMPS [42] (Large-scale Atomic\Molecular Massively Parallel Simulator) developed by Sandia National Laboratories, USA was used. The topology data file of pristine monolayer Gr was generated using the open source software VMD (Visual Molecular Dynamics) [43]. That topology data file was then imported to Avogadro [44], an open source cross-platform molecular editor, for manipulating the atoms of Gr. The modified topology data file from Avogadro, was then imported to the input script of LAMMPS for simulating the tensile test on the modified Gr model. OVITO [45]
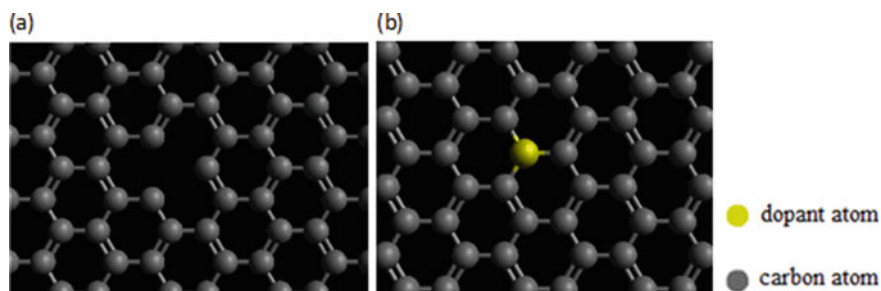
Fig. 1 **a** SV defect, **b** Substitutional doping

(Open-Visualization Tool) supported files were generated by LAMMPS to visualize the fracture process of the Gr model. Also, the simulation results from LAMMPS were imported in MATLAB to extract the desired mechanical properties of all the considered Gr models.

2.2 Molecular Model of Graphene

Molecular models were constructed to analyse the mechanical properties of Gr. The SV defect concentration varied from 0 to 2%, and boron and nitrogen doping concentration varied from 0 to 5% in Gr models. The defect and doping concentrations were defined as the percent of atoms eliminated or substituted from pure Gr, respectively. These defects and dopants were randomly allocated on Gr sheets. In present study, SV defect was established by randomly eliminating one carbon atom from the Gr as shown in Fig. 1a. Doping was done by substituting one carbon with a dopant atom in the Gr as shown in Fig. 1b.

The molecular model of Gr was composed of 2232 carbon atoms having the dimension of 75 Å × 75 Å. The Models of the pristine Gr sheet and doped Gr sheet with SV defect as shown in Fig. 2 were considered for the present study.

All the sample models, showing the distribution of the defects and dopant atoms across the Gr sheet with varying doping concentrations at each defect concentration from 0 to 2%, are attached in Appendix 2.

2.3 Interatomic Potentials

The accuracy of the MD modelling is influenced critically by the interatomic potentials selected for the atomic structures under investigation. For the current work, Tersoff potential was selected for representing the interatomic interactions of Gr. This kind of potential was specifically developed and proved to be reliable for carbon
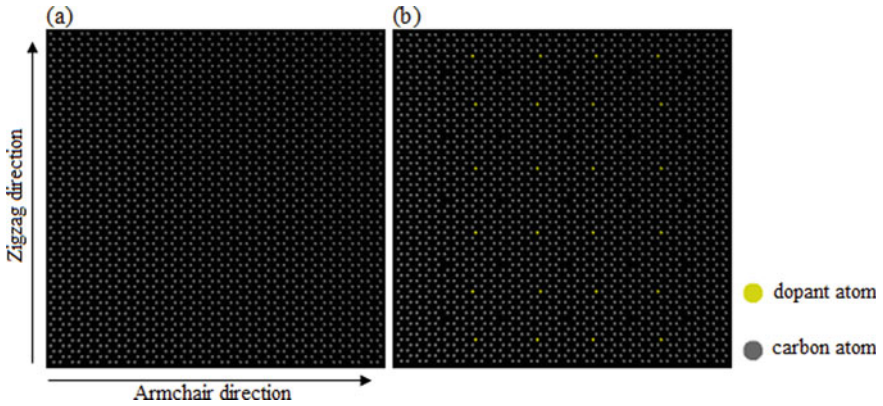
Fig. 2 Molecular models of 75 Å × 75 Å. **a** Pristine Gr sheet, **b** 1% B or N doped Gr sheet with 1% SV defect

allotropes, like diamond, graphite, nanotubes, and fullerene [46–48]. The function is expressed as follows:

$$E = \sum_i E_i = \frac{1}{2} \sum_{i \neq j} V_{ij} \tag{1}$$

$$V_{ij} = f_C (r_{ij}) \left[f_R (r_{ij}) + b_{ij} f_A (r_{ij}) \right] \tag{2}$$

where, E is the potential energy, E_i is the site energy, V_{ij} is the bonding energy, r_{ij} is the distance between i and j atoms, f_R and f_A are the repulsive and attractive pair potential respectively, and f_C is a smooth cutoff function [49].

$$f_R(r) = A e^{(-\lambda_1 r)} \tag{3}$$

$$f_A(r) = -B e^{(-\lambda_2 r)} \tag{4}$$

$$f_C(r) = \begin{cases} 1, & r < R - D \\ \frac{1}{2} = \frac{1}{2} \sin\left(\frac{\pi}{2} \frac{(r-R)}{D}\right), & R - D < r < R + D \\ 0, & r > R + D \end{cases} \tag{5}$$

The parameters R (cut off radius) and D (cut off switching parameter) have been selected for including only in the first-neighbor shell for defined structure "for carbon, $R = 1.8$ Å". "The f_C function decreases from 1 to 0 in the range: $R - D < r < R + D$".

The distinctive characteristics of Tersoff potential are the reactive short-range bonded interactions for carbon-based systems. Hence during the course of simulations, chemical bonds can break and form. Until now, an integrated interatomic potential has not been developed for the doped Gr models, however various interatomic potentials were utilized for Gr doped with various foreign atoms [50–55]. Thus, referring the previous works, certain interatomic potentials were selected for Gr doped with discrete foreign atoms. An optimized Tersoff potential was selected for representing the C–C bonds in Gr, and an optimized BNC Tersoff potential was selected for representing the C–C, C–B and C–N bonds, in B-doped Gr and N-doped Gr. The modified Tersoff potential was obtained by changing the values of cut off radius R from 1.95 to 2.00 and cut off switching parameter D from 0.15 to 0, in the original Tersoff potential, to avoid the unnecessary interatomic interactions between the atoms after the point of fracture [56].

2.4 Computation of Mechanical Properties

Uniaxial tensile tests of pristine Gr sheet and doped Gr sheets having SV defects were performed by the MD simulations in LAMMPS. Prior to performing the analysis, the sample sheets were equilibrated by minimizing the energy using conjugate gradient (CG) algorithm [57]. After the equilibration, a constant strain rate of 1×10^{-3} ps^{-1} was exerted along the armchair direction of Gr sheets. Generally, the atomistic stresses in MD simulation are portrayed with Cauchy stress and virial stress. Although, Cauchy stress gives better computational efficiency than virial stress, but at higher temperatures it induces non-physical initial stress, i.e. at zero strain unlike virial stress [58]. Hence, virial stress was used in present study. The virial stress is expressed as:

$$\sigma_{ij} = \frac{1}{V} \sum_{\alpha} \left[\frac{1}{2} \sum_{\beta=1}^{N} \left(R_i^\beta - R_i^\alpha \right) F_j^{\alpha\beta} - m^\alpha v_i^\alpha v_j^\alpha \right] \tag{6}$$

where, i and j are the directional indices; α and β are numbers assigned to neighboring atoms; R_i^β is the atomic position of β along the direction i; $F_j^{\alpha\beta}$ is the force on atom α along direction j that is caused by the atom β; m^α is the mass of the atom α; v^α is the velocity of the atom α; V is the total volume of the system. Further, the elastic constants of Gr are calculated using the stress tensors with a constant strain rate. The in-plane stress and strain relation can be represented as follows:

$$\begin{pmatrix} \sigma_{11} \\ \sigma_{22} \\ \tau_{12} \end{pmatrix} = \begin{pmatrix} C_{11} & C_{12} & 0 \\ C_{21} & C_{22} & 0 \\ 0 & 0 & C_{66} \end{pmatrix} \begin{pmatrix} \varepsilon_{11} \\ \varepsilon_{22} \\ \gamma_{12} \end{pmatrix} \tag{7}$$

On account of constitutive matrix being symmetric, the elastic constants can be expressed as:

$$C_{11} = C_{22} \tag{8}$$

$$C_{12} = C_{21} \tag{9}$$

$$C_{66} = \frac{C_{11} - C_{12}}{2} \tag{10}$$

Thus the Young's modulus of Gr can be calculated as [59]:

$$E = \frac{C_{11}\ C_{22}\ -\ C_{12}\ C_{21}}{C_{22}} \tag{11}$$

In order to eradicate the defined length effects, periodic boundary conditions (PBCs) were applied along the zigzag and armchair direction of Gr. PBCs are often used to simulate a part of a large system, such that the atoms exit and enter the simulation box with similar frequencies and there is no flux of atoms out of the system.

3   Results and Discussion

3.1   Fracture Process

The LAMMPS simulations results were imported to OVITO software to visualize the fracture process of all the Gr models. It is observed that the fracture crack propagates vertically through the vacancies created due to SV defects. The B-doped and N-doped Gr models shows a straight sharp cut after fracture due to the modified Tersoff potential that avoids interatomic interactions after the fracture. Figures 3 and 4 represents fracture process of Gr sheet with 1% defect and 1% Boron and Nitrogen doping concentration respectively.

All the values of mechanical properties from the simulation results of Gr at each defect concentration with varying doping concentrations fron 0 to 5%, are attached in Appendix 1.

3.2   Fracture Strength

The LAMMPS simulation results were imported to MATLAB for extracting the values of mechanical properties of all the developed Gr models with defined defect
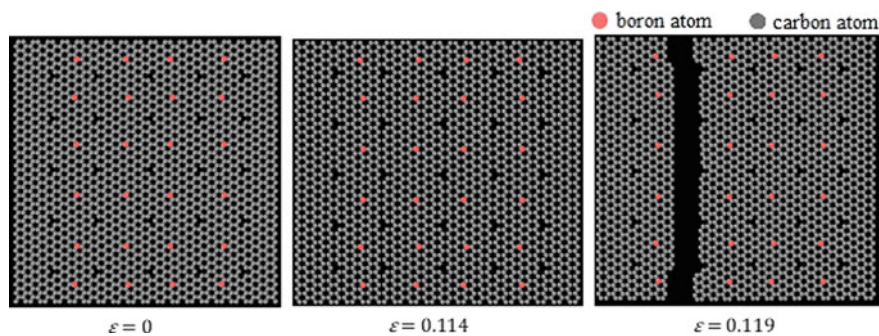
Fig. 3 Fracture process of Gr sheet with 1% defect and 1% Boron doping concentration under uniaxial tensile loading in armchair direction
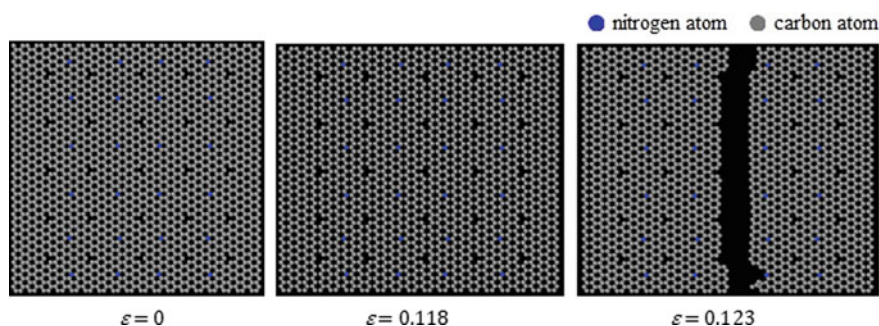

Fig. 4 Fracture process of Gr sheet with 1% defect and 1% Nitrogen doping concentration under uniaxial tensile loading in armchair direction

and doping concentrations. The values of fracture strength obtained at 0–5% doping concentrations of B doped and N doped Gr sheets, at each defect concentrations from 0 to 2% are represented using column chart in Fig. 5a, b respectively.

The fracture strength of Gr decreases with increase in defect concentration, except at 1 and 2% a little rise was observed due to the defect density. This abrupt change is observed in the trend due to varying defect and dopant density, as per their distribution across the Gr sheet (Appendix 2).The fracture strength value of pure Gr decreases by minimum 30% to maximum 40% of its pure value due to B doping, while it decreases by minimum 26% to maximum 37% of its pure value due to N doping. Here, the term "pure value" means, the value of respective mechanical property at 0% doping concentration.

For the considered defect and dopant distribution across the Gr sheet (Appendix 2), the doping concentrations of each dopant element that shows maximum and minimum values of the mechanical properties of graphene at each defect concentrations were identified from Appendix 1, excluding the values obtained at 0% doping concentration. The maximum fracture strength achieved by B-doped Gr sheet was

Fig. 5 Fracture strength (in GPa) values at respective defect and doping concentrations for **a** B-doped Gr sheets and **b** N-doped Gr sheets

52.031 GPa at 1% defect with 2% doping concentration, whereas the minimum was 45.122 GPa at 1% defect with 5% doping concentration. The maximum fracture strength achieved by N-doped Gr sheet was 57.048 GPa at 0.5% defect with 3% doping concentration, whereas the minimum was 44.297 GPa at 2% defect with 1% doping concentration.

3.3 Fracture Strain

The values of fracture strain at 0–5% doping concentrations of B doped and N doped Gr sheets, at each defect concentration from 0 to 2%, are represented using column chart in Fig. 6a, b respectively.

The fracture strain of Gr shows uneven rise and fall with defect concentration. This abrupt change is observed in the trend due to varying defect and dopant density,
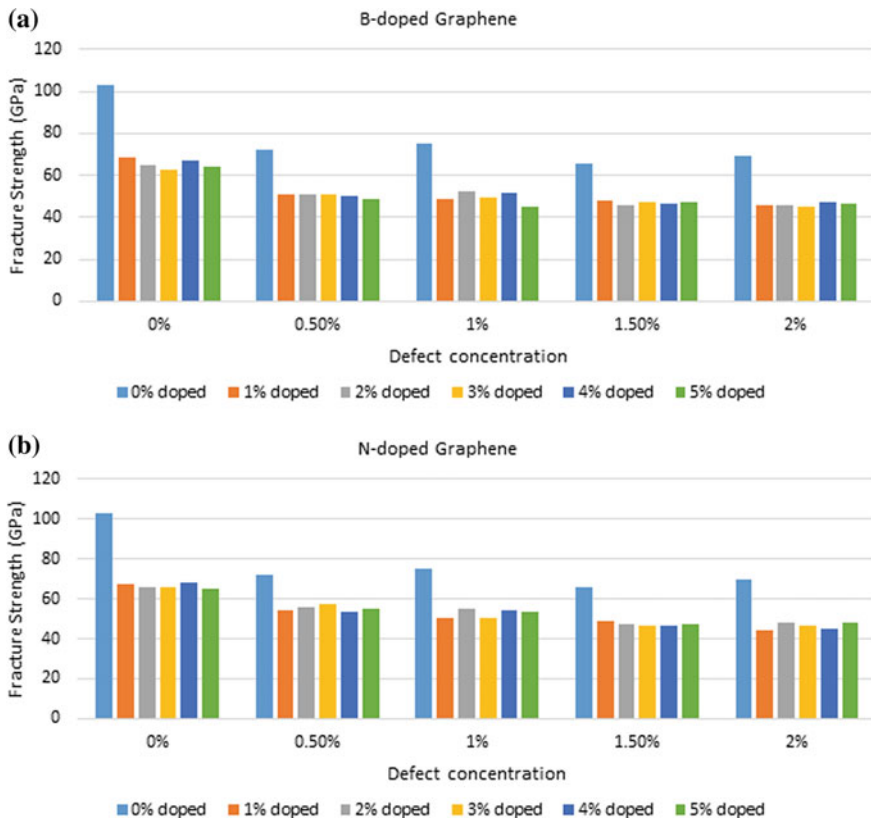
Fig. 6 Fracture strain values at respective defect and doping concentrations for **a** B-doped Gr sheets and **b** N-doped Gr sheets

as per their distribution across the Gr sheet (Appendix 2). The fracture strain value of pure Gr decreases by minimum 11% to maximum 43% of its pure value due to N doping, while it varies from increase up to 5% of its pure value to decrease up to 36% of its pure value, due to B doping. Here, the term "pure value" means, the value of respective mechanical property at 0% doping concentration.

For the considered defect and dopant distribution across the Gr sheet (Appendix 2), the doping concentrations of each dopant element that shows maximum and minimum values of the mechanical properties of graphene at each defect concentra-

(a) B-doped Graphene

(b) N-doped Graphene

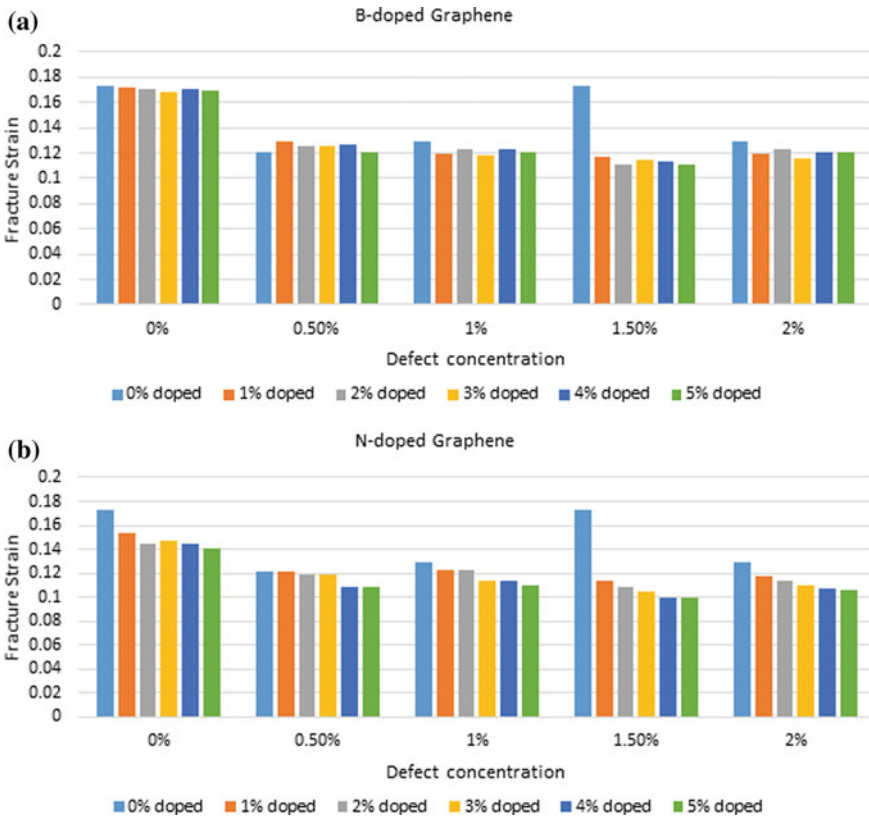**Fig. 7** Young's modulus (in GPa) values at respective defect and doping concentrations for **a** B-doped Gr sheets and **b** N-doped Gr sheets

tions were identified from Appendix 1, excluding the values obtained at 0% defect concentrations and 0% doping concentrations. The maximum fracture strain achieved by B-doped Gr sheet was 0.129 at 0.5% defect with 1% doping concentration, whereas the minimum was 0.111 at 1.5% defect with 2% and 5% doping concentration. The maximum fracture strain achieved by N-doped Gr sheet was 0.123 at 1% defect with 1 and 2% doping concentration, whereas the minimum was 0.099 at 1.5% defect with 5% doping concentration.

3.4 Young's Modulus

Young's modulus results obtained at 0–5% doping concentrations of B doped and N doped Gr sheets, at each defect concentration from 0 to 2%, are represented using column chart in Fig. 7a, b respectively.

Table 1 Comparison of present study results with previous research results of pristine Gr sheet

References	Method	Young's modulus (GPa)	Fracture strength (GPa)	Fracture strain
Lee [4]	Experimental	1020	130 ± 10	0.25
Liu [60]	DFT	1050	110	0.19
Pei [61]	MD (AIREBO)	890	105	0.17
Ansari [62]	MD (Tersoff-Brenner)	790	123	0.23
Present study	MD (Modified Tersoff)	640	103	0.17

The Young's modulus of Gr decreases with increase in defect concentration. The Young's modulus value of pure Gr decreases by minimum 32% of its pure value to maximum 47% of its pure value, due to B doping,while it decreases by minimum 25% of its pure value to maximum 47% of its pure value, due to N doping. Here, the term "pure value" means, the value of respective mechanical property at 0% doping concentration.

For the considered defect and dopant distribution across the Gr sheet (Appendix 2), the doping concentrations of each dopant element that shows maximum and minimum values of th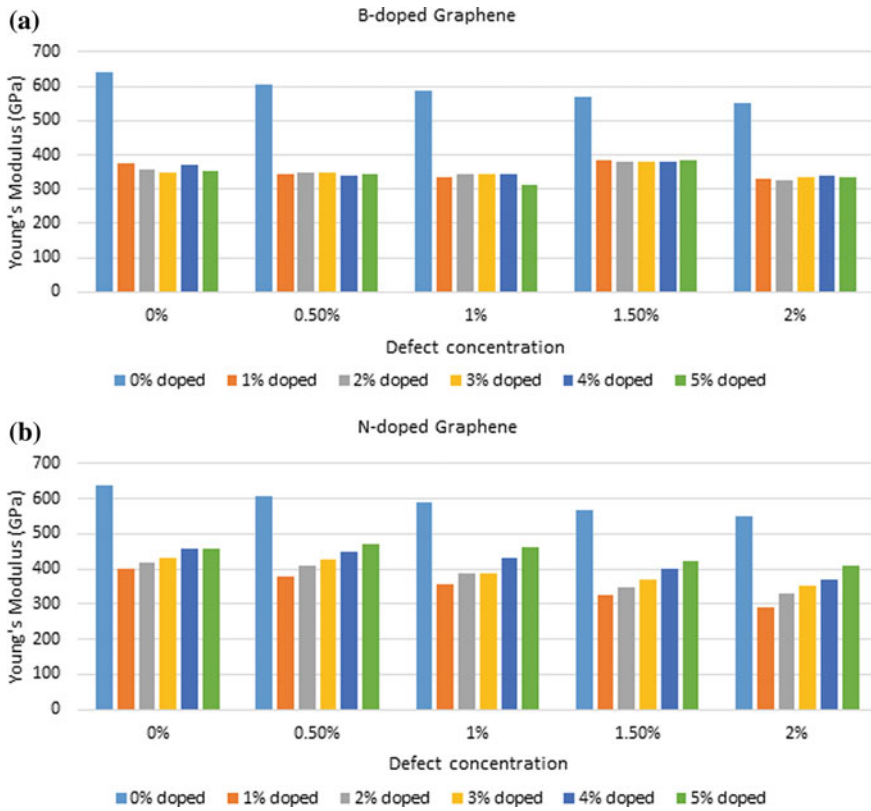e mechanical properties of graphene at each defect concentrations were identified from Appendix 1, excluding the values obtained at 0% defect concentrations and 0% doping concentrations. The maximum Young's modulus achieved by B-doped Gr sheet was 383.525 GPa at 1.5% defect with 5% doping concentration, whereas the minimum was 312.392 GPa at 1% defect with 5% doping concentration. The maximum fracture strain achieved by N-doped Gr sheet was 472.763 GPa at 0.5% defect with 5% doping concentration, whereas the minimum was 290.06 GPa at 2% defect with 1% doping concentration.

3.5 Validation of Results

Tensile test simulation results of pristine Gr sheet from LAMMPS were validated with the previous research results of the same. The present study results matched closely with the previous research results as observed from Table 1.

4 Conclusions

In the present work, the effects of SV defects with B and N doping were analysed for the mechanical properties of Gr sheets. Results indicated that Fracture strength and Young's modulus of Gr decreases drastically with the increase in defect concentration, whereas the fracture strain falls and rises unevenly with defect concentration. For

the considered defect and dopant distribution across the Gr sheet (Appendix 2), the doping concentrations of each dopant element that shows maximum and minimum values of the mechanical properties of graphene at each defect concentrations were identified from Appendix 1, excluding the values obtained at 0% defect concentrations and 0% doping concentrations. Appendix 1 would help to get clear idea and proper understanding of the results of the present study.

The maximum fracture strength achieved by B-doped Gr sheet was 52.031 GPa at 1% defect with 2% doping concentration, whereas the minimum was 45.122 GPa at 1% defect with 5% doping concentration. The maximum fracture strength achieved by N-doped Gr sheet was 57.048 GPa at 0.5% defect with 3% doping concentration, whereas the minimum was 44.297 GPa at 2% defect with 1% doping concentration.

The maximum fracture strain achieved by B-doped Gr sheet was 0.129 at 0.5% defect with 1% doping concentration, whereas the minimum was 0.111 at 1.5% defect with 2% and 5% doping concentration. The maximum fracture strain achieved by N-doped Gr sheet was 0.123 at 1% defect with 1 and 2% doping concentration, whereas the minimum was 0.099 at 1.5% defect with 5% doping concentration.

The maximum Young's modulus achieved by B-doped Gr sheet was 383.525 GPa at 1.5% defect with 5% doping concentration, whereas the minimum was 312.392 GPa at 1% defect with 5% doping concentration. The maximum fracture strain achieved by N-doped Gr sheet was 472.763 GPa at 0.5% defect with 5% doping concentration, whereas the minimum was 290.06 GPa at 2% defect with 1% doping concentration.

Comparing the values of mechanical properties from Appendix 1, confirmed that N-doped Gr sheets with SV defects proved to be better in Fracture strength and Young's modulus aspects whereas, B-doped Gr sheets with SV defects proved to be better in Fracture strain aspect. The obtained MD simulation results would thus help to enhance the development of Gr-based Micro/Nano electro-mechanical systems (M/NEMS) by selection of the optimal doping concentration, affordable defect concentration and suitable dopant atom.

Appendix 1

See Table 2.

Table 2 Mechanical properties of B-doped and N-doped Gr sheets at respective defect and doping concentrations obtained from molecular dynamics simulation results

Defect concen-tration (%)	Doping concen-tration (%)	Fracture strength (GPa)		Fracture strain		Young's modulus (GPa)			
		Boron	Nitrogen	Boron	Nitrogen	Boron	Nitrogen		
0	0	103.15	103.15	0.173	0.173	640	640		
	1	68.448	67.413	0.172	0.154	373.873	400.109		
	2	65.139	65.621	0.171	0.145	355.575	419.023		
	3	62.81	65.621	0.168	0.147	349.311	431.01		
	4	67.21	68.038	0.171	0.144	369.189	456.414		
	5	63.829	64.882	0.17	0.141	351.235	459.787		
0.5	0	72.422	72.427	0.121	0.121	605.16	605.16		
	1	51.051	54.535	0.129	0.122	342.795	377.91		
	2	50.723	55.767	0.125	0.119	348.535	408.552		
	3	51.225	57.048	0.126	0.119	346.804	426.825		
	4	50.4	53.788	0.127	0.109	339.832	450.622		
	5	48.379	55.164	0.121	0.108	342.913	472.763		
1	0	74.803	74.803	0.129	0.129	588.741	588.741		
	1	48.434	50.782	0.119	0.123	334.387	356.272		
	2	52.031	55.344	0.123	0.123	342.901	389.125		
	3	49.285	50.235	0.118	0.114	343.244	388.582		
	4	51.757	54.174	0.123	0.114	342.286	429.829		
	5	45.122	53.843	0.121	0.11	312.392	460.246		
1.5	0	65.607	65.607	0.173	0.173	567.851	567.851		
	1	48.175	48.804	0.117	0.114	383.091	323.553		
	2	46.027	47.276	0.111	0.109	377.701	347.459		
	3	47.281	46.644	0.115	0.105	380.832	369.028		
	4	46.825	46.827	0.113	0.1	379.423	399.949		
	5	46.89	47.218	0.111	0.099	383.525	421.196		
2	0	69.595	69.595	0.129	0.129	549.243	549.243		
	1	45.773	44.297	0.12	0.117	328.726	290.06		
	2	45.432	48.163	0.123	0.114	325.775	330.119		
	3	45.122	46.609	0.116	0.11	336.007	350.689		
	4	47.04	45.362	0.121	0.107	339.493	369.234		
	5	46.529	47.979	0.121	0.106	334.116	409.279		

Appendix 2: Defect and Dopant Distributions Across the Graphene sheet

Attached are the exact samples of Graphene with SV defects and dopant atoms, modelled using Avogadro software, considered to study the effect of B and N dopant atoms at different doping concentrations (1–5%) at each defect concentration from 0 to 2%.

1. **Dopant distribution at 0% defect concentration in Graphene**
    See Fig. 8.
2. **Dopant distribution at 0.5% defect concentration in Graphene**
    See Fig. 9.
3. **Dopant distribution at 1% defect concentration in Graphene**
    See Fig. 10.
4. **Dopant distribution at 1.5% defect concentration in Graphene**
    See Fig. 11.
5. **Dopant distribution at 2% defect concentration in Graphene**
    See Fig. 12.

(a)   (b)   (c)

(d)   (e)
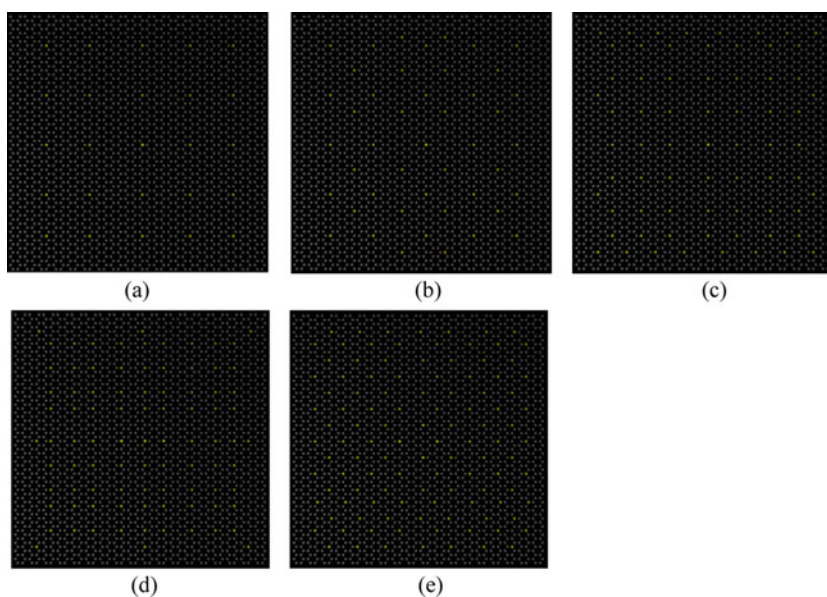
Fig. 8 Molecular models of 75 Å x 75 Å Gr sheet with 0% SV defects and doping concentration of **a** 1%, **b** 2%, **c** 3%, **d** 4%, **e** 5%. The yellow spheres represent the dopant atoms and the grey spheres represent the carbon atoms

Fig. 9 Molecular models of 75 Å x 75 Å Gr sheet with 0.5% SV defects and doping concentration of **a** 1%, **b** 2%, **c** 3%, **d** 4%, **e** 5%. The yellow spheres represent the dopant atoms and the grey spheres represent the carbon atoms
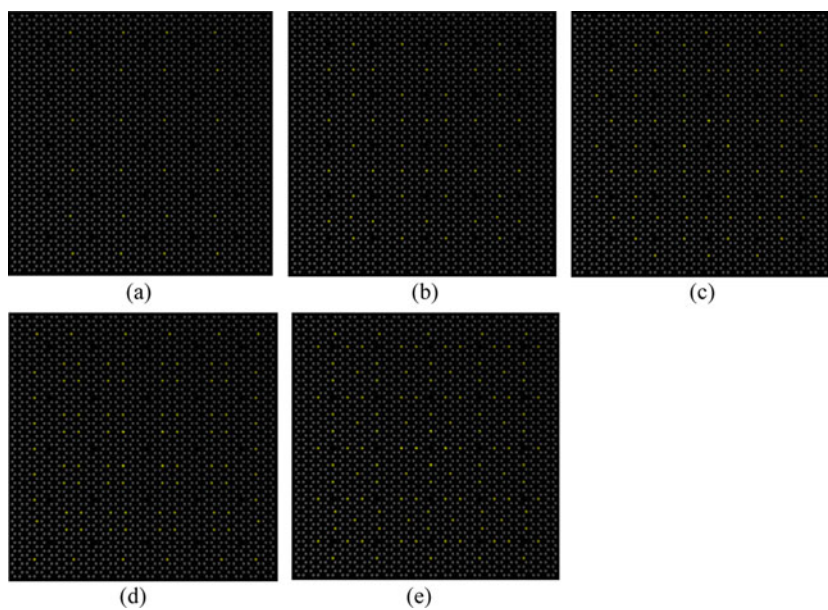
Fig. 10 Molecular models of 75 Å x 75 Å Gr sheet with 1% SV defects and doping concentration of **a** 1%, **b** 2%, **c** 3%, **d** 4%, **e** 5%. The yellow spheres represent the dopant atoms and the grey spheres represent the carbon atoms

Fig. 11 Molecular models of 75 Å x 75 Å Gr sheet with 1.5% SV defects and doping concentration of **a** 1%, **b** 2%, **c** 3%, **d** 4%, **e** 5%. The yellow spheres represent the dopant atoms and the grey spheres represent the carbon atoms
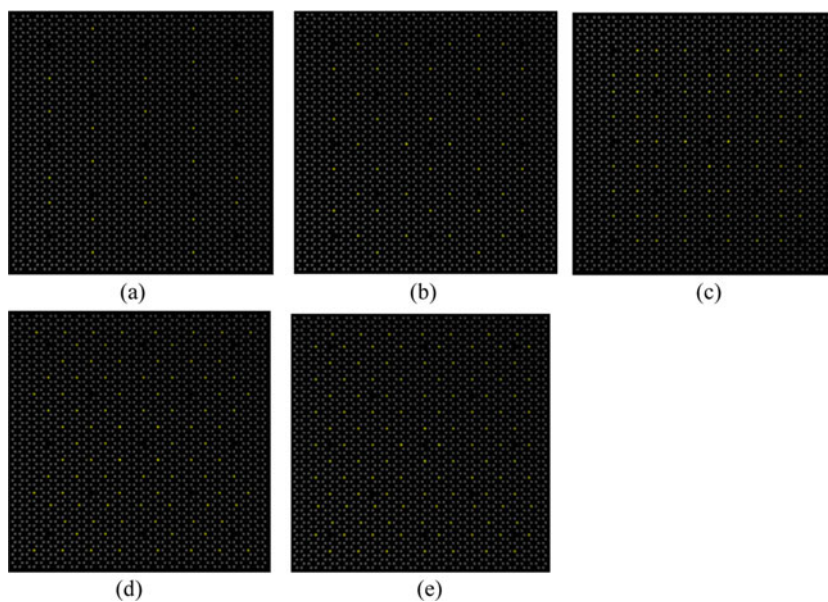

Fig. 12 Molecular models of 75 Å x 75 Å Gr sheet with 2% SV defects and doping concentration of **a** 1%, **b** 2%, **c** 3%, **d** 4%, **e** 5%. The yellow spheres represent the dopant atoms and the grey spheres represent the carbon atoms
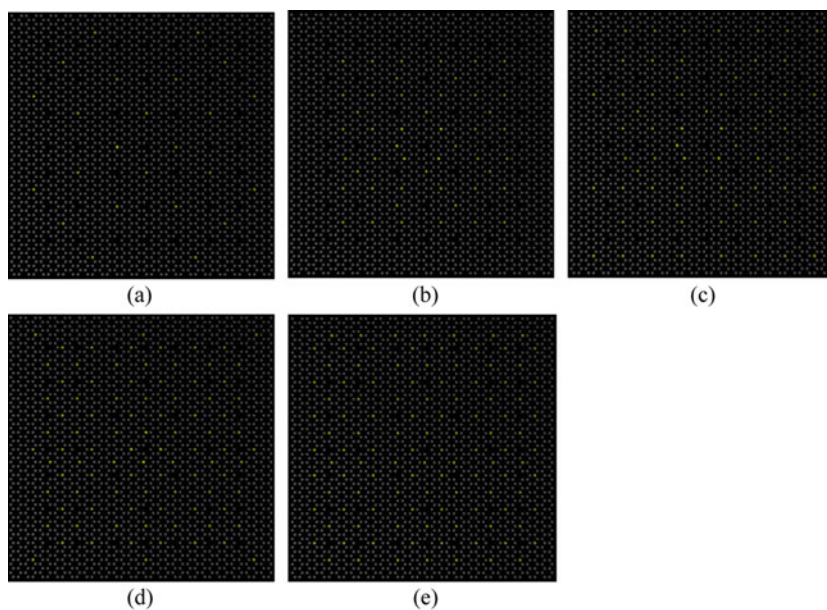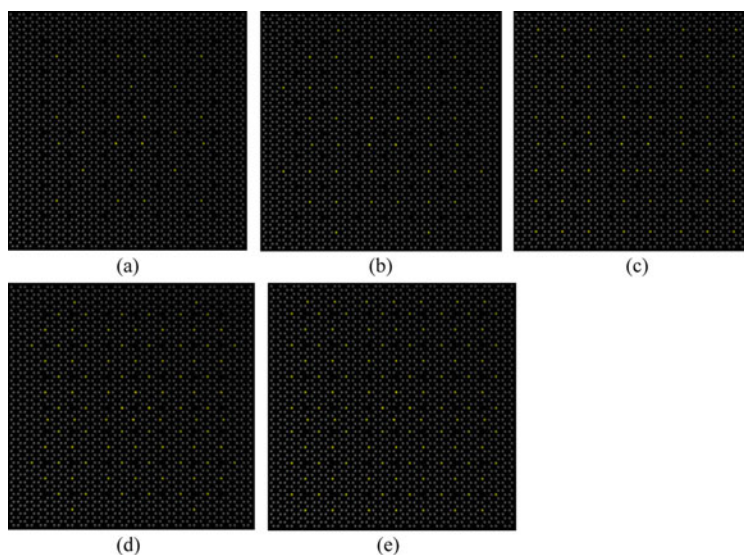
References

1. Novoselov KS, Geim AK, Morozov SV, Jiang D, Zhang Y, Dubonos SV, Grigorieva IV, Firsov AA (2004) Electric field in atomically thin carbon films. Science 306:666–669. https://doi.org/10.1126/science.1102896

2. Van Den Brink J (2007) Graphene: From strength to strength. Nat Nanotechnol 2:199–201. https://doi.org/10.1038/nnano.2007.91

3. Geim AK, Novoselov KS (2009) The rise of graphene. Nanosci Technol A Collect Rev from Nat J 11–19. https://doi.org/10.1142/9789814287005_0002

4. Lee C, Wei X, Kysar JW, Hone J (2008) Measurement of the elastic properties and intrinsic strength of monolayer graphene. Science 321:385–388. https://doi.org/10.1126/science.1157996

5. Balandin AA, Ghosh S, Bao W, Calizo I, Teweldebrhan D, Miao F, Lau CN (2008) Superior thermal conductivity of single-layer graphene. Nano Lett 8:902–907. https://doi.org/10.1021/nl0731872

6. Novoselov KS, Fal'Ko VI, Colombo L., Gellert PR, Schwab MG, Kim K (2012) A roadmap for graphene. Nature 490:192–200. https://doi.org/10.1038/nature11458

7. Schwierz F (2010) Graphene transistors. Nat Nanotechnol 5:487–496. https://doi.org/10.1038/nnano.2010.89

8. Brownson DAC, Banks CE (2012) Limitations of CVD graphene when utilised towards the sensing of heavy metals. RSC Adv 2:5385–5389. https://doi.org/10.1039/c2ra01279k

9. Areshkin DA, White CT (2007) Building blocks for integrated graphene circuits. Nano Lett 7:3253–3259. https://doi.org/10.1021/nl070708c

10. Hashimoto A, Suenaga K, Gloter A, Urita K, Iijima S (2004) Direct evidence for atomic defects in graphene layers. Nature 430:870–873. https://doi.org/10.1038/nature02817

11. Terrones M, Botello-Méndez AR, Campos-Delgado J, López-Urías F, Vega-Cantú YI, Rodríguez-Macías FJ, Elías AL, Muñoz-Sandoval E, Cano-Márquez AG, Charlier JC, Terrones H (2010) Graphene and graphite nanoribbons: morphology, properties, synthesis, defects and applications. Nano Today 5:351–372. https://doi.org/10.1016/j.nantod.2010.06.010

12. Araujo PT, Terrones M, Dresselhaus MS (2012) Defects and impurities in graphene-like materials. Mater Today 15:98–109. https://doi.org/10.1016/S1369-7021(12)70045-7

13. Berman D, Erdemir A, Sumant AV (2014) Graphene: a new emerging lubricant. Mater Today 17:31–42. https://doi.org/10.1016/j.mattod.2013.12.003

14. Henderson MA (1999) A surface perspective on self-diffusion in rutile TiO_2. Surf Sci 419:174–187. https://doi.org/10.1016/S0039-6028(98)00778-X

15. Yazyev OV, Louie SG (2010) Topological defects in graphene: dislocations and grain boundaries. Phys Rev B Condens Matter Mater Phys 81:1–7. https://doi.org/10.1103/PhysRevB.81.195420

16. Wei Y, Wu J, Yin H, Shi X, Yang R, Dresselhaus M (2012) The nature of strength enhancement and weakening by pentagong-heptagon defects in graphene. Nat Mater 11:759–763. https://doi.org/10.1038/nmat3370

17. Meyer JC, Kisielowski C, Erni R, Rossell MD, Crommie MF, Zettl A (2008) Direct imaging of lattice atoms and topological defects in graphene membranes. Nano Lett 8:3582–3586. https://doi.org/10.1021/nl801386m

18. Gass MH, Bangert U, Bleloch AL, Wang P, Nair RR, Geim AK (2008) Free-standing graphene at atomic resolution. Nat Nanotechnol 3:676–681. https://doi.org/10.1038/nnano.2008.280

19. Cretu O, Krasheninnikov AV, Rodríguez-Manzo JA, Sun L, Nieminen RM, Banhart F (2010) Migration and localization of metal atoms on strained graphene. Phys Rev Lett 105:1–4. https://doi.org/10.1103/PhysRevLett.105.196102

20. Ma J, Alfè D, Michaelides A, Wang E (2009) Stone-wales defects in graphene and other planar s p2-bonded materials. Phys Rev B Condens Matter Mater Phys 80:1–4. https://doi.org/10.1103/PhysRevB.80.033407

21. El-Barbary A, Telling H, Ewels P, Heggie I, Briddon R (2003) Structure and energetics of the vacancy in graphite. Phys Rev B Condens Matter Mater Phys 68:1–7. https://doi.org/10.1103/PhysRevB.68.144107

22. Krasheninnikov AV, Lehtinen PO, Foster AS, Nieminen RM (2006) Bending the rules: contrasting vacancy energetics and migration in graphite and carbon nanotubes. Chem Phys Lett 418:132–136. https://doi.org/10.1016/j.cplett.2005.10.106

23. Carr LD, Lusk MT (2010) Defect engineering: graphene gets designer defects. Nat Nanotechnol 5:316–317. https://doi.org/10.1038/nnano.2010.93

24. He L, Guo S, Lei J, Sha Z, Liu Z (2014) The effect of Stone-Thrower-Wales defects on mechanical properties of graphene sheets—a molecular dynamics study. Carbon N. Y. 75:124–132. https://doi.org/10.1016/j.carbon.2014.03.044

25. Sha ZD, Pei QX, Liu ZS, Shenoy VB, Zhang YW (2014) Is the failure of large-area polycrystalline graphene notch sensitive or insensitive? Carbon N. Y. 72:200–206. https://doi.org/10.1016/j.carbon.2014.02.003

26. Sha ZD, Quek SS, Pei QX, Liu ZS, Wang TJ, Shenoy VB, Zhang YW (2014) Inverse pseudo Hall-Petch relation in polycrystalline graphene. Sci Rep 4:7–12. https://doi.org/10.1038/srep05991

27. Riedl C, Coletti C, Starke U (2010) Structural and electronic properties of epitaxial Graphene on SiC (0001): a review of growth, characterization, transfer doping and hydrogen intercalation. J Phys D Appl Phys 43. https://doi.org/10.1088/0022-3727/43/37/374009

28. Guo B, Liu Q, Chen E, Zhu H, Fang L, Gong JR (2010) Controllable N-doping of graphene. Nano Lett 10:4975–4980. https://doi.org/10.1021/nl103079j

29. Cheng M, Yang R, Zhang L, Shi Z, Yang W, Wang D, Xie G, Shi D, Zhang G (2012) Restoration of graphene from graphene oxide by defect repair. Carbon N. Y. 50:2581–2587. https://doi.org/10.1016/j.carbon.2012.02.016

30. Ci L, Song L, Jin C, Jariwala D, Wu D, Li Y, Srivastava A, Wang ZF, Storr K, Balicas L, Liu F, Ajayan PM (2010) Atomic layers of hybridized boron nitride and graphene domains. Nat Mater 9:430–435. https://doi.org/10.1038/nmat2711

31. Wang Y, Shao Y, Matson DW, Li J, Lin Y, nn100315s,Nitrogen-doped graphene and its application in electrochemilal biosensing.pdf. 4

32. Chi M, Zhao YP (2009) Adsorption of formaldehyde molecule on the intrinsic and Al-doped graphene: a first principle study. Comput Mater Sci 46:1085–1090. https://doi.org/10.1016/j.commatsci.2009.05.017

33. Wang X, Li X, Zhang L., Yoon Y, Weber PK, Wang H, Guo J, Dai H (2009) N-doping of graphene through electrothermal reactions with ammonia. Science 324:768–771. https://doi.org/10.1126/science.1170335

34. Mortazavi B, Ahzi S, Toniazzo V, Rémond Y (2012) Nitrogen doping and vacancy effects on the mechanical properties of graphene: a molecular dynamics study. Phys Lett Sect A Gen At Solid State Phys 376:1146–1153. https://doi.org/10.1016/j.physleta.2011.11.034

35. Mortazavi B, Ahzi S (2012) Molecular dynamics study on the thermal conductivity and mechanical properties of boron doped graphene. Solid State Commun 152:1503–1507. https://doi.org/10.1016/j.ssc.2012.04.048

36. Zheng Q, Li Z, Yang J (2013) Effects of N doping and NH2 grafting on the mechanical and wrinkling properties of graphene sheets. RSC Adv 3:923–929. https://doi.org/10.1039/c2ra22274d

37. Senturk AE, Oktem AS, Konukman AES (2018) Influence of defect locations and nitrogen doping configurations on the mechanical properties of armchair graphene nanoribbons. J Mol Model 24:0–9. https://doi.org/10.1007/s00894-018-3581-3

38. Izadifar M, Abadi R, Jam AN, Rabczuk T (2017) Investigation into the effect of doping of boron and nitrogen atoms in the mechanical properties of single-layer polycrystalline graphene. Comput Mater Sci 138:435–447. https://doi.org/10.1016/j.commatsci.2017.06.038

39. Ganesan Y, Peng C, Lu Y, Ci L, Srivastava A, Ajayan PM, Lou J (2010) Effect of nitrogen doping on the mechanical properties of carbon nanotubes. ACS Nano 4:7637–7643. https://doi.org/10.1021/nn102372w

40. Dai Z, Wang G, Zheng Z, Wang Y, Zhang S, Qi X, Tan P, Liu L, Xu Z, Li Q, Cheng Z, Zhang Z (2019) Mechanical responses of boron-doped monolayer graphene. Carbon N. Y. 147:594–601. https://doi.org/10.1016/j.carbon.2019.03.014
41. Ha YM, Kim YN, Kim YO, So C, Lee JS, Kim J, Jung YC (2020) Enhanced mechanical properties and thermal conductivity of polyimide nanocomposites incorporating individualized boron-doped graphene. Carbon Lett 30:457–464. https://doi.org/10.1007/s42823-019-00115-y
42. Plimpton S (1995) Fast parallel algorithms for short-range molecular dynamics
43. Humphrey W, Dalke A, KS (1996) VMD: visual molecular dynamics. J Mol Graph 14(1):33–38. https://doi.org/10.1016/0263-7855(96)00018-5
44. Hanwell, M.D., Curtis, D.E., Lonie, D.C., Vandermeerschd, T., Zurek, E., Hutchison, G.R.: Avogadro: An advanced semantic chemical editor, visualization, and analysis platform. J. Cheminform. 4, (2012). https://doi.org/10.1186/1758-2946-4-17
45. Stukowski A (2010) Visualization and analysis of atomistic simulation data with OVITO-the open visualization tool. model. Simul Mater Sci Eng 18. https://doi.org/10.1088/0965-0393/18/1/015012
46. Bu H, Chen Y, Zou M, Yi H, Bi K, Ni Z (2009) Atomistic simulations of mechanical properties of graphene nanoribbons. Phys Lett Sect A Gen At Solid State Phys 373:3359–3362. https://doi.org/10.1016/j.physleta.2009.07.048
47. Mortazavi B, Rémond Y, Ahzi S, Toniazzo V (2012) Thickness and chirality effects on tensile behavior of few-layer graphene by molecular dynamics simulations. Comput Mater Sci 53:298–302. https://doi.org/10.1016/j.commatsci.2011.08.018
48. Gupta S, Dharamvir K, Jindal VK (2005) Elastic moduli of single-walled carbon nanotubes and their ropes. Phys Rev B Condens Matter Mater Phys 72:1–16. https://doi.org/10.1103/PhysRevB.72.165428
49. Tersoff J (1988) New empirical approach for the structure and energy of covalent systems. Phys Rev B 37:6991–7000. https://doi.org/10.1103/PhysRevB.37.6991
50. Tersoff J (1989) Modeling solid-state chemistry: interatomic potentials for multicomponent systems. Phys Rev B 39:5566–5568. https://doi.org/10.1103/PhysRevB.39.5566
51. Lindsay L, Broido DA (2010) Optimized Tersoff and Brenner empirical potential parameters for lattice dynamics and phonon thermal transport in carbon nanotubes and graphene. Phys Rev B Condens Matter Mater Phys 81:1–6. https://doi.org/10.1103/PhysRevB.81.205441
52. KInacI A, Haskins JB, Sevik C, ÇağIn T (2012) Thermal conductivity of BN-C nanostructures. Phys Rev B Condens Matter Mater Phys 86:1–8. https://doi.org/10.1103/PhysRevB.86.115410
53. Matsunaga K, Fisher C, Matsubara H (2000) Tersoff potential parameters for simulating cubic boron carbonitrides. Japanese J Appl Phys Part 2 Lett 39. https://doi.org/10.1143/jjap.39.l48
54. Moon WH, Son MS, Hwang HJ (2003) Molecular-dynamics simulation of structural properties of cubic boron nitride. Phys B Condens Matter 336:329–334. https://doi.org/10.1016/S0921-4526(03)00299-0
55. Stuart SJ, Tutein AB, Harrison JA (2000) A reactive potential for hydrocarbons with intermolecular interactions. J Chem Phys 112:6472–6486. https://doi.org/10.1063/1.481208
56. Mahdizadeh SJ, Goharshadi EK, Akhlamadi G (2016) Thermo-mechanical properties of boron nitride nanoribbons: a molecular dynamics simulation study. J Mol Graph Model 68:1–13. https://doi.org/10.1016/j.jmgm.2016.05.008
57. Stich I, Car R, Parrinello M, Baroni S (1989) Conjugate gradient minimization of the energy functional: a new method for electronic structure calculation. Phys Rev B Am Phys Soc 39
58. Dewapriya MAN, Rajapakse RKND, Phani AS (2014) Atomistic and continuum modelling of temperature-dependent fracture of graphene. Int J Fract 187:199–212. https://doi.org/10.1007/s10704-014-9931-y
59. Kumar Gupta K, Mukhopadhyay T, Roy A, Dey S (2020) Probing the compound effect of spatially varying intrinsic defects and doping on mechanical properties of hybrid graphene monolayers. J Mater Sci Technol 50:44–58. https://doi.org/10.1016/j.jmst.2020.03.004
60. Liu F, Ming P, Li J (2007) Ab initio calculation of ideal strength and phonon instability of graphene under tension. Phys Rev B Condens Matter Mater Phys 76:1–7. https://doi.org/10.1103/PhysRevB.76.064120

61. Pei QX, Zhang YW, Shenoy VB (2010) A molecular dynamics study of the mechanical properties of hydrogen functionalized graphene. Carbon N. Y. 48:898–904. https://doi.org/10.1016/j.carbon.2009.11.014
62. Ansari R, Motevalli B, Montazeri A, Ajori S (2011) Fracture analysis of monolayer graphene sheets with double vacancy defects via MD simulation. Solid State Commun 151:1141–1146. https://doi.org/10.1016/j.ssc.2011.05.021

An Innovative Slag Engineering Approach for Improving De-Sulphurisation Efficiency in Silicon Killed Steels

Somnath Kumar , **K. K. Keshari, A. K. Bandhyopadhyay,**
Abdhesh Prasad, Vikash Kumar, N. Sen, K. Choudhury, and R. Kumar

1 Introduction

Requirements of customers are becoming very stringent with respect to low levels of total residuals (P, S, gases, inclusions) in steel. Sulphur in steel is mostly undesirable and is a detrimental impurity that affects the mechanical properties and the quality of the steel in a deleterious manner. Thus, desulfurization of steel i.e. removal of sulphur from liquid steel is very much required. The desulphurisation of steel is a key process in ladle metallurgy that is mainly achieved in ladles during secondary steelmaking. Low level of sulphur in end product is required for enhanced mechanical

S. Kumar (✉) · K. K. Keshari · A. K. Bandhyopadhyay · A. Prasad · V. Kumar · N. Sen
R & D Centre for Iron & Steel, Steel Authority of India Limited, Ispat Bhavan, Doranda, Ranchi,
Jharkhand 834002, India
e-mail: somnath07@sail.in

K. K. Keshari
e-mail: kkkeshari@sail.in

A. K. Bandhyopadhyay
e-mail: akb@sail.in

A. Prasad
e-mail: abdhesh@sail.in

V. Kumar
e-mail: vikash.singh@sail.in

N. Sen
e-mail: niladrisen@sail.in

K. Choudhury · R. Kumar
Durgapur Steel Plant, Steel Authority of India Limited, Durgapur, West Bengal 713205, India
e-mail: k.chowdhury@sail.in

R. Kumar
e-mail: rajeev1963@sail.in

properties of steel. Sulphur in steel reduces the mechanical properties of steel by increasing brittleness; it also decreases weldability and corrosion resistance. The desulphurization process of steel in ladle furnace with a suitably engineered refining slag is one of the most important refining operations in the steelmaking process.

Durgapur Steel Plant (DSP) an integrated steel plant of Steel Authority of India Limited (SAIL) is a foremost producer of long products & the lone manufacturer of Forged Railway Wheels & Axles in India. Steel Melting Shop (SMS), of DSP basically produces a wide variety of silicon/aluminium killed steel grades through BOF-LF/VAD-CC routes. The average hot metal sulphur is 0.045%. Average final sulphur in Si-killed steels at Durgapur Steel Plant is 0.028%. The desulphurisation rate from BOF turndown to tundish is 17% and from HM to tundish is 37% only. High sulphur in steel is one of the bottlenecks in improving the quality of steel as well as is one of the reasons of low throughput of continuous casters at DSP. There are also some incidences of off heats/diversions due to high sulphur in steel at DSP.

The desulphurisation potential in ladle furnace not only depends on parameters like temperature of bath, dissolved oxygen level in steel, initial sulphur content in the steel, but also mainly depends on chemical composition and physical characteristics of ladle top slag [1]. The basic requirements for efficient desulphurization are minimum amount of easy reducible oxides in the slag, high basicity of slag, intense purging for slag metal reaction etc. Desulphurization in steel is mainly dependent upon the physico-chemical properties of the ladle top slag. Properly deoxidized slag with good fluidity plays a vital role in desulphurization [2]. It is very important to limit the amount of carry over slag in the ladle during tapping as they contain easily reducible oxides like FeO and MnO which are detrimental to desulphurization capacity of the slag. Proper deoxidation practice also plays an important role in governing desulphurisation. Fully killed (Al, Al–Si) steel has a good desulphurisation potential. It is necessary to have a low oxygen potential in steel and slag in order to have a good degree of desulphurization.

De-Sulphurisation of silicon killed steel is a difficult task owing to inherent nature of steel melt as well as because of ladle top slag. In case of Si killed steel, the ladle top slag which is basically siliceous in nature has a lower sulphide capacity, lower partition ratio, and adverse physio-chemical characteristics (higher melting point & viscosity). Also the oxygen potential of both the bath as well as slag is higher as compared to normal Al killed steels.

Various earlier work carried out on desulphurisation basically focuses on either desulphurisation of steel using a highly basic slag or in steels deoxidised by aluminium. However, in many steel grades deoxidation is carried out by Si and Mn. In these Si killed steels the ladle top slag basicity is low ranging from 1.2 to 1.8. The studies on improving desulphurisation of silicon killed steel in a low basicity slag comprising of $CaO–SiO_2–Al_2O_3–MgO$ are few. The present paper discusses the various measures taken to improve the desulphurisation potential in silicon killed steels by creating the conditions conducive for desulphurisation. Slag engineering was done in a novel way to make slag physico-chemical characteristics favourable for desulphurisation of steels. Deoxidation and flux addition practice was modified in an

innovative way to decrease the SiO_2 generation and also to reduce the oxygen potential of slag. The work carried out has resulted in higher degree of desulphurisation in steel.

2 Theoretical Considerations

Sulphur is a strong surface active element. Sulphur in molten iron can exist in two forms i.e. either as an interstitial solution or in form of partially substitutional solutions. It has been seen that activity of sulphur rises considerably when silicon and carbon are present in the steel. That is why the hot metal can be desulphurised more easily than steel.

2.1 Effects of Sulphur on Steel

The solubility of sulphur in solidified iron is ~0.002% (max.) in α-iron at room temperature and ~0.013% (max.) in γ-iron at 1000 °C. Upon cooling when steel solidifies the solubility of sulphur decreases and it is ejected from the solution as iron sulfide (FeS). FeS forms a eutectic with the neighbouring iron. This eutectic segregates at the grain boundaries of iron.

The temperature of Fe–FeS eutectic is relatively low ~988 °C. This low melting eutectic weakens the attachment between the grains and causes sharp drop in mechanical properties of the steel (brittleness) at the temperatures of Rolling, Forging etc. This brittleness of steel at higher temperature operations is called hot shortness which is basically due to presence of low-melting iron sulfides which got segregated at grain boundaries. The following deleterious effects of sulphur become more prominent when the oxygen content in steel is low [3]

i.   Inter granular weaknesses and cracks in steel during solidification due to formation of undesirable sulphides
ii. Sulphur increases the brittleness of steel and when it exists in the form of sulphide, the sulphide inclusions acts as stress raiser points in steel products.

2.2 Thermodynamics and Kinetics of Desulphurisation

It is only the liquid phases of the complex slag system that participates in the desulfurization reaction. Normally slags saturated with CaO gives better results w.r.t desulphurisation of steel. The solid phase of CaO present in the slag is found to be essential to keep the liquid phases of slag saturated with CaO, thus the CaO activity in the liquid phase is expected to be equal to unity [4].

The following reaction is normally used to describe sulphur movement from the metal to the ladle top slag:

$$[S] + (O^{2-}) \leftrightarrow (S^{2-}) + [O] \tag{1}$$
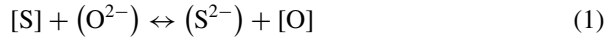
where [A] indicates A dissolved in the metal and (A) indicates component dissolved in the slag.

In the presence of Si and Al, the desulfurization reaction takes place according to Eqs. (2) and (3).

$$4(CaO) + 2[S] + 2[Si] = 2(CaS)_s + (Ca_2SiO_4)_s \tag{2}$$

$$\frac{2}{3}[Al] + [s] + (CaO) = (CaS) + \frac{1}{3} Al_2O_3 \tag{3}$$
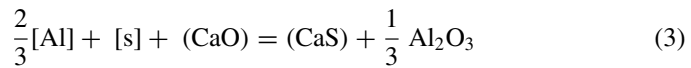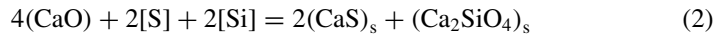
Many relationships are available for expressing slag desulphurization potential. Most of the correlations are functionally dependent on each other. They are mainly sulphide capacity, sulphur distribution coefficient, desulphurisation potential of slag, optical basicity, content of easily reducible oxides (FeO, MnO) in slag etc.

2.3 Sulphide Capacity of Slag

Sulphide capacity is an important property of slags which plays a fundamental role in the analysis and control of desulphurization reaction. It is the potential capacity of a fully homogeneous molten slag to absorb sulphur during slag metal reaction. It is a property of the slag, which is dependent on factors like temperature and on physio-chemical characteristics of slag. Sulphide capacity is used to estimate the amount of sulphur that a slag will retain under a specified condition [5]. It is also used to establish the sulphur partition ratio between slag and metal at equilibrium conditions.

The sulphide capacity of a slag can be represented as:

$$C_s = \frac{K_1 \cdot a_{O^{2-}}}{f_{S^{2-}}} = (\%S)_{slag} \cdot \sqrt{\frac{P_{O_2}}{P_{S_2}}} \tag{4}$$

where $a_{O^{2-}}$ is the activity oxygen of in slag is phase, P_{O_2} and P_{S_2} are the partial pressures of O_2 (g) and S_2 (g) and, $f_{S^{2-}}$ is the activity coefficient of sulphur in slag. K_1 is the equilibrium constant for the desulphurisation reaction:
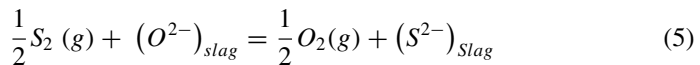
$$\frac{1}{2}S_2 (g) + (O^{2-})_{slag} = \frac{1}{2}O_2(g) + (S^{2-})_{Slag} \tag{5}$$
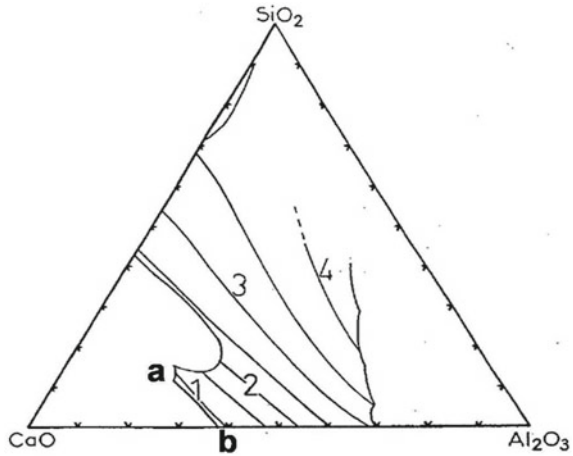
Figure 1 represents the sulphide capacities of a CaO–Al$_2$O$_3$–SiO$_2$ slag system at different slag compositions. For an optimum slag composition to achieve an effective desulphurisation, compositions nearer to the line ab ($-\text{Log } C_s = 1$) should be ensured. Compositions close to the line a-b have CaO activity value close to unity as well as high basicity which are important parameters for desulphurisation [6].

It is understood that desulphurization capability is improved with higher slag basicity. Basic slags have high quantity of basic oxides (CaO mainly) which acts as network breakers and has ability to liberate its oxygen ion (O^{2-}) in substitute for sulphur dissolved in steel. Many correlations are available between sulphide capacity and basicity. Three different sulphide capacity models are shown in Fig. 2. The three models in Fig. 2 show that increased basicity improves sulphide capacity of slag [3].
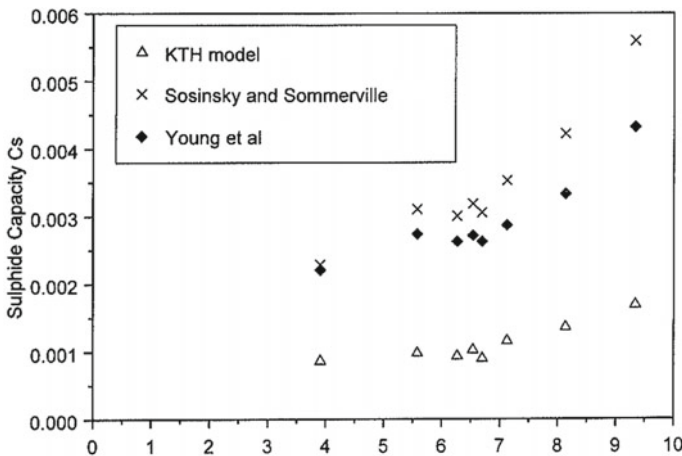

Fig. 2 Sulphide capacity values as functions of basicity [3]

2.4   Viscosity of Ladle Top Slag

Thermo-physical property of slag greatly influences the kinetics of the ladle metallurgical operations. The interaction between slag and metal during the ladle refining is significantly affected by the viscosity of both the steel and slag. At lower viscosity of the slag, transfer rate of sulphur from liquid steel to ladle top slag is improved because of higher the slag/metal interfacial area [7]. A low melting point, fluid CaO rich slag can be obtained by adding an accurate proportion of Al_2O_3. In some steel plants the viscosity is adjusted by the addition of CaF_2 [7]. Viscosity values for steels are well established at steel making conditions but the viscosities of slags are not well established. Slag viscosities are extrapolation of temperature and composition in a multi-component slag system.

3   Conventional Industrial Practice

Steel Melting Shop of Durgapur Steel Plant (DSP) mainly produces wide variety silicon killed steel through BOF-LF/VAD-CC/BRC route. The charge mainly consists of 125 tons of hot metal and ~10 tons of scrap. The average heat weight is around 118 tons. De-oxidation and alloying is carried out by addition of coke, silico manganese & ferro silicon etc. Lime (~6–7 kg/ton) is added in the ladle during tapping to achieve the desired top slag basicity for effective desulphurization and slag conditioning. Calcined bauxite (~0.8–1.0 kg/tcs) is also added as a slag modifier to make the slag fluid in nature for inclusion absorption, better slag metal mixing and for low noise level during arcing. Currently no pet coke is added in the ladle bottom for initial de-oxidation by carbon. Problem faced by DSP is high and fluctuating sulphur content of hotmetal. The average sulphur level in hotmetal is ~0.040%. Sulphur varies from an average level of 0.040% to as high as 0.074%. This high sulphur in steel is difficult to remove and ultimately leads to product diversion/down gradation. Incidences of strand break out are also evident due to high sulphur content of steel. Only 37% desulphurization is achieved form hotmetal to tundish and from BOF turndown to tundish, % De-S is only 17.5%, which is quite a low figure which can been in Fig. 3.

The following approach was identified to achieve objectives desulphurisation level at ladle furnace at SMS, DSP:

- Identification of critical parameters responsible for lesser desulphurisation under DSP condition.
- Slag engineering to form low melting point slag & lowering the viscosity of the slag.
- Optimization of flux, deoxidation and refining practices to achieve low level of dissolved oxygen in melt as well as lower level of easily reducible oxides in ladle top slag.
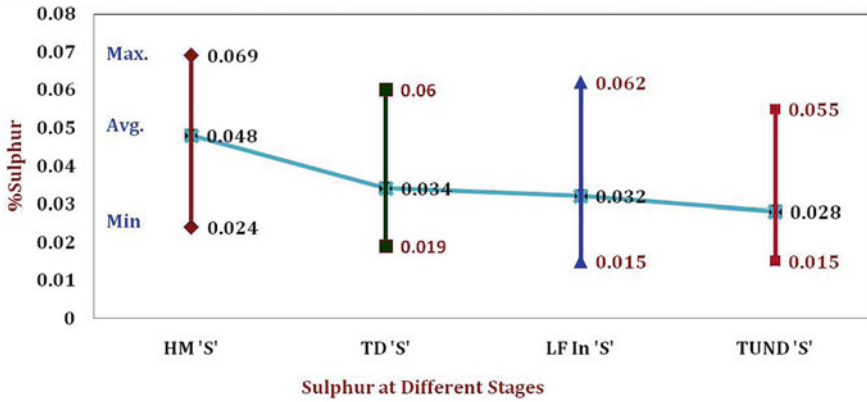
Fig. 3 Sulphur level at different stages of steelmaking at SMS, DSP

4 Experimentation

4.1 Identification of Critical Factors Affecting De-S

In order to firm up improvement measures it was necessary to identify the main contributing factors which were affecting the de-sulphurisation of steel. To understand the specific reasons of low desulphurisation, the existing practice of secondary refining was studied in detail. Ladle top slag samples were collected at the LF final stage of refining to measure the slag melting point and viscosity using empirical correlations & FactSAGE. Analysis of existing practice of steel refining at LF revealed the following probable reasons responsible for lower desulphurisation:

- **Viscous slag during ladle furnace operation**: Physical observation of slag at Ladle Furnace revealed that slag was crusty in nature (Fig. 4). Ladle furnace slag samples were collected, their melting point and viscosity were calculated,

Fig. 4 Crusty ladle top slag at Ladle Furnace
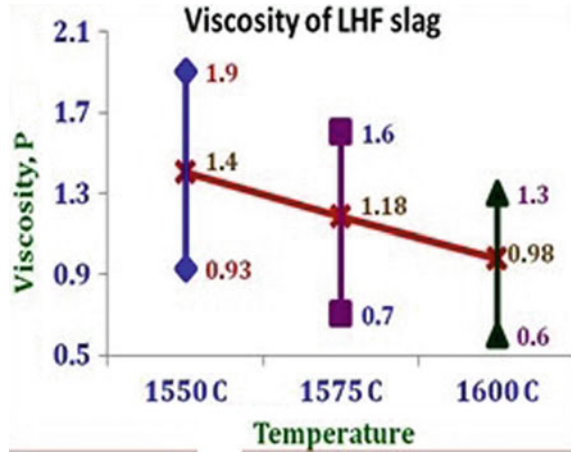
where it was found that average melting point of the slag was around 1510 °C, which was very close to liquidus of steels (C: 0.10–0.23%) processed through LF. In order to maintain a fluid slag during refining and casting operation, the difference between melting point of slag and liquidus temperature of steel should be a minimum value of 40–50 °C. The calculated viscosity was found at a level of 0.98 poise at 1600 °C, which showed that slag, was quite viscous in nature (Fig. 5). Owing to poor fluidity of ladle top slag, proper mixing of slag and metal at ladle furnace was not feasible, resulting in poor desulphurization. Optimization of slag composition and adoption of suitable flux addition was necessary for making a fluid slag for better slag metal interaction.

- **High oxygen potential of metal and slag**: Since the heats made at DSP are of silicon killed grade and deoxidation during tapping was done with SiMn, the level of dissolved oxygen in steel is was normally around 30–40 ppm. It is also evident from the slag analysis that $FeO + MnO$ content in the slag is higher, ranging from avg 6.05% (Table 1) to as high as 7.5%. Sometimes slag is blackish in appearance. This shows that the slag is not properly deoxidized and hence not very conducive for desulphurization.

- **High carryover slag from BOF converter**: Primary steel making slag has high percentage of easily reducible oxides. These easily reducible oxides are very detrimental for desulphurisation point of view. Some amount of this slag comes into the ladle from BOF converter during tapping because of carryover of slag. The carryover slag form converter results in high and variable amount of oxides like

Table 1 Ladle Furnace final slag analysis in conventional practice

CaO	SiO$_2$	Al$_2$O$_3$	MgO	FeO	MnO	P$_2$O$_5$	S	TiO$_2$	FeO + MnO	Basicity (CaO/SiO$_2$)
47.20	28.44	5.32	11.58	3.16	2.89	0.11	0.14	0.97	6.05	1.65

FeO and MnO to the ladle top slag. At DSP carryover slag is sizeable (~6–8 kg/tcs) and also varies considerably from heat to heat.

4.2 Plant Trials with Modified Practice

For improvement of steel desulphurization, plant trials were conducted separately for heats through bloom caster and vacuum arc degasser (VAD) unit. For bloom caster heats, initial deoxidation was carried out by addition of ~100 kg pet coke in the ladle bottom. As the product of deoxidation by carbon is gaseous, it helped in good mixing of metal and slag and in initial reduction of dissolved oxygen content. It was also beneficial for steel cleanliness. Initial deoxidation with pet coke also helped in reducing silica content in ladle top slag which adversely affects the sulphide capacity of slag.

Calcined bauxite was used as slag fluidiser, and was added during taping of steel. Alumina is considered as the third "best" flux after B_2O_3 and CaF_2 to break Ca_2SiO_4 complex and increase the solubility of CaO in slag. A sizeable amount of alumina is required to increase the CaO solubility at 1600 °C [8].

The improvement in i.e. increase in CaO solubility in slag above the minimum Al_2O_3 threshold value is also related to the levels of SiO_2 content of the slag. The Al_2O_3 in the slag act as $CaO–SiO_2$ chain breaker and hence brings CaO into the solution. Thus breakage of Calcium silicate chain lowers the viscosity of slag and improves its fluidity. In Fig. 6 we can see the effect of alumina replacing the SiO_2 and improving CaO saturation in slag.

Figure 6 shows that in the $CaO–Al_2O_3–SiO_2$ (CAS) system, initially the CaO solubility is decreases as the replacement of SiO_2 with Al_2O_3 progresses. A great enhancement in CaO solubility occurs when the alumina levels of the slag increases beyond 25% Al_2O_3 and the silica level of the slag is lowered to less than 10% SiO_2.

In plain silicon killed steel, there is remaining dissolved oxygen at the level of 35–50 ppm. In the base heats wherein dissolved oxygen level was measured after treatment finish in ladle furnace, the dissolved oxygen level was found in between 35 and 40 ppm. In order to minimize the dissolved oxygen level in steel melt, Al–Si deoxidation was introduced instead of plain Si deoxidation. For this ~80 kg of Al was added in ladle bottom along with petcoke before start of tapping. In order to make the slag fluid in nature for better slag metal mixing and inclusion absorption, around 200 kg of calcined bauxite was added in ladle during tapping from BOF.

The amount of 80 kg Al addition for deoxidation was decided based on earlier industrial experience. The amount of Al was fixed at this level, as it was found that this was not leading to any nozzle clogging in SEN (as the heats were not calcium treated). The amount of calcium bauxite was fixed to 200 kg based on calculations to achieve ~10% of Al_2O_3 in the ladle top slag (targeted ladle top slag chemistry is shown in Table 2).
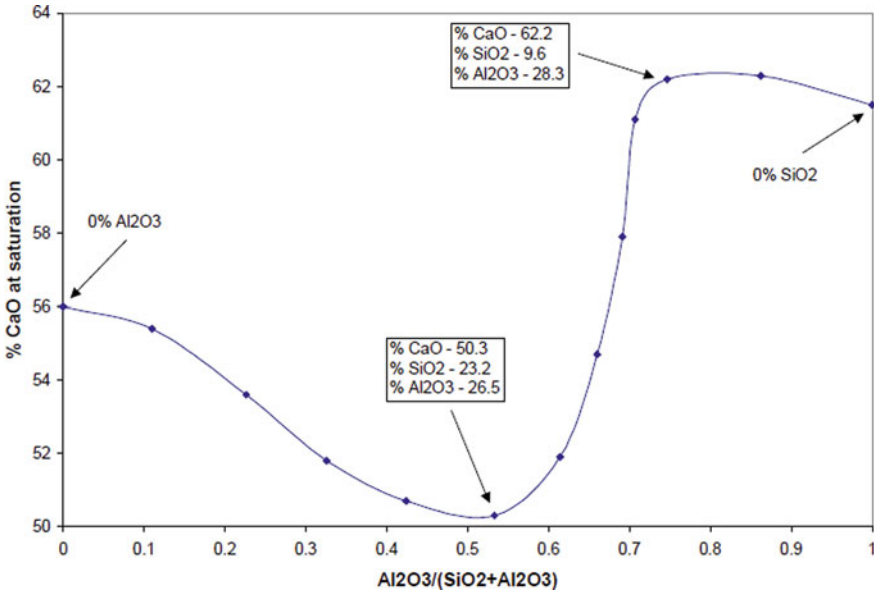
Fig. 6 The solubility of CaO as Al_2O_3 is replacing SiO_2 at 1600 °C

Table 2 The targeted ladle top slag chemistry

CaO%	SiO_2%	Al_2O_3%	MgO%	FeO + MnO%	Basicity
47–50	20–25	10–12	6–8	<2	1.8–2.2

Pet coke is a very good deoxidiser, as it does not leave behind any deoxidation product (the deoxidation product is carbon monoxide gas). During the earlier industrial experience what we have seen that addition of ~0.8–1.0 kg/tcs of pet coke in ladle bottom does not lead to any carbon pick up. Based on this assumption the amount of 100 kg pet coke addition in ladle bottom was finalised.

Presence of FeO, MnO in ladle top slag greatly reduces the desulphurisation capability of slag. One of the basic pre conditions for steel desulphurisation of steel is high basicity (CaO saturated) and completely reduced slag. FeO & MnO, also known as easily reducible oxides significantly reduces the desulphurisation potential of ladle top slag. The presence of FeO & MnO reduces the sulphide capacity and sulphur partition ratio of ladle to slag. The effect of FeO + MnO on steel desulphurisation is shown in Fig. 7.

In order to reduce the levels of these oxides, slag deoxidation technique was tried out. The purpose of addition of FeSi + Coke or any other slag deoxidisers (like Al shots) is to reduce the FeO & MnO in ladle top slag After completion of tapping, a 50–50-% mixture of FeSi fines & Coke fines (~60 kg) were added in the ladle top slag for reduction of FeO + MnO.
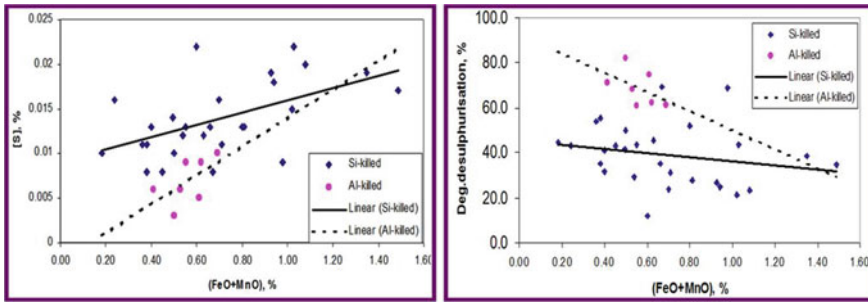
Fig. 7 Effect of easily reducible oxides on Steel Desulphurisation

In order to assess the effectiveness of modified flux, de-oxidation and refining practices, data was collected for sulphur level in liquid steel for evaluation of product quality. The LF final slag was also collected for determining the viscosity and melting point of the modified slag. For VAD heats the lime addition was reduced from 1000–1200 kg to 850–900 kg. Slag deoxidation method was also adopted for VAD heats.

Further addition of flux (as required) and trimming addition of ferro alloys were carried in ladle furnace. Final LF slag samples were collected and analysed for comparison.

5   Result and Discussion

De-Sulphurisation of silicon killed steel is a difficult task owing to inherent nature of steel melt as well as because of ladle top slag. In case of Si killed steel, the ladle top slag which is basically siliceous in nature has a lower sulphide capacity, lower partition ratio, and adverse physio-chemical characteristics (higher melting point & viscosity). Also the oxygen potential of both the bath as well as slag is higher as compared to normal Al killed steels.

Trials for desulphurization were carried out for bloom caster heats. During the trial period, heats were treated with suggested flux addition. The quality of slag was monitored at LF. The refining slag was found to be more fluid with the modified flux and deoxidation practice for bloom caster heats, as compared to normal practice. The analysis of slag samples of Si-Al killed bloom caster heats revealed reduction in melting point and viscosity of LF slag which was achieved by incorporating initial de-oxidation by carbon and further killing by Al in combination with normal de-oxidation practice. Slag viscosity reduced from 0.98 to 0.75 poise at 1600 °C (Fig. 8) and slag melting point reduced from 1510 to 1445 °C (Fig. 9)**.**

Due to the inherent characteristics of Si killed steels the De-S capability of slag is generally low (low sulphide capacity/ low sulphur partitioning ability of slag) as can be seen from Fig. 10. From Fig. 11, it can be seen that the present slag system was falling into a region of low sulphur partition and sticky slag zone. Slag melting

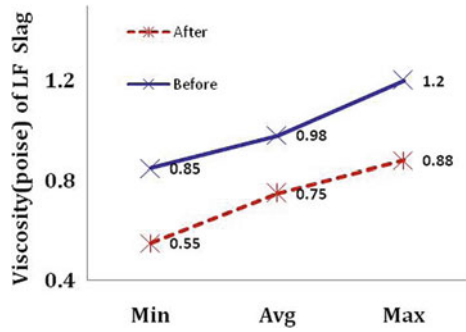**Fig. 8** Viscosity of LF Slag at 1600 °C in conventional and modified practice

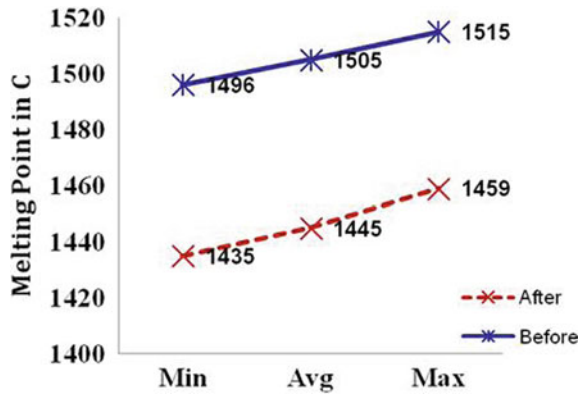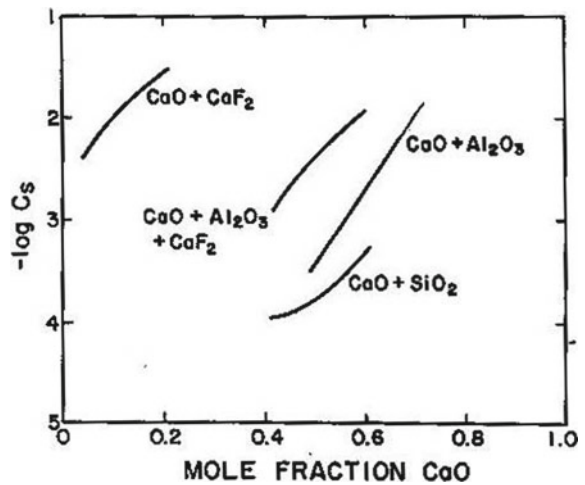**Fig. 9** Melting point in conventional and modified practice

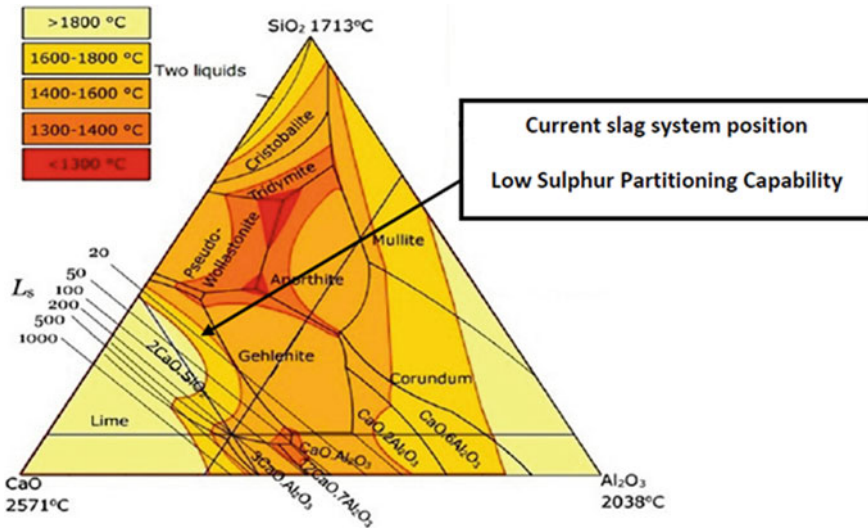**Fig. 10** Sulphide capacities of Slags

Fig. 11 Position of current slag in low sulphur partition region

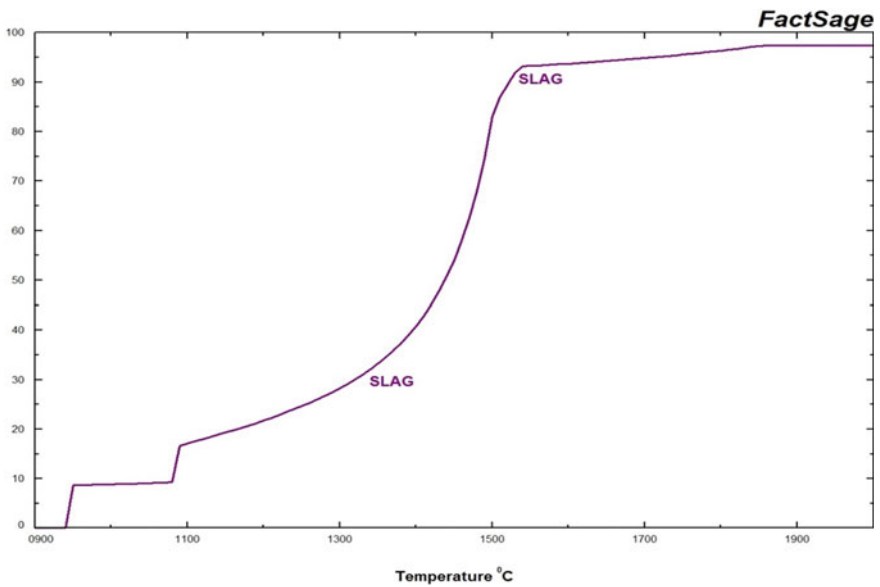characteristics was worked out for the modified slag system which can be seen from Fig. 12.

Fig. 12 Slag melting behaviour showing around 90% slag liquid at 1600 °C

To make conditions more conducive for desulphurisation, changes in ladle top slag chemistry was achieved by incorporating Al-Si deoxidation and slag deoxidation method. The targeted ladle top slag chemistry is shown in Table 2:

The modified practice helped in improving the desulphurisation of heats through bloom caster. Analysis of trial results showed average tundish sulphur level of 0.015% as compared to 0.028% for earlier heats through bloom caster (Table 3). Around 62% De-S from HM to tundish was achieved in trial heats in which modified practice was followed. The modified practice helped to achieve low dissolved oxygen level of 7–10 ppm as compared to 35–40 ppm and low (FeO + MnO) level of <2.5% as against ~5% in normal practice. Changing the deoxidation practice from Si killed to Si- Al killed helped to reduce SiO_2 generation thereby increasing the average slag basicity from 1.7 to 2.04 which facilitated desulphurization. The Alumina level in the slag increased from 4 to 5% to ~9–10% in ladle top slag thereby improving the sulphide capacity of slag.

In some trial heats required De-S was not achieved. During the analysis of trial results it was found that, the rate of carryover slag was substantial in those heats. One of the preconditions for De-S is that the carry over slag from BOF to ladle should be as low as possible. The presence of easily reducible oxides in carry over slag makes the conditions for De-S unfavourable and since there is a limited treatment time available at the LFs, the extent of De-S achievable is less. We can see in Fig. 13, that in cases when FeO + MnO level in slag is more, the appearance of ladle top slag is blackish (it is the case when carryover slag is higher), whereas in case of fully killed, lime saturated slag (which is beneficial for De-S) the slag appearance is white.

The slag deoxidation technique was found to be very helpful in reducing the ladle top slag oxygen potential. Significant decrease in FeO, MnO levels was observed in heats through VAD in which slag deoxidisers were added. This in combination with controlling lime addition between 850 and 950 kg also helped in improving desulphurisation level in heats through VAD (Table 4).

In all the trials heats through bloom caster in which Al-Si deoxidation was practiced, no stopper rod fluctuations was observed.. Very smooth casting was observed in heats in which aluminium was added. This is a good indication that no clogging tendency was found even with addition of Al in ladle during tapping. It is also very significant that no calcium treatment was carried out in the trials heats with Al addition. Apart from Al & coke addition in ladle bottom, all the other processing parameters were similar as compared to normal heat making at DSP for bloom heats.

6 Conclusions

Critical factors responsible for poor desulphurisation were identified. It was found that high FeO + MnO in slag due to high slag carry over, high dissolved oxygen and low basicity coupled with low fluidity of slag were the main reasons for poor desulphurisation at DSP.

Table 3 Trial data of heats through bloom caster

| Heat id	HM'S'	Ladle additions								Tundish Sulphur	% De-S
		Lime	Cal. Baux	SiMn	Al	FeSi	Pet Coke	Coke + FeSi		Sulphur	HM to Tundish
1	0.046	867	196	1615	80	154	209	–		0.017	63.04
2	0.045	861	214	1397	80	140	157	–		0.016	64.44
3	0.037	822	193	2016	80	99	74	–		0.015	59.46
4	0.038	811	195	1991	80	212	80	–		0.014	63.16
5	0.037	594	168	1579	–	215	215	60		0.013	64.86
6	0.037	812	198	1044	–	246	130	60		0.013	64.86
7	0.038	794	193	1902	–	193	90	60		0.017	55.26
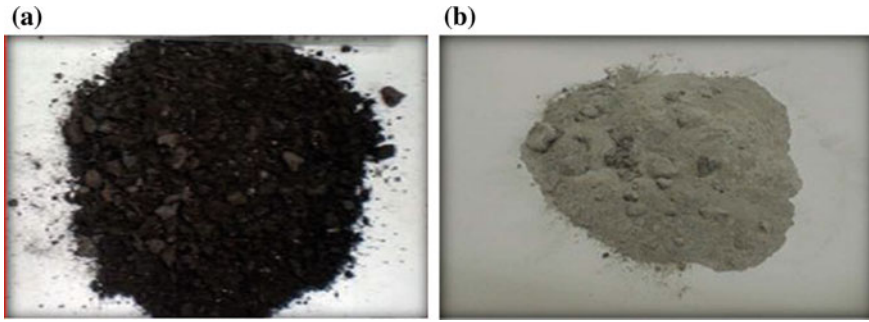
Fig. 13 **a** LF Slag black in appearance (Higher Oxy Potential). **b** Completely deoxidised LF slag white in appearance

The process of deoxidation and flux addition was modified. Initial deoxidation with carbon and further killing of the bath by Al in combination with normal de-oxidation practice for bloom caster heats was established. Innovative slag deoxidation practice using coke + FeSi fines was found to be very beneficial for reducing ladle top slag.

These modifications helped in achieving average sulphur levels of 0.015% (as compared to 0.035% in base heats) in trials heats through bloom casters (~60% de-S from HM to tundish as compared to 37% earlier). In VAD heats where slag deoxidation method was adopted, coupled with reduced lime addition (~850–950 kg), ~60% de-S (from 0.035% to 0.013%S) was achieved from HM to VAD finish.

In all the trial heats through bloom casters no stopper rod fluctuations was observed. This is a good indication that in case of higher HM S, the suggested practice can be adopted for desulphurising the steel without having any apprehension of nozzle clogging. No calcium treatment practice was followed in trial heats. But any delayed addition of Al in ladle furnace may result in tendency of nozzle clogging.

The change in flux and deoxidation practice for improvising the desulphurisation process does not have any additional risk involved.

The modified practice cost is minimal (~Rs 200/tcs) as compared to grade rejection or grade down gradation on account of higher sulphur in steel. Higher Sulphur also sometimes leads to breakout leading to strand loss and consequently huge loss productivity loss.

This novel slag engineering method using calcined bauxite as slag modifier helped in increasing the solubility of CaO in slag resulting in lowering down of melting point of slag. This method can be utilized for improving desulphurisation of steel whenever the hot metal sulphur is high.

Table 4 Details of trials heats through VAD in which slag deoxidation were carried out

Heat id	Ladle analysis, %							Teeming analysis, %						% De-S
	HM S	C	Mn	S	P	Si	Al	C	Mn	S	P	Si	Al	HM to teem
1	0.034	0.43	0.58	0.033	0.019	0.2	0.002	0.62	0.72	0.009	0.027	0.22	0.005	73.53
2	0.038	0.505	0.56	0.043	0.015	0.2	0.002	0.625	0.76	0.017	0.016	0.25	0.003	55.26
3	0.039	0.38	0.54	0.03	0.018	0.2	0.001	0.64	0.73	0.014	0.02	0.23	0.004	64.10
4	0.037	0.31	0.5	0.04	0.018	0.2	0.002	0.45	0.78	0.016	0.024	0.27	0.013	56.76
5	0.034	0.43	0.58	0.033	0.019	0.2	0.002	0.62	0.72	0.009	0.027	0.22	0.005	73.53
6	0.035	0.46	0.58	0.03	0.013	0.22	0.002	0.615	0.73	0.012	0.024	0.23	0.005	65.71
7	0.037	0.315	0.5	0.032	0.018	0.11	0.001	0.45	0.76	0.013	0.022	0.26	0.005	64.86
8	0.05	0.35	0.65	0.04	0.018	0.2	0.002	0.61	0.74	0.014	0.021	0.2	0.006	72.00
9	0.048	0.39	0.57	0.05	0.022	0.21	0.002	0.63	0.81	0.02	0.028	0.2	0.007	58.33
10	0.047	0.4	0.57	0.035	0.017	0.2	0.002	0.63	0.77	0.017	0.026	0.23	0.005	63.83

References

1. Buĺko B, Kijac J, Domec M (2009) Optimalization slag composition in ladle furnace considering to effective steel desulfurization. Acta Metallurgica Slovaca 15(2):93–99
2. Pretorius EB (2015) Fundamentals of EAF and ladle slags and ladle refining principles. https://www.semanticscholar.org/paper/Fundamentals-of-Eaf-and-Ladle-Slags-and-Ladle-PretoriusRefractories/5109946bfbb401ec66c8bf13bc34298c48b6be59
3. Andersson MA, Jönsson PG, Nzotta MM (1999) Application of the sulphide capacity concept on high-basicity ladle slags used in bearing-steel production. ISIJ Int 39(11):1140–1149. https://doi.org/10.2355/isijinternational.39.1140
4. Xu JF, Huang FX, Wang XH (2016) Desulfurization behavior and mechanism of CaO-saturated slag. J Iron Steel Res Int 23(8):784–791. https://doi.org/10.1016/S1006-706X(16)30121-2
5. MM N, Sichen D, Seetharaman S (1998) Sulphide capacities in some multi component slag systems. ISIJ Int 38(11):1170–1179.https://doi.org/10.2355/isijinternational.38.1170
6. Atlas S (1995) Verein deutscher eisenhüttenleute. Verlag Stahleisen GmbH, Düsseldorf, 5, pp 258–259
7. Boström A (1997) A model for multi component reactions between metal/slag using thermo-calc: applied for removal of sulphur during ladle treatment (Doctoral dissertation, Institutionen för tillämpad process metallurgi). (Licentiate thesis, 1997, KTH)
8. PG J, Jonsson L, Sichen D (1997) Viscosities of LF slags and their impact on ladle refining. ISIJ Int 37(5):484–491.https://doi.org/10.2355/isijinternational.37.484

Medium Manganese Steel: Revealing the High Sensitivity of Microstructure and Mechanical Properties on Intercritical Annealing Temperature and Time

Avanish Kumar Chandan, Gaurav Kumar Bansal, Biraj Kumar Sahoo, and Jay Chakraborty

1 Introduction

Demand of lighter yet stronger steels for automobiles is driven by the ever increasing passenger safety standards and fuel economy. From the metallurgist's eye, the challenge is to produce a material having an inherent property of combined strength and ductility. Strong material will thereby take care of the required strength. At the same time, a ductile material will be formable and thus can be rolled into thin sheets, rendering them lighter which in turn will take care of the light weighting, fuel economy and the overall carbon footprint. Endeavors for such a material is still a challenge to the research community as producing a strong material is always associated with the decrease in ductility and vice versa, a phenomenon commonly known as strength-ductility trade-off. Steels has been the first choice of budget carmakers owing to its appropriate properties, low cost and a proven technology for mass production and processing. Steel for automotive applications have evolved over the decades in order to stay alive amidst the competition being put up by several alternative materials such as magnesium alloys, aluminum alloys, plastics, composites etc. In this regards, evolution of various grades of advanced high strength steels (AHSS) has a major role to play. AHSS are the improved version of high strength steels (HSS). As per the World Auto Steel [1], "HSS and AHSS come from same steel family sharing common behaviors. AHSS exhibits enhanced strength-ductility combination in comparison to various HSS grades such as IF, BH, HSLA etc. Definition-wise, the steels having yield strength (YS) in the range of 210–550 MPa are termed as HSS and anything stronger than that as AHSS." AHSS is a steel class which covers a broad gamut of steel grades with variations in processing, composition, microstructure and properties. Till now, AHSS has evolved up to three generations (Gen). Figure 1 shows the

A. K. Chandan (✉) · G. K. Bansal · B. K. Sahoo · J. Chakraborty
Materials Engineering Division, CSIR-National Metallurgical Laboratory, Jamshedpur, India
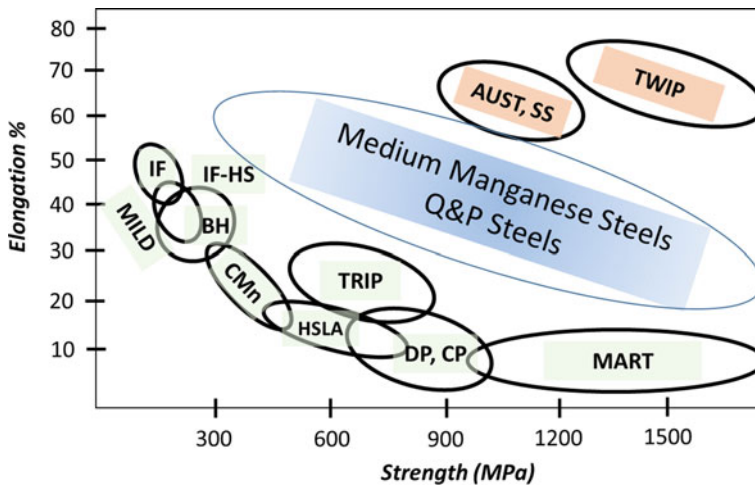e-mail: avanish@nmlindia.org

Fig. 1 Schematic of strength—elongation map for various AHSS grades

evolution of various Gen AHSS with respect to strength and elongation. 1st Gen AHSS consists of martensitic steels, dual phase (DP) steels, transformation-induced plasticity (TRIP) aided steels, etc. 1st Gen steels possessing strength levels in the range ~400–600 MPa and ductility ~10–20%, are becoming obsolete as they do not match with the modern car safety standards. Such a critical caveat led to the evolution of AHSS to 2nd Gen grades. 2nd Gen AHSS are basically high manganese (Mn) (>15–20 wt.% Mn) steel grades such as TRIP or/and twinning-induced plasticity (TWIP) steels. 2nd Gen AHSS grades possess an excellent balance of strength and ductility with tensile strength as high as 1000 MPa at the same time, a uniform ductility of more than 50% can be achieved. But all these comes at a highly increased cost due to heavy alloying in the steel. Additionally, 2nd Gen AHSS suffers major weldability issues which again is a consequence of high alloying content. These factors made budget carmakers reluctant to use these steel and there has been a requirement of alternatives. Such prevailing situation of dismal performance by 1st Gen AHSS and high cost of 2nd Gen AHSS had led to the evolution of 3rd Gen AHSS which include steel grades such as medium Mn steel [2–5] and quench and partitioned (Q&P) steel [6–9]. Medium Mn steels are considered as a promising future steel grade for automobile's body in white (BIW) parts and an alternative to the 2nd Gen AHSS with significantly lower cost. Medium Mn steels contains considerably low Mn (3–12 wt. %) [10] as compared to the 2nd Gen steel grades. In contrast to the fully austenitic microstructure of 2nd Gen AHSS, microstructure of medium Mn steels consists of ultrafine ferrite and martensite phases along with a significant amount of film and/or blocky retained austenite phase (generally >15–20 vol. %). Mechanical properties of medium Mn steels have been found to be comparable to that of 2nd Gen steels. Enhanced mechanical properties of medium Mn steels, containing considerably lower Mn content than the 2nd Gen AHSS, is primarily

attributed to the presence retained austenite (γ_{ret}) in the ultrafine ferrite/martensite (α) matrix. Retained austenite stabilization in the final microstructure is carried out via the heat treatment technique, austenite reverted transformation (ART) annealing, commonly known as intercritical annealing (IA). Apart from the amount of retained austenite, there are various other factors which directly or indirectly affect the final mechanical properties, such as alloy composition, intercritical annealing parameters such as time and temperature, prior austenite grain size, crystallographic orientation, lath size, composition dependent stacking fault energy (SFE) of austenite phase etc. Each of these factors influences the mechanical properties of the steel. Therefore, a comprehensive understanding about the above mentioned factors is critical for designing a medium Mn steel with the desired properties. Among these, IA temperature and time are primarily the most important parameters which influences all the other factors such as amount of retained austenite phase, composition of the retained austenite which in turn affects its SFE, fineness of the martensite laths and austenite films which is directly associated with the stability of the retained austenite etc.

In the present work, an attempt has been made to discern the influence of the intercritical annealing temperature and time on microstructure and the consequent mechanical properties of medium Mn steels. A thermodynamic model calculation has been utilized for establishing the importance of intercritical annealing temperature on the microstructure and the consequent mechanical properties of medium Mn steels has been discussed. Importance of intercritical annealing time has been elucidated in terms of stacking fault energy and austenite stability.

2 Results and Discussion

2.1 Effect of Intercritical Temperature

The simplest possible way to stabilize austenite phase would be to isothermally hold the steel specimen in the intercritical phase field (between Ac_1 and Ac_3) after the austenization treatment, followed by cooling [11]. However, this simple process will result in soft large grained ferrite matrix + the retained austenite. In this particular case, achievement of the required strength will be compromised as the large ferrite grains would limit the mechanical properties that could have been achieved with a fine grain structure. The schematic of the above mentioned process is presented in Fig. 2a. The concept of ART annealing for medium Mn steel emphasize to produce ultrafine microstructure of retained austenite embedded in-between the ferrite/martensite laths. ART annealing involves holding of steel having a fully martensitic fine microstructure in the intercritical phase field region during which fine austenite forms and undergoes sufficient enrichment of austenite stabilizers such as carbon and Mn. These austenite stabilizers in turn decrease the martensitic start temperature (M_s) (as per the equation (i)) of the intercritical austenite phase to a sufficient extent and at the same time the CCT curve of the intercritical austenite
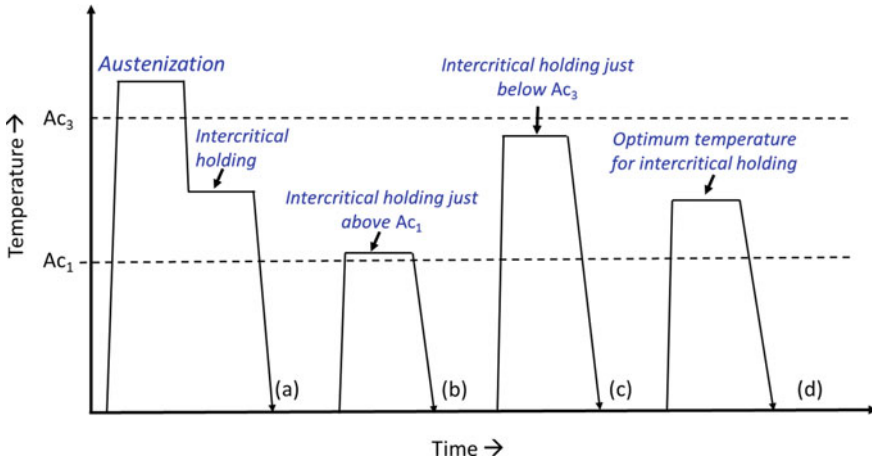
Fig. 2 Various heat treatment routes in medium Mn steel

phase shifts to the right due to enrichment of the austenite phase. Both the above mentioned factors allows retention of a significant amount of austenite phase in the final microstructure after the final quenching to room temperature. The amount of enrichment of C and Mn in the intercritical austenite phase and subsequent amount of retained austenite in the final microstructure will be dependent on the temperature of isothermal intercritical holding of the steel specimen (as per the phase diagram). In this context, it is important to select the correct holding temperature in order to obtain maximum amount of retained austenite with the required phase stability. Steel specimen held just above the Ac_1 temperature would have little amount of intercritical austenite phase and a high amount of solute elements available for its enrichment (Fig. 2b). Consequently, a small amount of retained austenite will be obtained but with a significant solute enrichment. Another option is to choose the intercritical holding temperature just below the Ac_3 temperature, i.e. a higher intercritical temperature (Fig. 2c). In this case, the amount of intercritical austenite phase will be high which might result in greater retained austenite content in the microstructure. However, since the amount of solute element for enrichment of austenite is fixed, this will result in low concentration of solute elements in the high volume of intercritical austenite phase. Hence, after quenching the steel specimen after intercritical holding, the amount of retained austenite will again be on the lower side. This suggests that there has to be an optimum intercritical holding temperature for obtaining the maximum retained austenite volume fraction (Fig. 2d).

One way of finding the optimum temperature is by performing the ART annealing at different intercritical temperatures followed by measurement of the volume fraction of retained austenite by some suitable technique like X-ray diffraction (XRD). However, this is not encouraged due to its experiment intensive nature. Instead, it is suggestive to utilize the thermodynamic model developed by Moor et al. [12]. The same has been vastly utilized by the research fraternity due to its large success in

predicting the amount of retained austenite near-correctly. In the following, description of the model calculation has been presented for a theoretical steel of composition, Fe-5Mn-0.25C wt.%. The model consists of the following steps:

(i)   As the first step, the temperature dependent evolution of the equilibrium phases is being done. Figure 3a shows the evolution of various phases with temperature as calculated from the ThermoCalc program [13].

(ii)   Second step is to predict the composition of the equilibrium austenite phase at different temperatures. Figure 3b, c presents the C and Mn concentration of the austenite phase predicted using the ThermoCalc program for the mentioned steel composition.

(iii) In third step, M_s temperature of the austenite phase is calculated by using the following equation [14]:

$$M_s = 539 - 423 * \%C - 30.9 * \%Mn - 7.5 * \%Si + 30 * \%Al \quad (1)$$

It is clear from the above equation that M_s temperature of the austenite phase is dependent on the intercritical annealing temperature as the solute content in the austenite phase vary with the temperature. The amount of martensite forming after
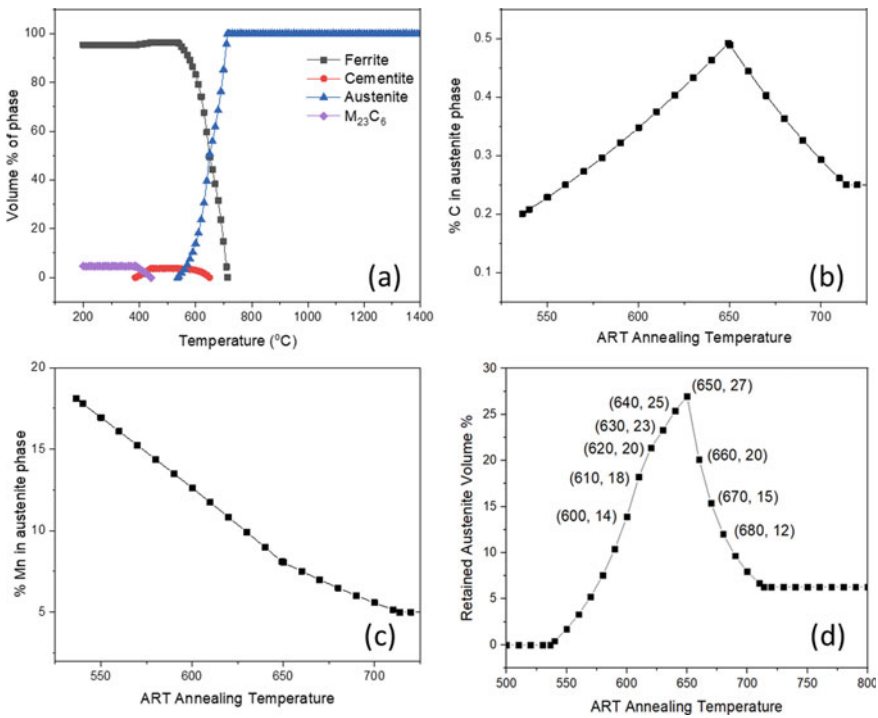

Fig. 3 **a** Phase evolution with increasing temperature, **b** Carbon, **c** Manganese and **d** volume % of retained austenite as a function of intercritical holding temperature

quenching the specimen to room temperature, initially held at an intercritical temperature has been estimated using the empirical Koistinen–Marburger (KM) equation [15]:

$$f_m = 1 - exp(-0.011(M_s - QT)) \tag{2}$$

where, M_s is martensitic start temperature and QT is quenching temperature. QT has been taken to be 30 °C (room temperature) in this particular case.

(iv)   The final retained austenite fraction in the microstructure can be estimated by subtracting the amount of freshly formed martensite (after the final quenching from intercritical temperature) from the equilibrium austenite fraction present at that particular intercritical temperature (Fig. 3d).

Figure 3d shows the predicted amount of retained austenite using the above formalism with the intercritical temperature. The predicted maximum retained austenite volume % occurred at the dissolution temperature of the cementite phase (Fig. 3a). Further, it is apparent that the predicted amount of retained austenite is highly sensitive to the variation in the intercritical temperature. A small change in the intercritical temperature in order of just 20 degrees leads to significant difference in the predicted retained austenite volume %. This is due the fact that C and Mn content of the intercritical austenite phase varies significantly with the temperature, leading to alteration in the M_s temperature and hence in the amount of retained austenite phase. Figures 3b, and c depicts the change in absolute value of the predicted amount of C and Mn, respectively, showing that again a small change in temperature lead to a considerable change in the C and Mn content of the austenite phase. To the end, it is important to note that M_s temperature is largely dependent on the carbon content of the austenite phase. A change of 0.1 wt. % C in the austenite phase lead to a difference of 42.3 °C in the M_s temperature (as per equation (i)). Furthermore, the C content of the intercritical austenite phase varies in the order of 0.1 wt. % (Fig. 3b). Thus, as far as the prediction is concerned, the retained austenite content is greatly influenced by the intercritical temperature of ART treatment. Microstructure evolution after the ART treatment in a medium Mn steel having composition, Fe-5Mn-0.25C wt.%, is displayed in Fig. 4. Figure 4a shows the as-rolled microstructure consisting of full-martensite microstructure. Highly dense martensite laths can be observed within various prior austenite grain boundaries. The steel when ART treated at 650 °C resulted in the stabilization of austenite phase (shown with arrows in Fig. 4b) along with the martensite phase (Fig. 4b).

Dependence of experimental retained austenite volume % has been found to be in compliance with the prediction made from the above model calculation. Determination of retained austenite volume % using thermodynamic calculations has been a routine thing to be carried out for medium Mn steels. Several authors have reported the effect of intercritical temperature on the retained austenite stabilization and the ensuing mechanical properties. To this end, a significant difference in the retained
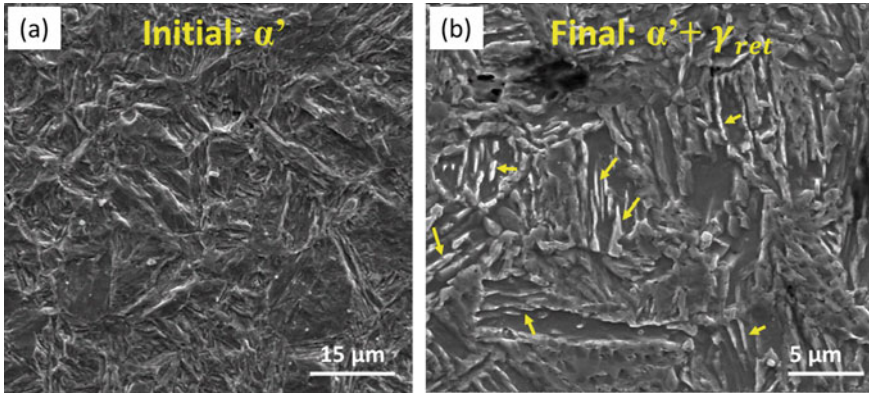
Fig. 4 **a** As hot-rolled microstructure consisting of martensite laths, **b** microstructure after ART treatment possessing retained austenite, indicated with arrows

austenite content was observed in the Fe-5Mn-0.25C wt.% medium Mn steel. Accordingly, the tensile properties showed marked variation. Figure 5 shows the true stress–strain curve of the Fe-5Mn-0.25C wt.% medium Mn steel ART treated at 650 °C, and 670 °C, respectively. The corresponding retained austenite content before the tensile test in heat treated specimens has been shown in Fig. 5. It is noteworthy that there occurred a significant variation in the retained austenite volume % even with a small variation in the intercritical temperature of 20 °C. The retained austenite content was found to be in compliance with the predicted values in Fig. 3d. Further, the tensile properties also found to vary significantly with the intercritical temperature. The specimen with greater retained austenite content showed lower strength but higher ductility in comparison with the specimen having lesser retained austenite content. In this context, austenite phase having the FCC structure have higher number of

Fig. 5 A true stress–strain plot of Fe-5Mn-0.25C medium Mn steel ART treated at 650 and 670 °C
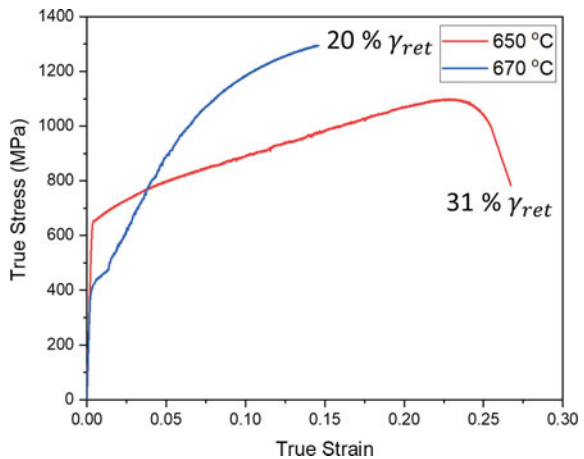
slip system than BCC structure and therefore can be easily deformed upon loading. In an another work, Bansal et al. [5] have also showed variation in the retained austenite content with intercritical annealing temperature. In that study, a medium Mn steel of composition, Fe-4.75Mn -0.09C-1.24Si-0.64Al wt.%, was found to be sensitive with the intercritical temperature. Retained austenite content first increased and then decreased with increasing the ART annealing temperature in an interval of 20 °C. The maximum retained austenite was stabilized for the temperature greater than the cementite dissolution temperature, confirming the importance of the C in austenite stabilization. Further, the strength as well as the ductility increased with the increase in the retained austenite content in the microstructure. In an another study, the temperature sensitivity of retained austenite formation in a medium Mn steel (Fe-6Mn-0.15C-1.5Si-1Al wt.%) was showcased by Kim et al. [16]. Retained austenite volume % was found to increase significantly with the increase in the ART annealing temperature by just 20 °C. The tensile properties of the steel also varied drastically with a small variation in temperature of the order of 10–20 °C. Interestingly, the specimen with greater retained austenite content exhibited greater strength. In this context, it is general belief that a greater retained austenite content in the microstructure lead to improvement in ductility and decrease in the strength of the steel. This is because of the fact that austenite phase is a close packed face centered cubic crystal structure with a large number of slip systems and hence can be deformed easily. This notion is partially true and needs an amendment. Along with slip, austenite phase can deform via martensitic transformation and/or twinning. Both the martensitic transformation and twin is known to provide excellent work hardening during deformation and the related phenomena are known as TRIP and TWIP effects, respectively. Hence, the presence of austenite in the microstructure can improve the strength as well. SFE of the austenite phase greatly influences the onset of TRIP or TWIP effect [17–22]. It is known that SFE less than 18–20 mJ/m^2 triggers TRIP effect while that in between 20–45 mJ/m^2 triggers TWIP effect in the austenite phase. Austenite phase with SFE greater than 45 mJ/m^2 deform preferably via slip. In the purview of work hardening during the deformation, TWIP effect is known to be the superior. SFE is composition and temperature dependent, therefore, can be tuned as per the requirement. Hence, in the above mentioned cases, the increase in strength as well as ductility can be associated with optimum SFE which would have triggered TRIP or/and TWIP effects in the specimens during deformation instead of just simple slip.

2.2　Influence of Intercritical Annealing Time

The model for retained austenite volume % prediction has an inherent assumption that all the processes are being carried out at equilibrium. The kinetics of evolution of austenite phase during intercritical holding and subsequent partitioning of alloying

elements was not considered. However, this may not be correct for each case as the austenite evolution kinetics is highly dependent on various other factors such as initial state of the specimen (forged/hot rolled or cold rolled) and initial microstructure (prior austenite grain size, presence of pre-existing austenite, martensite lath characteristics). One of the major objective of the ART annealing treatment is to obtain the maximum amount of retained austenite in the final microstructure and the amount of retained austenite depends on the factors such as intercritical austenite volume %, the extent of elemental partitioning, the morphological evolution of the intercritical austenite etc. All these factors are time dependent and have a direct influence on the retained austenite content in the final microstructure. Hence, in order to obtain maximum amount of retained austenite in the final microstructure, it is important to perform ART annealing treatment for an optimum time duration such that the above mentioned time dependent factors must be well taken into account. Various authors have revealed the kinetics effect of austenite reversion in medium Mn steel [2, 5, 23]. Kinetics of austenite reversion and subsequent partitioning of alloying elements have important implications on the mechanical properties of the steel. Mechanical stability of the retained austenite phase is directly dependent on the stacking fault energy (SFE) of the austenite phase as discussed in the previous section. The occurrence of various work hardening effects in the austenite phase is SFE dependent. Since SFE is composition dependent and the composition of the austenite phase in medium Mn steel evolve with time, the mechanical properties of the steel would vary with varying the duration of ART annealing. In this context, Chandan et al. has showcased the importance of intercritical annealing duration vis-à-vis SFE of the austenite phase on the deformation behavior (of retained austenite) and mechanical properties of a Fe-4.75Mn-0.18C-0.4Al-0.8Si medium Mn steel [3]. It has been shown that the SFE of the austenite phase varies from 9 mJ/m^{-2} to 20 mJ/m^{-2} in the hot-rolled steel which was ART treated at 650 °C for 2 h and 4 h, respectively. The consequent deformation behavior of the retained austenite phase changed from TRIP in the 2 h annealed specimen to TWIP in the 4 h annealed specimen. The change in the deformation behavior from TRIP to TWIP led to significant enhancement in the tensile property of the 4 h annealed specimen [3]. It was shown that the increase in the SFE of the 4 h annealed specimen was primarily due to the increase in the Mn content of the austenite phase with increased intercritical holding time. Bansal et al. carried out a detailed study on the temporal evolution of retained austenite in a medium Mn steel of composition, Fe-4.75Mn −0.09C-1.24Si-0.64Al wt.% [5]. They also proposed a methodology to predict the retained austenite content at room temperature for varied annealing durations. It was shown that the samples annealed at different temperatures ranging from 570 to 670 °C (at an interval of 20 °C) stabilized increasing amount of retained austenite with increasing time duration. This increase in the austenite volume fraction with increasing time duration has an important implication on the mechanical properties of medium Mn steels. In this context, Xu et al. showed that both strength and ductility of the medium Mn steel increased with the increase in the retained austenite fraction which was resultant of the increased time duration of ART annealing. Thus, introduction of retained

austenite in the microstructure can be useful in overcoming the so-called strength-ductility trade-off. The simultaneous improvement in strength and ductility can be associated with the onset of TRIP and/or TWIP mechanism in the austenite phase during deformation of the steel.

3 Concluding Remarks

From the above discussion, it is clear that both intercritical annealing temperature and time are most important parameters to be controlled in order to achieve the required retained austenite phase content in the final microstructure. Furthermore, both temperature and time must be suitably chosen in order to achieve the appropriate stability and SFE of the retained austenite phase and hence enhanced mechanical property. The importance of temperature lies in the fact that the elemental distribution in austenite phase is highly dependent on the intercritical temperature as per the equilibrium condition. However, the achievement of equilibrium requires a finite amount of time, which are generally not possible to employ in an industrial environment. Therefore, the kinetics of intercritical austenite phase evolution and subsequent partitioning of alloying elements needs to be considered as well. Apart from the ART temperature and time, selecting an alloy with suitable composition is another facet which must be looked upon carefully. The thermodynamic model calculation described can be utilized for predicting the retained austenite and its composition. Additionally, thermodynamic models for composition and temperature based SFE calculations [18, 19] can be employed for prediction of the tentative SFE of the austenite phase. Accordingly, the deformation behavior of the austenite phase can be ensured to either TRIP or TWIP or combination of both. In this way, the mechanical property of medium Mn steels, which is highly dependent on the austenite phase, can be tuned as per the requirement.

References

1. Worldautosteel (2011) Future steel vehicle—final engineering report. http://Www.Autosteel.Org/Programs/Future%20steel%20vehicle.Aspx
2. Mishra G, Chandan AK, Kundu S (2017) Hot rolled and cold rolled medium manganese steel: mechanical properties and microstructure. Mater Sci Eng A 701:319–327. https://doi.org/10.1016/j.msea.2017.06.088
3. Chandan AK, Mishra G, Mahato B, Chowdhury SG, Kundu S, Chakraborty J (2019) Stacking fault energy of austenite phase in medium manganese steel. Metall Mater Trans A 50:4851–4866. https://doi.org/10.1007/s11661-019-05367-x

4. Chandan AK, Bansal GK, Kundu J, Chakraborty J, Chowdhury SG (2019) Effect of prior austenite grain size on the evolution of microstructure and mechanical properties of an inter-critically annealed medium manganese steel. Mater Sci Eng A 768(138458). https://doi.org/10.1016/j.msea.2019.138458

5. Bansal GK, Madhukar DA, Chandan AK, Ashok K, Mandal GK, Srivastava, VC (2018) On the intercritical annealing parameters and ensuing mechanical properties of low-carbon medium-Mn steel. Mater Sci Eng A 733:246–256. https://doi.org/10.1016/j.msea.2018.07.055

6. Bansal GK, Rajinikanth V, Ghosh C, Srivastava VC, Kundu S, Chowdhury SG (2018) Microstructure–property correlation in low-Si steel processed through quenching and nonisothermal partitioning. Metall Mater Trans A 49:3501–3514. https://doi.org/10.1007/s11661-018-4677-1

7. Bansal GK, Junior LP, Ghosh C, Rajinikanth V, Tripathy S, Srivastava VC, Bhagat AN, Chowdhury SG (2020) Quench temperature-dependent phase transformations during nonisothermal partitioning. Metall Mater Trans A 51:3410–3424. https://doi.org/10.1007/s11661-020-05779-0

8. Bansal GK, Rajinikanth V, Ghosh C, Srivastava VC, Dutta M, Chowdhury SG (2020) Effect of cooling rate on the evolution of microstructure and mechanical properties of nonisothermally partitioned steels. Mater Sci Eng A 788, art no. 139614. https://doi.org/10.1016/j.msea.2020.139614

9. Bansal GK, Pradeep M, Ghosh C, Rajinikanth V, Srivastava VC, Bhagat AN, Kundu S (2019) Evolution of microstructure in a low-Si micro-alloyed steel processed through one-step quenching and partitioning. Metall Mater Trans A 50:547–555. https://doi.org/10.1007/s11661-018-5039-8

10. Lee Y-K, Han J (2015) Current opinion in medium manganese steel. Mater Sci Technol 31:843–856. https://doi.org/10.1179/1743284714Y.0000000722

11. Zackay VF, Parker ER, Fahr D, Busch R (1967) The enhancement of ductility in high-strength steels. ASM Trans Quart 60(2):252

12. Emmanuel DM, David KM, Speer JG, Matthew JM (2011) Austenite stabilization through manganese enrichment. Scripta Mater 64:185–188. https://doi.org/10.1016/j.scriptamat.2010.09.040

13. Andersson JO, Helander T, Hoglund L, Shi PF, Sundman B (2002) Thermo-Calc and DICTRA, computational tools for materials science. Calphad 26:273–312. https://doi.org/10.1016/S0364-5916(02)00037-8

14. Mahieu J, Maki J (2002) Phase transformation and mechanical properties of si-free CMnAl transformation induced plasticity-aided steel. Metall Mater Trans A 33:2573. https://doi.org/10.1007/s11661-002-0378-9

15. Koistinen DP, Marburger RE (1959) A general equation prescribing the extent of the austenite-martensite transformation in pure iron-carbon alloys and plain carbon steels. Acta Metall 7:59–60. https://doi.org/10.1016/0001-6160(59)90170-1

16. Kim JK, Kim JH, Suh DW (2019) Partially-recrystallized ferrite grains and multiple plasticity enhancing mechanisms in a medium Mn steel. Mater Charact 15:109812. https://doi.org/10.1016/j.matchar.2019.109812

17. El-Danaf E, Kalidindi, Doherty SR (1999) Influence of grain size and stacking-fault energy on deformation twinning in fcc metals. Metall. Mater Trans A 30A:1223–33. https://doi.org/10.1007/s11661-999-0272-9

18. Curtze S, Kuokkala V (2010) Dependence of tensile deformation behavior of TWIP steels on stacking fault energy, temperature and strain rate. Acta Mater 58:5129–5141. https://doi.org/10.1016/j.actamat.2010.05.049

19. Allain S, Chateau JP, Bouaziz O, Migot S, Guelton N (2004) Correlations between the calculated stacking fault energy and the plasticity mechanisms in Fe–Mn–C alloys. Mater Sci Eng A 387–389:158–162. https://doi.org/10.1016/j.msea.2004.01.059

20. Lee Y-K (2012) Microstructural evolution during plastic deformation of twinning-induced plasticity steels. Scripta Mater 66:1002–1006. https://doi.org/10.1016/j.scriptamat.2011.12.016

21. Sato K, Ichinose M, Hirotsu Y, Inoue Y (1989) Effects of deformation induced phase transformation and twinning on the mechanical properties of austenitic Fe–Mn–Al Alloys ISIJ Int 29:868–77. https://doi.org/10.2355/isijinternational.29.868
22. Cooman BCD, Kwon O, Chin K-G (2012) State-of-the-knowledge on TWIP steel. Mater Sci Technol 28:513–527. https://doi.org/10.1179/1743284711Y.0000000095
23. Xua HF, Zhaoa J, Cao WQ, Shi J, Wang CY, Wang C, Li J, Dong H (2012) Heat treatment effects on the microstructure and mechanical properties of a medium manganese steel (0.2C–5Mn). Mater Sci Eng A 532:435–442. https://doi.org/10.1016/j.msea.2011.11.009